UNIVERSITÉ DE GRENOBLE

THÈSE

Pour obtenir le grade de

DOCTEUR DE L'UNIVERSITÉ DE GRENOBLE

Spécialité : **Géochimie de l'Environnement**

Arrêté ministériel : 7 août 2006

Présentée par

« Regina / KIRSCH »

Thèse dirigée par **« Laurent/ CHARLET »** et
codirigée par **« Andreas C./ Scheinost »**

préparée au sein de l'**Institut des Sciences de la Terre (ISTerre)**
dans **l'École Doctorale : Terre, Univers, Environnement**

Réactions redox du plutonium et de l'antimoine avec des minéraux de fers en milieux anoxique

Thèse soutenue publiquement le **« xx xx xx »**,
devant le jury composé de :

Prof. Horst Geckeis Pr. à l'Université de Karlsruhe, Dir. de l'Institut für nukleare Entsorgung (KIT-INE)	Rapporteur
Dr. Guillaume Morin Directeur de recherches au CNRS, IMPCM, UPMC, Paris	Rapporteur
Prof. Christophe Den Auwer Pr. à l'Université de Nice Sophia Antipolis, PCRE	Examinateur
Dr. Christoph Hennig HZDR, Dresden et ROBL beamline (ESRF), Grenoble	Examinateur
Prof. Laurent Charlet Pr. à l'Université de Grenoble	Directeur
Andreas C. Scheinost HZDR, Dresden et ROBL beamline (ESRF), Grenoble	Co-Directeur

Abstract

Redox reactions of Sb(V) and Sb(III) with mackinawite (FeS) and of aqueous Pu(III) and Pu(V) with various Fe(II)-bearing minerals and Fe(III)-oxides have been investigated under anoxic conditions. X-ray absorption spectroscopy was used to analyze oxidation state and local coordination environment of Sb and Pu associated with the solid phase.
After reaction with mackinawite, chukanovite and magnetite, PuO_2, Pu(III) or mixtures of the two oxidation states were observed. On magnetite, a tridentate Pu(III) surface complex could be identified from EXAFS combined with Feff-Monte-Carlo simulation. The relative amount of Pu(III) depends on the type of mineral, the solid/solution ratio, the system pe and pH, and, potentially, the particle size and crystallinity of the formed PuO_2 solid phase. With mackinawite at pH 6.2 and a surface loading of 67 nmol/m^2 and with magnetite up to pH 8.4 and a surface loading of 56 nmol/m^2, only Pu(III) was identified associated with the solid phase. With maghemite containing residual Fe(II) at pH6, Pu(III) and Pu(IV) were present in, probably, inner-sphere surface complexes similar to the one formed by Pu(III) on magnetite. Under the given conditions (surface loadings ≤ 77 nmol/m^2) formation of PuO_2 was not observed. After reaction with hematite and goethite, Pu(IV) was the predominant oxidation state associated with the solid phase.
Sorption and reduction of Sb(V) on mackinawite were strongly pH dependent. At acidic pH, sorption was fast and Sb(V) was completely reduced to an Sb(III)-sulfide complex associated with the solid phase. Reduction of Sb(V) was coupled to oxidation of mackinawite and formation of a greigite (Fe_3S_4) phase could be observed by XRD. At basic pH, Sb(V) was slowly removed from solution and reduction to Sb(III) was complete only at very small Sb/FeS ratios. At higher Sb/FeS, Sb(V) removal occurred partly through reduction to solid phase associated Sb(III)-S_3 and partly through co-precipitation with Fe(III).
In conclusion, it could be shown that Fe(II) bearing minerals can effectively contribute to the reduction and immobilization of antimony and plutonium, two contaminants of growing environmental importance.

Résumé

Les réactions d'oxydoréduction de l'antimoine (V) et (III) avec la mackinawite (FeS) et du plutonium (III) et (V) avec plusieurs minéraux à fer(II) et des oxydes de fer(III) ont été étudiées dans des conditions d'anoxie. La spectroscopie d'absorption des rayons X fut utilisée pour l'analyse de l'état d'oxydation et de la structure locale du Sb et Pu associés à la phase solide.
Après réaction avec la mackinawite, la chukanovite et la magnétite, PuO_2, Pu(III) ou des mixtures des deux états d'oxydation ont été observé. A la surface de la magnétite un complexe tridenté du Pu(III) a pu être mis en évidence à l'aide des spectres EXAFS couplé à une simulation de Monte-Carlo utilisant le code de calcul Feff. La quantité relative de Pu(III) est fonction de l'espèce minérale, du ratio solide/liquide, des valeurs pe et pH du système et, potentiellement, de la taille de particule et de la cristallinité de la phase solide de PuO_2 en présence de laquelle le Pu(III) existe. Avec la mackinawite à pH 6,2 et à une occupation de surface de 67 nmol/m^2 et avec la magnétite jusqu'à pH 8.4 et 56 nmol/m^2 de Pu, uniquement du Pu(III) fut trouvé associé à la phase solide. Avec la maghémite contenant du fer(II) résiduel à pH6 Pu(III) et Pu(IV) était, probablement, présents dans des complexes de surfaces similaire à celui formé par le Pu(III) sur la magnétite. Dans les conditions expérimentales (couverture de surface ≤ 77 nmol/m^2), aucune formation de PuO_2 ne fut observé. Après réaction avec l'hématite et la goethite Pu(IV) était l'état d'oxydation prédominant associé à la phase solide.
La sorption et la réduction du Sb(V) avec la mackinawite était fortement fonction du pH. A pH acide la sorption était rapide et Sb(V) fut complètement réduit en Sb(III), formant un complexe Sb(III)-S_3 probablement associé à la surface de la mackinawite. La réduction du Sb(V) était couplée à l'oxydation de la mackinawite et la greigite (Fe_3S_4) fut détectée par XRD. A pH basique, la sorption du Sb(V) est lente et la réduction vers le Sb(III) n'était complète qu'à des ratios de Sb/FeS très bas. Pour des valeurs plus élevé de Sb/FeS la sorption de Sb se faisait en partie par la réduction envers le complexe de Sb(III)-S_3 et en partie par une co-précipitation avec le Fe(III).
Il a pu être démontré que les minéraux à fer(II) peuvent effectivement contribuer à la réduction et à l'immobilisation de l'antimoine et du plutonium qui sont des contaminants environnementaux d'importance croissante.

Index

List of abbreviations

BET	Brunnauer Emmet Teller
CN	Coordination Number
DW	Debye-Waller Factor
EV	Eigen vector
EXAFS	Extended X-ray Absorption Fine Structure
FT	Fourier Transform
HG-AFS	Hydride Generation – Atomic Fluorescence Spectroscopy
ICP-MS	Inductively Coupled Plasma – Mass Spectrometry
ITT	Iterative target test (implemented in ITFA)
ITFA	Iterative transformation factor analysis, PCA software from A. Rossberg et al. (2003)[1]
LSC	Liquid Scintillation Counting
LC	Linear combination (used in the context of linear combination fitting)
NOM	Natural organic matter
PCA	Principal component analysis
SSA	Specific Surface Area
$sigma^2$, σ^2	Mean square radial displacement (also called Debye Waller factor)
WL	White line
XAS	X-ray Absorption Spectroscopy
XANES	X-ray Absorption Near Edge Structure

1. Introduction

Chemically and structurally, i.e. with respect to their electron configurations and the types of solids and solution complexes they form, Sb and Pu do not have much in common, apart, probably, from the fact that, similarly to many other elements, they can both exist in several, in their characteristics differing, oxidation states. In addition to the zero-valent elements these are –III, III and V for Sb[2] and III, IV, V, VI,[3] and, under certain conditions, VII or VIII for Pu.[4]

Plutonium is similar to e.g. chromium and technetium among the transition metals, selenium among the main group elements, and uranium among the actinides in having one oxidation states that through the solids, coprecipitates or surface complexes it forms has a much lower solubility than the others[5-9]. For antimony, the dependence of solution concentration on the oxidation state is more complex: solubility controlling solid phases are dependent on the environment (e.g. Sb_2S_3 in anoxic sulfidic vs Sb_2O_3 under oxic conditions), both Sb(III) and Sb(V) can be adsorbed to iron(hydr)oxides, clays and other minerals and solubilities of mixed oxides such as e.g. tripuhyite ($FeSbO_4$) have not been determined.[10-12]

Generally, oxidation states often differ in their hydrolysis constants and complexation reactions of dissolved species in presence of organic or inorganic ligands, in sorption reactions to biologic or mineral surfaces and in solubility of the solids they form. Due to blocking of active sites of enzymes or passing through ion channels of cells by one but not by another, species of different oxidation states of a given element also often vary in their toxicity towards living organims. The oxidation state therefore crucially influences the environmental migration behavior of an element, that is, by virtue of what mechanisms and to what extent it is transported.

Changes in oxidation state occur through redox reactions that thermodynamically can be described through equilibrium constants as a function of the activities of the species taking part in the reaction. If half-reactions are written in which electrons appear as separate species similar to protons, a parameter that characterizes the redox potential, the pe, can be defined, in analogy to pH, as the negative decadic logarithm of the electron activity, which is, however, a hypothetic value as electrons do not exist as separate, hydrated entities in solutions.[13] Which oxidation state predominates over the others under certain conditions can then be calculated as a function of system parameters such as pe, pH, ionic strength and temperature.

A contaminant's oxidation state is largely though not necessarily completely[14, 15] controlled by the redox reactions it undergoes with the components of the system, or the "environment", it is part of, i.e. a more or less open or closed system composed of solid, liquid and gaseous phases, organic and inorganic matter and, potentially, living organisms. Thus, the better an environment can be characterized with respect to its system parameters and components and the better the thermodynamics and kinetics of the chemical reactions between these components and a contaminant element are

known, the better the element's oxidation state and speciation and its migration behavior can be understood and, potentially, modelled and predicted.

Unfortunately, it is difficult to fully and accurately characterize many, in particular, inhomogeneous, natural systems whose components are not necessarily in equilibrium with each other. Thus it is, e.g., not always clear what a measured redox potential represents and to what extent one value captures correctly what redox reaction a contaminant might undergo once it enters into the system to which this value was assigned.

Apart from these general difficulties, a predictive approach based on system parameters and the implementation of chemical reactions into geochemical (transport) models is, at present, often hampered by a lack of thermodynamic parameters for reactions that potentially could be important but that have never been investigated or not under environmentally relevant conditions.

Sorption onto mineral surfaces and (surface mediated) redox reactions with minerals under anoxic conditions are part of these reactions that are relevant to the prediction of the environmental fate of many metal and metalloid contaminants but that have not been investigated extensively and for which thermodynamic constants are often not available.

Probably two reasons are mainly responsible for the relatively large amount of still unexplored reactions in this domain, one being the difficulty, at least with actinides, to work under anoxic conditions. The second reason is that spectroscopic techniques, such as X-ray absorption spectroscopy, for the *in-situ* characterization of the reaction products with respect to oxidation state and local coordination environment have become available only quite recently for the analysis of radioactive and environmental samples containing relatively low concentrations of the element being analyzed.

Antimony and plutonium have thus in common that many of their sorption and redox reactions with minerals in general, and with iron minerals in particular, have either not been investigated or not under anoxic conditions.

The importance of iron minerals lies in their ubiquity as soil and sediment constituents and, in the context of nuclear waste disposal, in their occurrence as corrosion products of steel that is used as barrier material in most concepts for the geologic long-term confinement of nuclear waste.

In water-logged soils and sediments, anoxic conditions are established through microbial activity due to the consumption of oxygen as electron acceptor, the oxygen inflow through diffusion being very small compared to the consumption. Once oxygen has been consumed, a range of other electron acceptors can be used in microbially mediated redox processes, among them the reduction of Fe(III) oxide to Fe(II) and sulfate reduction.[13] In presence of Fe(II) and sulfide, nanoparticulate mackinawite (tetragonal FeS), is the first, thermodynamically metastable iron sulfide that precipitates and over time and through different pathswyas transforms into pyrite (FeS_2).[16]

Also for repositories for high and intermediate level nuclear waste, near field anoxic conditions have been predicted[17] to be established after an initial oxic phase. Steel corrosion experiments and archeologic analogues studies have shown a range of iron minerals to be formed under the predicted

conditions, among them magnetite, mackinawite, and chukanovite.[18]

Investigating the redox chemistry of antimony and plutonium under anoxic conditions is thus important for understanding and predicting their environmental fate. Using X-ray absorption spectroscopy, it is possible to assess the *in-situ* oxidation states and local structures of the reaction products, leading to a better understanding and, ultimately, therdmodynamic description, of the reactions involved.

1.1. Antimony in the environment

Antimony is a toxic trace element with no known biologic function and, due to their toxicity, antimony containing compounds are used for the treatment of protozoan diseases such as leishmaniasis.[19] For more than thirty years, antimony and its compounds have been considered as pollutants of priority interest by USEPA (1979) and the EU (1976); in the EU a maximum admissible concentration in drinking water of 5 µg/L was established in 1998.[20] Sb(III) is reported to be more toxic than Sb(V) and can enter cells by passing through specific transport channels such as aqua- and glyceroporins.[21-23]

Antimony has wide range of industrial applications including alloying to lead in car batteries and amunition, use as a catalyst in PET production, addition of Sb_2S_3 to brake linings and in the semiconductur industry, where it is, e.g., the most common n-type dopant for SnO_2.[20, 24] More than 80 % of the annually produced about 140.000 tons (in 1999) are mined in China and more than half of antimony is used in the form of Sb_2O_3 as flame retardant in plastics, leading to high concentrations in municipal (10 – 60 ppm) and electronic waste (up to 3-4 wt % for higly fire-retarded plastics).[20, 25] As a byproduct of Cu, Pb and Zn smelting, during municipal waste incineration and burning of coal considerable amounts of Sb are introduced into the atmosphere, having led to a 50% enrichment increase in arctic air during the last three decades.[26, 27] Up to 300 mg/L antimony have been found in leachates from industrial landfills and several hundred ppm in contaminated soils and sediments near smelters and mines;[20, 28, 29] through intake of water and locally grown vegetables such high concentrations can lead to considerable health risks for local populations.[30]

Antimony distribution in Europe is highly heterogenous and distribution paterers on the continental scale are dominated by natural variation (Fig. 1.1a). The border between higher and lower Sb soil contents between southern and northern Europe follows the extent of glaciation and is related to the soil properties (younger, coarser grained soils in northern vs older, finer grained soils in souhern Europe).[31] However, urban Sb contamination, that is largely caused by mechanical wear of Sb containing brake linings,[32-34] is common (Fig. 1.2b) and urban soils show the highest median Sb contents of any soils.[31]

Based on thermodynamics, Sb(V) is expected to be the stable oxidation state under oxic conditions whereas Sb(III) is expected to dominate under anoxic conditions. However Sb(III) has been detected in oxic and up to 50 % Sb(V) in anoxic waters. Similar to arsenic, antimony can undergo biomethylation by bacteria and fungi, which can lead to increased mobility under reducing

conditions.[20, 35-37] Stibnite, Sb_2S_3, is the common antimony mineral and both Sb(III) and Sb(V) can form soluble sulfide complexes.[20, 38-42]

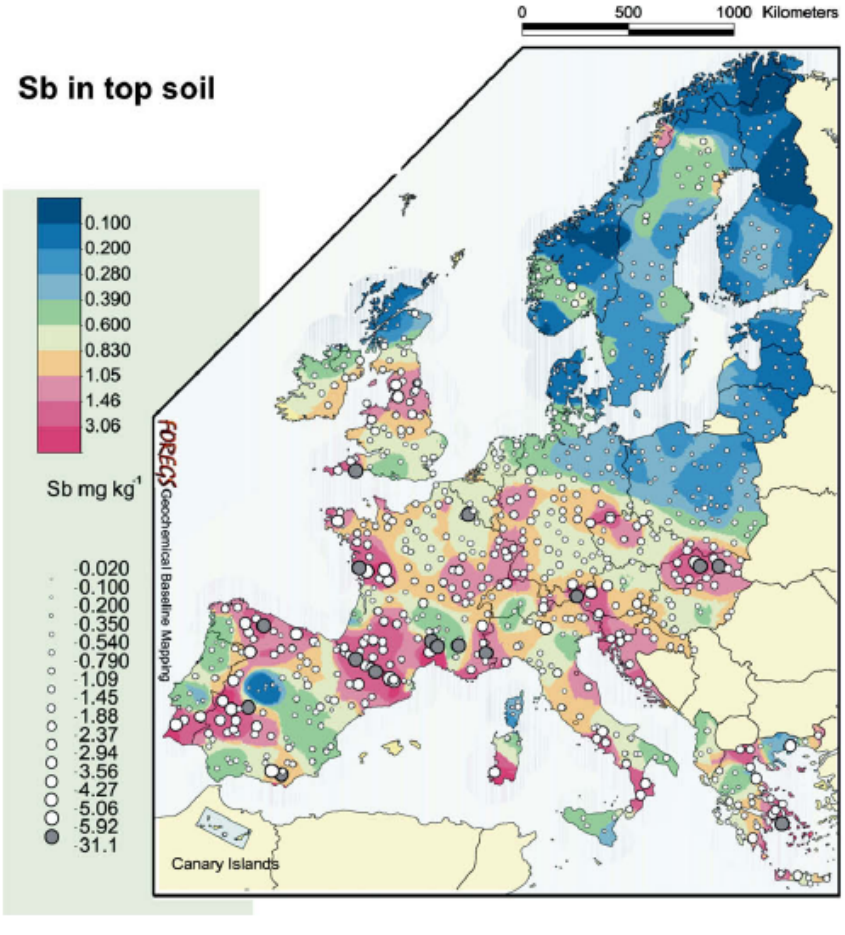

Figure 1.1. a) Antimony concentrations in top soil in Europe, b) antimony concentration in Berlin top soils (both from Reimann et al., 2010).[31]

In aerobic soils Sb(V) is the dominant species and has been shown by EXAFS to be bound to iron (hydr)oxides.[43, 44] Antimony was also found complexed by humic acids and is, for this reason, enriched in organic soils[31, 45, 46]. In mine tailing under oxic conditions at circumneutral pH, Sb was

found to be less mobile than As.[47, 48] Unlike As, Sb does not inhibit crystallization of iron oxides, its retention in iron oxides is not limited by certain Fe/Sb ratio and at high Fe and Sb concentrations, tripuhyite ($FeSbO_4$) can precipitate.[47, 49] While the oxidation of Sb(III) by various oxidants including mineral surfaces was intensively investigated in recent years,[11, 50-52] still little is known about the kinetics and mechanism of Sb(V) reduction on mineral surfaces. E.g., Sb(V) formed inner- and outer-sphere complexes with sulfate green rust, but was not reduced with this potentially reductive phase.[53] With magnetite, in contrast, pH dependent reduction of Sb(V) to Sb(III) was observed by XAS.[54] For reducing freshwater lake sediments, control of Sb solubility by iron sulfides was suggested.[55]

Antimony also occurs as a fission product of uranium; among the radioactive isotopes ^{125}Sb is the longest lived with a half-life of 2.7 years.[56] After the nuclear accident in Chernobyl in 1986, its deposition pattern was found similar to that of cesium, suggesting that it behaved like a volatile nuclide concerning release and transport.[57] Due to its presence in low-level liquid radioactive waste, also ^{124}Sb is of concern.[58]

1.2. Plutonium in the environment

Plutonium is the major transuranium actinide in civial and military nuclear waste. Through atmospheric and underground weapons testing (e.g. at the Nevada test site), nuclear accidents (Tchernobyl, Fukushima) and leakage or "controlled release" from storage and processing plants of nuclear material considerable environmental contamination with plutonium has occurred, e.g. at he Savannah River and Hanford (US) sites, in the Lake Karachai region (Mayak, Russia), and in Sellafield (UK)). Due to its high chemical and radio-toxicity, its migration behavior has been intensively studied, e.g. through lysimeter experiments with natural sediments.[59-61] Pu is not equally associated with different types of minerals and e.g. after sorption to natural tuff, Pu has been found associated with a manganese oxide andnot with hematite[62]. In other circumstances, Pu was found associated with iron (hydr)oxide colloides,[63, 64] through which it underwent colloid-facilitated transport. Processes influencing Pu migration behavior and uptake by living organisms, e.g. complexation and redox reactions of Pu with humic substances, peptides, and proteins, with bacteria and with minerals have been investigated.[65-70] Minerals adsorption studies were mostly carried out under oxic conditions, thus limiting the applicability of these results to anoxic, reducing environments.

1.2.1. Plutonium redox chemistry

In aqueous systems Pu exits commonly in four oxidation states: III, IV, V, VI.[14] Tri- and tetravalent ions exist hydrated in solution while penta and hexavalent Pu exists in the form of trans-dioxo cations (PuO_2^+ and PuO_2^{2+}), resulting in effective charges of +4 for Pu(IV), +3.3 for Pu(VI), +3 for Pu(III) and +2.3 for Pu(V). Hydrolysis, complex formation with dissolved ligands and sorption to surfaces are for Pu, a hard Lewis acid, highly electrostatic in nature and the stability of solution complexes and solids follows the order of effective charges. This results in Pu(IV) solids ($Pu(OH)_4$(s) or PuO_2(am,hyd))

being the most stable and least soluble and in Pu(V) complexes and solids being the least stable and most soluble among the four oxidation states.[14, 71] The migration of Pu(V) is thus expected to be least impeded by precipitation of a Pu(V) solid or by sorption onto mineral surfaces. As a Pu contamination is thus more likely to migrate as Pu(V) than as Pu(IV), for example, and because Pu(V) is expected to be the dominant oxidation state in aerobic waters,[14] the sorption of Pu(V) to mineral surfaces has been extensively studied under oxic conditions. In a number of cases when Pu(V) was sorbed to iron(III) oxides, reduction to Pu(IV) was observed, even though no obvious reductant was present. This was explained either by the presence of traces of Fe(II) or by the stability of the forming Pu(IV) surface complexes or hydrolysis products.[72-75]

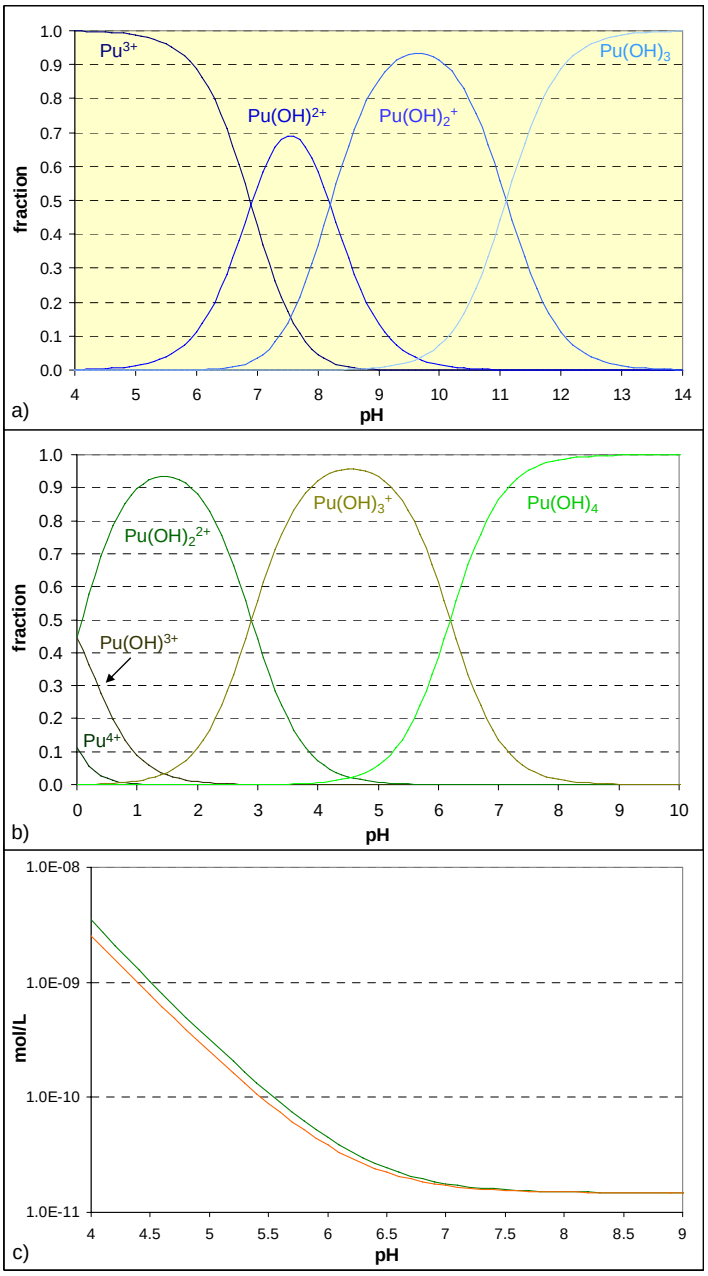

Figure 1.2. Hydrolysis species of Pu(III) (a) and hydrolysis species of Pu(IV) (b) as a function of pH at I = 0 mol/kg. c) Dissolved Pu(IV) in equilibrium with PuO_2(am,hyd) as a function of pH at I = 0 m (orange) and I = 0.1 m (green).

Generally, reduction of Pu(V) to Pu(IV) can lead to the immobilization of Pu in a Pu(IV) solid phase and thus retard its migration in the environment. However, Pu(IV) hydrolysis species tend to oligomerize and form intrinsic colloids that can be very stable over long periods of time, are characterized by a solubility about two order of magnitude higher than PuO_2(am,hyd) and can be transported, as eigen- or pseudo-colloids, over long distances, thus complicating predictions on Pu concentrations and migration behavior.[8, 63, 64, 76, 77] Under reducing acidic conditions Pu(V) is expected to be reduced to Pu(III), not Pu(IV). However, PuO_2(am,hyd) is expected to be the solubility controlling solid phase in equilibrium with Pu(III) as $Pu(OH)_3$(s) was found to be unstable and convert unter reducing conditions in the stability field of water into PuO_2(s,hyd).

pe-pH predominance diagrams are commonly used to visualize changing relative stabilities between solution species or solution species and solids as a function of redox potential and pH. In each region, enclosed by boundary lines that were calculated based on equilibrium constants, a solid phase or solution species will be predominant.[78] The first step to establish which equilibria between hydrolysis species of the different oxidation states have to be considered for the calculation of a pe-pH diagram is to calculate the hydrolysis species of Pu as a function of pH (Fig. 1.2).

For example, the equilibrium between Pu^{3+} and $PuOH^{2+}$ can be expressed by the following equation:

$$Pu^{3+} + H_2O \rightleftarrows PuOH^{2+} + H^+ \quad (1.1)$$ with

$$K = \{PuOH^{2+}\}\ \{H^+\} / \{Pu^{3+}\}\{H_2O\} \quad (1.2).$$

The equilibrium constant K (eq. 1.2) can be obtained from the D_rG value of the reaction that can be calculated if the Δ_fG values for all participating species are known as

$$\ln K = -\Delta_rG / RT \quad (1.3)$$

(with R – gas constant (8.314 J/mol K) and T – temperature in K).

The pH at which the two species have the same activity, pH_{eq}, is then, if the activity of water is 1, obtained from: $\log K = \log(\{PuOH^{2+}\}/\{Pu^{3+}\}) - pH$,

thus $pH_{eq} = -\log K$. In the same way, equations between different redox species can be written, e.g.

$$Pu(OH)_3^+ + e^- + 3\ H^+ \rightleftarrows Pu^{3+} + 3\ H2O \quad (1.4)$$

and, if $\{H_2O\} = 1$,

$$pe = \log K - \log(\{Pu^{3+}\}/\{Pu(OH)_3^+\}) - 3\ pH. \quad (1.5)$$

The redox equilibrium between Pu^{3+} and PuO_2(am,hyd) can be expressed as

$$PuO_2(am,hyd) + e^- + 4\ H^+ \rightleftarrows Pu^{3+} + 2\ H_2O \quad (1.6),$$

thus

$$K = \{Pu^{3+}\}\ \{H_2O\}^2 / \{e^-\}\{H^+\}^4 \quad (1.7)$$

and

$$pe = \log K - \log\{Pu^{3+}\} - 2 \log \{H_2O\} - 4\ pH \quad (1.8).$$

As shown in eq. 1.8, to plot the dependence of pe over pH as a line delineating the predominance fields of Pu^{3+} and PuO_2(am,hyd) into a pe-pH diagram for Pu, a Pu^{3+} activity has to be fixed (Fig. 1.3). If, in contrast, one is interested in the activity of Pu^{3+} in equilibrium with a PuO_2(am,hyd) solid phase, pH and pe have to be given as input.

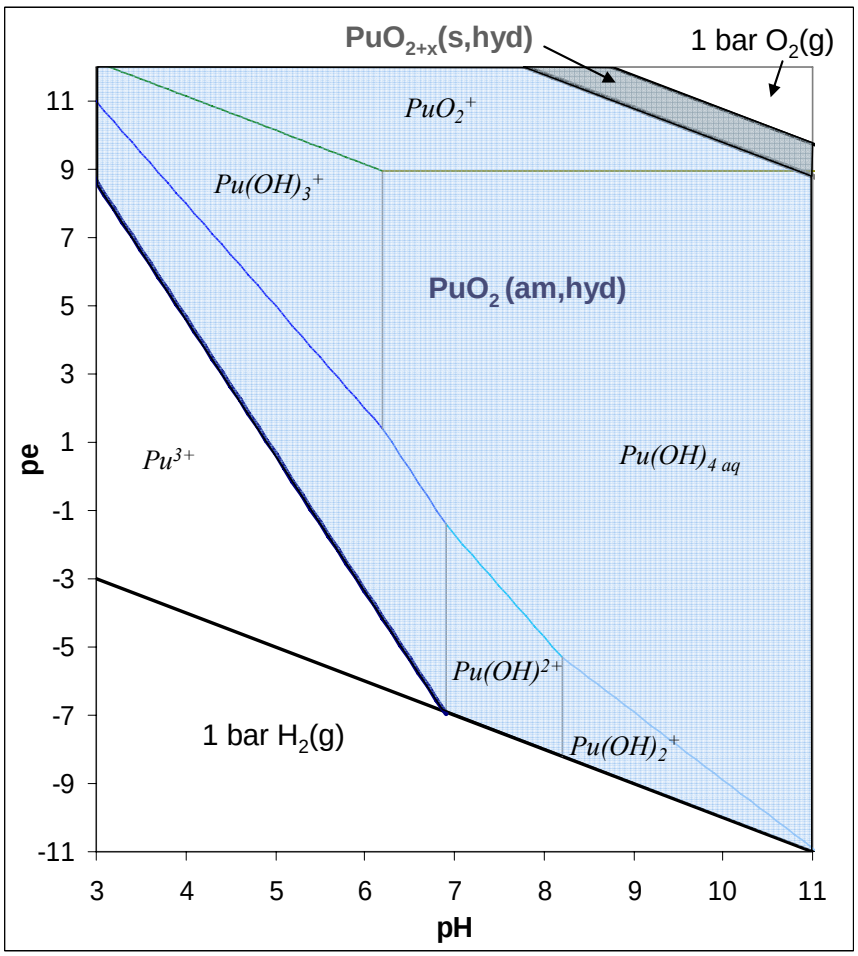

Figure 1.3. pe-pH predominance diagram for plutonium at I = 0. Solution species are written in italics, solid phases in bold. Thin lines delineate fields between solution species. The thick blue line delineates the equilibrium between solution Pu^{3+} and PuO_2(am,hyd), [Pu^{3+}] = $5 \cdot 10^{-6}$ M, the thick grey the equilibrium between PuO_{2+x}(s,hyd) and PuO_2(am,hyd).

Dissolved Pu(IV) concentrations in equilibrium with PuO_2(am,hyd) are independent of the redox potential and, at near neutral pH, are below 10^{-10} M (Fig 1.2c). Under reducing conditions, e.g. pH 7 and pe -4 and I = 0, [Pu^{3+}] would be $5 \cdot 10^{-9}$ M, two orders of magnitude above [Pu(IV)].

With increasing ionic strength the activity of a given Pu^{3+} concentration in solution decreases rapidly and to be in equilibrium with PuO_2(am,hyd) a higher concentration is then necessary.

The activity coefficients γ_j, relating activity and concentration, e.g. {Pu^{3+}} = [Pu^{3+}] γ_{Pu3+}, can be calculated according to different theories, among them the specific ion interaction theory (SIT) from Bronsted-Guggenheim-Scatchard.[79] For Pu^{3+} in NaCl of a given ionic strength, e.g., γ_{Pu3+} can be calculated when the interaction parameter between Pu^{3+} and Cl^-, $\varepsilon(Pu^{3+}, Cl^-)$, is known:

$$\log\gamma_{Pu3+} = -z_{Pu3+}^2 \, D + \Sigma \, \varepsilon(Pu^{3+},Cl^-) \, m(Cl^-) \qquad (1.9)$$

$$D = A \, \mathrm{sqrt}(I_m) / (1 + Ba_j \cdot \mathrm{sqrt}(I_m)) \qquad (1.10)$$

In equation 1.9, z is the charge of the ion (+3 in this case), m is the ionic strength in mol/kg, and D is the Debye-Hückel term in which for the SIT theory at 25ºC A = 0.509 and Ba_j = 1.5. $\Delta_f G$ values used for the calculation of the diagrams in figures 1.2 and 1.3 and epsilon parameters used to calculate the

concentrations of Pu(III) and Pu(IV) in equilibrium with PuO_2(am,hyd) are given in Table 1.1. For Pu(III), epsilon values of the analogue americium species were used.[8]

Table 1.1. Gibbs free energies of formation and ion interaction parameters for selected Pu species.

oxidation state	species	$\Delta_f G$ [kJ/mol]	source	ε(X, Cl^-) [kg/mol]	source
Pu(III)	Pu^{3+}	-578,984	NEA-TDB[80]	0,23	Am analogue, NEA-TDB[80]
	$PuOH^{2+}$	-776,739	"	-0,04	"
	$Pu(OH)_2^+$	-967,075	Neck et al., 2007[8]	-0,27	"
	$Pu(OH)_3$(aq)	-1140,86	"		"
Pu(IV)	Pu^{4+}	-477,988	NEA-TDB[80]	0,4	Neck et al., 2001[81]
	$PuOH^{3+}$	-718,553	"	0,2	"
	$Pu(OH)_2^{2+}$	-955,693	"	0,1	"
	$Pu(OH)_3^+$	-1176,28	"	0,05	"
	$Pu(OH)_4$(aq)	-1378,03	"		
	PuO_2(am, hyd)	-965,538	calculated from hydrolysis constant in NEA-TDB[80]		
Pu(V)	PuO_2^+	-852,646	NEA-TDB[80]		
	$PuO_{2.5}$(s, hyd)	-971,206	calculated from Neck 2007[8]		
	OH^-	-157,22	NEA-TDB[80]		
	H_2O(l)	-237,14	"		

2. Materials and methods

2.1. Mineral synthesis and characterization

Magnetite, mackinawite and chukanovite were synthesized and characterized as described in chapter 3.2. Hematite (α-Fe_2O_3) was synthesized similarly to Sorum (1928).[82] 250 mL of 0.4 M $FeCl_3$ (Fluka, p.a.) were slowly (at a rate of about 5 mL/min) added to 1.5 L of boiling ultrapure water that had been acidified with 3 mL of 1 M HCl (thus being 0.002 M in HCl). After all $FeCl_3$ had been added, the solution was kept boiling for another 3 hours and was then left to cool. The hematite was dialyzed against de-ionized water (Spectra/Por®, MWCO: 6-8000) four one week, changing water daily. Subsequently hematite was washed by centrifugation (3 times in 0.01M NaCl) (Beckman Avanti J-20 centrifuge, with JA 14 rotor), and was finally resuspended in 0.01M NaCl. Thus synthesized hematite was characterized by Powder XRD (Fig. 2.1).

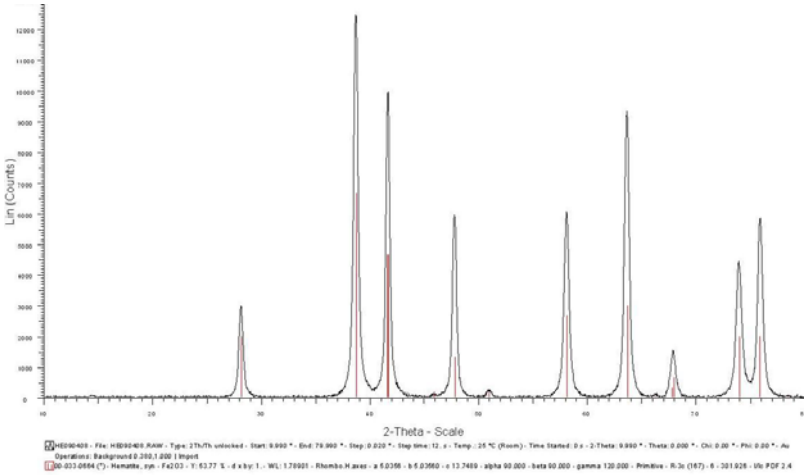

Figure 2.1.X-ray diffraction pattern for hematite measured with a step width of 0.02º2θ and step time of 12 s from 10 to 80º2θ. Red lines indicate pattern from reference spectrum (pdf 00-033-0664).

Goethite (α-FeOOH) was synthesized similar to sample G in Varanda et al (2002)[83], a sample that was characterized in the article with powder XRD as being nanoparticulate goethite and with TEM as containing mainly particles of 60 nm length and 10 nm width (L/W = 6) and a polydispersity < 0.1. In the original synthesis $Fe_2(SO_4)_3$ x 6 H_2O is used as the Fe(III) salt. To 50 mL of a 0.1M $Fe_2(SO_4)_3$ solution 2.5 M NaOH is added to a radio OH/Fe = 0.35. After aging for 4h at 21°C, Na_2CO_3 is added to obtain $[CO_3^{2-}]/[Fe]$ = 3.75 and water to attain a final volume of 100 mL. The suspension is then aged for 48h at 40°C and then for 72h at 60°C. After up-scaling (9 times the original amount), the synthesis was performed in the following manner: A 450 mL solution of 0.1 M Fe(III) sulfate (0.09 mol Fe) was prepared from 22.86g of $Fe_2(SO_4)_3$ x xH_2O (Sigma) to which 31.5 ml 1M NaOH (0.0315 mol OH^-) were added and aged for 4h at RT. Subsequently, 250 mL of a solution containing 96.6 g of Na_2CO_3 x 10 H_2O (0.3375 mol Na_2CO_3) (Labosi, p.a.) were added and 168 mL H_2O to a final volume of 900 mL. Aging at 40°C and 60°C was carried out as described above. The resulting solid was

washed 4 times with ultrapure water resulting in a suspension pH of 7. Then, the solid was washed another three times with and re-suspended in 10 mM NaCl. The washing was performed by centrifugation at 20°C (2500 rpm, 5 min) (Beckman Avanti J-20 centrifuge, with JA 14 rotor). Thus synthesized goethite was characterized by Powder XRD (Fig. 2.2).

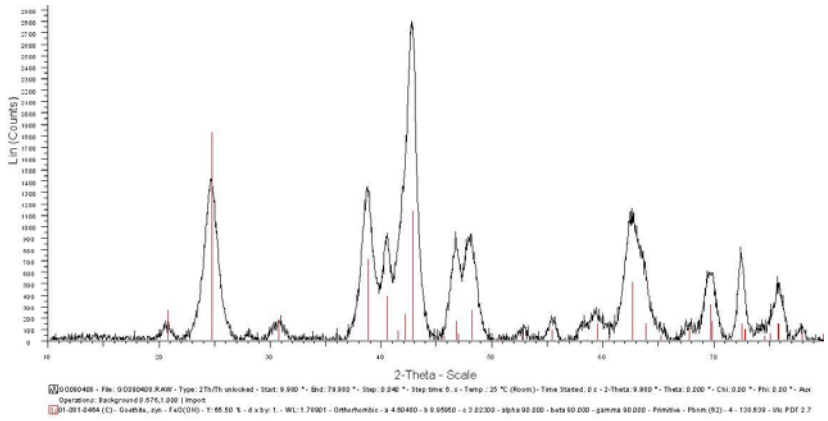

Figure 2.2. X-ray diffraction pattern for goethite measured with a step width of 0.04º2θ and step time of 6 s from 10 to 80º2θ. Red lines indicate pattern from reference spectrum (pdf 01-081-0464).

Hematite and goethite were also characterized by Mössbauer spectrometry. Dried powders were measured at 300 and 77 K using a conventional constant acceleration transmission spectrometer with a ^{57}Co(Rh) source and a bath cryostat. An α-Fe foil was used as a calibration sample. Spectra were fitted using the MOSFIT[84] program. Isomer shifts are quoted with respect to that of α-Fe at 300K. Measurement and fitting were carried out by J.-M. Grenèche, University du Maine, Le Mans.

The goethite spectrum at 300 K, composed of a collapsing sextet and paramagnetic doublet, strongly ressembles the spectrum of a nanoparticulate goethite samples published by Gotic and Music (2007)[85]. At 77 K, the sextet is ressolved. These spectra provide no indication for presence of Fe(II). The hematite spectra equally do indicate presence of Fe(II) and correspond well to the values published for hematite in Fysh and Clark (1983)[86].

Table 2.1. Moessbauer parameters for hematite and goethite

sample		δ (mm/s)	Γ (mm/s)	Δ or E_Q (mm/s)	B_{hf} (T)	Area (%)
goethite, 300K	D	0.37	0.55	0.52		33
	S	0.31		-0.11	22	67
goethite, 77K	S	0.48		-0.21	48.6	100
hematite, 300K	S	0.37		-0.21	47.4	100
hematite, 77K	S	0.48		-0.20	52.7	100

key: D = doublet, S = sextett, δ = isomer shift, Γ = full width at half maximum, Δ or E_Q = quadrupole splitting, B_{hf} = hyperfine field

Before use under anoxic conditions, hematite and goethite suspensions were bubbled for several hours with N_2 and were then transferred into first an N_2, then Ar glovebox. The mineral suspensions were kept anoxic glovebox atmospheres for several months before they were reacted with plutonium. Even though Moessbauer spectra do not indicate presence of Fe(II), its presence cannot be excluded due to

potential Fe(II) contamination in the original Fe(III) salts used for synthesis. In particular at the low pH at which the employed hematite synthesis route takes place, trace Fe(II) might not be oxidized. Detection limit of Fe(II) in by Mössbauer spectrometry is about 1 %. In addition, hematite and goethite were dried before Mössbauer analysis while the minerals used for reaction with plutonium were always suspended and thus less exposed to oxydation by air.

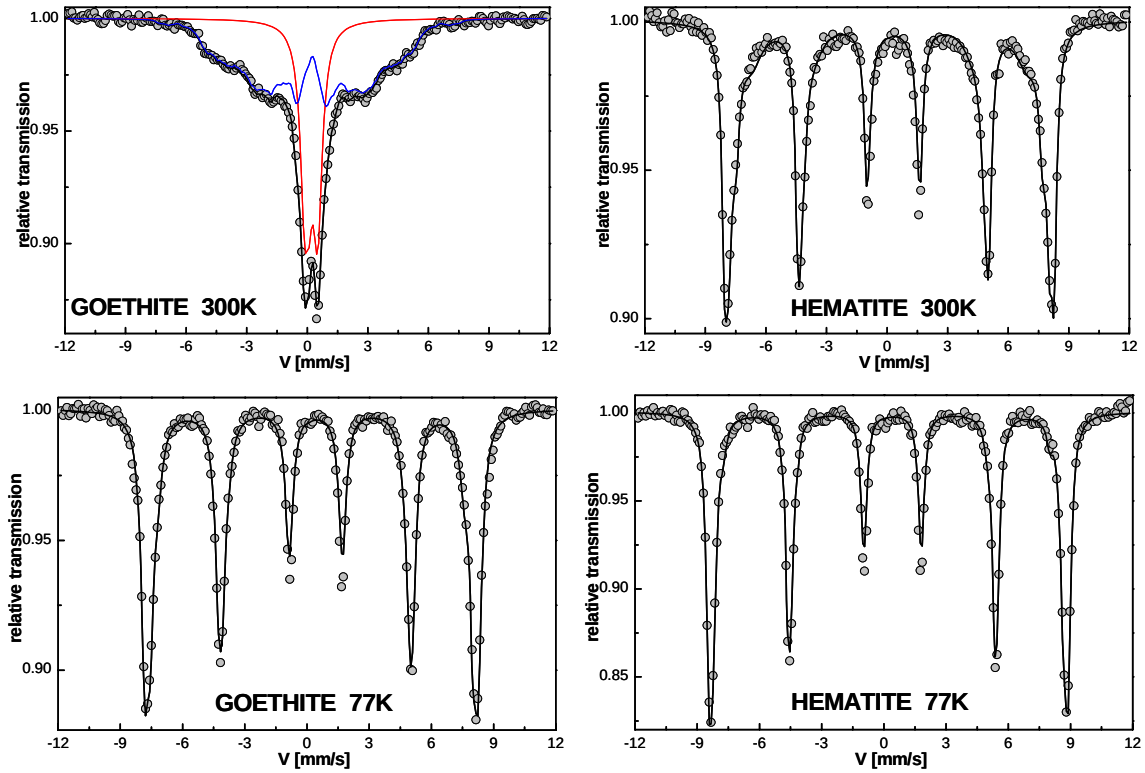

Figure 2.3. Mössbauer spectra of goethite (left) and hematite (right) measured at 300 K and 77 K.

For preparation of maghemite, magnetite was oxidized using H_2O_2.[87, 88] For the first batch used for the 40 d Pu experiments this was done in the following manner: To 35 mL of a magnetite suspension (45 g/L) were added 40 mL of H_2O_2 (30 %) and left to react for 1 h. After 1 h, the solution was decanted and another 40 mL H_2O_2 were added. The resulting suspension was heated to about 90ºC for 1 h. After cooling, the solid was washed three times with 0.01 M NaCl and finally resuspended in 0.01 M NaCl. For the second batch, used for the 8-months Pu samples, a 45 mL magnetite suspension was reacted 6 times with 50 mL 30 % H_2O_2 (five times for two hours and once over night) and was kept at about 90ºC for the last three reactions with H_2O_2.

For Moessbuaer spectrometry, the same mistake as for goethite and hematite had been made, that is the powder resulting from oxidation of magnetite was dried in the air and residual Fe(II), if present, got oxidized from oxygen in the air (not shown). When the solid resulting from H_2O_2 oxidation of magnetite was dissolved in acid to determine spectrophotometrically the Fe(II) content, concentrated HCl as used, thus resulting in reduction of Fe(III) to Fe(II) and not providing reliable information on the Fe(II) content of the maghemite or partially oxidized magnetite.

2.2. Sb and Fe total concentration analysis with ICP-MS

Filtered, acidified (HNO_3) solutions from Sb mackinawite experiments were diluted to a concentration below 100 ppb Sb and below 10,000 ppm Fe with 2 % in-house double-distilled HNO_3. For preparation of calibration standards and sample dilution, acid leached centrifuge tubes were used (leached for one months in an acid bath containing 100 mL HNO_{3conc} and 1 mL HF_{conc} for 5 Litres H_2O). Dilution was carried out by weighing sample and dilutant; the resulting volume of the diluted samples was calculated from transferred mass using the density of HNO_3 (1.012g/L for 2 % HNO_3). Half of the total samples volume consisted of HNO_3 that had been spiked with ^{72}Ge, ^{115}In, ^{9}Be, and ^{169}Tm. Sb, Fe standards used were 10 ppt Sb, 1 ppb Fe for the most diluted and 100 ppb Sb, 10,000 ppm Fe for the most concentrated one. For preparation of the calibration standards, the following solutions were used: For Fe, 1000 ± 4 mg/L TraceCert (Fluka) in 2 % HNO_3, for Sb 1.000 g/L in 5 M HCl, d_4^{20} = 1.08 (Fluka). For Sb and Fe, signals for isotopes ^{121}Sb, ^{123}Sb and ^{56}Fe were acquired. For construction of calibration curves and sample signal analysis, counts for Sb and Fe were corrected according to the spike signals. The spike level for each sample and standard was calculated from the exact amount of spiked HNO_3 used, asigning a spike level of 1 to a sample half of whose volume consisted of spiked HNO_3. Counts for the spiked elements were then divided through the spike level and were normalized with respect to the 1ppb standard. ^{121}Sb and ^{123}Sb counts in caliration standards and samples were corrected according to their isotopic mass using ^{115}In and ^{169}Tm according to: $countsSb_{corr}$ =

$$countsSb \cdot (CountsIn_{norm} \cdot ((m(Tm) - m(In)) - (m(Sb) - m(In))) / (m(Tm) - m(In)) + CountsTm_{norm} \cdot ((m(Tm) - m(In)) - (m(Tm) - m(Sb))) / (m(Tm) - m(In)))$$

with $countsX_{norm}$ for each standard or sample being

$countsX_{norm} = (countsX_{1ppb}/spikelevel_{1ppb})/(countsX_{sample}/spikelevel_{sample})$, X being In or Tm. m(X) is the mass of the isotope of X. Given concentrations are the geometric averages of the concentrations found from the two isotopes. Corrected counts for ^{56}Fe were calculated similarly from ^{9}Be and ^{72}Ge according to: $countsFe_{corr}$ =

$$countsFe \cdot (CountsBe_{norm} \cdot ((m(Ge) - m(Be)) - (m(Fe) - m(Be))) / (m(Ge) - m(Be) + CountsTm_{norm} \cdot ((m(Ge) - m(Be)) - (m(Ge) - m(Sb))) / (m(Ge) - m(Be))).$$

The detection limit (blank + 3 standard deviations) for Sb was $1.04 \cdot 10^{-7}$ M.

For SLRS-4 (river water reference material for trace metals), the following concentrations were obtained: for Sb 0.026 ± 0.01 ppb, for Fe 95 ± 3 ppb. Certified values are for Sb 0.23 ± 0.04 ppb and for Fe 103 ± 5 ppb. Measurements were carried out using an Agilent 7500ce quadrupole ICP-MS equipped with a hydrogen collision cell using the ChemStation software provided by the manufacturer. Between samples, the sampling needle was washed for two minutes per washing solution first in 5 % HNO_3 and then two times in 2 % HNO_3.

2.3. Sb speciation analysis with HG-AFS

Hydride generation atomic fluorescence spectrometry was used for the quantitative determiantion of [Sb(III)] and approximate determination of [Sb]total of Sb-mackinawite sorption samples using a Millenium Excalibur-System, PSA 10.xxx, PS Analytical LTD spectrometer equipped with a Sb boosted hollow cathode lamp (xxx). Approximate $[Sb]_{tot}$ values were used to determine the dilution level necessary for the accurate determination of $[Sb]_{tot}$ by ICP-MS.

Similarly to the method used by Leuz and Johnson(2005)[51], after filtration, Sb sorption samples were treated as follows: Sb(III) samples (10mL) were stabilized by mixing with an equal volume of 1 M Disodiumhydrogencitrate (Fluka, ≥ 99%)[89], Sb_{tot} samples (10mL) were stabilized by addition of 3.5 mL concentrated HCl (37 %, Fluka) and kept at 4ºC until analysis. Sb(III) samples (flow rate of 9 mL/min) were measured using a 0.5 M Disodium-hydrogencitrate as carrier solution (9 mL/min) and 1 % NaBH4 (Sigma-Aldrich, 99 %) in 0.1 M NaOH (Roth, p.a.) (4.5 mL/min) as reductant. Antimony in Sb_{tot} samples was reduced to Sb(III) before analysis by HG-AFS by adding 1 mL of a 10% cysteine solution in 1 M HCl and bringing the total volume to 20 mL (thus 0.005 % cysteine in 2.16 M HCl).[90] For measurement, 2 M HCl was used as carrier solution (9 mL/min) and 1 % NaBH4 in 0.1 M NaOH (4.5 mL/min) as reductant. Standards (0-400ppb, 2 M HCl and 0.5 % cysteine for Sbtot samples, 0.5 M disodiumydrogencitrate with 12.5 mM $CaCl_2$ for Sb(III) samples) were prepared by dilution of a Sb_2O_3 1000 ppm standard (Fluka, 5 M HCl) The measurement method used a gain of 1 (peak height or area) or 10 (peak height), analysis time 5 or 10s, delay 10 s, memory 40 s; primary lamp current was 17.5 mA, boost current waas 10.1 mA.

2.4. X-ray absorption spectroscopy measurements

XAS spectra were collected at the Rossendorf Beamline at the European Synchrotron Radiation Facility (ESRF, Grenoble). The energy of the X-ray beam was tuned by a doubled crystal monochromator operating in channel-cut mode using a Si(111) crystal pair. Two platinum-coated Si mirrors before and after the monochromator were used to collimate the beam into the monochromator and to reject higher harmonics. XAS measurement and data treatment details for Pu samples are given in chapter 3.2. Sb K-edge spectra were collected in fluorescence mode using a 13-element energy dispersive solid state Ge detector (Canberra) together with a digital signal processing unit (XIA). Spectra were collected at 15 K using a closed cycle He cryostat (CryoVac). Energy calibration was done using the zero crossing of the second derivative of the K-edge of metallic Sb (30491 eV). Between two and six scans were recorded for each Sb-sample. Dead time correction of the fluorescence signal, energy calibration and the averaging of the individual scans were performed with the software package SixPack[91]. Normalization, transformation from energy into k-space and subtraction of a spline background were performed with Athena[92] using routine procedure. Shell fitting was carried out in WinXAS 3.11[93] using theoretical backscattering amplitudes and phase shifts

calculated with feff8.2[94] from stibnite (ICSD 22176)[95] and tripuhyite (ICSD 99790)[96] crystallographic data. S_0^2 was set to a value of 1 to obtain a Sb-O coordination number (CN) of 6 for Sb(V) (calculated with Sb(V) adsorbed onto hematite). Fourier Transforms were done in WinXAS using a Bessel window function (window parameter set to 3). All fits were carried out in R-space in k^3+k^2 fit mode.

3. Reactions of plutonium with iron minerals under anoxic conditions

3.1. Experimental setup

Aqueous tri- or pentavalent plutonium was added to suspensions of different iron oxides (hematite, goethite, maghemite, magnetite), an iron-(II)-sulfide (mackinawite) and an iron-(II)-hydroxy-carbonate (chukanovite) resulting in a total of 22 Pu-mineral samples that were analyzed by XAS after a reaction time of 40 days for the first 10 and 7.6 months for the remaining 12 samples. Specific surface areas of the minerals and solid/liquid ratios of the used mineral suspensions are outlined in Table 3.1.1. A summary of the general reaction conditions for all 22 samples (pH, initial and final [Pu], resulting loading on the minerals) is given in Table 3.1.2.

Table 3.1.1. BET specific surface areas for mineral phases and solid/liquid ratios of mineral suspensions used for preparation of 40 d and 6 months Pu-mineral samples.

Mineral name	Formula	reaction time	specific surface area* [m^2/g]	solid/liquid [g/L]	solid/liquid [mol/L]	surface area [m^2/L]
Hematite	α-Fe_2O_3	40 d	42	11.48	0.072	479
		7.6 m		5.74	0.036	240
Goethite	α-FeOOH	40 d	209	2.01	0.023	419
Magnetite	Fe_3O_4	40 d	75	5.55	0.024	418
		7.6 m		2.78	0.012	209
Maghemite	γ-Fe_2O_3	40 d	97	5.64	0.035	548
		7.6 m	72	2.82	0.018	203
Mackinawite	FeS	40 d	53	3.43	0.039	183
		7.6 m		1.71	0.019	91
Chukanovite	$Fe_2(CO_3)(OH)_2$	40 d	112	1.98	0.010	221
		7.6 m		1.65	0.008	184

*the experimental uncertainty of the value is on the order of 5-10 %

All work was carried out under anoxic conditions (Ar-glovebox with O_2 levels usually ≤ 10ppmv), for preparation of solutions and mineral suspensions only degassed (O_2 and CO_2 free) MilliQ® (18.2 MΩ) water was used. One week prior to Pu addition, the mineral suspensions were adjusted to an ionic background of 0.1 M NaCl and for hematite, goethite, magnetite, maghemite and mackinawite, the suspension pH was adjusted with 1 M or 4 M NaOH or HCl, while the chukanovite suspension was used as is. Pu(V) or Pu(III) stock solutions were added to the mineral suspensions to obtain [Pu(tot)] of 1.17 - 1.57· 10^{-5} M (Table 3.1.2). Changes in suspension pH due to addition of the acidic Pu stock solutions were minor. The samples were allowed to react in the dark (wrapping in aluminum foil) for 41 and 230 days for initially added Pu(V) and 39 and 229 days for initially added Pu(III). Wet pastes of the minerals were then separated from the suspension by centrifugation and transferred into double confinement PE XAS sample holders that were heat sealed and subsequently kept shock frozen in a liquid nitrogen dewar until measurement. [Fe(II)] and [Fe(total)] concentrations were determined using the Ferrozine method[29] and [Pu] with LSC after 10kD ultra-filtration of aliquots of the mineral

suspensions. pH and pe were determined both: in suspension and in the clear supernatant after centrifugation of an aliquot of the sample, with the solid at the bottom of the centrifuge tube. During pH measurements, a stable potential was usually reached within 5 minutes. Redox potentials were read after 10 to 15 min in suspensions and after 15 to 30 min in centrifuged solutions (for a discussion of different pH and pe measurement approaches, see p.35). pH was measured using a combined glass electrode with ROSS reference system calibrated against pH standard buffer solutions (Merck). Redox potentials E(V) were measured with a Pt-combination electrode with Ag/AgCl reference system (Metrohm, reference electrolyte 3 M KCl) and converted into Eh according to Eh = E(V) + 0.208 V at 23°C and 3 M KCl. pe is subsequently calculated according to pe = (F/(2.303 RT)) · Eh.

Table 3.1.2. List of Pu-mineral samples detailing the for the different reaction times of 40 d and 6 months the equilibrium pH, total and final Pu concentrations, percentage of Pu removed from solution (% Pu sorbed) and resulting mineral loadings expressed as mass and surface loadings. The latter are calculated from the total amount of Pu removed from solution and BET determined specific surface areas for the minerals (Table 3.1.1). When surface complexation does not occur as Pu is removed from solution as a PuO_2 solid phase, surface loadings are only hypothetical values.

Mineral	sample abbreviation	reaction time	Pu added as*	pH $_{final}$**	$[Pu]_{start}$ [µmol/L]	$[Pu]_{final}$ [nmol/L]	% Pu sorbed	Pu/mineral loading		
								m/m [ppm]	[µmol/g]	[nmol/m^2]
Hematite	He-40d-V	40 d	Pu(V)	7.5	13.4	≤ 1#	99.993	282	1.2	28
	He-8m-V	7.6 m	Pu(V)	7.5	15.7	6.1	99.961	662	2.7	65
	He-8m-III	7.6 m	Pu(III)	7.2	11.7	0.2	99.998	492	2.0	49
Goethite	Go-40d-V	40d	Pu(V)	7.9	13.4	1.9	99.986	1617	6.7	32
Magnetite	Mg-40d-V-pH8	40d	Pu(V)	7.9	13.4	≤ 1	99.993	584	2.4	32
	Mg-8m-V-pH8	7.6 m	Pu(V)	8.4	15.7	≤ 0.04	100.000	1367	5.6	75
	Mg-40d-III-pH6	40d	Pu(III)	6.1	12.2	3.5	99.971	532	2.2	29
	Mg-40d-III-pH8	40d	Pu(III)	7.9	12.2	≤ 1	99.992	532	2.2	29
	Mg-8m-III-pH8	7.6 m	Pu(III)	8.3	11.7	≤ 0.04	100.000	1017	4.2	56
Maghemite	Mh-40d-V	40d	Pu(V)	5.8	13.4	≤ 1	99.993	575	2.4	24
	Mh-8m-V	7.6 m	Pu(V)	5.9	15.7	0.05	100.000	1347	5.6	77
	Mh-40d-III	40d	Pu(III)	5.8	12.2	0.9	99.993	523	2.2	22
	Mh-8m-III	7.6 m	Pu(III)	5.7	11.7	0.08	99.999	1002	4.1	57
Mackinawite	Mk-40d-V-pH8	40d	Pu(V)	8.0	13.4	≤ 1	99.993	947	3.9	73
	Mk-40d-III-pH6	40d	Pu(III)	6.4	12.2	202.1	98.343	862	3.6	67
	Mk-8m-V-pH7	7.6 m	Pu(V)	6.9	15.7	2.51	99.984	2221	9.2	172
	Mk-8m-V-pH8	7.6 m	Pu(V)	8.4	15.7	≤ 0.04	100.000	2221	9.2	172
	Mk-8m-III-pH7	7.6 m	Pu(III)	7.1	11.7	25	99.786	1653	6.8	128
	Mk-8m-III-pH8	7.6 m	Pu(III)	8.0	11.7	≤ 0.04	100.000	1653	6.8	128
Chukanovite	Chuk-40d-V	40d	Pu(V)	8.4	13.4	≤ 1	99.993	1638	6.8	61
	Chuk-8m-V	7.6 m	Pu(V)	8.5	27.0	≤ 0.04	100.000	3957	16.4	147
	Chuk-8m-III	7.6 m	Pu(III)	8.6	20.1	0.04	100.000	2945	12.2	109

* Initial Pu oxidation state

** pH measured in suspension at the end of the reaction period

The values preceded by a ≤ sign correspond to the detection limit for Pu concentrations by LSC. As the detection limit changed with the amount of sample solution used, different detection limits (1 vs 0.04 nM) were obtained at the end of the 40 d and 6 m experiments.

Preparation of all Pu-mineral samples was carried out jointly by David Fellhauer (DF) (EC-JRC-ITU), Marcus Altmaier (MA) (KIT-INE) and myself (RK). My contribution to these experiments was: first suggestion of the experimental setup (minerals to be used, reaction pH, solid/liquid ratio), mineral synthesis, washing and preparation for characterization by PXRD (of the pure minerals) and XAS. Volker Neck (VN) (KIT-INE) (deceased 01. Aug. 2009) contributed by suggestions concerning the use of Pu(III) in addition to Pu(V) as initial Pu oxidation state and through discussions concerning the experimental setup (total Pu-concentration, ionic strength, pH). He also commented on the outcome of the of XAS measurements on the first 10 samples (40 d reaction time).

Solution and suspension pH and redox potential were measured jointly by RK and DF during sample preparation and harvest (though at harvest of the 6 months samples mostly by DF) and measured only by DF during the sample aging period. Dissolved Fe was measured jointly at the start of the experiments and by DF during sample aging and at "harvest". All determinations of Pu in solution after 10kd ultra-filtration were carried out by DF alone. Sample "harvesting" (separation of liquid and solid phase by centrifugation and preparation of XAS samples (filling and sealing of double confinement PE sample holders)) was carried out by myself (RK).

Samples Mg-40d-V-pH8, Mg-40d-III-pH6, Mg-40d-III-pH, Mk-40d-V-pH8, and Chuk-40d-V are discussed in chapter 3.2, which was published as an article entitled "Oxidation state and local structure of plutonium reacted with magnetite, mackinawite and chukanovite" in the journal Environmental Science and Technology. To this article, AR contributed the results of a MC-Feff simulation to resolve the structure of a Pu(III)-magnetite surface complex. In addition to joint sample preparation (as outlined above), DF calculated the pe-pH diagram depicted in Fig. 3. All treatment of the XAS data (energy correction, normalization, extraction of chi-spectra), PCA and LC fitting and shell-fitting of the EXAFS data was done by myself.

M.A., ACS and LC contributed through discussion of XAS results and their environmental impact.

The references to the main text (published article) of chapter 3.2 are listed at the end of the article on pages 30-33, The references of the online supporting information to this article, which is printed here as part of chapter 3.2, are listed on pp. 55-56.

3.2. Oxidation state and local structure of plutonium reacted with magnetite, mackinawite and chukanovite (published in Environ. Sci. Technol. 2011, 45, 7267–7274.)

Regina Kirsch[,1,2], David Fellhauer[3], Marcus Altmaier[4], Volker Neck[4], Andre Rossberg[1], Thomas Fanghänel[3], Laurent Charlet[2], Andreas C. Scheinost[*,1]*

[1]Institut für Radiochemie, Helmholtz Zentrum Dresden Rossendorf, Postfach 510119, 01314 Dresden, Germany; [2]Institute des Sciences de la Terre, Université Joseph Fourier, CNRS, BP 53, 38041 Grenoble, France; [3]European Commission, Joint Research Center, Institute for Transuranium Elements, P.O. Box 2340, 76125 Karlsruhe, Germany; [4]Institut für Nukleare Entsorgung, Karlsruhe Institute of Technology, Postfach 3640, 76021 Karlsruhe, Germany

ABSTRACT Due to their redox reactivity, surface sorption characteristics, and ubiquity as corrosion products or as minerals in natural sediments, iron(II)-bearing minerals control to a large extent the environmental fate of actinides. Pu-L_{III}-edge XANES and EXAFS spectra were used to investigate reaction products of aqueous ^{242}Pu(III) and ^{242}Pu(V) reacted with magnetite, mackinawite and chukanovite under anoxic conditions. As Pu concentrations in the liquid phase were rapidly below detection limit, oxidation state and local structure of Pu were determined for Pu associated with the solid mineral phase. Pu(V) was reduced in presence of all three minerals. A newly identified, highly specific Pu(III)-sorption complex formed with magnetite. Solid PuO_2 phases formed in the presence of mackinawite and chukanovite; in the case of chukanovite, up to one third of plutonium was also present as Pu(III). This highlights the necessity to consider, under reducing anoxic conditions, Pu(III) species in addition to tetravalent PuO_2 for environmental risk assessment. Our results also demonstrate the necessity to support thermodynamic calculations with spectroscopic data.

Introduction

Plutonium is the major transuranium actinide in civil and military nuclear waste. It is of environmental concern because of its high radiotoxicity and the long half-life of relevant nuclides (^{239}Pu: 24 100 a, ^{242}Pu: 375 000 a, ^{244}Pu: $8.0 \cdot 10^7$ a).[1] The solubility and complexation behavior of plutonium in aqueous systems and therefore its environmental fate are highly oxidation state dependent.[2] Due to its predominance over a wide pe/pH range and the possibility of colloid formation,[3,4] PuO_2 is considered one of the most important solids for Pu risk assessment. Under reducing conditions in the acidic to neutral pH range and particularly in presence of dissolved Fe(II) or Fe(II)-bearing minerals, however, Pu(III) is relevant and compared to Pu(IV) often forms more soluble species.[5-7] Generally, sorption on minerals and redox reaction with them are among the individual processes that largely impact migration behavior of plutonium.[8] Since iron minerals form as corrosion products of zero-valent iron and steel (the first engineered physical barrier to Pu mobilization in most nuclear waste repository concepts) and are present in many "far field" barriers (clay or granite), their reactions with plutonium

are of particular importance. Depending on redox conditions, ground water composition and microbial activity, Fe(II), Fe(III) or mixed Fe(II)-Fe(III) minerals such as magnetite ($Fe^{II}Fe^{III}_2O_4$), maghemite (γ-Fe_2O_3), green rust, siderite ($FeCO_3$), chukanovite ($Fe_2(CO)_3(OH)_2$) and mackinawite (FeS) have been observed as corrosion products of steel.[9-11] Magnetite and mackinawite are widespread in natural sediments;[12, 13] chukanovite was found to result from microbial reduction of magnetite and lepidocrocite.[14, 15] Sorption of plutonium to iron[16-19] and manganese minerals[16, 20] can be accompanied by redox processes, leading to reduction or oxidation of the initial Pu oxidation state. For example, sorption of Pu(V) to hematite, goethite and magnetite was found to be accompanied by surface mediated reduction to Pu(IV).[16-19, 21] While the reductive capacity of the Fe(II)-Fe(III) mixed valence spinel magnetite is well known[22, 23] the reduction of Pu(V) with iron(III) minerals hematite and goethite was attributed to the presence of traces of Fe(II) or to a stabilization of solid-state Pu(IV).[18] Due to a lack of measured redox potentials and Fe(II) concentrations, it is not possible to clearly link these observations with thermodynamic predictions on Pu oxidation states. Also, in many of the Pu-mineral interaction studies, the oxidation state distribution of plutonium on the solid phase and in solution was assessed indirectly, that is after leaching of plutonium from the solid phase and applying solvent extraction schemes to separate the different Pu oxidation states.

To investigate redox reactions of Pu with chemically and structurally differing Fe(II)-bearing minerals under anoxic conditions, we chose magnetite (an iron oxide), mackinawite (an iron sulfide) and chukanovite (an iron hydroxy carbonate), which after its first identification in 1976[24] was largely overlooked until recently.[9, 11] The magnetite and mackinawite studies were performed in carbonate free solutions. Cryogenic X-ray absorption spectroscopy (XAS) was used to assess *in-situ* oxidation states and local structures of resulting Pu-solid phases or surface complexes. To permit linking of thermodynamic modeling to Pu oxidation state distribution derived from X-ray absorption near edge structure (XANES) and extended X-ray absorption fine structure (EXAFS) spectra, care was taken to characterize sample redox conditions (pe, pH, [Fe(II)]). While the reactions of U(VI)[25] and Np(V)[26] with mackinawite have been investigated previously, we are not aware of any similar experiment involving Pu. The reduction of Pu(V) with magnetite[17] has been investigated in detail as a function of pH, but not with XAS and not under anoxic conditions, thereby limiting the applicability of the results to anoxic conditions typical of deep-underground repositories and groundwater aquifers. The reaction of Pu with chukanovite has, to our knowledge, never been investigated.

Materials and Methods

Generally, all sample manipulations, including mineral synthesis and washing, UV-Vis measurements and preparation of samples for XAS measurements, were carried out under anoxic conditions in nitrogen or argon glove-boxes with 0-10 ppmv O_2. Experiments were carried out at RT (23 ± 3°C); de-ionized (18.2 MΩ MilliQ), degassed (O_2 and CO_2 free) water was used for all purposes.

Mineral synthesis and characterization. Magnetite (Fe_3O_4), mackinawite (FeS) and chukanovite ($Fe_2(CO_3)(OH)_2$) were synthesized as detailed in the Supporting Information (SI). The identity of the reaction products was confirmed using synchrotron powder XRD (magnetite, mackinawite[27], chukanovite Fig S1). Specific surfaces areas (Table S2) were determined with the BET method[28] (for details see SI).

Preparation of Pu-stock solutions. A well characterized $2.2 \cdot 10^{-2}$ mol/L Pu(VI) stock solution was obtained after purification and electrochemical oxidation. The isotopic composition of plutonium was 99.4 wt.% Pu-242, 0.58 wt.% Pu-239, 0.005 wt.% Pu-238, and 0.005 wt.% Pu-241; interfering radiolytic reactions can therefore be excluded. Stock solutions of $8.6 \cdot 10^{-4}$ M Pu(V) and $7.3 \cdot 10^{-4}$ M Pu(III) were then prepared electrolytically in 0.5 M NaCl and 0.1 M $NaClO_4$, respectively. Prior to addition of Pu(V) or Pu(III) to mineral suspensions, the pH was raised by addition of 1 M or 4 M NaOH to pH 3.0 for Pu(V) and to pH 2.0 for Pu(III), and the initial oxidation state was confirmed by UV-Vis spectroscopy using a diode array spectro-photometer (Carl Zeiss Jena). The added Pu(V) stock solution contained up to 2% of Pu(VI), no other oxidation states or Pu(IV) colloids could be identified in the Pu(III) stock solution (wavelengths used for quantification were 601 nm for Pu(III), 569 nm for Pu(V), 830 nm for Pu(VI)). Total [Pu] in the stock solutions was determined using liquid scintillation counting (LSC). Similar [Pu] before and after 10 kD (~2 nm) ultrafiltration (Microsep 10k Omega filters) indicated the absence of significant amounts of PuO_2 colloids in the stock solutions.

Sample preparation and wet chemical characterization. Relevant experimental values are summarized in Table 1. One week prior to Pu addition, the mineral suspensions were adjusted to an ionic background of 0.1 M NaCl. For magnetite and mackinawite, the suspension pH was adjusted, while the chukanovite suspension was used as is. Pu(V) or Pu(III) stock solutions were added to the mineral suspensions to obtain [Pu(tot)] of $1.3 \pm 0.1 \cdot 10^{-5}$ M; no significant changes in sample pH were observed. Samples were allowed to react in the dark for 41 (Pu(V)) and 39 days (Pu(III)). Wet pastes of the minerals were then separated from the suspension by centrifugation and transferred into double confinement PE XAS sample holders that were heat sealed and subsequently kept shock frozen in a liquid nitrogen dewar until measurement. [Fe(II)] and [Fe(total)] concentrations were determined using the Ferrozine method[29] and [Pu] with LSC after 10kD ultra-filtration of aliquots of the mineral suspensions. pH and pe were determined in two ways: in suspension and in the clear supernatant after centrifugation of an aliquot of the sample, with the solid at the bottom of the centrifuge tube. During pH measurements, a stable potential was usually reached within 5 minutes. Redox potentials were read after 10 to 15 min in suspensions and after 15 to 30 min in centrifuged samples (for a discussion of different pH and pe measurement approaches, see SI, p.S4). pH was measured using a combined glass electrode with ROSS reference system calibrated against pH standard buffer solutions (Merck). Redox potentials E(V) were measured with a Pt-combination electrode with Ag/AgCl reference system (Metrohm, reference electrolyte 3 M KCl) and converted into Eh according to Eh = E(V) + 0.208 V at 23°C and 3 M KCl. pe is subsequently calculated according to pe = (F/(2.303 RT)) · Eh.

Table 1. Experimental conditions at the start and end of the reaction period for Pu(III) and Pu(V) ($[Pu(tot)]_{initial}$ $1.3 \pm 0.1 \cdot 10^{-5}$ M) reacted with magnetite, mackinawite and chukanovite.

sample	pH_{sus} start#	pH_{cen} start‡	pe_{sus} start	pe_{cen} start	pH_{sus} end#	pH_{cen} end	pe_{sus} end	pe_{cen} end	$[Fe(II)]_{start}$ [µmol/l]	$[Fe(II)]_{end}$ [µmol/l]	$[Fe(III)]_{start}$ [µmol/L]
Pu(III) + magnetite, pH 6	6.3	6.1	-1.2	-0.2	6.1	5.5	-1.3	2.9	4940	3130	199
Pu(III) + magnetite, pH 8	7.9	7.7	-5.0	-2.5	7.9	7.4	-4.9	2.1	22.7	21.8	bdl**
Pu(V) + magnetite, pH 8	7.7	7.9*	-4.8	1.5*	7.9	7.2	-5.0	2.4	15.1	19.3	bdl
Pu(V) + mackinawite, pH 8	8.2	8.4*	-5.2	-5.7*	8.0	8.4	-4.9	-2.1	16.6	8.0	bdl
Pu(V) + chukanovite, pH 8	8.4	8.7*	-4.9	-5.0*	8.4	8.0	-5.8	-3.3	13.9	69.2	1.5

†sus: pH or pe measured in suspension, ‡cen: pH or pe measured after centrifugation
#start, end: start values measured 1 day after addition of plutonium to the mineral suspensions, end values
measured at maximum 1 day prior to harvesting
*values acquired 1 day before addition of plutonium
**bdl: below detection limit, detection limit for Fe(II) and Fe(III) is approx. 1×10^{-7} mol/L

XAS spectra acquisition and data treatment. XANES and EXAFS spectra were acquired in fluorescence mode at the Pu-L_{III} edge (18.057 keV) at the Rossendorf Beamline at ESRF, France. During the measurement, samples were kept at 15 K using a closed-cycle He cryostat, thereby reducing thermal disorder and preventing beam-induced oxidation state changes. Details of experimental setup and treatment of spectra are given in the Supporting Information.

Reference spectra of acidic $(Pu^{III})_{aq}$, $(Pu^{IV})_{aq}$ and $(Pu^{V})_{aq}$ (measured at RT, courtesy of Ch. Den Auwer, CEA, Marcoule, France) and of crystalline PuO_2(cr) (measured at 15 K, courtesy of Ph. Martin, CEA, Cadarache, France)[30] had been measured in transmission mode and at the same beamline. Photon energies of the inflection points of absorption edges and white line maxima (peak positions) were determined for all sample and reference spectra (Table S3). The EXAFS data were fit with WinXAS[31] using theoretical backscattering amplitudes and phase shifts calculated with FEFF 8.2[32, 33] on clusters (R_{max} = 8 Å) of PuO_2[34] and Pu_2O_3.[35] Uncertainties of the fits are about ± 0.02 Å for distances and about ± 20-25 % for coordination numbers.[36] Statistical analysis of spectra (Eigen analysis and iterative target test) were performed with the ITFA program package.[37]

Thermodynamic model. The diagram shown in Figure 3 was calculated using thermodynamic constants from the NEA TDB[38] where available. If data for Pu species were not available, complex formation constants and ion-interaction parameters (SIT coefficients) for ionic strength corrections were obtained from analogue actinide species. The thermodynamic model will be described in detail in a forthcoming article (Fellhauer et al., in prep.).

Results and Discussion

For all five samples (Table 1), aqueous Pu concentrations dropped within 30 minutes and for the whole duration of the experiment to values near or below the detection limit of LSC ($\leq 1 \cdot 10^{-9}$ mol/L), thereby reaching uptake levels of ≥ 99.95 %.

Reaction of Pu(III) and Pu(V) with magnetite. Figure 1a shows Pu-L_{III}-edge XANES spectra of the Pu-magnetite samples along with $(Pu^{III})_{aq}$, $(Pu^{IV})_{aq}$, and $(Pu^{V})_{aq}$ references. The three Pu-magnetite

samples are characterized by very similar edge and peak positions, irrespective of the initial Pu oxidation state and the reaction pH (Table S3) and strongly resemble the $(Pu^{III})_{aq}$ spectrum in position and shape (for description of XANES as a function of oxidation state, see SI, 2.1). To quantify the oxidation state composition, the XANES region was analyzed using Iterative Target Testing (ITT)[37]. ITT calculates the composition of sample spectra using factors that are extracted from all spectra analyzed together (sample and reference spectra). The reference spectra of $(Pu^{III})_{aq}$, $(Pu^{IV})_{aq}$, and $(Pu^{V})_{aq}$ were assumed to represent pure oxidation states and therefore assigned to 100 % contents of the factors representing the respective states. For all three Pu-magnetite samples, Pu(III) contents higher than 90 % are found (Table S4a). Pu(IV) and Pu(V) percent contents are not significant, given an absolute uncertainty of up to 10 %. ITT was also applied to k^3-weighted $\chi(k)$-spectra obtained by back transform of the first peak in the Fourier Transform (FT). In this way, only the oxygen coordination shell is considered and the differences in longer range structure between samples and references are excluded. The ITT results based on the such-obtained $\chi(k)$-spectra confirm the prevalence of trivalent Pu (Table S4b). Shell fitting of the first FT peak yields Pu-O distances of 2.48 Å to 2.49 Å, characteristic of aqueous Pu(III) complexes[39-41] (Tables S5). In conclusion, edge and peak positions, ITT of the XANES and EXAFS regions and shell fitting of the first FT peak all suggest Pu(III) as the predominant oxidation state. Under the given experimental conditions (Table 1), the oxidation state of Pu after reaction with magnetite was independent of the initial oxidation state (III or V), suggesting that thermodynamic equilibrium has been attained. The fact that Powell et al.[17] found predominantly Pu(IV) is likely due to the presence of oxygen during their experiment. A similar impact of oxygen on the extent of reduction was observed by Nakata et al.[42] for the reaction between Np(V) and magnetite under aerobic and anaerobic conditions.

To elucidate the structure of the Pu(III) species on magnetite, shell fitting was extended to the FT peaks beyond the oxygen coordination sphere. A second shell could be fitted with backscattering from three to five Fe atoms at a distance of 3.54 Å, suggesting either a sorption complex or formation of a solid phase. To test the hypothesis of a sorption complex and to find a corresponding structure, FEFF-Monte Carlo (MC) modeling[43] was applied to the k^3-weighted EXAFS spectrum of the Pu(V) + magnetite, pH 8 sample (for modeling details, see SI, 1.3). A box-procedure position-search was conducted using a model slab of magnetite ($18 \cdot 15 \cdot 5$ Å^3), exposing two (111) faces, one with octahedral and one with mixed tetrahedral/octahedral termination (Fig. S2). One or two Pu atoms were allowed to move randomly and independently from each other in an empty 25*25*15 Å^3 box surrounding the slab. For each Pu position in relation to the magnetite slab, a theoretical EXAFS spectrum was calculated with FEFF8.2 considering backscattering between Pu and magnetite; a constant scattering contribution for oxygen atoms of water molecules coordinated to aqueous Pu was then added. For 6, 7 or 8 coordinated water molecules only one geometrically specific position in relation to the magnetite slab, situated on the (111) surface with octahedral termination, was identified (Fig. 1d). In the corresponding surface complex, one Pu atom is linked via three oxygen atoms to three

edge-sharing FeO_6-octahedra. As Pu atoms remained always separated by more than 9 Å, a contribution of Pu-Pu backscattering to the experimental spectrum could be ruled out, thereby excluding formation of a dimeric surface complex or of Pu^{III}(hydr)oxide clusters. The position search was repeated using a different approach that minimizes the standard deviation (SD) of each new position compared to the previous one (see SI) and lead to the identification of the same geometric position.

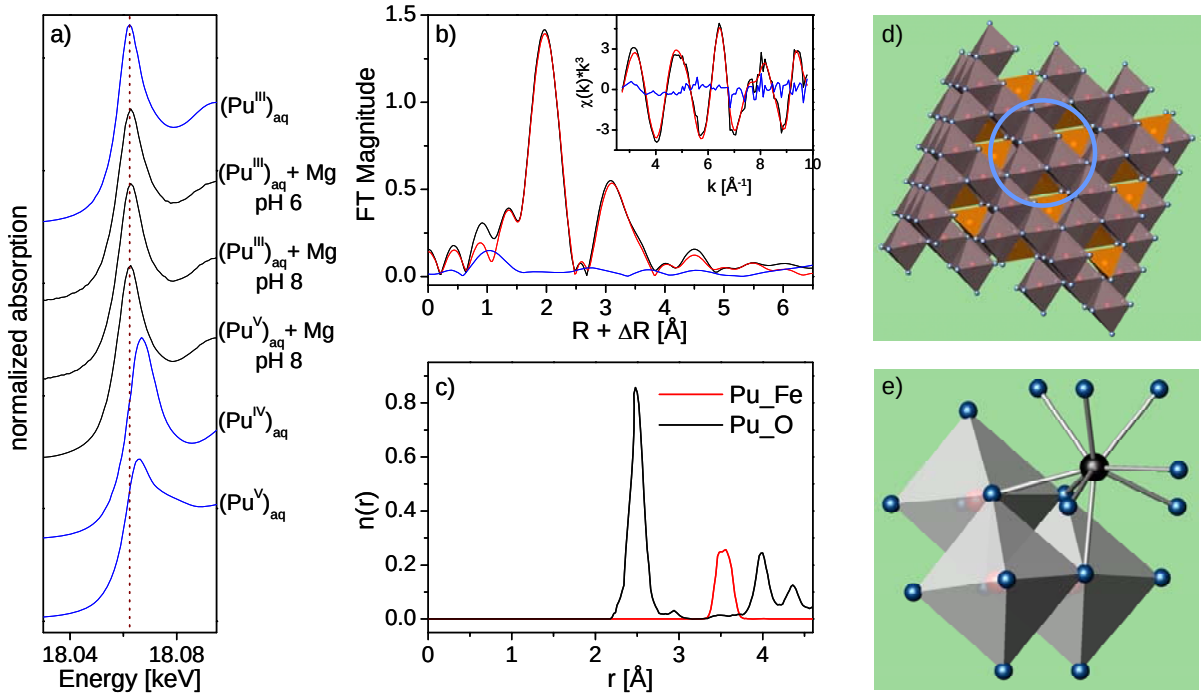

Figure 1. a) Experimental Pu-L_{III} XANES spectra of Pu reacted with magnetite (black) and $(Pu^{III})_{aq}$, $(Pu^{IV})_{aq}$ and $(Pu^{V})_{aq}$ for reference (blue). b) Experimental Pu-L_{III} EXAFS spectrum of $(Pu^{V})_{aq}$+Mg, pH 8 sample (black) and theoretical spectrum (red) resulting from radial refinement by MC simulation, FT and chi-spectrum (inset) (blue - residual). c) Pu-O and Pu-Fe radial pair distribution functions resulting from radial refinement. d) Octahedrally terminated (111) face of magnetite with one out of 7 possible positions for Pu(III) sorption marked by a blue circle. e) Sorption complex structure of Pu(III) on edge-sharing FeO_6-octahedra (Pu – black, O – blue, Fe – red).

The distances between the central Pu and the surrounding atoms in the thus identified structure of the sorption complex were refined by reverse Monte Carlo (RMC) simulation[44, 45] RMC allows small movements of all atoms surrounding Pu (up to 6.5 Å) to take structural disorder and possible relaxation effects of the magnetite surface into account (Fig. 1e). During this radial refinement the number of coordinated water molecules was fixed at 6. As can be seen in Figure 1b, the resulting $\chi(k) \times k^3$ spectrum and the experimental spectrum are in excellent agreement. The refinement yields the Pu-O and Pu-Fe radial pair distribution functions (RPDF) (Fig. 1c), wherein the first Pu-O peak corresponds to 9 oxygen atoms at 2.49 Å and the first Pu-Fe peak to three iron atoms at 3.54 Å. The Pu(III) position is close to an Fe-octahedral position and can be described as a tridentate, trinuclear, triple edge-sharing surface complex. Surface complexation at the octahedrally terminated (111) face

geometry is in line with results from X-ray crystal truncation rod (CTR) diffraction from which 75 % oxygen octahedral-iron (OOI) termination for magnetite (111) was deduced[46]. Due to the tridentate nature of the complex, it is likely to be very stable and play an important role in controlling Pu-magnetite reactions and Pu mobility.

Reaction of Pu(V) with mackinawite and chukanovite. XANES and EXAFS spectra of Pu(V) reacted with mackinawite (Pu(V)-Mack) and chukanovite (Pu(V)-Chuk) are similar to those of crystalline PuO_2(cr), suggesting the prevalence of tetravalent Pu in the samples and structural similarities with PuO_2(cr) (Fig. 2). However, a higher white line (WL) intensity of the Pu(V)-Mack and a slight low-energy shift of the Pu(V)-Chuk spectrum compared to PuO_2(cr) are apparent (Fig. 2a). While EXAFS frequencies and FT peak positions largely coincide for all three samples, the EXAFS amplitudes and FT peak heights decrease from PuO_2(cr) to Pu(V)-Chuk. Notable is the quasi congruence between the PuO_2(cr) and Pu(V)-Mack spectra below 7 $Å^{-1}$, and between Pu(V)-Mack and Pu(V)-Chuk above 9 $Å^{-1}$. The EXAFS spectrum of Pu(V)-Chuk shows in the lower k-range significant additional differences to that of PuO_2(cr) (arrows in Fig. 2b). As has been observed previously,[4, 47] the WL peak heights of PuO_2 colloids are higher than the ones found for well crystallized PuO_2(cr). This fact precludes or at least significantly hampers the use of linear combination fitting or ITT to quantify PuO_2 in spectra containing a mixture of oxidation states. For the Pu(V)-Mack sample, the XANES region gives no indication for the presence of either tri- or pentavalent plutonium species (compare also Fig. S3, S4).

Table 2. Shell fit of Pu(V)-Mack and PuO_2(cr) samples with fixed coordination numbers. Fit carried out in R-space, for details see SI, section 2.3).

	Pu(V)-Mack			PuO_2(cr)		
path	**CN**	**R [Å]**	**σ^2 [Å^2]**	**CN**	**R [Å]**	**σ^2 [Å^2]**
Pu - O	8	2.32	0.0081[d]	8	2.33	0.0054[d]
Pu - Pu	12	3.81	0.0059	12	3.83	0.0032
Pu - O	24	4.40	0.0088	24	4.43	0.0061
Pu-O MS	8	4.64[f]	0.0081[d]	8	4.66[f]	0.0054[d]
Pu - Pu	6	5.36	0.0084	6	5.37	0.0068
Pu - Pu	24	6.69	0.0142	24	6.68	0.0087
	E_0-shift		5.83 eV	E_0-shift		6.81 eV
	Residual		7.94 %	Residual		8.34 %
	f: fixed, d: correlated					

When the Pu(V)-Mack and the PuO_2(cr) reference spectrum are fitted with a PuO_2 model in similar k-ranges (3.0-12.2 $Å^{-1}$) and with coordination numbers fixed to their crystallographic values, the goodness of fit obtained is similar for both spectra, suggesting that a PuO_2 solid phase formed in the Pu(V)-Mack sample (Table 2). The higher Debye-Waller factors (σ^2), corresponding to a higher mean square radial displacement of the backscattering atoms, indicate that the PuO_2 formed in the Pu(V)-Mack sample is characterized by higher structural disorder in the coordination and all further shells compared to calcinated PuO_2(cr). A fit of the first peak in the FT (at 1.8 Å in Fig. 2c) with two oxygen

shells was only possible when the σ^2 values for the hypothetical two distances were correlated and then yielded unrealistically small values (Table S11). However, we cannot exclude the presence of Pu-OH or Pu-OH_2 groups that might contribute to the higher structural disorder in the coordination shell of the PuO_2 contained in the Pu(V)-Mack sample.[4] No indication for the presence of Pu(V) could be derived from shell fitting. By fitting the Pu(V)-Mack and PuO_2(cr) reference sample with adjustable coordination numbers, we also find similar Pu-Pu coordination numbers for both (Table S10). The number of backscattering Pu atoms at 3.82 Å decreases considerably with decreasing particle size only for PuO_2 particles with diameters below 2.5 nm. Between diameters of 8 nm and 3 nm, this coordination number decreases only from approx. 11.5 to 10.3 (calculated by assuming PuO_2 clusters, taking into account the change in Pu backscatterer numbers as a function of position in the cluster). As Pu-Pu coordination numbers for the PuO_2(Mack) sample and the PuO_2(cr) reference are similar given the fit uncertainty of up to 25 %, the only conclusion that can be drawn concerning particle size is that the PuO_2 particles formed with mackinawite likely have a diameter greater than the above mentioned value of approx. 2.5 nm.

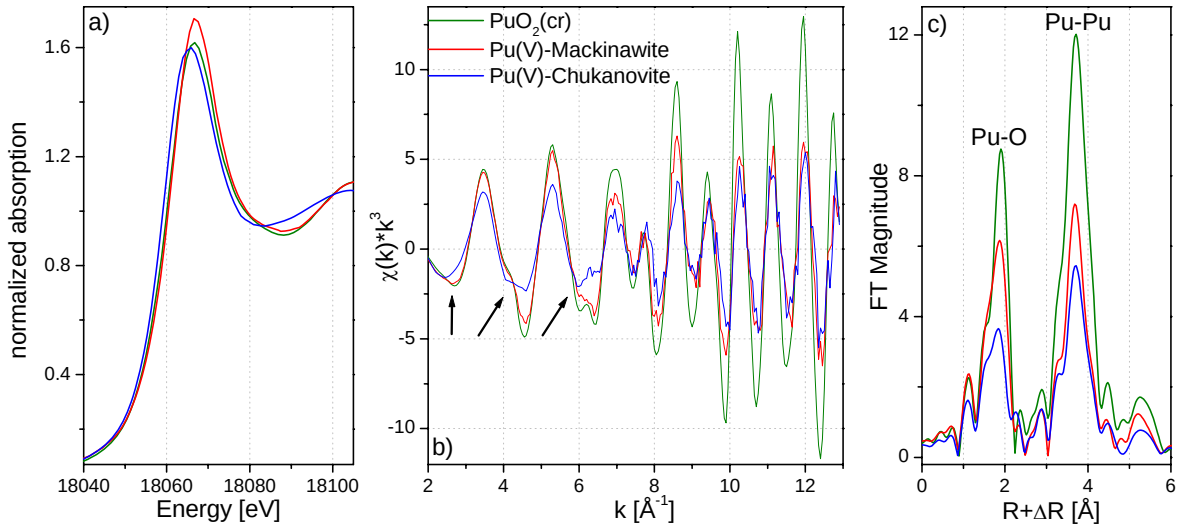

Figure 2. Experimetal Pu-L_{III} spectra of Pu(V)-Mack (red), Pu(V)-Chuk (blue) and PuO_2(cr) (green). a) XANES b) $\chi(k) \times k^3$ c) Fourier Transform ($3.0 < k < 12.6$ Å^{-1}).

Despite the particularity of varying WL peak intensities for PuO_2 colloids, the edge and WL peak positions for such colloids are, in comparison to crystalline PuO_2(cr), shifted to higher energies.[47] The slight low-energy shift of the XANES region of the Pu(V)-Chuk sample therefore points to a contribution of a lower oxidation state to the spectrum. As is detailed in the SI (section 2.5), both the low energy shift in the absorption edge and the low k-range differences between Pu(V)-Chuk, Pu(V)-Mack, and PuO_2(cr) spectra (arrows in Fig. 2) can be explained as resulting from contribution of both Pu(III) and PuO_2 to the spectrum and the resulting interference between their corresponding backscattering waves (Figure S11). Tentative quantification with ITT using $(Pu^{III})_{aq}$ and PuO_2(cr) or

the Pu(V)-Mack sample as references results for the XANES and EXAFS region in a Pu(III) content of 33 % (Table S12) and also suggests that the Pu(V)-Mack spectrum might be a more suitable PuO_2 reference for the Pu(V)-Chuk spectrum than PuO_2(cr). Shell fitting applied to theoretical PuO_2-$(Pu^{III})_{aq}$-mixture spectra underscores the ITT-results concerning composition of the Pu(V)-Chuk sample (SI, section 2.7) and highlights the limits of shell fitting to elucidate coordination shell structures in samples with mixed oxidation states.

Since a hypothetical solubility controlling Pu(III) phase, such as $Pu(OH)_3$, would lead to concentrations much higher than PuO_2(am,hyd) under our experimental conditions and furthermore would yield Pu concentrations higher than the LSC detection limit of 10^{-9} M, the observed low Pu concentration must be explained by a different Pu(III) species, most likely an inner-sphere sorption complex on the iron mineral phases. The present spectroscopic data, however, do not allow to differentiate between Pu(III) inner and outer sphere complexes or to identify the underlying mineral surface. The contribution of a heavy element backscatterer such as Fe or Pu to the spectrum of this hypothesized Pu(III)-sorption complex is however unlikely due to the overall spectral similarity of Pu(V)-Chuk to a theoretical $(Pu^{III})_{aq}$-PuO_2 mixture (Figure S11).

Impact of mineral phases on reaction products For the three investigated reactions of Pu(V) with magnetite, mackinawite and chukanovite at about pH 8, the concentration of dissolved Fe(II) and the pe values are on the same order of magnitude (Table 1) and thus, by themselves, can only partly account for the different reaction products, suggesting that the Pu redox state distribution found was influenced by the exact type of mineral surfaces present. For the (semi)conductors magnetite and mackinawite (magnetite: band gap of 0.1 eV[48], mackinawite: metallic conductance[49]), a number of metal/metalloid contaminants are reduced by multi-electron transfer reactions taking place at their surfaces (e.g. Se(IV) => Se(-II)[27], Cr(VI) => Cr(III)[50, 51], Sb(V) => Sb(III)[52]). With respect to Pu surface complexation, it is of relevance that, in contrast to magnetite, mackinawite surfaces are sulfur terminated,[49] which should considerably reduce their capability to serve as a ligand, as Pu is a hard Lewis acids and therefore oxyphilic.[53] If, for this reason, surface complexation with Pu(V) does not occur, electrons for a two-electron reduction from Pu(V) to Pu(III) cannot be provided directly by the mineral. The one electron necessary for the reduction from Pu(V) to Pu(IV) might be transferred from a Fe(II) aquo-ion or co-adsorbed surface species. In the absence of a surface that allows formation of stable surface complexes, Pu(IV) precipitates as PuO_2. A similar behavior with mackinawite was observed for U(VI) that also does not form inner sphere surface complexes with surface sulfur atoms and, after partial reduction, forms a mixed U(VI) / U(IV) oxide solid phase.[25, 54] In contrast, mackinawite removed only a small fraction of Np(V) from solution, which was reduced to Np(IV) present in sulfur coordinated inner-sphere surface complexes.[26] Should surface complexation between Pu and mackinawite have occurred in our experiment, it must, due to the absence of any identifiable Pu-S scattering path, be very limited in extent.

As the mineral chukanovite was identified and characterized only recently,[55] not much is known about the mobility of electrons in its structure or reactivity towards other contaminants. We can only speculate that the partial reduction of Pu(V) to Pu(III) in chukanovite, but not in mackinawite suspensions, might be due to the complexation behavior of Pu, prefering oxygen over sulfur terminated surfaces, and thus be related to the thermodynamic stability of the respective surface complexes. Our data do not permit to draw a conclusion on whether electrons are provided from structural, co-adsorbed or dissolved Fe(II).

Implications for environmental studies Assessment of the long-term safety of nuclear waste repositories and contaminated sites are largely based on thermodynamic model calculations to predict the chemical behavior and potential release of radionuclides to the environment. Based upon macroscopic thermodynamic data for solids and aqueous species and assuming equilibrium conditions, solubility limits are calculated as a function of different geochemical boundary conditions (e.g. the Pu source term under near-field conditions). Using the same modeling approach and thermodynamic data, predominance fields for the expected Pu oxidation states and species can be predicted as a function of pe and pH conditions (Fig. 3).

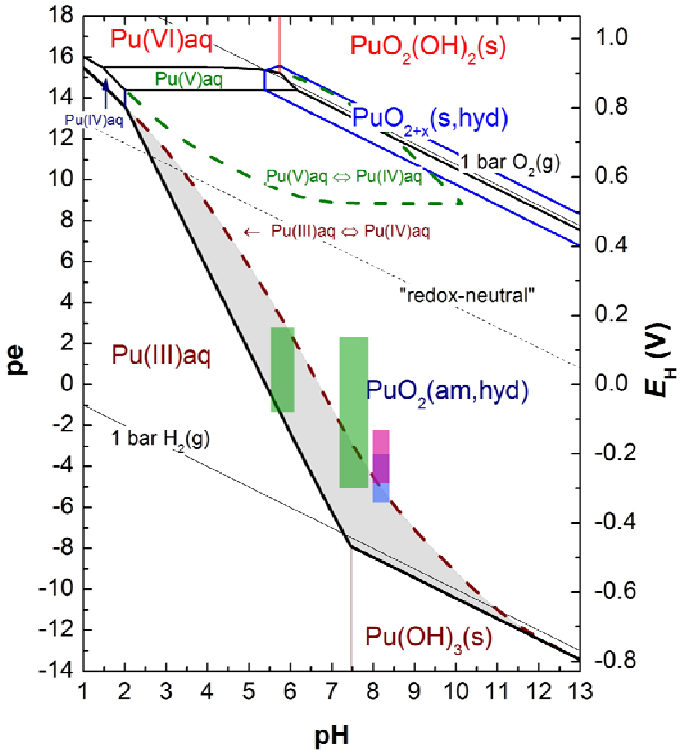

Figure 3. pe-pH predominance diagram for [Pu] = $1 \cdot 10^{-5}$ M in 0.1 M NaCl. For construction of the full black lines, PuO_2(am,hyd) is the considered Pu(IV) equilibrium species. Dashed lines result from use of Pu(IV)aq instead of PuO_2(am,hyd) as redox partner for Pu(III)aq (brown) or Pu(V)aq (green). The grey shaded area highlights the increase of the Pu(III)aq predominance field when Pu(IV)aq instead of solid PuO_2(am,hyd) is the redox partner for Pu(III)aq. Final reaction conditions of the investigated mineral systems are depicted by superposed, colored bars (upper limit – supernatant values, lower limit – suspension values): magnetite (green), mackinawite (pink) and chukanovite (blue) systems (Table 1).

As simplifications are made in the underlying chemical models (e.g. selection of species) and due to the lack of thermodynamic data for solids, surface complexes and aqueous species, applying this approach to natural systems characterized by conditions overlapping with the predominance fields of different species is limited and associated with rather large uncertainties. Also, the precise characterization of reaction conditions of natural systems can be challenging and result in large uncertainties in measured pe and iron speciation (for a more detailed discussion, see SI, page S4).

For example, as indicated in Fig. 3, the equilibrium line between Pu oxidation states three and four may be presented by the aquo-species $(Pu^{III})_{aq}$ on one side, and either the aquo-species $(Pu^{IV})_{aq}$ (brown dashed line) or colloidal PuO_2(am, hyd) (full black line) on the other side, resulting in a pH shift of more than one unit (grey shading in Fig. 3). Bars shaded in green (magnetite), pink (mackinawite) and blue (chukanovite) delineate the pe values measured in clear supernatant (top) and in suspension (bottom), both values differing by up to seven pe units (Table 1). When comparing the spectroscopically observed oxidation states with the experimentally found pe/pH conditions (colored bars) and the predominance field of Pu oxidation states (Fig. 3), it appears that the $(Pu^{III})_{aq}$ / $(Pu^{IV})_{aq}$ redox equilibrium and the pe values determined in suspension come closest to our spectroscopic results. However, it cannot be excluded that the true equilibrium between the observed $(Pu^{III})_{adsorbed}$ species and Pu(IV) is shifted to higher pe values compared to the dashed brown $(Pu^{III})_{aq}$ / $(Pu^{IV})_{aq}$ line, as relying on the pe values measured in the clear supernatant would suggest. The discrepancy between suspension and supernatant pe and pH values in comparison to Pu redox chemistry highlights the need to obtain reliable data for complex laboratory and natural conditions.

In order to derive better and more comprehensive quantitative models to predict Pu (redox) chemistry and Pu mobility in the environment, it will be necessary to include sorption effects into consistent thermodynamic models based upon data for aqueous species, Pu solids, iron and other common mineral solids *and* Pu surface complexes on these minerals. To identify, characterize and parameterize the processes taking place at mineral surfaces, a detailed understanding on a molecular level is needed and can be obtained by systematic application of advanced analytical/spectroscopic tools in combination to thermodynamic modeling. As we attempted to show, XAS allows in many cases to clearly identify Pu reaction products at the mineral surface, thereby enabling conclusions on the stability and expected environmental relevance of the identified species.

Our results highlight that Pu(III) is an important oxidation state in reducing anoxic environments; models based entirely on tetravalent Pu(IV) species are, therefore, inadequate. Consequently, to improve predictions on the fate of Pu in nuclear waste repositories and environmental systems, sorption of Pu(III) to relevant mineral surfaces should be investigated in more detail, also to lower the uncertainty of present predictions based upon analogy with other trivalent actinides, e.g. Am(III) and Cm(III). Relevant Pu(III) complexation and solubility constants should be determined to obtain more reliable quantitative models for Pu. Regarding the applicability of our results to natural settings, it should be considered that other factors (i.e. sorption of Pu on additional mineral surfaces, interaction

of Pu with dissolved ligands, variation of Pu / surface ratio or competitive sorption effects) can impact reaction outcomes and should be further investigated.

ACKNOWLEDGMENTS

This work has been financially supported by HZDR, KIT-INE, ISTerre (UJF/CNRS/INSU), PACHEM-Paris and IUF. The research leading to these results has received funding from the European Community's Seventh Framework Programme (FP7/2007-2013) under Grant Agreement n° 232631. We are most grateful to Ch. Den Auwer (CEA, Marcoule) and Ph. Martin (CEA, Cadarache) for providing reference spectra, to T. Kisely (KIT-INE) for measuring BET specific surface areas, to D. Schild (KIT-INE) for Raman measurements, to A. Fernandez-Martinez (ILL) and G. Garbarino (ESRF) for XRD measurements, to D. Falkenberg (HZDR) for his flexibility in building XAFS double-confinement sample holders, to Ch. Hennig (HZDR) for helpful discussions, to X. Gaona and E. Wieland (PSI) who lent us a LN_2 transport dewar inset and to the radioprotection responsibles at KIT-INE (Ch. Marquard) and ESRF (P. Colomp and Y. Pira) for the smooth collaboration before and during the XAFS experiment at ESRF.

Supporting information available

Details are provided on mineral synthesis and characterization, XAFS spectra acquisition and data treatment, Monte Carlo simulation, sample reaction conditions, XANES analysis, ITT analysis and shell fitting, analysis of theoretical PuO_2-Pu(III) mixture spectra. This information is available free of charge via the Internet at http://pubs.acs.org/.

REFERENCES

(1) Magill, J.; Pfennig, G.; Galy, J., *Chart of the nuclides*. 7th ed.; European Commission - DG Joint Research Centre - Institute of Transuranium Elements: Karlsruhe, 2006; p 44.

(2) Runde, W., The chemical interactions of actinides in the environment. *Los Alamos Science* **2000,** *26*, 392-411.

(3) Dardenne, K.; Seibert, A.; Denecke, M. A.; Marquardt, C. M., Plutonium(III,IV,VI) speciation in Gorleben groundwater using XAFS. *Radiochim. Acta* **2009,** *97* (2), 91-97.

(4) Rothe, J.; Walther, C.; Denecke, M. A.; Fanghanel, T., XAFS and LIBD investigation of the formation and structure of colloidal Pu(IV) hydrolysis products. *Inorg. Chem.* **2004,** *43* (15), 4708-4718.

(5) Rai, D.; Gorby, Y. A.; Fredrickson, J. K.; Moore, D. A.; Yui, M., Reductive dissolution of PuO_2(am): The effect of Fe(II) and hydroquinone. *J. Solution Chem.* **2002,** *31* (6), 433-453.

(6) Felmy, A. R.; Moore, D. A.; Rosso, K. M.; Qafoku, O.; Rai, D.; Buck, E. C.; Ilton, E. S., Heterogeneous reduction of PuO_2 with Fe(II): importance of the Fe(III) reaction product. *Environ. Sci. Technol.* **2011,** *45*, 3952-3958.

(7) Neck, V.; Altmaier, M.; Fanghanel, T., Solubility of plutonium hydroxides/hydrous oxides under reducing conditions and in the presence of oxygen. *C. R. Chimie* **2007,** *10* (10-11), 959-977.

(8) Kalmykov, S. N.; Kriventsov, V. V.; Teterin, Y. A.; Novikov, A. P., Plutonium and neptunium speciation bound to hydrous ferric oxide colloids. *C. R. Chimie* **2007,** *10* (10-11), 1060-1066.

(9) Saheb, M.; Descostes, M.; Neff, D.; Matthiesen, H.; Michelin, A.; Dillmann, P., Iron corrosion in an anoxic soil: Comparison between thermodynamic modelling and ferrous archaeological artefacts characterised along with the local in situ geochemical conditions. *Appl. Geochem.* **2010,** *25* (12), 1937-1948.

(10) El Hajj, H.; Abdelouas, A.; Grambow, B.; Martin, C.; Dion, M., Microbial corrosion of P235GH steel under geological conditions. *Phys. Chem. Earth* **2010,** *35,* 248–253.

(11) Lee, T. R.; Wilkin, R. T., Iron hydroxy carbonate formation in zerovalent iron permeable reactive barriers: Characterization and evaluation of phase stability. *J. Contam. Hydrol.* **2010,** *116* (1-4), 47-57.

(12) White, A. F.; Peterson, M. L.; Hochella, M. F., Electrochemistry and dissolution kinetics of magnetite and ilmenite. *Geochim. Cosmochim. Acta* **1994,** *58* (8), 1859-1875.

(13) Spadini, L.; Bott, M.; Wehrli, B.; Manceau, A., Analysis of the Major Fe Bearing Mineral Phases in Recent Lake Sediments by EXAFS Spectroscopy. *Aquat. Geochem.* **2003,** *9* (1), 1-17.

(14) Ona-Nguema, G.; Morin, G.; Wang, Y. H.; Menguy, N.; Juillot, F.; Olivi, L.; Aquilanti, G.; Abdelmoula, M.; Ruby, C.; Bargar, J. R.; Guyot, F.; Calas, G.; Brown, G. E., Arsenite sequestration at the surface of nano-$Fe(OH)_2$, ferrous-carbonate hydroxide, and green-rust after bioreduction of arsenic-sorbed lepidocrocite by Shewanella putrefaciens. *Geochim. Cosmochim. Acta* **2009,** *73* (5), 1359-1381.

(15) Kukkadapu, R. K.; Zachara, J. M.; Fredrickson, J. K.; Kennedy, D. W.; Dohnalkova, A. C.; McCready, D. E., Ferrous hydroxy carbonate is a stable transformation product of biogenic magnetite. *Am. Mineral.* **2005,** *90,* 510–515.

(16) Keeney-Kennicutt, W. L.; Morse, J. W., The redox chemistry of $Pu(V)O_2^+$ interaction with common mineral surfaces in dilute solutions and seawater. *Geochim. Cosmochim. Acta* **1985,** *49,* 2577-2588.

(17) Powell, B. A.; Fjeld, R. A.; Kaplan, D. I.; Coates, J. T.; Serkiz, S. M., $Pu(V)O_2^+$ adsorption and reduction by synthetic magnetite (Fe_3O_4). *Environ. Sci. Technol.* **2004,** *38* (22), 6016-6024.

(18) Powell, B. A.; Fjeld, R. A.; Kaplan, D. I.; Coates, J. T.; Serkiz, S. M., $Pu(V)O_2^+$ adsorption and reduction by synthetic hematite and goethite. *Environ. Sci. Technol.* **2005,** *39* (7), 2107-2114.

(19) Sanchez, A. L.; Murray, J. W.; Sibley, T. H., The adsorption of plutonium IV and V on goethite. *Geochim. Cosmochim. Acta* **1985,** *49,* 2297-2307.

(20) Powell, B. A.; Duff, M. C.; Kaplan, D. I.; Fjeld, R. A.; Newville, M.; Hunter, D. B.; Bertsch, P. M.; Coates, J. T.; Eng, P.; Rivers, M. L.; Sutton, S. R.; Triay, I. R.; Vaniman, D. T., Plutonium oxidation and subsequent reduction by Mn(IV) minerals in Yucca Mountain tuff. *Environ. Sci. Technol.* **2006**, *40* (11), 3508-3514.

(21) Kersting, A. B.; Zhao, P.; Zavarin, M.; Sylwester, E. R.; Allen, P. G.; Williams, R. W., Sorption of Pu(V) on Mineral Colloids. In *Colloidal-Facilitated Transport of Low-Solubility Radionuclides: A Field, Experimental, and Modeling Investigation; Report UCRL-ID-149688,* Kersting, A. B.; Remus, P. W., Eds., Lawrence Livermore National Laboratory, Livermore, CA: 2003.

(22) Duro, L.; El Aamrani, S.; Rovira, M.; De Pablo, J.; Bruno, J., Study of the interaction between U(VI) and the anoxic corrosion products of carbon steel. *Appl. Geochem.* **2008,** *23,* 1094-1100.

(23) White, A. F.; Peterson, M. L., Reduction of aqueous transition metal species on the surfaces of Fe(II)-containing oxides. *Geochim. Cosmochim. Acta* **1996,** *60* (20), 3799-3814.

(24) Erdös, E.; Altorfer, H., Ein dem Malachit aehnliches basisches Eisenkarbonat als Korrosionsprodukt von Stahl. *Werkst. Korros.* **1976,** *27,* 304-312.

(25) Moyes, L. N.; Parkman, R. H.; Charnock, J. M.; Vaughan, D. J.; Livens, F. R.; Hughes, C. R.; Braithwaite, A., Uranium uptake from aqueous solution by interaction with goethite, lepidocrocite, muscovite, and mackinawite: An X-ray absorption spectroscopy study. *Environ. Sci. Technol.* **2000,** *34* (6), 1062-1068.

(26) Moyes, L. N.; Jones, M. J.; Reed, W. A.; Livens, F. R.; Charnock, J. M.; Mosselmans, J. F. W.; Hennig, C.; Vaughan, D. J.; Pattrick, R. A. D., An X-ray absorption spectroscopy study of

neptunium(V) reactions with mackinawite (FeS). *Environ. Sci. Technol.* **2002,** *36* (2), 179-183.

(27) Scheinost, A. C.; Kirsch, R.; Banerjee, D.; Fernandez-Martinez, A.; Zaenker, H.; Funke, H.; Charlet, L., X-ray absorption and photoelectron spectroscopy investigation of selenite reduction by FeII-bearing minerals. *J. Contam. Hydrol.* **2008,** *102,* 228-245.

(28) Brunauer, S.; Emmett, P. H.; Teller, E., Adsorption of gases in multimolecular layers. *J. Am. Chem. Soc.* **1938,** *60* (2), 309-319.

(29) Viollier, E.; Inglett, P. W.; Hunter, K.; Roychoudhury, A. N.; Van Cappellen, P., The ferrozine method revisited: Fe(II)/Fe(III) determination in natural waters. *Appl. Geochem.* **2000,** *15* (6), 785-790.

(30) Martin, P.; Grandjean, S.; Valot, C.; Carlot, G.; Ripert, M.; Blanc, P.; Hennig, C., XAS study of $(U_{1-y}Pu_y)O_2$ solid solutions. *J. Alloys Compd.* **2007,** *444,* 410-414.

(31) Ressler, T., WinXAS: a program for X-ray absorption spectroscopy data analysis under MS-Windows. *J. Synchrotron Radiat.* **1998,** *5,* 118-122.

(32) Ankudinov, A. L.; Ravel, B.; Rehr, J. J.; Conradson, S. D., Real Space Multiple Scattering Calculation of XANES. *Phys. Rev. B* **1998,** *58,* 7565.

(33) Ankudinov, A. L.; Bouldin, C.; Rehr, J. J.; Sims, J.; Hung, H., Parallel calculation of electron multiple scattering using Lanczos algorithms. *Phys. Rev. B* **2002,** *65* (10), 104107.

(34) Belin, R. C.; Valenza, P. J.; Reynaud, M. A.; Raison, P. E., New hermetic sample holder for radioactive materials fitting to Siemens D5000 and Bruker D8 X-ray diffractometers: application to the Rietveld analysis of plutonium dioxide. *J. Appl. Crystallogr.* **2004,** *37,* 1034-1037.

(35) Wulff, M.; Lander, G. H., Magnetic structure of Pu ground state in beta-Pu_2O_3. *J. Chem. Phys.* **1988,** *89* (5), 3295-3299.

(36) Denecke, M. A., Actinide speciation using X-ray absorption fine structure spectroscopy. *Coord. Chem. Rev.* **2006,** *250* (7-8), 730-754.

(37) Rossberg, A.; Reich, T.; Bernhard, G., Complexation of uranium(VI) with protocatechuic acid - application of iterative transformation factor analysis to EXAFS spectroscopy. *Anal. Bioanal. Chem.* **2003,** *376* (5), 631-638.

(38) Guillaumont, R.; Fanghänel, T.; Fuger, J.; Grenthe, I.; Neck, V.; Palmer, D. A.; Rand, M. H., *Update on the Chemical Thermodynamics of Uranium, Neptunium, Plutonium, Americium and Technetium.* Elsevier: Amsterdam, 2003.

(39) Allen, P. G.; Bucher, J. J.; Shuh, D. K.; Edelstein, N. M.; Reich, T., Investigation of aquo and chloro complexes of UO_2^{2+}, NpO_2^{+}, Np^{4+}, and Pu^{3+} by X-ray absorption fine structure spectroscopy. *Inorg. Chem.* **1997,** *36,* 4676-4683.

(40) Conradson, S. D.; Clark, D. L.; Neu, M. P.; Runde, W. H.; Tait, C. D., Characterizing the plutonium aquo ions by XAFS spectroscopy. *Los Alamos Science* **2000,** *26,* 418-421.

(41) Matonic, J. H.; Scott, B. L.; Neu, M. P., High-yield synthesis and single-crystal X-ray structure of a plutonium(III) aquo complex:$[Pu(H_2O)_9][CF_3SO_3]_3$. *Inorg. Chem.* **2001,** *40,* 2638-2639.

(42) Nakata, K.; Nagasaki, S.; Tanaka, S.; Sakamoto, Y.; Tanaka, T.; Ogawa, H., Sorption and reduction of neptunium(V) on the surface of iron oxides. *Radiochim. Acta* **2002,** *90* (9-11), 665-669.

(43) Rossberg, A.; Scheinost, A. C., Three-dimensional modeling of EXAFS spectral mixtures by combining Monte Carlo simulations and target transformation factor analysis. *Anal. Bioanal. Chem.* **2005,** *383* (1), 56-66.

(44) Gurman, S. J.; McGreevy, R. L., Reverse Monte-Carlo simulation for the analysis of EXAFS data. *J. Phys.: Condens. Matter* **1990,** *2* (48), 9463-9473.

(45) Winterer, M., Reverse Monte Carlo analysis of extended x-ray absorption fine structure spectra of monoclinic and amorphous zirconia. *J. Appl. Phys.* **2000,** *88* (10), 5635-5644.

(46) Petitto, S. C.; Tanwar, K. S.; Ghose, S. K.; Eng, P. J.; Trainer, T. P., Surface structure of magnetite (111) under hydrated conditions by crystal truncation rod diffraction. *Surf. Sci.* **2010,** *604,* 1082–1093.

(47) Conradson, S. D.; Abney, K. D.; Begg, B. D.; Brady, E. D.; Clark, D. L.; den Auwer, C.; Ding, M.; Dorhout, P. K.; Espinosa-Faller, F. J.; Gordon, P. L.; Haire, R. G.; Hess, N. J.;

Hess, R. F.; Keogh, D. W.; Lander, G. H.; Lupinetti, A. J.; Morales, L. A.; Neu, M. P.; Palmer, P. D.; Paviet-Hartmann, P.; Reilly, S. D.; Runde, W. H.; Tait, C. D.; Veirs, D. K.; Wastin, F., Higher order speciation effects on plutonium L_3 X-ray absorption near edge spectra. *Inorg. Chem.* **2004,** *43* (1), 116-131.

(48) Cornell, R. M.; Schwertmann, U., *The Iron Oxides - Structure, Properties, Reactions, Occurrences and Uses Second, completely Revised and Extended Edition.* Wiley-VCH: Weinheim, 2003.

(49) Devey, A. J.; Grau-Crespo, R.; de Leeuw, N. H., Combined density functional theory and interatomic potential study of the bulk and surface structures and properties of the iron sulfide mackinawite (FeS). *J. Phys. Chem. C* **2008,** *112* (29), 10960-10967.

(50) Mullet, M.; Boursiquot, S.; Ehrhardt, J. J., Removal of hexavalent chromium from solutions by mackinawite, tetragonal FeS. *Colloids Surf., A* **2004,** *244* (1-3), 77-85.

(51) Jung, Y.; Choi, J.; Lee, W., Spectroscopic investigation of magnetite surface for the reduction of hexavalent chromium. *Chemosphere* **2007,** *68* (10), 1968-1975.

(52) Kirsch, R.; Scheinost, A. C.; Rossberg, A.; Banerjee, D.; Charlet, L., Reduction of antimony by nano-particulate magnetite and mackinawite. *Mineral. Mag.* **2008,** *71* (1), 185-189.

(53) Morss, L. R.; Edelstein, N. M.; Fuger, J., Eds. *The chemistry of the actinide and transactinide elements,* 3rd ed.; Springer: Dordrecht, 2006; Vol. 4, p 2524-2621.

(54) Hua, B.; Deng, B., Reductive immobilization of uranium(VI) by amorphous iron sulfide. *Environ. Sci. Technol.* **2008,** *42,* 8703-8708.

(55) Pekov, I. V.; Perchiazzi, N.; Merlino, S.; Vyacheslav, N.; Merlini, M.; Zadov, A. E., Chukanovite, $Fe_2(CO_3)(OH)_2$, a new mineral from the weathered iron meteorite Dronino. *Eur. J. Mineral.* **2007,** *19* (6), 891-898.

Supporting Information to "Oxidation state and local structure of plutonium reacted with magnetite, mackinawite and chukanovite"

1. Supporting Information for Materials and Methods section

1.1 Mineral synthesis and characterization

NaCl, $FeCl_2 \times 4H_2O$, $FeCl_3 \times 6H_2O$ (Fluka), $Na_2CO_3 \times 10\ H_2O$ (Labosi) and $CaCl_2$ (Riedel de Häen) used for mineral syntheses and Ferrospectral, NH_4Ac, $NH_2OH{\cdot}HCl$ and 1000 ppm Fe-standard (Certipur) (Merck) used for photometric iron determinations were all analytical grade; $FeCl_2$ salt was kept under N_2-atmosphere in a glove box to prevent oxidation.

A magnetite (Fe_3O_4) suspension was prepared by slowly adding 6 M NH_3 to a solution with Fe(II) / Fe(III) = 0.5 ([$FeCl_2$] = 0.4 M and [$FeCl_3$] = 0.8 M) (V (6 M NH_3) / V(Fe-solution) = 1.2)[1]. According to TEM analysis, the magnetite particles have an average size of 9.4 nm[i]. Mackinawite (tetragonal FeS) was prepared by mixing equal volumes of 0.6 M Fe(II) and 0.6 M S(-II) solutions obtained using Mohr's salt, ($Fe(NH_4)_2(SO_4)_2{\cdot}4H_2O$), p.a. (Fluka), and Na_2S (60-62%, Riedel de Häen). This recipe[2, 3] results in the formation of nano-crystalline mackinawite, which is characterized by crystallite diameters in the range of 2 to 10 nm and correspondingly high surface areas. Pair distribution functions (PDF) analysis from high energy X-ray scattering (HEXS), assuming spherical particles, yielded a mean particle size of 5 nm[4]. Chukanovite ($Fe_2(CO_3)(OH)_2$) was prepared from equal volumes of 0.4 M $FeCl_2$ and 0.8 M Na_2CO_3 solutions by slowly adding the Fe(II) solution to the magnetically stirred Na_2CO_3 solution. The precipitated solids were washed by centrifugation (at least 3 washing cycles) and kept in suspension in 0.01 M NaCl. BET specific surfaces areas measurements (Table S1) were carried out using a Quantachrome Autosorb-1 apparatus (Quantachrome Instruments, Boynton Beach, Florida, USA). After drying in the glove-box for 24h, the sample powders were further dried on the BET machine under helium at 77 K and the adsorption measurement itself was carried out in duplicate at 97°C with nitrogen as adsorbate gas (Table S1).

Table S1. BET specific surface areas for mineral phases, characteristics of mineral suspensions used for sample preparation and resulting Pu loadings.

Mineral name	Formula	specific surface area [m^2/g]*	solid/liquid [g/L]	solid/liquid [mmol/L]	surface area [m^2/L]	Pu loading [ppm]**
Magnetite	Fe_3O_4	75	5.55	24	416	570
Mackinawite	FeS	53	3.43	39	183	920
Chukanovite	$Fe_2(CO_3)(OH)_2$	112	1.98	9.6	221	1590

*the experimental uncertainty of the given values is on the order of 5-10%

**mass Pu / mass iron mineral phase

The synchrotron X-ray powder diffraction data for chukanovite (Fig. S1) were collected at the ID27

[i] personal communication from Siriwan Dulnee, FZD, November 2010, unpublished data.

beamline (ESRF, Grenoble, France). A monochromatic beam (λ = 0.3738 Å, calibrated using the K-edge of iodine) was used and the diffracted radiation was collected using a MAR CCD detector. The beam dimension on the sample was 3 × 3 µm. The sample to detector distance (~230 mm) and the CCD detector tilt were calibrated by X-ray powder diffraction of a Si standard. Data were collected up to 2θ = 22°, corresponding to a d-space resolution of 0.98 Å. Data were reduced with the Fit2D software.[5] In Figure S1 the experimental chukanovite diffraction pattern is compared to two simulated diffraction pattern with different peak width (U = 0, V = 0, W = 10^{-5}0 or W = 0.03)[6] calculated with the Visualize tool (Version 1.0.1.2) in the FindIt Software (Version 1.4.6).

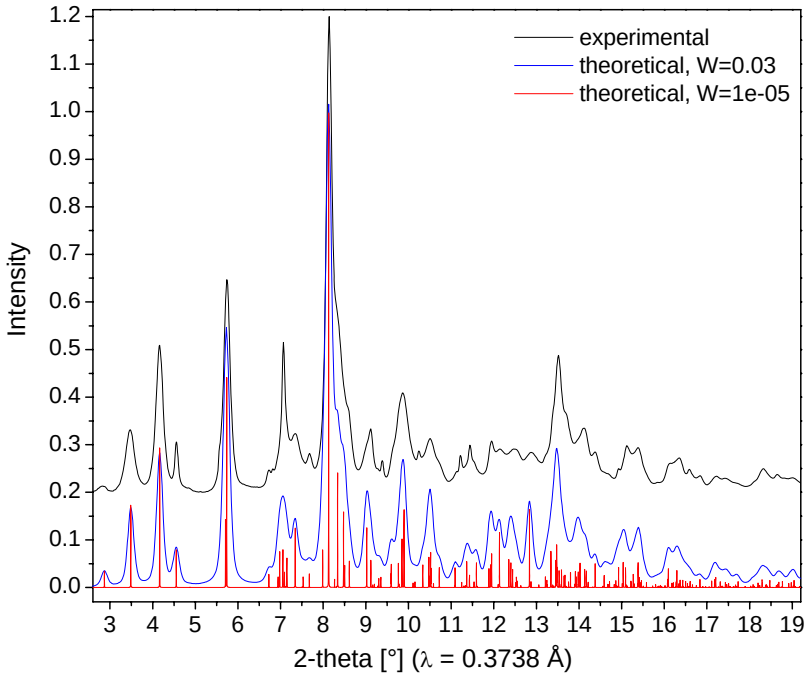

Figure S1. Synchrotron powder diffraction pattern for chukanovite (black) and simulated diffraction patterns with two different peak widths (blue, red) generated from the mineral data file (ICSD 159109[7]).

1.2 pH and pe measurement approaches

Both pH and pe are defined for aqueous solutions, representing the "relative tendency of a solution to accept or transfer protons" or to "accept or transfer electrons"[8]; pH is the negative logarithm of the proton activity in solution, pe is the negative logarithm of the apparent electron activity in solution. The pH suspension effect (SE) is, according to IUPAC recommendations, defined as "the difference in cell potential for two suspension potentiometric cells, one with both electrodes in the separated equilibrium solution (eqs) and the other with both electrodes in the sediment or suspension".[9] The extent of the suspension effect is influenced by a number of parameters, such as type of particles present, particle size and concentration, ion activities in solution and the type of reference electrode used. The suspension effect arises from the change in potential of the indicator electrode, which as a consequence of the overlapping of its diffuse double layer with that of the particles changes to an

irreversible mixed potential probe, and from the change in the liquid junction potential of the reference electrode, as the interaction of electrolyte flowing out from the salt bridge with the particles gives rise to an anomalous junction potential.[10] However, in many studies involving mineral or soil suspensions, pH is solely measured with combination electrodes present in suspension. By acquiring pH in the equilibrium solution (supernatant after centrifugation) and in suspension, the SE can be assessed, which can be of interest for comparison to other studies involving similar experimental conditions but where pH was acquired only in suspension.

To obtain reliable measurements of redox potential, a certain exchange current i_0 ($> 10^{-7}$ A) at the sensing electrode is necessary. As i_0 is dependent on the concentration of electro-active species, the range of ion concentrations wherein precise measurements can be made is limited, the lower limit for the Fe(III)/Fe(II) couple being on the order of 10^{-5} M.[8] Whether measuring a redox potentials in a solution in equilibrium with an iron mineral (under absence of other electro-active species) yields reliable results, will then largely depend on mineral solubility and pH, as these largely determine the concentrations of dissolved Fe(II) and Fe(III). In addition, traces of oxygen can result in dissolved Fe(II) species being oxidized to Fe(III) thus affecting the measured redox potential[8] While measuring redox potential in the supernatant is in agreement with the definition of pe as a solution value, it is for our experimental conditions (at least at pH 8 due to the small concentrations of dissolved Fe(II) and Fe(III)) not likely to yield reliable values. Also, even though all measurements were carried out in an anoxic glove box with O_2 levels below 10ppmv, oxidation of dissolved Fe(II) by O_2 during the redox measurement cannot be excluded. Regarding redox potential measurements in suspension, it should be mentioned that Silvester et al.[11] obtained for the Fe(II) - (nano-FOH) and Fe(II)-HFO systems measured Eh values that were consistent with the theoretically calculated values and concluded that the particles most likely interacted electrochemically with the Pt electrode.

To comply with the definition of pe as a solution parameter, we measured the redox potential in the supernatant. To allow the Pt electrode to make contact with the mineral particles, we also determined Eh in suspension, using the same conventional combination redox electrode. During suspension measurements a stable reading was reached faster, the redox potential was more reproducible over time and is due to the buffering particles less likely to be influenced by diffusing oxygen. We therefore estimate that the pe acquired in suspension is more reliable and robust, even though this value may be affected by a systematic error, e.g. from the anomalous junction potential of the reference electrode.

The report to ReCosy Intercomparison Exercise on redox measurement techniques of natural and synthetic samples, comparing types of electrodes used, cleaning protocols, amperometric and potentiometric techniques, time of equilibration and other parameters, has recently been published (KIT Scientific Reports 7572) and is available online.[12]

1.3 XAFS spectra acquisition and data treatment

The energy of the X-ray beam was tuned by a double crystal monochromator operating in channel-cut mode using a Si (111) crystal pair. Collimation of the beam and rejection of higher harmonics was achieved using platinum-coated Si mirrors before and after the monochromator. A closed-cycle helium cryostat (CryoVac) set to 15 K was used for all measurements. Pu-L_{III}-edge X-ray Absorption Near-Edge Structure (XANES) and Extended X-ray Absorption Fine-Structure (EXAFS) spectra of the Pu-mineral samples were collected in fluorescence mode (seven to eleven spectra per samples) using a 13-element energy dispersive solid state Ge detector (Canberra) together with a digital signal processing unit (XIA). In the XANES region, data were collected in steps of 0.8 eV. A Zr-foil was used for energy calibration; the first inflection point (defined as the zero-crossing of the second derivative) of the Zr-spectrum was set to 17.998 keV. After energy and deadtime correction the spectra were averaged in Sixpack[13], v. 066. Reference spectra of $(Pu^{III})_{aq}$, $(Pu^{IV})_{aq}$ and $(Pu^{V})_{aq}$[ii] and of crystalline PuO_2[iii], all measured in transmission mode at the same beam-line (liquid samples at RT, PuO_2 at 15 K), were averaged using Athena[14],v. 0.8.056 and Sixpack, respectively. Table S3 lists the energy of the absorption edge and the white line (WL) peak for all sample and reference spectra. The edge energy, E_0, is defined as the inflection point of the absorption edge. The WL maximum is determined as the zero-crossing of the first derivative of the spectrum. The inflections points were determined numerically in a manner similar to the one described in Conradson *et al.*, 2004[15]. In short, second order polynomials (ax^2+bx+c) were fit to subsequent groups of seven subsequent data points along the edge so that each data point is one time at the 4th position and the values of the second derivatives of these polynomials ($2\cdot a$) were assigned to the 4th data points as their second derivative value. The point of zero crossing of the thus constructed second derivative of the edge was used as the edge energy. Compared to other methods that involve smoothing of data points before derivation, the energy of the thus numerically obtained inflection point is slightly lower. Considering for example the Pu-mineral sample fluorescence spectra and using WinXAS with its smoothing options, the numerically determined inflection point is between 0.1 and 0.3 eV lower than the one found by 4 pt smoothing in WINXAS and between 0.3 and 0.6 eV lower than found if 1 pt smoothing is applied. For reference spectra acquired in transmission mode, the difference between the numerical inflection point and the one obtained with smoothing in WINXAS is up to 0.2 eV with 4 pt smoothing and up to 0.5 eV with 1 pt smoothing. Spectra were normalized using routine procedures. Both in WinXAS (Pu-magnetite samples) and Athena (PuO_2, Pu-Mackinawite, Pu-Chukanovite), a linear polynomial is fit to pre-edge region and a 3rd degree polynomial to the post-edge region. For the extraction of $\chi(k)$ from the normalized data the atomic background function $\mu_0(E)$ was optimized to reduce spurious contributions below 0.9 Å (WINXAS) or 1 Å (Athena) using the Fourier transform of k^3- weighted (WINXAS) or k^2-weighted (Athena) data in a spline range of k = 0.5 to 13 Å^{-1} (Athena) or k = 2 to

[ii] provided by Christoph Den Auwer, CEA, Marcoule, France
[iii] provided by Philippe Martin, CEA, Cadarache. France

13 Å^{-1} (WINXAS). For the transformation of the abscissa units from energy into photoelectron wave vector (k) values (k = sqrt ((2m_e/ħ^2) * (E-E_0))[iv]) the inflection point of the absorption edge (with 4 pt smoothing in WinXAS) or the energy value where the absorption edge after normalization reaches an intensity value of one (Athena) was used as E_0.

For shell fits, goodness of fit is indicated by a residual value in percent, calculated in WINXAS as:

$$\text{Residual}\,[\%] = \frac{\sum_{i=1}^{N} \left| y_{\exp}(i) - y_{theo}(i) \right|}{\sum_{i=1}^{N} \left| y_{\exp}(i) \right|} * 100\,. \qquad (1)$$

1.4 Monte Carlo Simulation

For simulating possible Pu-magnetite sorption complexes by Monte Carlo modeling, a rectangular slab of magnetite sized 18 Å*15 Å*5 Å was cut out of the magnetite structure, exposing two (111) faces, one with octahedral and one with mixed tetrahedral/octahedral termination (Fig S2). With two different approaches, the most likely position for Pu on these (111) faces was identified and the radial distribution of atoms around Pu in the obtained surface sorption complex subsequently refined to extract radial pair distribution functions of Fe and O neighbors around the Pu atom.

In detail, a first position search was performed using one or two Pu atoms (Table S2, method 1a and 1b, resp.), that were randomly displaced in a 25*25*15 Å^3 box around the slab, thereby covering roughly the whole volume of the defined box. As the box exceeds the size of the slab, the two differently terminated (111) surfaces and edge position are accessible to the moving Pu atom(s). For each Pu position relative to the surface, the theoretical chi-spectrum is calculated with FEFF8.2. A constant backscattering contribution of six oxygen atoms was added to each Pu atom, thereby simulating a moving PuO_6 cluster. For each position the standard deviation (SD) between the theoretical and the experimental spectrum was calculated and mapped, resulting in a 3D map of standard deviations (Fig S2). For clarity, only positions with a SD below a cutoff value are shown; the green areas correspond to the lowest SD values present, red areas to higher ones. The 7 positions with the lowest SD (green dots in Fig. S2, lower left and middle) are characterized by three edge-sharing FeO_6-octahedra as present on octahedrally terminated (111) faces (blue circles in Fig. S2, lower right). On mixed terminated (111) faces no position with a similarly low SD was found. The distances between the Pu atom and the three surface oxygen atoms were on the order of 2.5 Å. When this position search procedure was done with two Pu atoms, each of the Pu atoms was situated at one of the 7 positions above three edge-sharing FeO_6-octahedra. In this case, the two Pu atoms were more than 9 Å away from each other, i.e. at a distance where their mutual backscattering interaction cannot be detected by EXAFS under the given conditions. The Pu sorption complex is therefore monomeric with respect to Pu: Would a Pu backscattering contribution be necessary to simulate the experimental

[iv] m_e – rest mass of the electron, ħ = h/2π, h – Plank's constant

spectrum, the lowest SD would be found for a situation when the two Pu atoms are situated closer to each other. To test the influence of the number of coordinated water molecules (the constant backscattering contribution) on the found position, a second type of position search was conducted (Table S2, method 2).

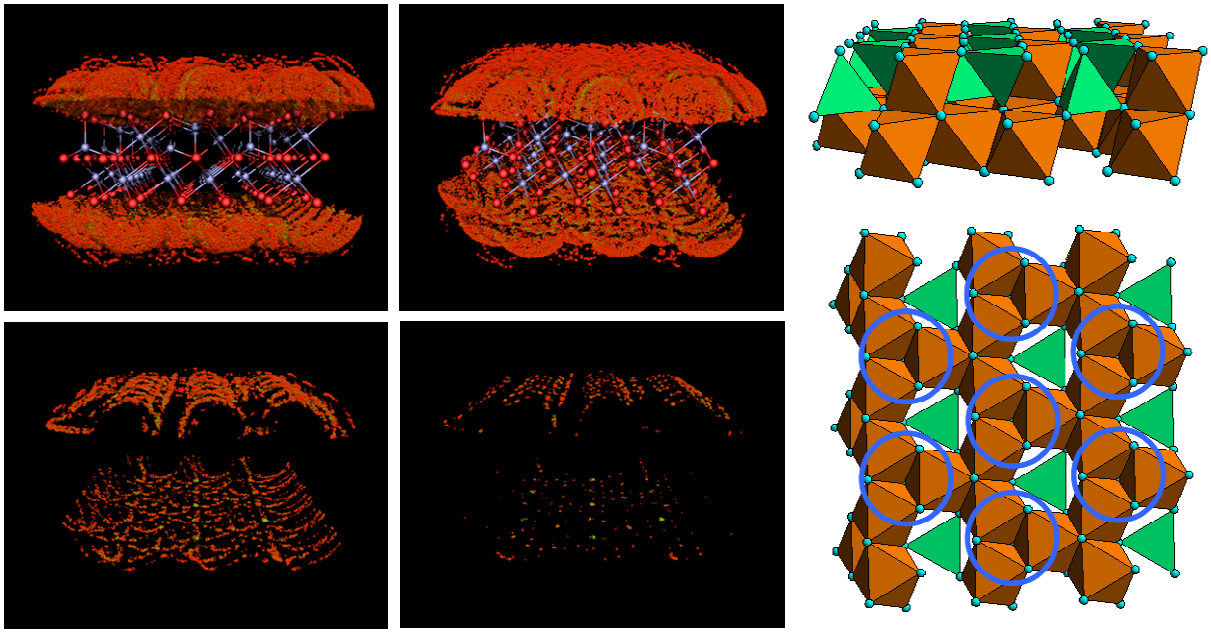

Figure S2. Monte Carlo simulation of Pu at the magnetite surface. Right: side and top view of used magnetite slab. Left and center: Side-view of 3D map of SD values in relation to magnetite slab with mixed tetrahedally-octahedrally terminated (111) face pointing upward and octahedrally terminated (111) face pointing downward. Red dots correspond to relatively higher, green dots to the Pu positions with lowest associated SD between modeled and experimental EXAFS spectra. Upper row: with magnetite slab shown, lower row: magnetite slab not shown. Points with higher SD are increasingly removed to reveal the positions with lowest SD, which are on top of the octahedrally terminated face (corresponding to the positions circled in blue at lower right).

Starting from a random position, only next positions with a lower SD than the former were accepted within a given radius. For each next position the search radius was reduced by dividing the former radius by a factor of 1.1. For backscattering contributions of either six or seven or eight oxygen atoms, always the same geometrical position was found, identical to the one found by the above described box-procedure. The thus identified position was independent of variations of the DW factors that were attributed to the atoms of the magnetite slab for the calculation of the theoretical chi-spectra. From the fact that at this position, the distance between Pu and the three closest surface oxygen atoms is about 2.5 Å and as aqueous Pu(III) is coordinated by 9 oxygen atoms at distances from 2.47 Å to 2.57 Å[16], it can be concluded that the complex is most likely tridentate, the surface contributing three oxygen atoms to the Pu coordination sphere and water molecules contributing the remaining oxygen atoms, thereby hydrating the Pu atom from the solution side of the surface complex. As these two simulation approaches yield exactly the same result of a tridentate Pu surface sorption complex, our conclusion on position and denticity of the sorption complex appears to be reliable. In a third step, a radial

distribution refinement of the structure was carried out with the aid of reverse Monte Carlo (RMC) simulation yielding radial pair distribution functions (RPDF) of Pu-O and Pu-Fe. The starting structure for RMC consists of one Pu atom at the found position with respect to the octahedrally terminated (111) surface and all surrounding atoms up to 6.5 Å. Six oxygen atoms were added to Pu in accordance with D_{3h} symmetry at a distance of 2.49 Å. The starting structure was replicated 600 times to obtain a statistical ensemble of atoms, enabling the simulation of the RPDF by the RMC method[17-19]. In short, for each starting structure the atoms were, one by one, slightly shifted. After each movement, a theoretical chi-spectrum (taking into account also three and four legged multiple scattering paths) was calculated and a new position was accepted when it resulted in a better or only slightly worse SD between the theoretical and experimental chi-spectra. This procedure was repeated until movements of the atoms did not lead to any further increase in agreement between experimental and theoretical spectra (~16×10^6 times). After refinement, the RPDF is calculated from the radial distances between Pu and the different types of atoms (O, Fe). Due to the restricted k-range of the χ(k)-spectrum (high noise level at k > 10 $Å^{-1}$), the extracted RPDFs for the Pu-O and Pu-Fe pairs are reliable only for distances below ~4.5 Å (Fig 1).

The following over-all parameters were used:
ΔE: 6.17 eV, k range: $2.7 \leq k \leq 9.8$ $Å^{-1}$, k-weighting: 3, S_0^2: 0.95.
Parameters that changed from one method to another are shown in Table S2.

Table S2. Monte Carlo simulation schemes.

	Method 1a) box procedure, 1 moving Pu atom	Method 1b) box procedure, 2 moving Pu atoms	Method 2 minimization of SD
Oxygen (coordinating water)	6 O atoms	6 O atoms	6 to 8 O atoms
σ^2 [$Å^2$]	0.009	0.0059	0.009
R [Å]	2.49	2.50	2.49
Oxygen (magnetite structure)			
σ^2 (value at R_{ref} [Å], slope [$Å^2$/Å])	0.005, constant	0.006, 3.0E-02	0.012, -4.7E-03
R_{ref} [Å]	2.49	2.50	2.49
σ^2			0.005 for R ≥ 3.96 Å
Iron (magnetite structure)			
σ^2 (value at R_{ref} [Å], slope [$Å^2$/Å])	0.005, 7.1E-03	0.018, 1.6E-02	0.008, 6.4E-03
R ref [Å]	3.54	3.54	3.53
R_{ref}: distance at which σ^2 corresponds to the given value			

2. Supporting Information for the Results and Discussion section

2.1 XANES analysis

Edge and peak positions and the difference between them as well as from the respective positions of PuO_2-spectra are detailed in Table S3. The uncertainty of the given edge position values is on the order of 0.3-0.4eV, if the spectra are compared among themselves, and may attain values as high as 0.6-0.7eV if compared with values obtained from different data treatments. The uncertainty for peak positions should not surpass 0.1-0.2 eV for transmission and 0.3-0.4 eV for fluorescence spectra with higher noise levels. The uncertainties associated with difference values are accordingly twice as high.

Table S3. XANES parameters of Pu-mineral sample and Pu reference spectra.

samples	edge position E_0 [eV]	peak position [eV]	peak intensity *	peak − edge [eV]	E_0(sample) $-E_0(PuO_2)$ [eV]	peak (sample) −peak (PuO_2) [eV]
$(Pu^{III})_{aq}$ (0.01 M, in 1 M $HClO_4$, stabilized with NH_3OHClO_4)	18058.6	18062.4	1.80	3.8	-2.2	-4.3
$(Pu^{IV})_{aq}$, (0.01 M, in 1M $HClO_4$, stabilized with $NaNO_2$)	18062.4	18066.9	1.84	4.5	1.6	0.2
$(Pu^{V})_{aq}$, (0.01M, 1M $HClO_4$, PIPES pH 3.5**)	18061.5	18065.9	1.46	4.4	0.7	-0.7
PuO_2(cr), (see [20] for preparation details)	18060.8	18066.6	1.62	5.8	0.0	0.0
Pu(III) + magnetite, pH6	18058.4	18062.8	1.71	4.4	-2.4	-3.9
Pu(III) + magnetite, pH8	18058.7	18062.9	1.74	4.2	-2.1	-3.8
Pu(V) + magnetite, pH8	18058.4	18062.6	1.74	4.2	-2.4	-4.0
Pu(V) + mackinawite, pH8	18061.6	18066.9	1.71	5.3	0.8	0.3
Pu(V) + chukanovite, pH8	18059.4	18065.7	1.60	6.3	-1.4	-0.9

* peak height after normalisation of the edge jump to a value of 1
** as described in detail in [21]

Description of the overall absorption process and edge shape variations as a function of actinide oxidation state:

For all actinides, $L_{II,III}$-absorption edge corresponds to the transition of the excited photoelectron from 2p to a mixed 6d-continuum state. Position, shape and intensity of the edge are influenced by the electronic structure and the geometry of the coordination environment of the central atom. As the effective charge of the central atom increases, the electronic core levels become stabilized and the absorption edge is shifted to higher energies[22] as can be seen for $(Pu^{III})_{aq}$ and $(Pu^{IV})_{aq}$, Fig 1. Penta- and hexavalent actinides, however, are characterized by the presence of a trans-dioxo group. The charge transfer from these oxo-groups to the central ion lowers its effective charge, Z_{eff}, to a value below the formal oxidation state ($Z_{eff}(An(V)) = +2.3$, $Z_{eff}(An(VI)) = +3.3$) [23]. The absorption edge of $(Pu^{V})_{aq}$ is accordingly at about the same energy as that of $(Pu^{IV})_{aq}$ (Fig. 1). Multiple scattering of the

photoelectron wave between the two axial oxo-oxygen atoms and the central actinide atom results in a shoulder on the high energy side of the white line peak[22], thereby contributing to differentiate An(III, IV) from An(V,VI) spectra.

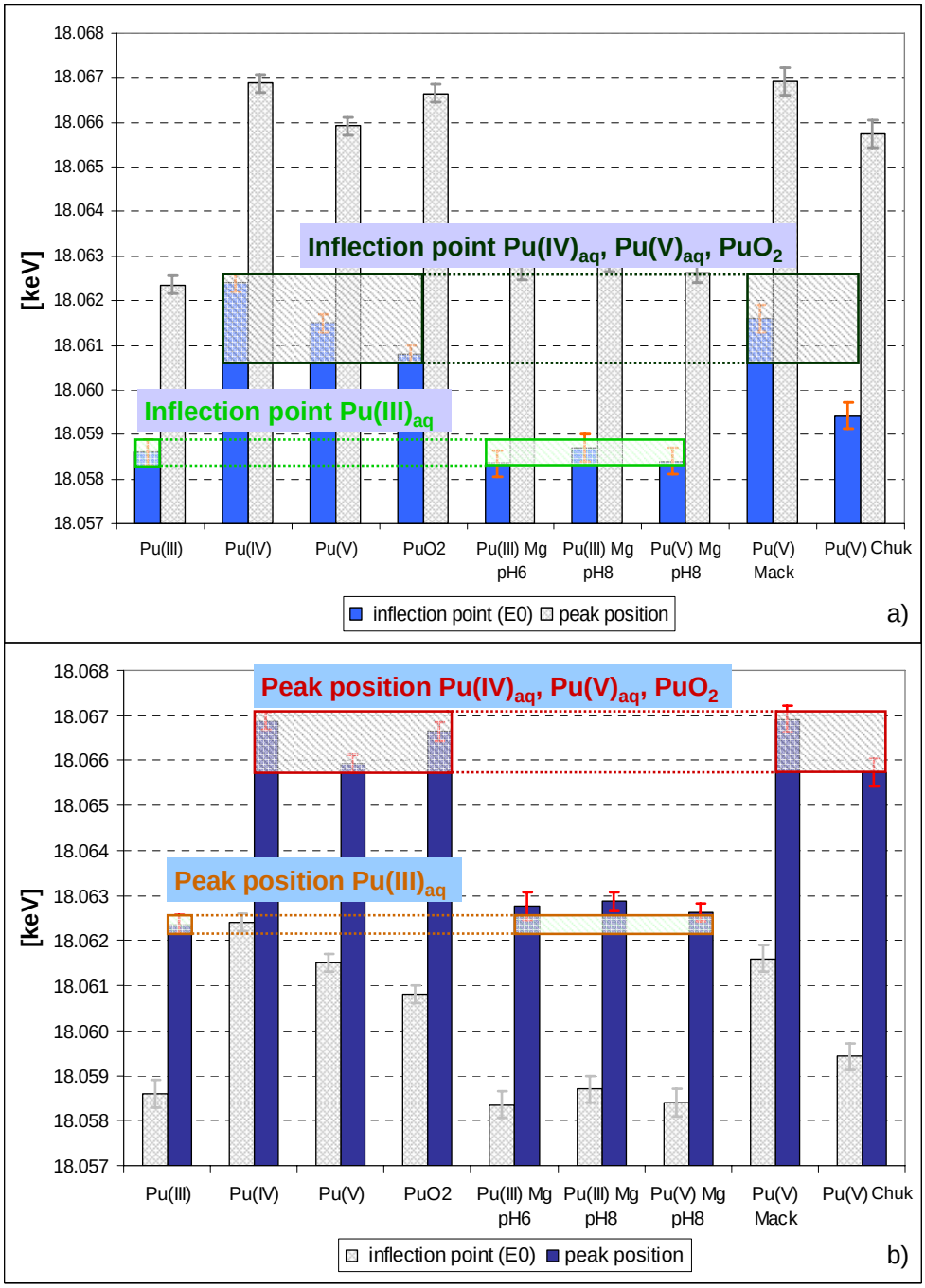

Figure S3. Graphical comparison of inflection points (a) and peak positions (b) for sample and reference spectra listed in Table S3. The inflection point of the Pu(V)-chukanovite sample clearly falls in between the $Pu(III)_{aq}$ and the $Pu(IV)_{aq}$ - $Pu(V)_{aq}$ - PuO_2 regions.

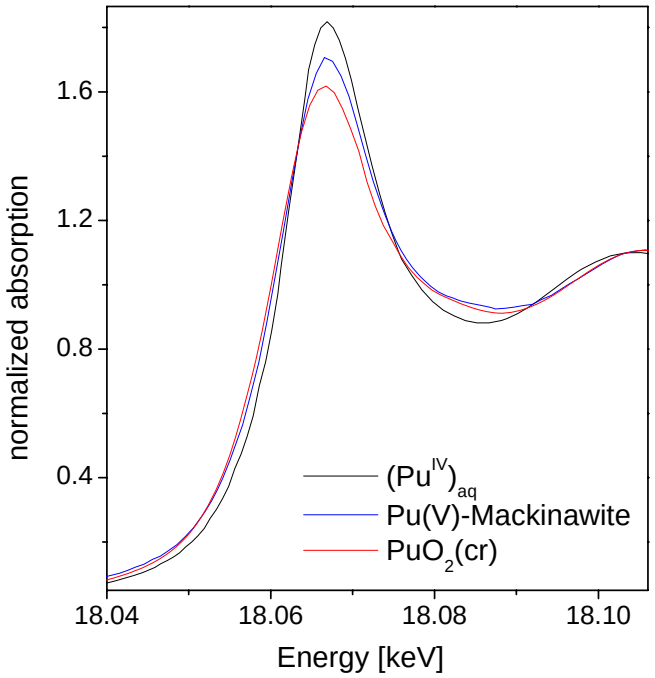

Figure S4. Comparison of $(Pu^{IV})_{aq}$, Pu(V)-mackinawite and PuO_2(cr) spectra in the XANES region. From one sample to the other, a small shift in the edge position and therefore inflection point of the edge is accompanied by a strong change in peak intensity.

2.2 Pu-magnetite spectra: XANES ITT analysis and linear combination, and EXAFS shell fitting

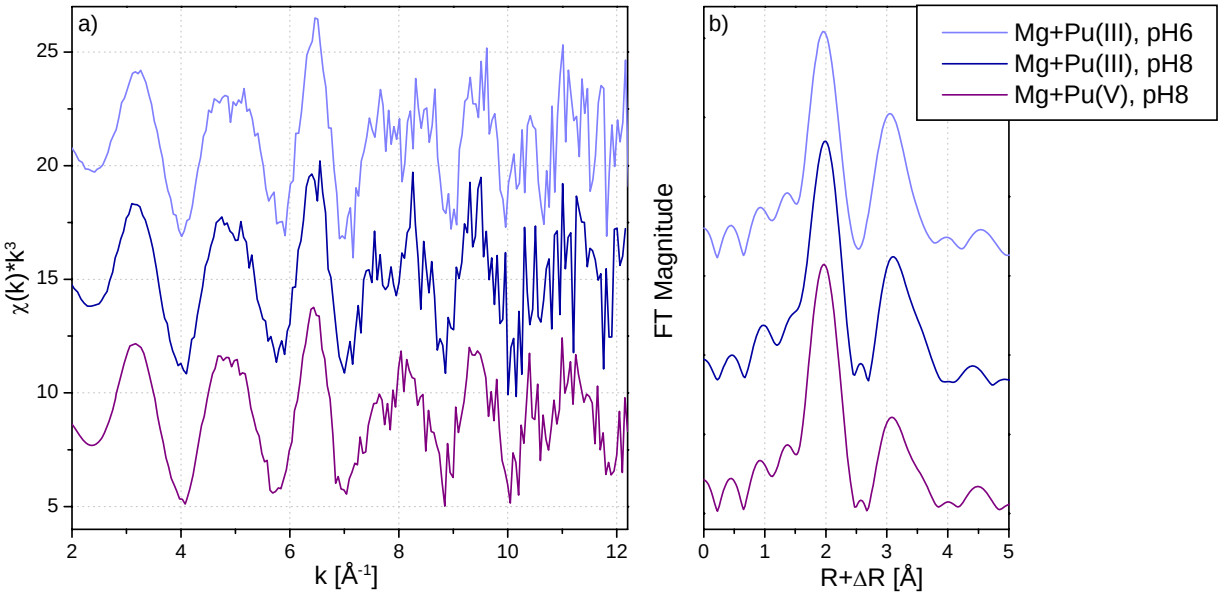

Figure S5. k^3-weighted χ(k) spectra of Pu(III) and Pu(V) reacted with magnetite at pH 6 and pH 8. FT carried out on a k-range of 2.7 $Å^{-1}$ < k < 10 $Å^{-1}$, no window function used.

Table S4. Oxidation state composition of Pu-Magnetite samples as found by Iterative Target Testing (ITT) with $(Pu^{III})_{aq}$, $(Pu^{IV})_{aq}$ and $(Pu^{V})_{aq}$ as references.

a) XANES region (18.03-18.1 keV)				
sample	**Pu(III)**	**Pu(IV)**	**Pu(V)**	**% total**
$(Pu^{III})_{aq}$+Mg, pH6	92%	3%	6%	101
$(Pu^{III})_{aq}$+Mg, pH8	92%	5%	4%	102
$(Pu^{V})_{aq}$+Mg, pH8	98%	0%	5%	103
b) chi spectra obtained from back transform of first peak - oxygen coordination shell*				
	Pu(III)	**Pu(IV)**	**Pu(V)**	**% total**
$(Pu^{III})_{aq}$+Mg, pH6	90%	7%	3%	100
$(Pu^{III})_{aq}$+Mg, pH8	100%	0%	2%	102
$(Pu^{V})_{aq}$+Mg, pH8	100%	0%	0%	100

*applying k^3-weighting to the spectra, $2.8 \leq k \leq 12.65$

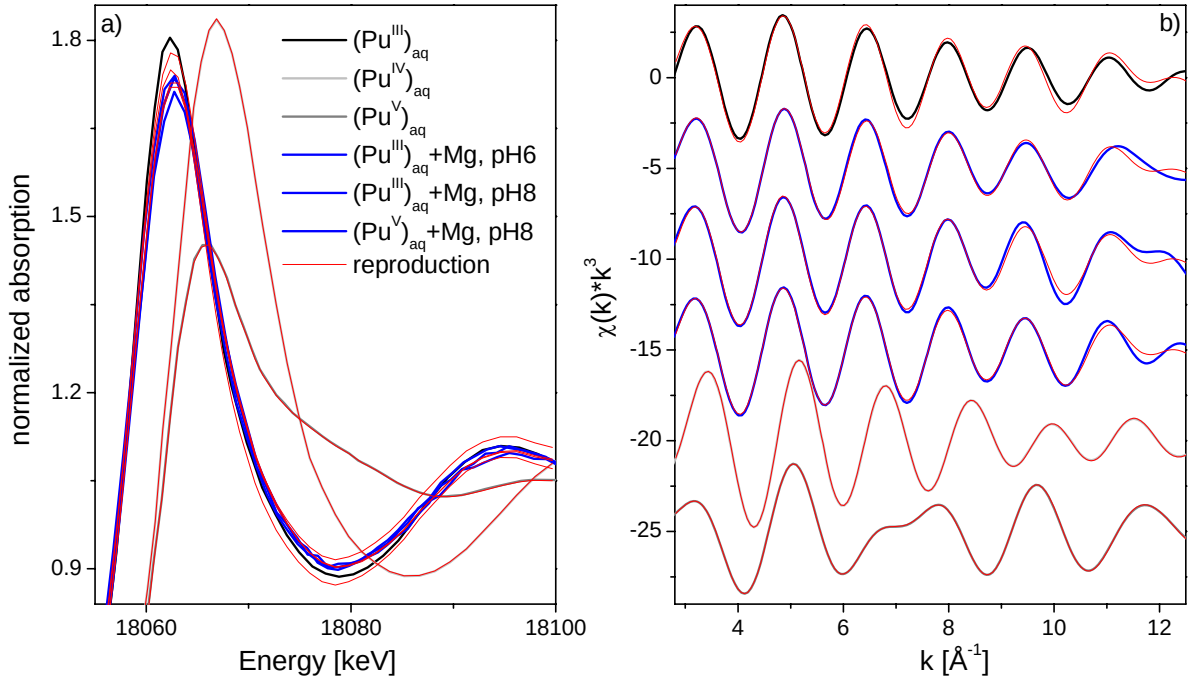

Figure S6. Reference ($(Pu^{III})_{aq}$, $(Pu^{IV})_{aq}$, $(Pu^{V})_{aq}$) and Pu-magnetite spectra with their reproductions obtained by ITT in the XANES (a) and EXAFS (b) range. a) Normalized spectra, b) chi spectra obtained by back-transform of first peak (see Table S4 for details).

Table S5. Shell fit of the first shell (Pu−O) for Pu(III) and Pu(V) reacted with magnetite at pH 6 and 8.

sample	**CN**	**dist (Å)**	**σ^2 [Å^2]**	**E_0-shift [eV]**
$(Pu^{III})_{aq}$+Mg, pH6	7.7	2.48	0.0071	6.11
$(Pu^{III})_{aq}$+Mg, pH8	8.1	2.49	0.0066	6.20
$(Pu^{V})_{aq}$+Mg, pH8	7.9	2.49	0.0062	5.89
$(Pu^{III})_{aq}$	8.6	2.50	0.0083	7.16

parameters: $S_0^2 = 0.95$, fit mode k^3+k^2, $2.71 \leq k \leq 10$, $1.54 \leq R \leq 2.43$, no window function for FT

Table S6. Oxidation state composition of Pu-Magnetite samples as found by linear combination (LC) fitting using $(Pu^{III})_{aq}$, $(Pu^{IV})_{aq}$ and $(Pu^{V})_{aq}$ as references.

XANES region (18.03-18.1 keV)				
sample	**Pu(III)**	**Pu(IV)**	**Pu(V)**	**% total**
$(Pu^{III})_{aq}$+Mg, pH6	91 ± 1 %	2 ± 2 %	7 ± 3 %	100 ± 6
$(Pu^{III})_{aq}$+Mg, pH8	92 ± 1 %	4 ± 2 %	5 ± 2 %	100 ± 5
$(Pu^{V})_{aq}$+Mg, pH8	97 ± 0 %	0 ± 0 %	3 ± 0 %	100 ± 0

As can been seen from comparison of Tables S4a and S6, ITT[24] and LC fitting yield almost identical oxidation state compositions for the Pu-magnetite samples.

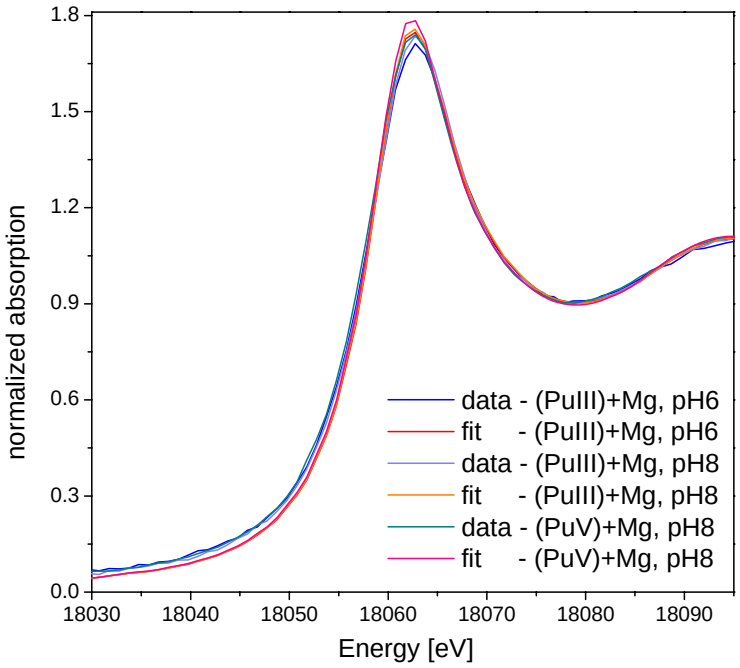

Figure S7. Linear combination (LC) fit of normalized Pu-magnetite spectra in the XANES region (18.3-18.1 keV) using $(Pu^{III})_{aq}$, $(Pu^{IV})_{aq}$, and $(Pu^{V})_{aq}$ as references.

The main difference between ITT and LC fit results lies in the fit residuals (or residuals between the spectra and their ITT reproductions) (Table S7). In LC fitting non-linear least square fitting is carried out using the reference spectra as is, so only the Pu-magnetite sample spectra are fitted and a residual between experimental data and fit can be calculated. In ITT however, the factors (component spectra) used for reconstruction of the sample (and reference spectra) are extracted from the whole set of data (samples and references). The ITT extracted factors are therefore not necessarily identical to the reference spectra used and the reproduction of the reference spectra themselves using the extracted factors also results in a residual. In the Pu-magnetite samples plus reference spectra set, the slightly lower white line peak height of the Pu-magnetite spectra compared to the $(Pu^{III})_{aq}$ reference spectrum results in a "Pu(III)" component extracted from the data set whose intensity is between the one of $(Pu^{III})_{aq}$ and Pu-magnetite spectra.

While the SD for the Pu-magnetite samples are lower for ITT reproductions than for LC fits (Table S7 and Fig. S8), the SD of the $(Pu^{III})_{aq}$ reference reproduction by ITT attains a similar value as the LC fitting SD for the Pu-magnetite samples. So in one case (ITT) the sample spectra are better reproduced at the cost of a Pu(III)-component factor slightly different from the $(Pu^{III})_{aq}$ reference spectrum, in the other case (LC fitting) the reference spectra are used as is but the sample spectra are reproduced less well.

Table S7. Standard deviation (SD) of Pu-magnetite spectra fits (LC) and reproductions (ITT) and of reference spectra reproductions (ITT)

spectrum	SD ITT	SD LC fit
$(Pu^{III})_{aq}$	0.025	
$(Pu^{IV})_{aq}$	0.001	
$(Pu^{V})_{aq}$	0.002	
$(Pu^{III})_{aq}$+Mg, pH6	0.010	0.026
$(Pu^{III})_{aq}$+Mg, pH8	0.007	0.019
$(Pu^{V})_{aq}$+Mg, pH8	0.017	0.026

SD values (σ) in Table S7 were calculated according to

$$\sigma = \sqrt{\frac{\sum_{i=1}^{n}(y_{i,fit} - y_{i,\exp})^2}{n}}, \qquad (2)$$

with n being the number of data point in the energy range under consideration (18.04-18.1 keV).

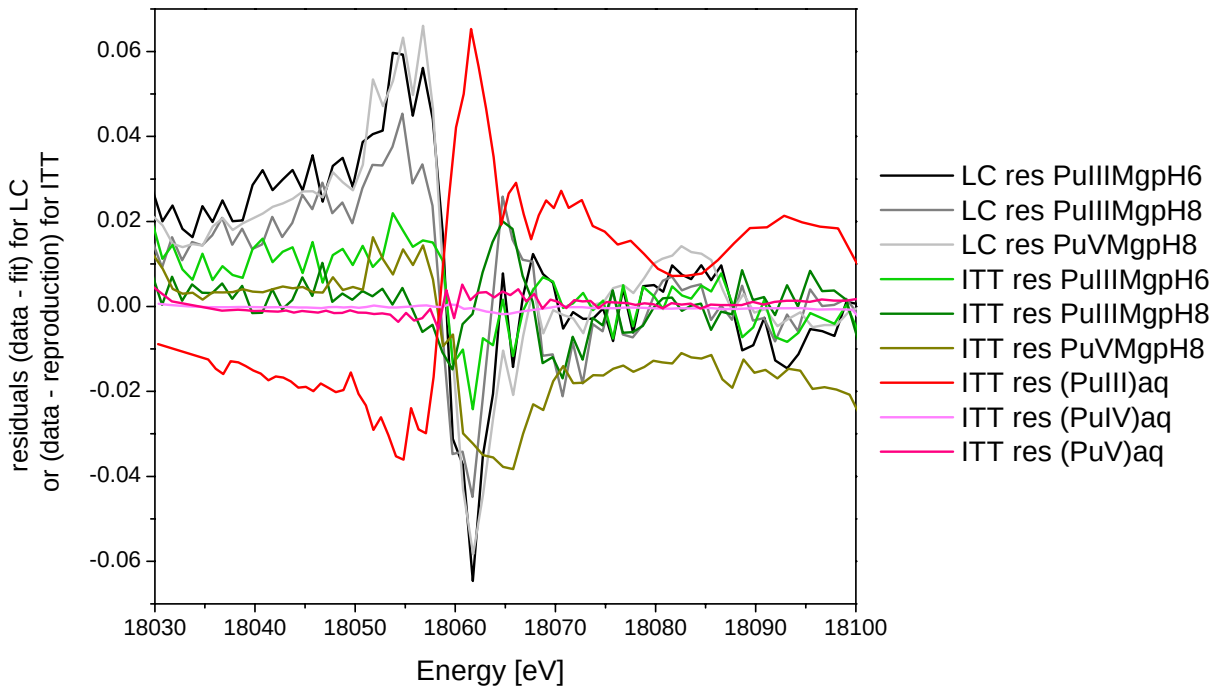

Figure S8. Residuals of Pu-magnetite spectra linear combination fits (LC) and reproductions (ITT) and of reference spectra reproductions (ITT).

2.3 EXAFS shell fitting of Pu(V)-mackinawite and PuO_2(cr) spectra

Characteristics of the backscattering paths used for fitting the PuO_2(cr) and Pu(V)-mackinawite spectra such as amplitude ratio, degeneracy, number of legs, effective radius and contributing atoms are listed in Table S8.

Table S8. FEFF paths selected for fitting from the PuO_2 structure[25] as found by FEFF8.2.

path index	amplitude ratio [%]	deg*	nb of legs	$r_{effective}$ [Å]	path	path -description
1	100	8	2	2.338	Pu - O	SS**
3	65.8	12	2	3.817	Pu - Pu	SS
6	35.3	24	2	4.476	Pu - O	SS
8	13.1	8	4	4.675	Pu-O-Pu-O	MS(4)** with two different O at 2.34 Å
16	11.8	6	2	5.398	Pu - Pu	SS
34	23.1	24	2	6.611	Pu – Pu	SS

*degeneracy
**SS: single scattering path, MS(X): multiple scattering path (number of legs of paths)

For these paths, fits with either fixed or fitted coordination numbers (CN) are compared in Tables S9 and S10. Fits were carried out in R-space, k^3-weighted EXAFS spectrum were Fourier transformed using a Bessel window function (window parameter set to 3), fit mode was k^3+k^2, $S_0^2 = 0.95$.

Table S9. Shell fit of Pu(V)-Mack sample and PuO_2 reference with fixed coordination numbers using paths **1, 3, 6, 8, 16, 34**. Distances and σ^2 of MS paths dependent on constituting SS paths.

	Pu(V)-Mackinawite			**PuO_2**			**PuO_2 - structure**	
path	**CN**	**R [Å]**	**σ^2 [Å^2]**	**CN**	**R [Å]**	**σ^2 [Å^2]**	**nb**	**dist [Å]**
Pu - O	8	2.32	0.0081	8	2.33	0.0054	8	2.34
Pu - Pu	12	3.81	0.0059	12	3.83	0.0032	12	3.82
Pu - O	24	4.40	0.0088	24	4.43	0.0061	24	4.48
Pu-O MS	8	4.64[f]	0.0081[d]	8	4.66[f]	0.0054[d]	8	4.68
Pu - Pu	6	5.36	0.0084	6	5.37	0.0068	6	5.40
Pu - Pu	24	6.69	0.0142	24	6.68	0.0087	24	6.61
	E_0-shift [eV]		5.83	E_0-shift [eV]		6.81		
	Res [%]		7.94	Res [%]		8.34		
	k range [Å^{-1}]	3.03-12.2		k range [Å^{-1}]	3.02-12.17			
	R range [Å]	1.3-6.9		R range [Å]	1.3-6.9			
	f: fixed			d: correlated to SS paths				

A shell fit with fixed CN (Table S9) results in almost identical distances for the Pu(V)-Mack sample and the PuO_2(cr) reference spectrum, while the Debye-Waller factors (DW or σ^2) for Pu(V)-Mack are significantly higher for all scattering paths.

A fit with free CN (Table S10) yields similar values for Pu-O (path 1) and Pu-Pu (paths 3, 16) for both spectra. Again, the DWs for Pu(V)-Mack are, apart from path 6, higher than for PuO_2(cr). Why the DW of path 6 in the Pu(V)-Mack sample is fitted with a lower value than in PuO_2(cr) is not clear. For

both fits, i.e. with fixed or fitted CN, the residual is slightly smaller for the Pu(V)-Mack sample, a fact that might indicate that less scattering paths are unaccounted for by the fit paths used. For both spectra, a DW for path 16 with a lower value than for path 3 (Pu-Pu at 5.37 vs Pu-Pu at 3.82) is unrealistic. This small value results from the fact that Pu-O and Pu-O-Pu paths in between paths 16 and 34 were not included into the fit. When they are included into a fit with free CN for the PuO_2(cr) spectrum, the DW of path 16 is found as 0.006. For the Pu(V)-mackinawite spectrum a fit with free CN including these paths does, however, due to the higher structural disorder in the sample, not converge, which is why paths 1, 3, 6, 8, 16 and 34 were used for comparison of the two PuO_2 spectra. The fits corresponding to Table S10 are shown in Figure S9.

Table S10. Shell fit of Pu(V)-Mack sample and PuO_2 reference with fitted coordination numbers using paths **1, 3, 6, 8, 16, 34**. Distances and σ^2 of MS paths dependent on constituting SS paths.

	Pu(V)-mackinawite			**PuO_2**			**PuO_2 - structure**	
path	**CN**	**R [Å]**	**σ^2 [Å^2]**	**CN**	**R [Å]**	**σ^2 [Å^2]**	**nb**	**dist [Å]**
Pu - O	8.9	2.32	0.0093	8.2	2.33	0.0056	8	2.34
Pu - Pu	10.2	3.81	0.0052	11.0	3.83	0.0026	12	3.82
Pu - O	16.3	4.41	0.0066	27.9	4.42	0.0089	24	4.48
Pu-O MS	8.9^f	4.63^f	0.0093^d	8.2^f	4.68^f	0.0056^d	8	4.68
Pu - Pu	2.2	5.36	0.0026	2.4	5.38	0.0017	6	5.40
Pu - Pu	13.6	6.67	0.0102	17.7	6.67	0.0069	24	6.61
	E_0-shift [eV]		5.50	E_0-shift [eV]		7.02		
	Res [%]		6.24	Res [%]		7.73		
	k range [Å^{-1}]		3.03-12.2	k range [Å^{-1}]		3.02-12.17		
	R range [Å]		1.3-6.9	R range [Å]		1.3-6.9		
	f: fixed			d: correlated to SS paths				

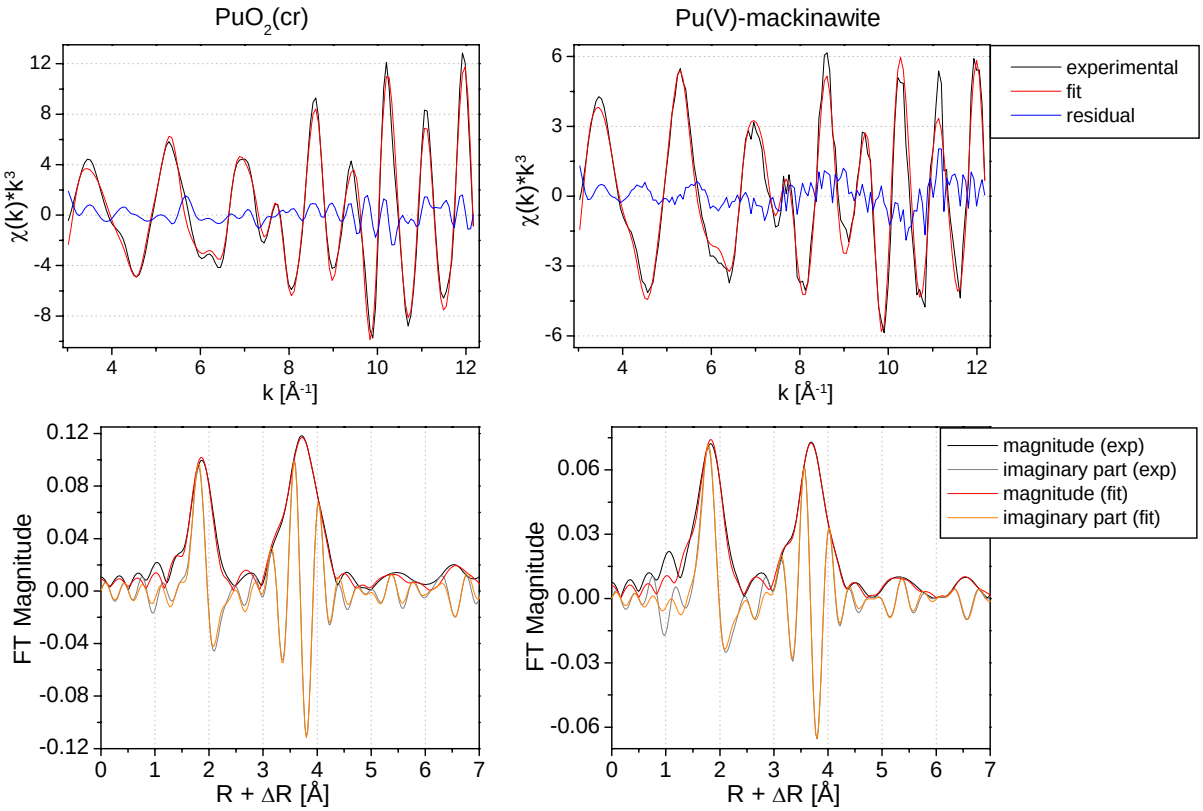

Figure S9. Shell fit with adjustable coordination numbers for PuO_2(cr) reference and Pu(V)-mackinawite sample using the FEFF paths 1, 3, 6, 8, 16 and 34 (fit parameters given in Table S10).

2.4 EXAFS shell fitting of Pu(V)-chukanovite spectrum - Comparison of coordination shell fits between Pu(V)-chukanovite, Pu(V)-mackinawite and PuO_2(cr)

When attempting to fit the first peak in the Pu(V)-chukanovite spectrum with one oxygen shell, 8 oxygen neighbors at a Pu-O distance of 2.32 Å are found with a DW factor of 0.015 $Å^2$, suggesting the presence of more than one Pu-O distance in the coordination shells of Pu atoms. A fit with two shells only converges when the DW factors of the two shells are correlated. The fitted CN and distances are 4.3 O at 2.27 Å and 3.2 O at 2.43 Å with a DW of 0.006 $Å^2$; the resulting weighted average distance of 2.34 Å is roughly within error of the single shell fit distance of 2.32 Å (Table S11). While such a two shell fit of the first peak is possible, it is not very convincing due to the facts that the DWs for the two distances need to be correlated and that the separation between the two distances is below the resolution limit for the given k-range ($\Delta R = \pi / (2 \times \Delta k) = 0.17$ Å). Also it does not explain where such Pu-O distances might originate from. In the absence of Pu(V) species that should be easily recognizable due to the characteristic shoulder following the WL peak and short Pu-O distances of 1.81 Å corresponding to the axial oxygen atoms, Pu(III) species with Pu-O of 2.49 Å and Pu(IV) species (other than PuO_2) with Pu-O of 2.39 Å [26] should increase the average first shell Pu-O distance of 2.33 Å characteristic of PuO_2. From the above described fit results, it is not clear, whether the average Pu-O distance in the Pu(V)-chukanovite sample is changed compared to PuO_2 or not. Due to negative interference and a lack of resolution between adjacent shells, it is often difficult if not impossible to determine the contributing

distances correctly. A fitted Pu-O distance must therefore not necessarily correlate with a physically existing distance.

When we attempt to fit the Pu(V)-mackinawite spectrum with two Pu-O paths, the DW factors need to be correlated, the found value becomes smaller than the one for PuO_2(cr), the shell separation (0.13 Å) is below the resolution limit (0.17 Å) and the fit residual does not decrease (Table S11). We conclude from this, that while the higher structural disorder in the Pu(V)-Mack sample compared with PuO_2(cr) is evident, there is no sufficient evidence to conclude that two distances corresponding to "two Pu-O shells" are prevalent among the Pu-O distances in the sample. As we show in the main article and in section 2.6, for a mixed oxidation state sample, such as Pu(V)-chukanovite, LC fitting or ITT are better suited to obtain information on contributing oxidation states and therefore also contributing distances and sample structure. For a graphic representation of the fits detailed in Table S11, see Figure S10.

Table S11. Coordination shell fits for Pu(V)-chukanovite, Pu(V)-mackinawite and PuO_2(cr) spectra with one or two Pu-O paths[a].

paths and parameters	Pu(V)-chukanovite			Pu(V)-chukanovite			Pu(V)-mackinawite			Pu(V)-mackinawite			PuO_2(cr)		
	CN	R [Å]	σ^2 [Å^2]	CN	R [Å]	σ^2 [Å^2]	CN	R [Å]	σ^2 [Å^2]	CN	R [Å]	σ^2 [Å^2]	CN	R [Å]	σ^2 [Å^2]
Pu - O	8.4	2.32	0.0150	4.3	2.27	0.0058[c]	8.8	2.31	0.0092	3.8	2.25	0.0022[c]	7.6	2.33	0.0049
Pu - O				3.2	2.43	0.0058[c]				3.9	2.38	0.0022[c]			
R range [Å]	1.26-2.44			1.26-2.44			1.27-2.40			1.27-2.40			1.50-2.28		
k range [Å^{-1}]	2.96-12.27			2.96-12.27			3.03-12.20			3.03-12.20			3.03-12.17		
Residual [%]	9.81			6.18			4.88			4.80			4.01		
E_0-shift [eV]	3.34			4.74			5.22			5.48			7.05		
Fig. S10	a)			b)			c)			d)			e)		
O average	8.4 O at 2.32 Å			7.5 O at 2.34 Å			8.8 O at 2.31 Å			7.6 O at 2.32 Å			7.6 O at 2.33		
				c: correlated						c: correlated					

[a]fit carried out in R, FT of $\chi(k)*k^3$ with Bessel window function (window parameter set to 3), fit mode k^3+k^2, S_0^2=0.95

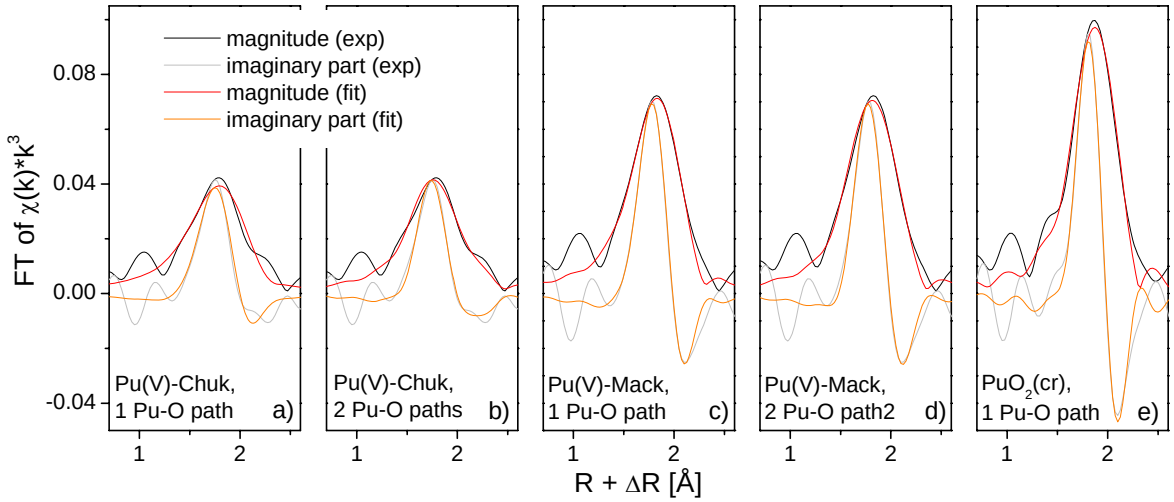

Figure S10. Graphical representation of the coordination shell fits (Table S11) for Pu(V)-chukanovite, Pu(V)-mackinawite and PuO_2(cr) spectra with one or two Pu-O paths (ordinate has same scale for all).

2.5 Comparison between Pu(V)-chukanovite and theoretical PuO_2-Pu(III) mixture spectrum

In Figure S11, theoretical mixtures of $(Pu^{III})_{aq}$ and PuO_2(cr) reference spectra in the XANES (Fig. S11a) and EXAFS (Fig. S11d) regions are presented and compared to the Pu(V)-Chuk spectrum. These theoretical mixture spectra result from summation of the normalized files according to $y = x*PuO_2 + (1-x)*(Pu^{III})_{aq}$ $(0 \leq x \leq 1)$, with $(Pu^{III})_{aq}$ and PuO_2(cr) taken as model compounds for a Pu(III) outer sphere complex and newly formed PuO_2 surface precipitate, respectively.

In the XANES region, the Pu(V)-Chuk spectrum is well within the resulting set of curves and closely follows the graphs corresponding to 60 and 70 % PuO_2. In the k^3-weighted EXAFS spectra (Fig. S11d), the high similarity between the theoretical spectrum composed of 60% PuO_2 and 40% $(Pu^{III})_{aq}$ and the Pu(V)-Chuk spectrum is apparent. The low k-range differences between Pu(V)-Chuk and Pu(V)-Mack and PuO_2 spectra (arrows in Fig. 2) can therefore be explained as resulting from contribution of both Pu(III) and PuO_2 to the sample spectrum and the accompanying interference between their corresponding backscattering waves. As one would expect and as can be seen from the inset (Fig S11c), both inflection point and WL peak maximum positions of Pu(V)-Chuk are within the range of values for PuO_2-Pu(III) mixtures. However, the peak height of Pu(V)-Chuk cannot directly be compared with the WL peak height variation of the PuO_2-Pu(III)-mixtures (Fig S11b) as the reference value for Pu(V)-Chuk sample, that is, the peak height of a sample consisting to 100% of the same 'type' of PuO_2 as is present in Pu(V)-Chuk, is not exactly known. This value would certainly be higher than the one of PuO_2(cr) and possibly close to the one of the Pu(V)-Mack sample. The fact that the peak height of the Pu(V)-Chuk sample is similar to the one of PuO_2(cr) is therefore not in disagreement with the assumption that the Pu(V)-Chuk sample contains a Pu(III)-PuO_2 mixture.

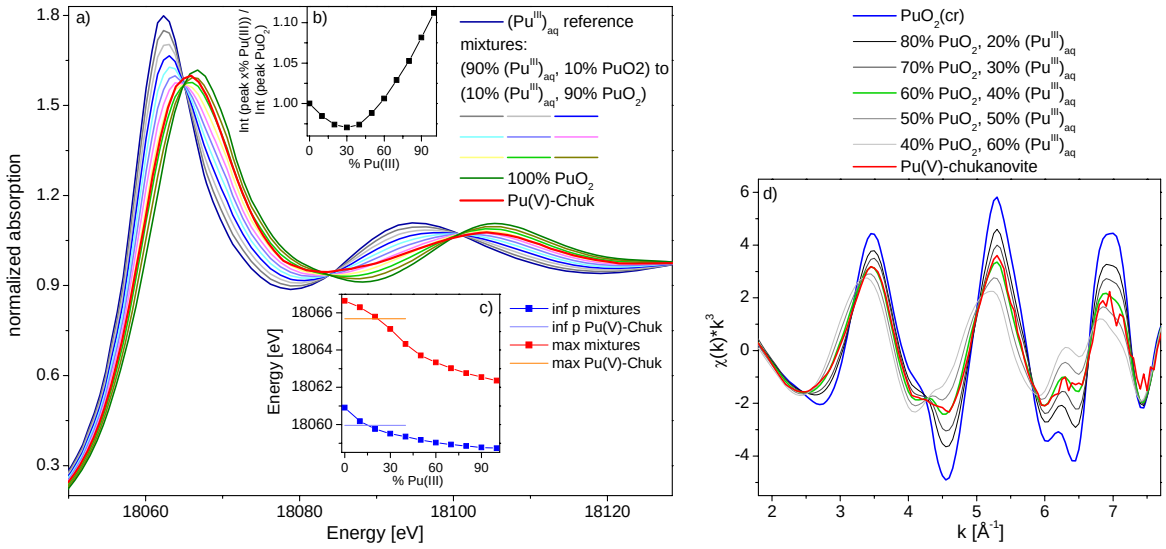

Figure S11. a) XANES region of theoretical PuO_2-Pu(III) mixtures b) relative WL peak height of pure compounds and mixtures compared to PuO_2(cr) c) energy of inflection point (inf p) and peak height maximum (max) as a function of the mixtures' Pu(III) content d) k^3-weighted $\chi(k)$ of PuO_2(cr), selected PuO_2(cr)-Pu(III) mixtures and Pu(V)-chukanovite.

2.6 ITT analysis of the Pu(V)-chukanovite spectrum with $(Pu^{III})_{aq}$ and PuO_2 as references

ITT results for the Pu(V)-chukanovite spectrum with $(Pu^{III})_{aq}$ and either PuO_2(cr) or the Pu(V)-mackinawite spectrum as PuO_2 reference are shown in Table S12 and Figure S12. While analysis of the XANES region gives a different composition depending on the PuO_2 reference used, analysis of the higher energy range (corresponding to a χ(k) range of 3.3-8.4 $Å^{-1}$) yields similar PuO_2 contents for the Pu(V)-chukanovite sample. The PuO_2 contents found when the PuO_2(mackinawite) reference is used are virtually unchanged whether the XANES or EXAFS region is analyzed. The difference between reproductions and Pu(V)-chukanovite spectrum and their corresponding standard deviation (SD) values are shown in Figure S13 and, unsurprisingly, use of the PuO_2(mackinawite) reference results in a lower SD and appears to be a better reference for the PuO_2 contained.

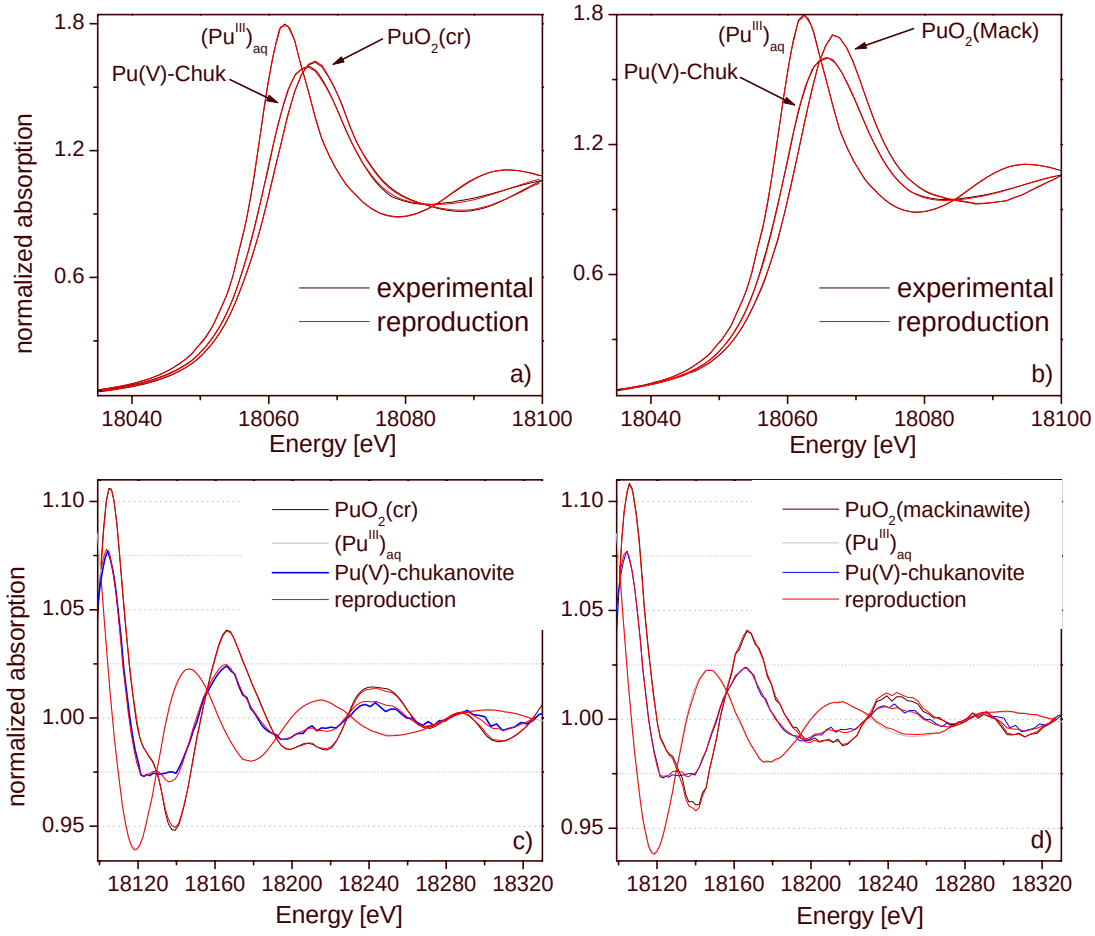

Figure S12. Normalized Pu(V)-chukanovite spectrum and ITT reproductions in the XANES (18.035 - 18.1 keV) and EXAFS (18.1-18.33 keV) energy range with $(Pu^{III})_{aq}$ and PuO_2(cr) (a and c) or $(Pu^{III})_{aq}$ and PuO_2 from the Pu(V)-mackinawite sample for reference (b and d).

Table S12. Oxidation state composition of the Pu(V)-chukanovite sample as found by Iterative Target Testing (ITT) with $(Pu^{III})_{aq}$ and PuO_2(cr) or PuO_2(mackinawite)* as references.

a) XANES region (18.035-18.100 keV)				
references	Pu(III)	PuO_2	% total	Figure S12
$(Pu^{III})_{aq}$, PuO_2(cr)	24.8 %	76.2 %	101.0	a)
$(Pu^{III})_{aq}$, PuO_2(Mack)	32.8 %	66.9 %	99.7	b)
b)EXAFS region (18.100-18.329 keV)				
references	Pu(III)	PuO_2	% total	Figure S12
$(Pu^{III})_{aq}$, PuO_2(cr)	33.8 %	66.3 %	100.1	c)
$(Pu^{III})_{aq}$, PuO_2(Mack)	33.1 %	66.8 %	99.9	d)

*tentatively, the spectrum from the Pu(V)-mackinawite sample is used here as reference for non calcinated PuO_2

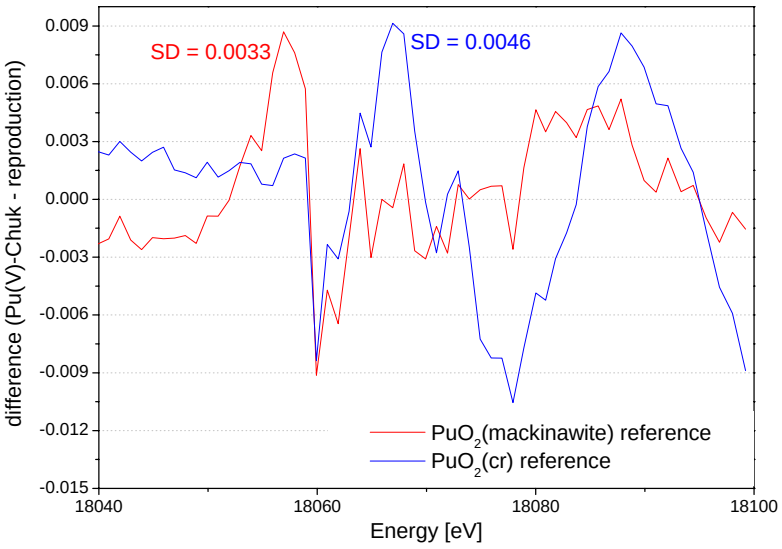

Figure S13. Difference spectra (XANES region) between reproductions (shown in Figure S12, a) and b)) and Pu(V)-chukanovite spectrum and corresponding SD values.

2.7 Shell fit comparison between Pu(V)-chukanovite and theoretical PuO_2-Pu(III) mixtures

We tried to further verify the result from ITT analysis according to which the Pu(V)-chukanovite sample basically constitutes a mixture of PuO_2 as contained in Pu(V)-mackinawite and Pu(III). Therefore, shell fitting was applied to artificial mixture spectra containing the ITT determined percentages of PuO_2(cr) or PuO_2(Mack) (i.e. the Pu(V)-mackinawite spectrum) and $(Pu^{III})_{aq}$. The PuO_2(Mack)-$(Pu^{III})_{aq}$ mixture results in a spectrum very similar to the one of Pu(V)-chukanovite (Fig S14) and the shell fit yields quasi identical coordination numbers and distances for the two spectra, the major difference being somewhat different DW for the oxygen coordination shell (Table S13). For the PuO_2(cr)-$(Pu^{III})_{aq}$ mixture spectrum, a fit with a split first shell was not possible. However, the reduced number of Pu-Pu backscatters at 3.82 Å is also here clearly visible and the CN obtained is very close to the one for the Pu(V)-chukanovite sample.

The effects of apparent first shell splitting and reduced coordination numbers for Pu in the Pu(V)-chukanovite sample spectrum can therefore all be attributed to the presence of two different Pu redox species, which we identify as structurally (somewhat) disordered PuO_2 and a Pu(III)-species that yields an EXAFS spectrum quite similar to the one of $(Pu^{III})_{aq}$.

Table S13. Shell fit comparison between Pu(V)-chukanovite and theoretical PuO_2-Pu(III) mixture spectra[a]. Mixture spectra were created from normalized files according to: y = x*PuO_2(cr or Mack) + (1-x)*$(Pu^{III})_{aq.}$

paths and parameters	Pu(V)-chukanovite			66% PuO_2(cr) + 34% $(Pu^{III})_{aq}$			67% PuO_2(Mack) + 33% $(Pu^{III})_{aq}$			PuO_2 structure	
	CN	R [Å]	σ^2 [Å^2]	CN	R [Å]	σ^2 [Å^2]	CN	R [Å]	σ^2 [Å^2]	CN	R [Å]
Pu - O	3.6	2.27	0.0041[c]	6.1	2.33	0.0084	3.8	2.27	0.0058[c]	8	2.34
Pu - O	2.9	2.43	0.0041[c]				2.9	2.43	0.0058[c]		
Pu-Pu	6.0	3.80	0.0043	5.9	3.81	0.0019	6.6	3.80	0.0053	12	3.82
Pu-O	10.4	4.42	0.0041[c]	14.7	4.44	0.006[f]	11.1	4.41	0.006[f]	24	4.48
R range [Å]	1.3-4.8			1.3-4.8			1.3-4.8				
k range [Å^{-1}]	2.96-12.26			2.98-12.18			3.0-12.23				
Residual [%]	8.99			7.14			7.72				
E_0-shift [eV]	5.43			5.39			5.6				
Fig. S14	a)			b)			c)				
				c: correlated			f: fixed				

[a]fit carried out in R, FT of $\chi(k)*k^3$ with Bessel window function (window parameter: 3), fit mode k^3+k^2, S_0^2=0.95

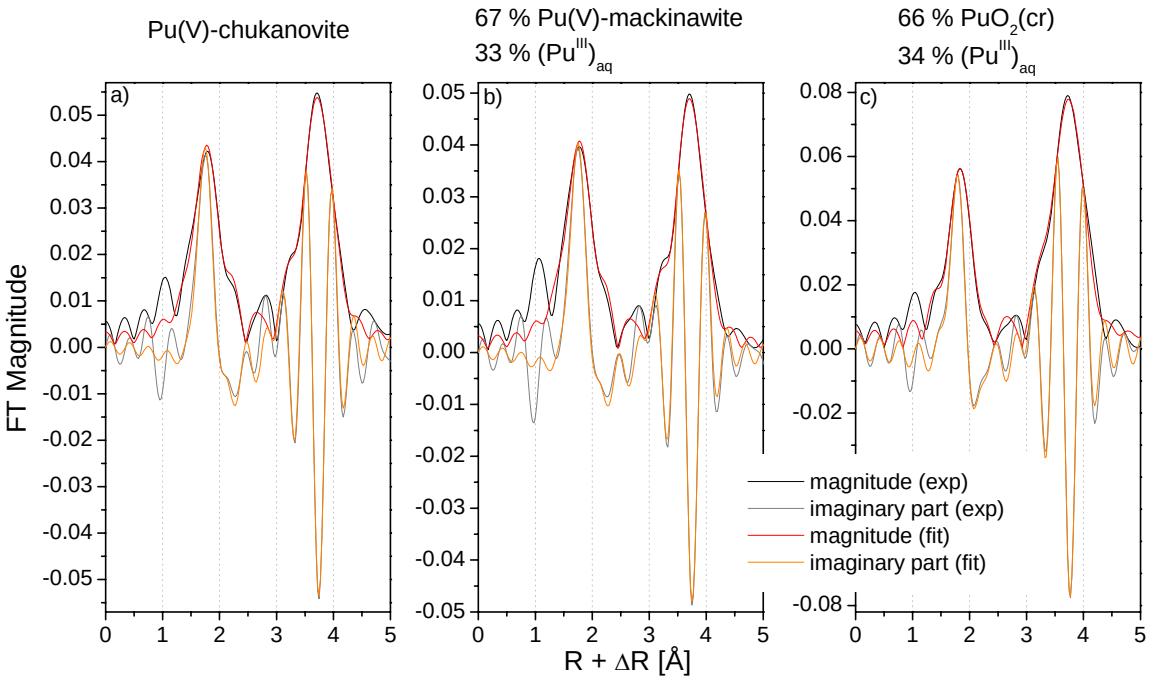

Figure S14. Shell fits corresponding to fit parameters detailed in Table S13 for Pu(V)-chukanovite (a) and artificially created mixture spectra of Pu(V)-mackinawite (b) or PuO_2(cr) (c) and $(Pu^{III})_{aq}$.

Cited Literature:

(1) Jolivet, J. P.; Belleville, P.; Tronc, E.; Livage, J., Influence of Fe(II) on the formation of the spinel iron-oxide in alkaline-medium. *Clays Clay Miner. 1992, 40* (5), 531-539.

(2) Ohfuji, H.; Rickard, D., High resolution transmission electron microscopic study of synthetic nanocrystalline mackinawite. *Earth. Planet. Sci. Lett.* **2006,** *241* (1-2), 227-233.

(3) Rickard, D. T., The chemistry of iron sulfide formation at low temperatures. *Stockholm Cont. Geol.* **1969,** *20,* 67-95.

(4) Scheinost, A. C.; Kirsch, R.; Banerjee, D.; Fernandez-Martinez, A.; Zaenker, H.; Funke, H.; Charlet, L., X-ray absorption and photoelectron spectroscopy investigation of selenite reduction by FeII-bearing minerals. *J. Contam. Hydrol.* **2008,** *102,* 228-245.

(5) Hammersley, A. P.; Svensson, S. O.; Hanfland, M.; Fitch, A. N.; Häusermann, D., Two-dimensional detector software: from real detector to idealised image or two-theta scan. *High Pressure Res.* **1996,** *14,* 235-248.

(6) Caglioti, G.; Paoletti, A.; Ricci, F. P., Choice of collimators for a crystal spectrometer for neutron diffraction. *Nucl. Instrum.* **1958,** *3* (4), 223-228.

(7) Pekov, I. V.; Perchiazzi, N.; Merlino, S.; Vyacheslav, N.; Merlini, M.; Zadov, A. E., Chukanovite, $Fe_2(CO_3)(OH)_2$, a new mineral from the weathered iron meteorite Dronino. *Eur. J. Mineral.* **2007,** *19* (6), 891-898.

(8) Stumm, W.; Morgan, J. J., *Aquatic Chemistry: chemical equilibria and rates in natural waters,* 3 rd ed.; John Wiley & Sons, Inc.: New York, 1996.

(9) Oman, S. F.; Camoes, M. F.; Powell, K. J.; Rajagopalan, R.; Spitzer, P., Guidelines for potentiometric measurements in suspensions, part B. Guidelines for practical pH measurements in soil suspensions. *Pure Appl. Chem.* **2007,** *79* (1), 81-86.

(10) Oman, S. F.; Camoes, M. F.; Powell, K. J.; Rajagopalan, R.; Spitzer, P., Guidelines for potentiometric measurements in suspensions, part A. The suspension effect. *Pure Appl. Chem.* **2007,** *79* (1), 67-79.

(11) Silvester, E.; Charlet, L.; Tournassat, C.; Gehin, a.; Greneche, J.-M.; Liger, E., Redox potential measurements and Mössbauer spectrometry of FeII adsorbed onto FeIII (oxyhydr)oxides. *Geochim. Cosmochim. Acta* **2005,** *69* (20), 4801–4815.

(12) Intercomparison of Redox determination methods on designed and near-natural aqueous systems : FP 7 EURATOM Collaborative Project "Redox Phenomena Controlling Systems". KIT Scientific Reports 7572; Karlsruhe Institute of Technology: Karlsruhe, 2011; p 266.

(13) Webb, S. M., SIXpack: a graphical user interface for XAS analysis using IFEFFIT. *Phys. Scr.* **2005,** *T115,* 1011-1014.

(14) Ravel, B.; Newville, M., Athena, Artemis, Hephaestus: data analysis for X-ray absorption spectroscopy using IFEFFIT. *J. Synchrotron Radiat.* **2005,** *12,* 537-541.

(15) Conradson, S. D.; Abney, K. D.; Begg, B. D.; Brady, E. D.; Clark, D. L.; den Auwer, C.; Ding, M.; Dorhout, P. K.; Espinosa-Faller, F. J.; Gordon, P. L.; Haire, R. G.; Hess, N. J.; Hess, R. F.; Keogh, D. W.; Lander, G. H.; Lupinetti, A. J.; Morales, L. A.; Neu, M. P.; Palmer, P. D.; Paviet-Hartmann, P.; Reilly, S. D.; Runde, W. H.; Tait, C. D.; Veirs, D. K.; Wastin, F., Higher order speciation effects on plutonium L_3 X-ray absorption near edge spectra. *Inorg. Chem.* **2004,** *43* (1), 116-131.

(16) Matonic, J. H.; Scott, B. L.; Neu, M. P., High-yield synthesis and single-crystal X-ray structure of a plutonium(III) aquo complex:$[Pu(H_2O)_9][CF_3SO_3]_3$. *Inorg. Chem.* **2001,** *40,* 2638-2639.

(17) Gurman, S. J.; McGreevy, R. L., Reverse Monte-Carlo simulation for the analysis of EXAFS data. J. Phys.: Condens. Matter 1990, 2 (48), 9463-9473.

(18) Winterer, M., Reverse Monte Carlo analysis of extended x-ray absorption fine structure spectra of monoclinic and amorphous zirconia. *J. Appl. Phys.* **2000,** *88* (10), 5635-5644.

(19) Rossberg, A.; Scheinost, A. C., Three-dimensional modeling of EXAFS spectral mixtures by combining Monte Carlo simulations and target transformation factor analysis. *Anal. Bioanal. Chem.* **2005,** *383* (1), 56-66.

(20) Martin, P.; Grandjean, S.; Valot, C.; Carlot, G.; Ripert, M.; Blanc, P.; Hennig, C., XAS study of $(U_{1-y}Pu_y)O_2$ solid solutions. *J. Alloys Compd.* **2007,** *444,* 410-414.

(21) Di Giandomenico, M. V.; Le Naour, C.; Simoni, E.; Guillaumont, D.; Moisy, P.; Hennig, C.; Conradson, S. D.; Den Auwer, C., Structure of early actinides(V) in acidic solutions. *Radiochim. Acta* **2009,** *97* (7), 347-353.

(22) Den Auwer, C.; Simoni, E.; Conradson, S. D.; Madic, C., Investigating Actinyl Oxo Cations by X-ray Absorption Spectroscopy. Eur. J. Inorg. Chem. 2003, 3843-3859.

(23) Runde, W., The chemical interactions of actinides in the environment. *Los Alamos Science* **2000,** *26,* 392-411.

(24) Rossberg, A.; Reich, T.; Bernhard, G., Complexation of uranium(VI) with protocatechuic acid - application of iterative transformation factor analysis to EXAFS spectroscopy. *Anal. Bioanal. Chem.* **2003,** *376* (5), 631-638.

(25) Belin, R. C.; Valenza, P. J.; Reynaud, M. A.; Raison, P. E., New hermetic sample holder for radioactive materials fitting to Siemens D5000 and Bruker D8 X-ray diffractometers: application to the Rietveld analysis of plutonium dioxide. *J. Appl. Crystallogr.* **2004,** *37,* 1034-1037.

(26) Conradson, S. D.; Clark, D. L.; Neu, M. P.; Runde, W. H.; Tait, C. D., Characterizing the plutonium aquo ions by XAFS spectroscopy. *Los Alamos Science* **2000,** *26,* 418-421.

3.3. Reaction of plutonium with mackinawite

In this chapter, the reaction of plutonium with mackinawite will be discussed based on all 6 plutonium-mackinawite samples one of which (Mk-40d-V-pH8) was already among the samples discussed in chapter 3.2. For ease of reading, the samples are listed again in table 3.3.1, an extract from table 3.1.2. The reaction conditions (pH, pe, [Pu], sorption) are summarized in figures 3.3.1-4 (Tables A3.1-6) and are discussed in some detail in particular with respect to factors influencing the pH measurements. Sorption of Pu to mackinawite is discussed with respect to its consequences for Pu concentrations in solution. During the following analysis of XAS data, the influence on XANES and EXAFS spectra of add-mixtures of Pu(III) or Pu(V) to PuO_2(cr) is discussed in some detail.

Table 3.3.1. List of Pu-mackinawite samples to be discussed in this chapter.

Mineral	sample abbreviation	reaction time	Pu added as*	pH $_{final}$**	$[Pu]_{start}$ [µmol/ L]	$[Pu]_{final}$ [nmol/ L]	% Pu sorbed	Pu/mineral loading m/m [ppm]	[µmol/ g]	[nmol/ m^2]
Mackinawite	Mk-40d-V-pH8	40d	Pu(V)	8.0	13.4	≤ 1	99.993	947	3.9	73
	Mk-40d-III-pH6	40d	Pu(III)	6.4	12.2	202.1	98.343	862	3.6	67
	Mk-8m-V-pH7	7.6 m	Pu(V)	6.9	15.7	2.51	99.984	2221	9.2	172
	Mk-8m-V-pH8	7.6 m	Pu(V)	8.4	15.7	≤ 0.04	100.000	2221	9.2	172
	Mk-8m-III-pH7	7.6 m	Pu(III)	7.1	11.7	25	99.786	1653	6.8	128
	Mk-8m-III-pH8	7.6 m	Pu(III)	8.0	11.7	≤ 0.04	100.000	1653	6.8	128

* Initial Pu oxidation state
** pH measured in suspension at the end of the reaction period
# The values preceded by a ≤ sign correspond to the detection limit for Pu concentrations by LSC. As the detection limit changed with the amount of sample solution used, different detection limits (1 vs 0.04 nM) were obtained at the end of the 40 d and 6 m experiments.

3.3.1. Reaction conditions – an overview

The pH-values plotted in figure 3.3.1 as a function of reaction time are pH values obtained from measurement in the mineral suspensions. Mainly due to ease of measurement, suspension pH (pH_{sus}) values were acquired more frequently than pH values measured after centrifugation (pH_{cen}) (Tables A3.1-6). It appears, however, that pH_{sus} is also a more robust parameter than pH_{cen} even though the latter better respects the thermodynamic definition of pH as a solution parameter (as discussed in more detail on pp. 35). In numerous measurements pH_{sus} and pH_{cen} were very similar and the suspension effect on the glass and the reference electrode[97] thus seems to be minor[i]. In other cases, however, pH_{cen} deviates for similar pH_{sus} values to lower or higher values by up to 0.6 pH units, in one case even by 1.5 pH units. To my understanding, such deviations to both higher and lower pH values of pH_{cen} compared to pH_{sus} can be explained by out gassing of H_2S, on the one hand, and by oxidation of

[i] The similarity between pH_{sus} and pH_{cen} cannot, however, proof that the suspension effect is minor as the reactions that potentially influence pH (and that are discussed in the following paragraph) might also have occurred when pH_{cen} is equal to pH_{sus}. Only, in this case, would these reactions have caused an error of similar magnitude and sign to the error of the measured signal caused by the suspension effect.

dissolved Fe^{2+} by traces of oxygen, on the other hand.

While outgassing of H_2S will increase the pH by a right shift of the equilibrium

$$HS^- + H^+ \rightleftarrows H_2S(aq) \rightleftarrows H_2S(g)$$

and should be more important at lower pH when a greater percentage of S(-II) is present as H_2S, oxidation of Fe^{2+} will decrease the pH due to precipitation of $Fe(OH)_3$ according to

$$Fe^{2+} + ¼\ O_2(g) + 2.5\ H_2O \rightleftarrows Fe(OH)_3(s) + 2\ H^+.$$

Due to surface complexation reactions,

$$\text{e.g. } \equiv FeSH^0 + H+ \rightleftarrows FeSH_2^+ \text{ and } \equiv FeSH^0 \rightleftarrows FeS^- + H^+,$$ [98]

suspended FeS particles have a buffering effect on pH and can thus reduce a pH shift due to out gassing of H_2S or oxidation of Fe^{2+} and may, in addition, also react with trace oxygen, thus limiting the oxidation of dissolved Fe^{2+} and formation of H^+ in the first place.

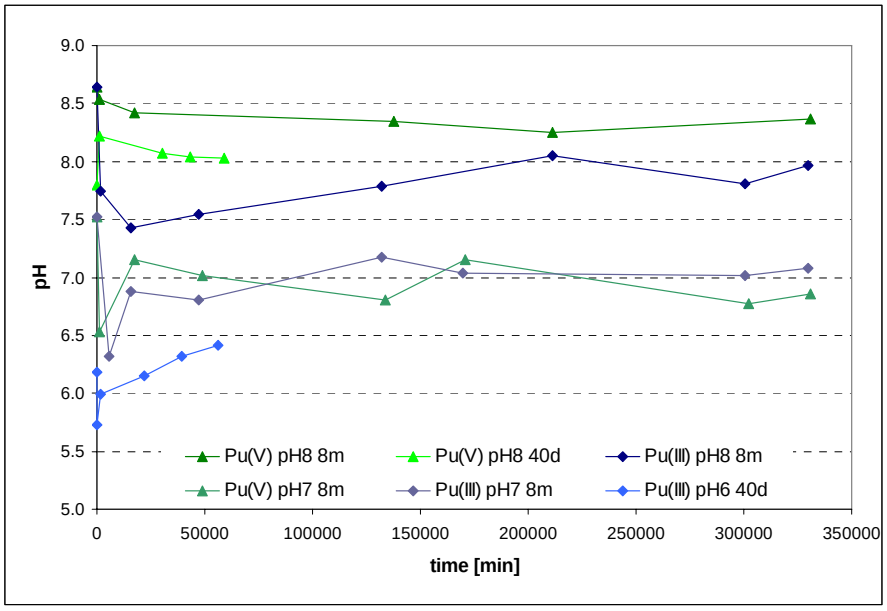

Figure 3.3.1. pH_{sus} values over time for Pu-mackinawite mineral samples. The samples are designated by the initial Pu oxidation state, pH and reaction time.

Oxidation of Fe^{2+} may occur despite the nominal small oxygen concentrations in the glove box atmosphere. For example, even an O_2 concentration of 5 ppmv corresponds to $2.04 \cdot 10^{-7}$ mol O_2/L or $1.23 \cdot 10^{17}$ molecules O_2/L (calculated with a molar volume 24.46 L / mol of gas molecules at 25°C). The reactions of Pu with mackinawite in the mineral suspensions took, however, place at much lower oxygen levels, as indicated by the pe values acquired in suspension (Fig. 3.3.2). Once the reaction vessel is closed, O_2(aq) present in the mineral suspension disappears as it oxidizes Fe^{2+}(aq) or FeS(s). This results in pe values between -4 and -5.5 at pH 6−8. As can be seen from the relation pe = ¼ logK + ¼ log$P(O_2)$ - pH, with logK = 20.77, a pe value of -5 at pH 8 corresponds to an oxygen partial pressure of $8.3 \cdot 10^{-72}$ bar. An oxygen concentration of 5 ppmv (= $5.065 \cdot 10^{-6}$ bar at a pressure of 1 atm = 1.013 bar), in contrast, should result in a pe value of 11.45. As shown in chapter 4.2, pe values acquired through suspension measurements are in good agreement with the thermodynamics of the Fe-S-H_2O system and seem to represent redox potentials in mackinawite suspensions quite accurately.

As can be seen in figure 3.3.1 and 3.3.2, the pH and the pe in the mineral suspensions were quite stable over the reaction time even though no pH (or pe) buffer other than mackinawite were used.
Differences in pe and pH for the 7.6 months samples prepared at pH 7 with either Pu(III) or Pu(V) as initial Pu oxidation state are minor and within the experimental uncertainty that I estimate to be about 0.1 pH and up to 1 pe unit. For pe, 1 unit corresponds to an uncertainty of about 60 mV in the redox potential measurement. Differences in reaction outcomes of these two samples should thus be related to the initial Pu oxidation state and not to differences in reaction conditions. After 150 days of equilibration differences in pH for the 7.6 months samples prepared at pH ≈ 8 are also small. For these two samples, differences in reaction products might, however, be due to the differences in pH over the first 5 month of reaction. With respect to pH, the Mk-40d-V-pH8 sample compares well with the longer reaction time samples at pH 8 while the pH of the Mk-40d-III-pH6 sample is considerable lower and the pe slightly higher than in the longer term pH 7 samples.

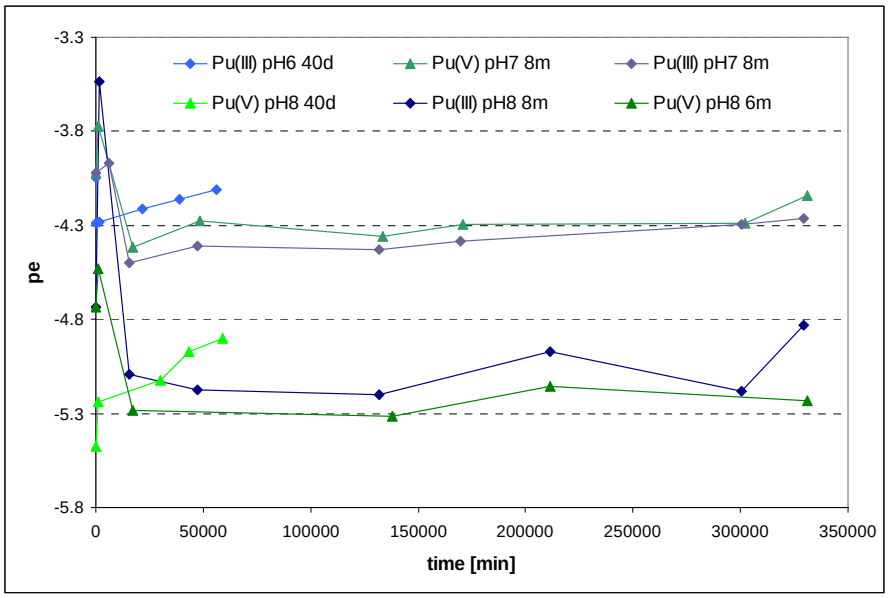

Figure 3.3.2. pe_{sus} values over time for Pu-mackinawite mineral samples. The samples are designated by the initial Pu oxidation state, pH and reaction time.

For all six Pu-mackinawite samples, initial Pu sorption[ii] was fast, with 75 to 100 % of Pu removed from solution within the first 15 to 25 minutes (Fig. 3.3.3. and Tables A3.1-6). However, notable differences exist between samples according to the reaction pH and possibly initial Pu oxidation state. For samples Mk-40d-V-pH8 and Mk-8m-V-pH8 that had a reaction pH above 8, Pu was removed from solutions within the first half hour of reaction down to $1 \cdot 10^{-9}$ M (the analytical detection limit) (Fig. 3.3.4). For sample Mk-8m-III-pH8, whose pH was slightly lower (pH 7.4−7.8 in the first 92 days of reaction) and to which, in contrast to the first two sample, Pu(III) and not Pu(V) had been added, removal of Pu down to a solution concentration of 10^{-9} M was achieved after more than 33 days of reaction. For the three remaining samples with a pH of 6−7 (Mk-40d-III-pH6, Mk-8m-V-pH7, Mk-

[ii] The term "sorption" is, in this case, used as equivalent to "Pu removal from solution" and no assumption on the mechanisms of Pu removal from solution such as either surface complexation or formation of a Pu solid phase is implied.

8m-III-pH7) Pu concentrations did not decrease below 10^{-7} M until the end of the experiment (for Mk-40d-III-pH6) or until about 210 days of reaction (for Mk-8m-V-pH7 and Mk-8m-III-pH7) after which they decreased abruptly by two orders of magnitude without, however, reaching quantitative removal. Between days 1 and 33 for Mk-8m-III-pH8 and between days 33 and 210 for Mk-8m-V-pH7 and Mk-8m-III-pH7, the decrease of the Pu concentration in solutions conforms to (pseudo-) first order kinetics as can be seen from a plot of $-\ln([Pu]_t/[Pu]_0)$ versus time (see Fig. 3.3.5 for plot and Table 3.3.2 for rate constants). [iii]

As was shown in the introduction (Fig. 1.2), the solubility of tetravalent Pu at pH 6−9 (assuming PuO_2(am,hyd) as the solubility controlling solid phase) is very low and cannot account for the Pu concentrations above 10^{-7} M that were observed for samples Mk-40d-III-pH6, Mk-8m-V-pH7 and Mk-8m-III-pH7.[iv] Depending on pe, pH and the crystallinity and particle size of a PuO_2 solid phase, solution concentrations of dissolved Pu(III) can, in contrast, be considerable. For example, in a system with pH 6.4, pe -4.1, and an ionic strength of 0.1 M (similar to sample Mk-40d-III-pH6) [Pu(III)] in equilibrium with PuO_2(am,hyd) would be $7.4 \cdot 10^{-6}$M. Formation of PuO_2(am,hyd) can result in Pu(III) concentrations similar to the ones observed for samples Mk-8m-V-pH7 and Mk-8m-III-pH7. For example, with a Δ_fG value for PuO_2(am,hyd) of -959.5 instead of -965.5 kJ/mol (the uncertainty for Δ_fG of PuO_2(am,hyd) is about 6 kJ/mol) the concentrations obtained for [Pu(III)] are, at an ionic strength of 0.1 M in NaCl, $2.3 \cdot 10^{-7}$ M at pH 7.1, pe -4.2 and $2.5 \cdot 10^{-6}$ M at pH 6.9, pe -4.5, which is the range of Pu concentrations measured for the pH 7 samples between 33 and 210 days of reaction. If the uncertainty in the value of Δ_fG is applied in the opposite direction, using a value of -971.5 kJ/mol, a Pu(III) concentration of $1.8 \cdot 10^{-9}$ M results for pH 7.1, pe -4.2 (and [Pu(III)] = $2.0 \cdot 10^{-8}$ M for Δ_fG = -965.5 kJ/mol), which corresponds well to the final concentrations that were measured for the two pH 7 samples that were $2.5 \cdot 10^{-9}$ M for Mk-8m-V-pH7 and $2.5 \cdot 10^{-8}$ M for Mk-8m-III-pH7.

Apart from formation of a PuO_2 solid phase, the process controlling dissolved Pu concentrations (and in this case Pu(III)aq concentrations) could be sorption of Pu(III) to a mineral surface according to the equilibrium

$$FeS + Pu(III)aq \rightleftarrows FeS{-}Pu(III)ads.$$

[iii] (Pseudo-) first order reactions can be described by $[C]_t = [C]_0\, e^{-kt}$, $[C]_t$ and $[C]_0$ being the concentration of substance C at time t and at the start of the reaction and k being the rate constant. This rate law can be linearized according to $[C]_t/[C]_0 = e^{-kt} \Rightarrow -\ln([C]t/[C0]) = kt$.

[iv] Speciation analysis by solvent extract was not performed and the given thermodynamic predictions can thus not be compared to experimental values.

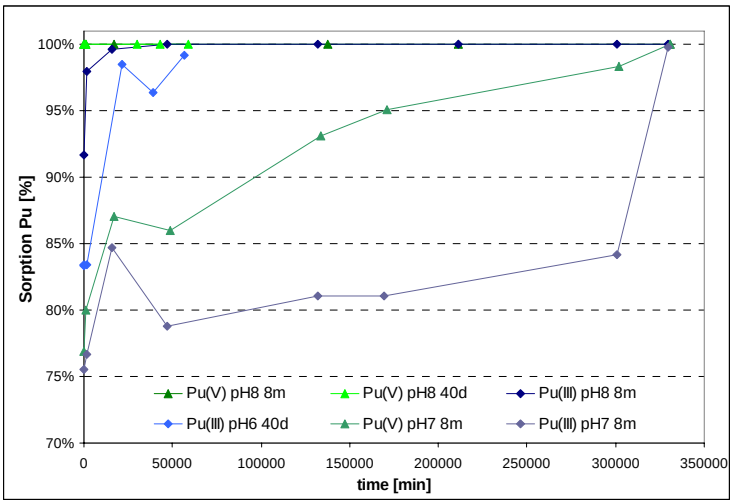

Figure 3.3.3. Removal of dissolved Pu from solution over time for Pu-mackinawite samples. The samples are designated by the initial Pu oxidation state, pH and reaction time.

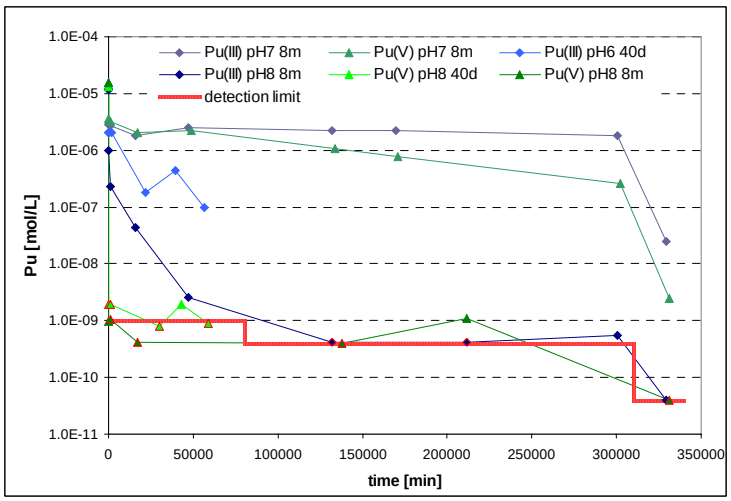

Figure 3.3.4. Total dissolved Pu over time for Pu-mackinawite samples. The samples are designated by the initial Pu oxidation state, pH and reaction time. Data points corresponding to values at or below the detection limit are marked by red outer line.

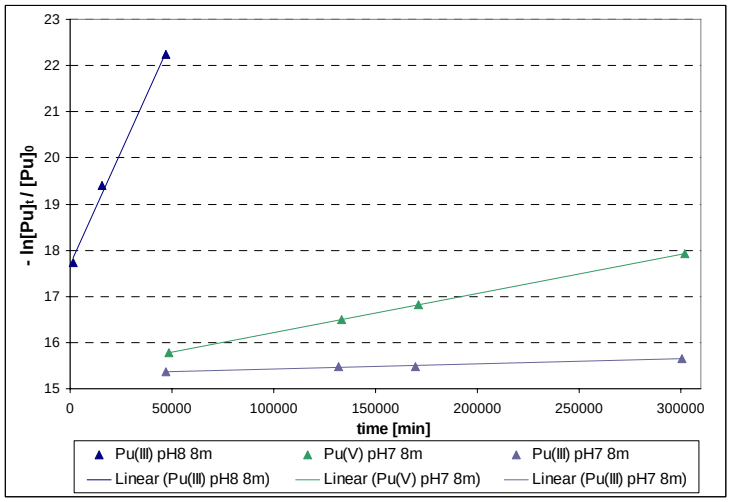

Figure 3.3.5. Kinetics of Pu removal from solution for samples Mk-8m-III-pH8, Mk-8m-V-pH7, and Mk-8m-III-pH7.

Table 3.3.2. Apparent rate constants and regression coefficients for removal of Pu from solution in mackinawite suspensions. Rate constants result from linearization according to (pseudo-) first order kinetics.

sample	apparent rate constant [min^{-1}]	apparent rate constant [s^{-1}]	regression coefficient R^2
Mk-8m-III-pH8	9.71E-05	1.62E-06	0.995
Mk-8m-V-pH7	8.46E-06	1.41E-07	1.000
Mk-8m-III-pH7	1.13E-06	1.88E-08	0.977

Whether Pu(III) associated to the solid phase can be found and to what extent formation of a PuO_2-solid phase occurs in the Pu-mackinawite samples can be assessed with X-ray absorption spectroscopy and will be discussed in the following paragraphs. Unfortunately, only one XAS measurement at the end of the 7.6 months reaction period was carried out and thus we cannot know how the solubility controlling solid phase changed at pH7 in the Mk-8m-V-pH7 and Mk-8m-III-pH7 samples from day 33 to 230, when first a slow and then a rapid change in Pu solution concentrations was observed (Fig. 3.3.4).

3.3.2. Results from X-ray absorption spectroscopy

In figure 3.3.6 XANES spectra of the six Pu-mackinawite samples are compared to reference spectra of aqueous Pu(III), Pu(IV), and Pu(V) and crystalline PuO_2. The six samples clearly separate into two distinct groups: one spectra similar to Pu(III)aq (groupe #1) and spectra similar to PuO_2 (groupe #2). Only the Mk-40d-III-pH6 spectrum corresponds to groupe #1. It is slightly shifted to higher energy compared to the Pu(III)aq reference but nevertheless contains predominantly Pu(III) (Table 3.3.3 for LC-fit results). All other spectra have their WL maxima between Pu(IV)aq and PuO_2(cr) as is typical for PuO_2-colloids[76, 99] or, more generally speaking, of non-calcinated PuO_2, and thus fall into group #2. Among the five spectra of the second group, two sub-groups emerge and are differentiated by the position and intensity of their WL maxima.

Comparison of chi-spectra and Fourier Transforms of sample Mk-40d-III-pH6 and the Pu(III)aq reference confirms that Pu is mainly present as Pu(III) in Mk-40d-III-pH6 (Fig. 3.3.7).
While the LC fit with Pu(III)aq and either Pu(IV)aq or non-calcinated PuO_2 (as present in sample Mk-8m-V-pH7) as references yielded a Pu(IV) content of about 8 % (Fig. 3.3.8, Table 3.3.3), no Pu(IV) contribution could be identified by applying LC fitting to the EXAFS spectra (LC fit of $\chi(k)*k^3$ with Pu(III)aq and Pu(IV)aq or PuO_2 as references, not shown).

In Fig. 3.3.7 the FT is shown up to an R+ΔR value of 10 Å to show the high noise level (in this case indicated by the amplitude of the peaks in the range starting at about 6 Å) of the Mk-40d-III-pH6 sample. It was thus not possible to meaningfully fit the small three peaks from 2.6 to 4.2 Å that have a magnitude just above the noise level. Thus only the first shell (Pu-O) was included into the shell fit and no information about further coordination environment of Pu(III) could be obtained (Table 3.3.4).

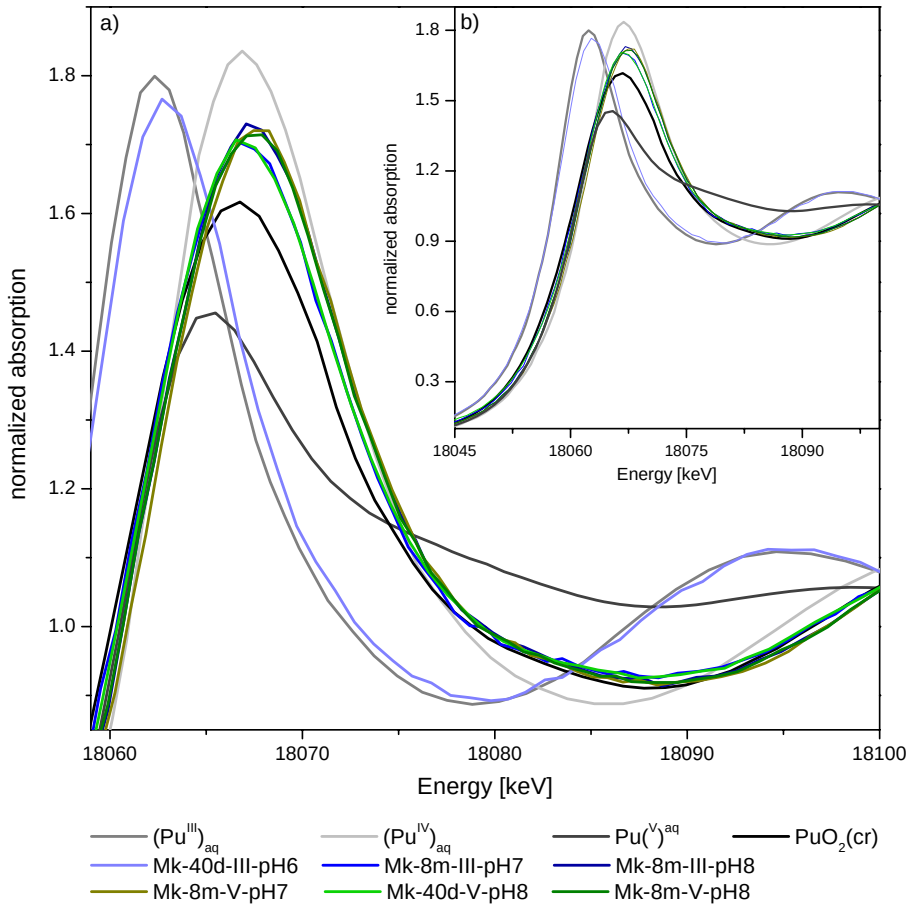

Figure 3.3.6. XANES region of Pu-L_{III}-edge X-ray absorption spectra of Pu-mackinawite samples and **Pu(III)aq**, **Pu(IV)aq**, **Pu(V)aq** and **PuO_2(cr)** for reference. Sample spectra were color coded according to the initial Pu oxidation state of Pu added to mackinawite suspensions: Pu(III) – blue, Pu(V) – green. a) Zoom of WL maximum and post WL minimum region b) overview of XANES region.

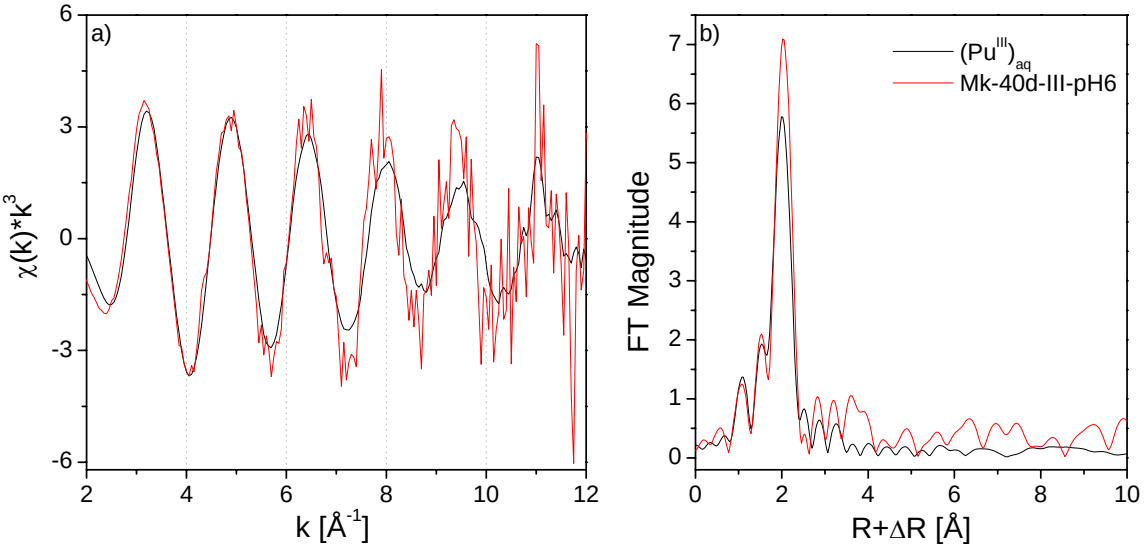

Figure 3.3.7. EXAFS spectrum (a) and FT (b) of sample Mk-40d-III-pH6 and Pu(III)aq reference (k-range for FT: $3 \leq k \leq 12$, hannig window with dk = 1).

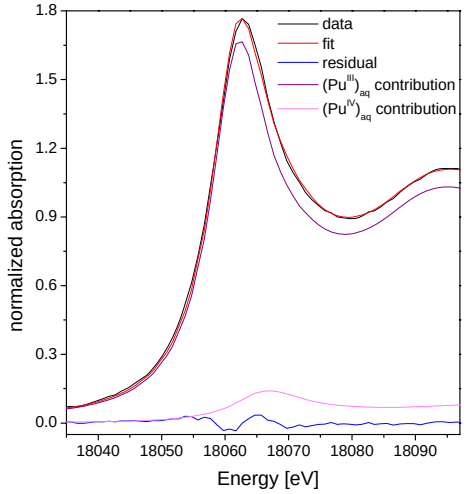

Figure 3.3.8. LC fit of Mk-40d-III-pH6 with Pu(III)aq and Pu(IV)aq as references.

Table 3.3.3. Linear combination fit of sample Mk-40d-III-pH6 with a Pu(III) and Pu(IV) references in the energy range 18.035 to 18.095 keV. For plot see Fig. 3.3.8.

References used	Pu(III)	+/- Pu(III)	Pu(IV)	+/- Pu(IV)	sum [%]	R-factor
Pu(III)aq and Pu(IV)aq	93.4 %	0.7 %	7.7 %	0.7 %	101.1	$2.3 \cdot 10^{-4}$
Pu(III)aq and PuO_2 (Mk-8m-V-pH7)	93.5 %	0.8 %	7.7 %	0.8 %	101.2	$2.7 \cdot 10^{-4}$

As visual observation and LC fit of the XANES (Fig. 3.3.6, Table 3.3.3) suggest a small contribution of Pu(IV) to the spectrum and as LC fitting of the EXAFS did not confirm this, two artificial mixture spectra of 90 Pu(III)aq and 10 % of Pu(IV) were created by summing the weighted normalized spectra (mixed spectrum = $0.9 \cdot (\text{Pu(III)aq})_{nrm} + 0.1 \cdot (\text{Pu(IV)aq})_{nrm}$) to serve as examples for how the presence of Pu(IV) affects an $\chi(k)$ spectrum containing mainly Pu(III) (Fig. 3.3.9) and in how far a relatively small contribution of Pu(IV) is detectable in the shell fit (Table 3.3.4 and Fig. 3.3.10). For mixing with Pu(III)aq either Pu(IV)aq or PuO_2(cr) were used as representatives of Pu(IV).

Table 3.3.4. Shell fit of Mk-40d-III-pH6, Pu(III)aq and artificial reference spectra for mixtures of Pu(III) and Pu(IV) with Pu(IV) being represented by either Pu(IV)aq or PuO_2(cr)[a].

paths and parameters	$(Pu^{III})_{aq}$			Mk-40d-III-pH6			90 %$(Pu^{III})_{aq}$ + 10 %$((Pu^{IV})_{aq}$			90 %$(Pu^{III})_{aq}$ + 10 %PuO_2(cr)		
	CN	R [Å]	σ^2 [Å^2]	CN	R [Å]	σ^2 [Å^2]	CN	R [Å]	σ^2 [Å^2]	CN	R [Å]	σ^2 [Å^2]
Pu - O	8.1	2.49	0.0078	7.2	2.5	0.0043	7.7	2.48	0.0087	7.6	2.48	0.0098
R range [Å]	1.3 – 2.6			1.3 – 2.6			1.3 – 2.5			1.3 – 2.6		
k range [Å^{-1}]	2.8 – 10.7			2.7 – 11.0			2.8 – 10.9			2.8 – 10.9		
Residual [%]	5.34			9.4			7.0			8.1		
E_0-shift [eV]	9.9			10.1			10.2			9.5		
Fig. 3.3.10	a, b			c, d			g, h			e, f		

[a]fit carried out in R space, FT of $\chi(k)*k^3$ with Bessel window function (window parameter = 3), fit mode: k^3+k^2, S_0^2=0.95

As can be seen in fig. 3.3.9., a decrease of the Pu(III) and increase of the Pu(IV) content (in the form of either Pu(IV)aq or solid PuO_2(cr)) of a spectrum result in changes of phase and amplitude of the resulting chi-spectra. Some of these changes are marked in Fig. 3.3.9 by arrows or circles. It can thus be seen that a Pu(IV) content of 10 percent, a value close to the one suggested for Mk-40d-III-pH6

from the LCfit, a) results in noticeable changes compared to the spectrum of pure Pu(III)aq and that b) the resulting mixture spectra are less similar to the spectrum of sample Mk-40d-III-pH6 than pure Pu(III)aq. In particular, spectral features of the Mk-40d-III-pH6 spectrum that differ from the Pu(III)aq reference such as the minimum at 7.2 $Å^{-1}$ can not be explained by a potential Pu(IV) content of the spectrum.

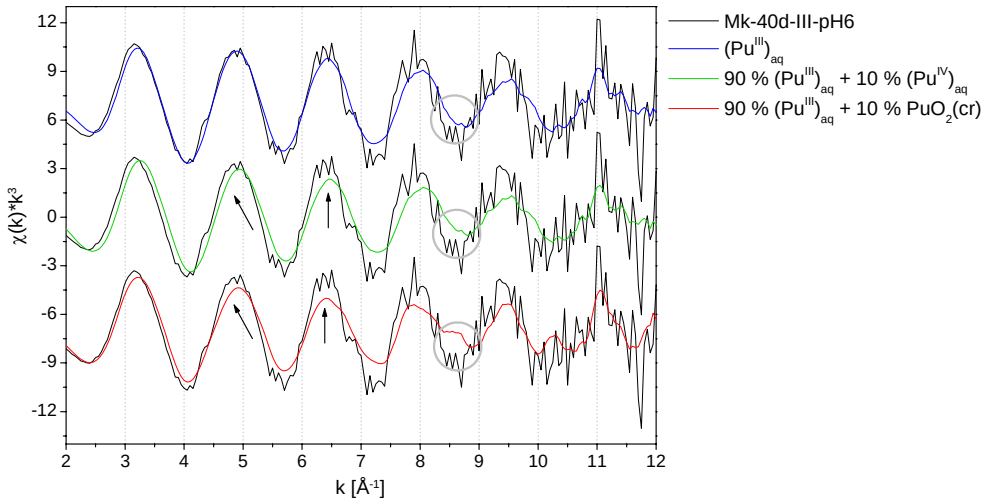

Figure 3.3.9. Comparison of Mk-40d-III-pH6 with Pu(III)aq and artificial mixture spectra of Pu(III)aq and Pu(IV).

In the shell fit, a Pu(IV) content of 10 % in the artificial spectra result in a slightly increase of the DW (0.009 and 0.01 compared to 0.008 $Å^2$ for Pu(III)aq) while the effect on the fitted Pu-O distance (2.48 instead of 2.49 Å) is not significant considering an uncertainty of about 0.02 Å. Also the Pu-O CN decreases only slightly. A direct comparison of the DW, as the fit parameter with the greatest response to an add-mixture of Pu(IV), to the Mk-40d-III-pH6 spectrum is hampered by the fact that the sample was measured at 15 K while the Pu(III)aq and Pu(IV)aq reference spectra were acquired at RT. The DW of Mk-40d-III-pH6 is thus far smaller than the one of pure Pu(III)aq. It is, interestingly, also smaller than the one found for the coordination shell of the three Pu(III)-magnetite spectra (0.006 – 0.007 $Å^2$) (Table S5, chap. 3.2) that were also acquired at 15 K. Possibly, the oxygen coordination environment of Pu(III) on magnetite, that forms an inner-sphere surface complex and shares three oxygen atoms with the surface, is slightly distorted (and thus structurally disordered) compared to a homogenous H_2O environment as one can suppose it exists for a Pu(III) outer-sphere on mackinawite. The above mentioned lower minimum at 7.2 $Å^{-1}$ of the Mk-40d-III-pH6 spectrum compared to Pu(III)aq results from this lower DW and the minimum is well reproduced in the shell fit (Fig. 3.3.10, c). The difference in CN compared to the Pu(III)aq reference (7.2 vs 8.1, i.e. about 11 %) is not significant with respect to uncertainties of up to 25 %.[100] One can thus conclude that the EXAFS spectrum itself and the shell fit do not provide indications for a presence of Pu(IV) in the Mk-40d-III-pH6 sample. If no Pu(IV) is present, it is, however, not clear what causes the slight shift of the absorption edge to higher energy compared to the Pu(III) reference[v]. Whether Pu(IV) is present in this

[v] It may be noted here that Pu(V) was not considered for the discussion of the XANES for this sample (Mk-40d-III-pH6) as it is far removed from the predominance field of Pu(V) but very close to the predominance field of

sample or not, it served as an instructive example to consider the impact of a small Pu(IV) add-mixture to a Pu(III)aq spectrum. It is interesting to note that such an add-mixture is quite well visible in the chi-spectrum while its main influence on the shell fit of the oxygen coordination shell is to increase the DW.

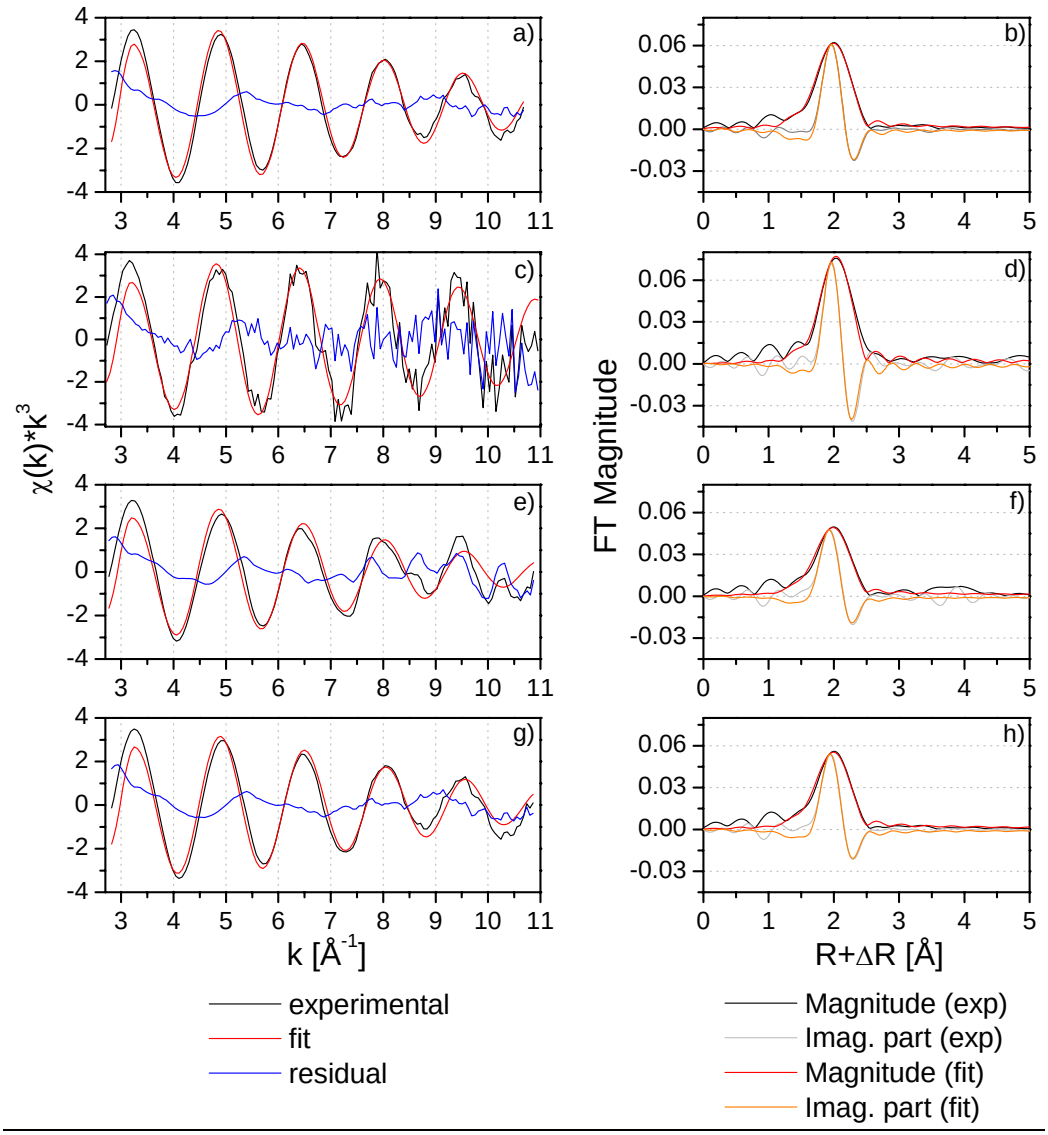

Figure 3.3.10. Shell fit of Mk-40d-III-pH6, Pu(III)aq and artificial reference spectra for mixtures of 90 % Pu(III) and 10 % Pu(IV) with Pu(IV) being represented by either Pu(IV)aq or PuO_2(cr). a) and b) Pu(III)aq, c) and d) Mk-40d-III-pH6, e) and f) 90 % Pu(III)aq + 10 % PuO_2(cr), g) and h) 90 % Pu(III)aq + 10 % Pu(IV)aq.

As Pu is coordinated to oxygen in the first shell and as no sulfur or iron back-scatterers could be identified, Pu(III) is probably adsorbed in an outer-sphere complex to the mackinawite surface. The point of zero charge of mackinawite lies at about pH 7.5[98] and the overall surface charge of the

PuO_2(am, hyd) and Pu(IV)aq. If, against all doubts, a LC fit with Pu(III)aq and Pu(V)aq is carried out for the sake of completeness, a contribution of 8 % Pu(V) is found. However, the R-factor associated with this fit is, with a value of $4.2 \cdot 10^{-4}$, almost twice as high as for a LC fit with Pu(III)aq and Pu(IV)aq as references (Table 3.3.3).

mackinawite particles at a pH below this value is therefore positive. Sites with negative surface charge (e.g. $\equiv FeS^-$) exist however also at lower pH. According to Wolthers et al. (2005),[98] the concentration of $\equiv FeS^-$ sites at pH 6.3 is, at the used solid/liquid ratio 3.43 g/L FeS (supposing a similar surface area of the FeS used by Wolthers et al. and used here), about $1.45 \cdot 10^{-4}$ mol/L. This value is about 10 times greater than the total added Pu concentration of $1.2 \cdot 10^{-5}$ mol/L. As until pH 6.9 Pu(III)aq is mainly present as triply positively charged Pu^{3+}, a high electrostatic driving force for formation of an outer-sphere surface complex with the oppositely charged $\equiv FeS^-$ surface sites exists and could explain the experimentally observed removal of 98 % of the added Pu(III) from solution. With decreasing pH, the number of available $\equiv FeS^-$ sites decreases and Pu(III) outer-sphere complexation with mackinawite can be expected to also decrease, resulting in a higher equilibrium Pu concentration in solution. In a system free of FeS, PuO_2(am,hyd) is the solid phase that controls Pu(III)aq concentrations in solution. If FeS is present, it can reduce [Pu(III)aq] to below the level imposed by PuO_2(am,hyd) or PuO_2(coll, hyd) as could be observed for sample Mk-40d-III-pH6 where the observed Pu concentration was $1 \cdot 10^{-7}$ M as opposed to $7 \cdot 10^{-6}$ M to $7 \cdot 10^{-5}$ M (which is a hypothetic value as it is above the start concentration) (for pH 6.4, pe -4.1 or pH 6.2, pe -4.3) expected for Pu(III) in equilibrium with PuO_2(am,hyd) (using $\Delta_f G$ = -965.5 kJ/mol). A thermodynamic answer to the spectroscopic question of whether Pu(IV) is present in the Mk-40d-III-pH6 is then that if, due to sorption to the FeS surface, the Pu(III) concentration is almost two order of magnitude lower than what is expected as the value in equilibrium with PuO_2(am,hyd), PuO_2 is not precipitated.
The main conclusion from the preceding rather lengthy discussion of spectroscopic data and thermodynamic reflections around sample Mk-40d-III-pH6 is that generally FeS can lower solution concentrations of Pu(III) to below [$Pu(III)_{eq/PuO2}$], the Pu(III) concentration that would be expected in equilibrium with a PuO_2(am,hyd) solid phase. To what extent [Pu(III)aq] decreases in a system containing FeS will depend on the amount or rather surface area of FeS present and on pH, as pH determines the percentage of negatively charged surface sites.

In the following paragraphs the remaining five PuO_2-like Pu-mackinawite sample spectra will be discussed. Figure 3.3.11 provides a zoom of the energy range at the end of and just above the XANES region of the five Pu-mackinawite spectra and Pu(III)aq, Pu(V)aq and PuO_2(cr) for reference. The WL intensity (Fig. 3.3.6) of these spectra will not be discussed in detail as, according to the literature, non-calcinated PuO_2 is not expected to have the same WL intensity as PuO_2(cr).[76, 99] As can be seen in Fig. 3.3.11, these five spectra, the two pinkish ones more than the three bluish ones, do not completely descend to the level of PuO_2(cr) in the energy range from 18080 to 18090 eV and again around 18130 eV. Also, from 18093 to about 18100 eV, the blue spectra are slightly shifted to the right (to higher energy) compared to PuO_2(cr). The question we might now ask is whether these slight differences of the normalized X-ray absorption spectra can tell us something about the composition of these samples, in particular, if an oxidation state other than Pu(IV) is present. As the spectra of both Pu(V)aq and Pu(III)aq are characterized by values higher than PuO_2(cr) in the range where the intensity of the Pu-mackinawite spectra is slightly higher than the one of the PuO_2(cr) spectrum, it might be suggested

that either Pu(III) or Pu(V) are present in at least the pinkish spectra. To try and differentiate between an add-mixture of Pu(III) and Pu(V) to PuO_2, difference spectra between Pu(V)aq and PuO_2(cr), between Pu(III)aq and PuO_2(cr), between artificial mixture spectra (90 % PuO_2(cr) + 10 % Pu(III)aq and 90 % PuO_2(cr) + 10 % Pu(III)aq) and PuO_2(cr), and between the two Pu-mackinawite spectra that are furthest apart from each other (Mk-8m-V-pH7, the spectrum with the WL maximum at the highest energy and which descends almost down to the level of PuO_2(cr) at 18090 and 18130 eV, and Mk-8m-III-pH7) were computed. These difference spectra are shown in the graphs of Fig. 3.3.12.

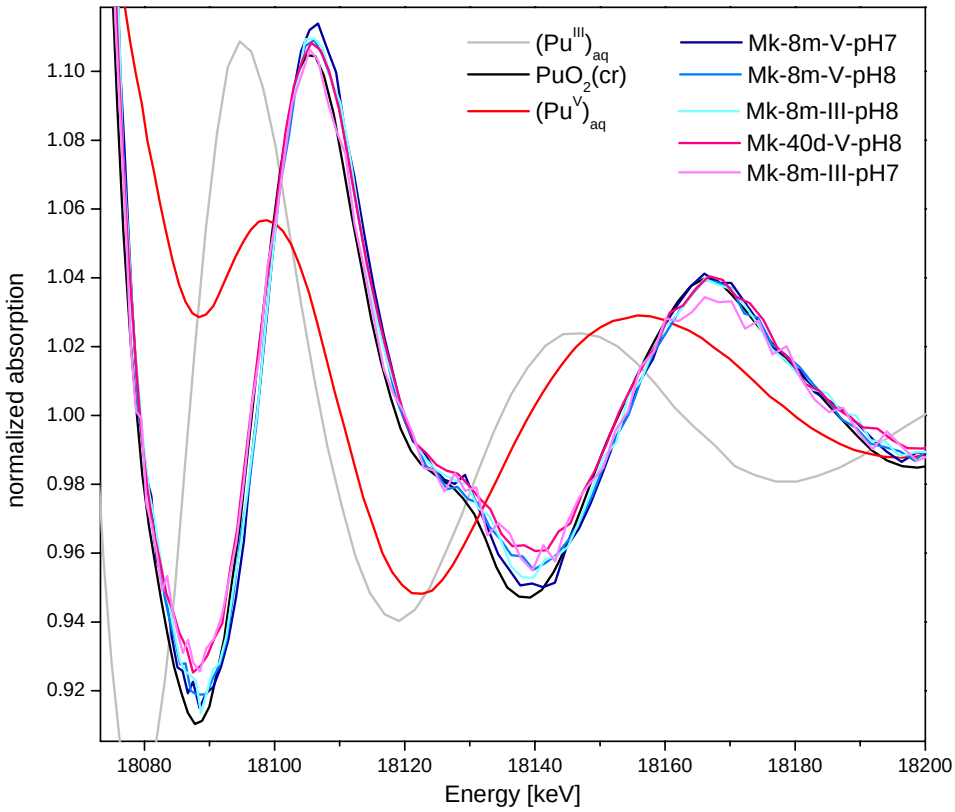

Figure 3.3.11. Zoom on the energy range above the XANES region of PuO_2-like Pu-mackinawite spectra with Pu(III)aq, Pu(V)aq and PuO_2(cr) spectra. Inset: Overview in the energy range 18060 to 18260 eV.

From the difference spectra in Fig. 3.3.12 it becomes clear that the difference between the two considered Pu-mackinawite spectra (Mk-8m-V-pH7 and Mk-8m-III-pH7) in the energy range 18040 to 18080 eV (yellow green and blue in Fig. 3.3.6, not shown in Fig. 3.3.11) and also in the range 18080 to 18100 eV (Fig. 3.3.11) resembles closely that between Pu(III) containing PuO_2(cr) and pure PuO_2(cr) (purple in Fig. 3.3.12) but differs markedly from the difference between Pu(V) containing PuO_2(cr) and pure PuO_2(cr) (rose). This analysis strongly suggests that Pu(III) is present in some of the Pu-mackinawite spectra under consideration and that Pu(V) is absent. As the WL maxima of samples Mk-8m-V-pH7 and Mk-8m-III-pH8 are situated at slightly higher energy than the one of Pu(IV)aq and of PuO_2(cr) (Fig. 3.3.6) and as, in addition, both spectra also slightly deviate from PuO_2(cr) in the direction opposite to what might be caused by the presence of Pu(III) (shift to higher energy at 18093 to 18100 eV, Fig. 3.3.11), a hypothetical Pu(III) content of these samples would have

to be very small. A comparison difference spectra between Mk-8m-V-pH7 and Mk-8m-III-pH8 and PuO_2(cr) with the difference spectra shown in Fig. 3.3.12 also gives no indication for Pu(III) in these samples (they behave quite oppositely to PuO_2(cr) containing either Pu(III) or Pu(V)). Therefore these two samples will hereafter be used to quantitatively assess the Pu(III) content of the two pinkish spectra in Fig. 3.3.11 and of Pu-chukanovite sample in chapter 3.4.

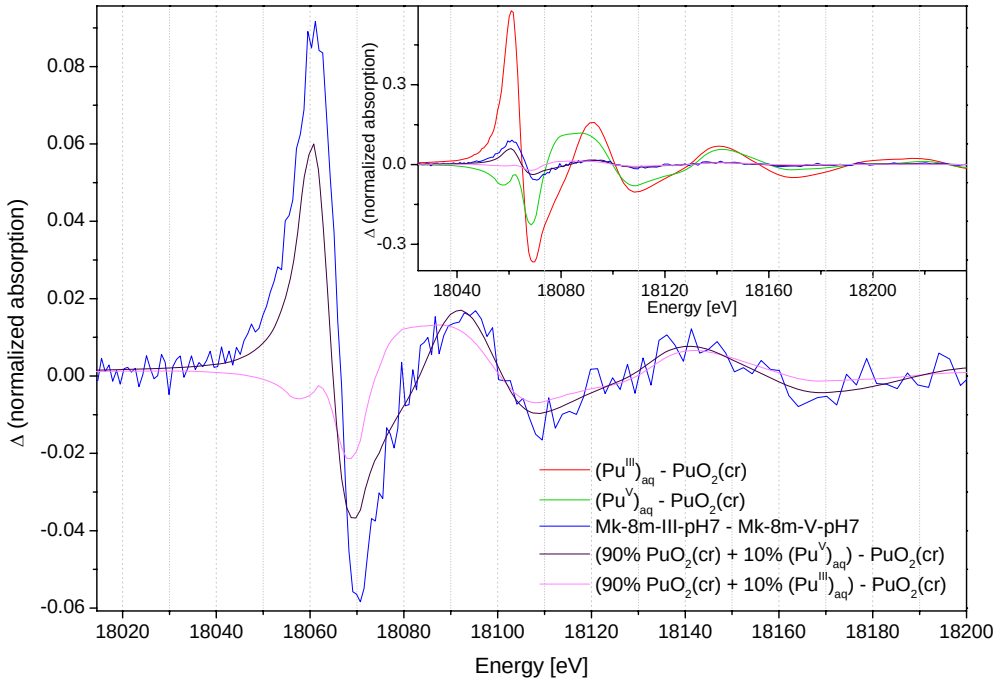

Figure 3.3.12. Difference spectra calculated by subtraction of normalized spectra from each other as indicated in the legend. Inset: Long energy range including difference spectra between pure oxidation states (red and green), main picture: zoom on difference spectra of the two considered Pu-mackinawite samples (blue) and artificial mixture spectra containing 90 % PuO_2(cr) (purple and rose).

The PuO_2 content found by LC fitting of the XANES region is slightly dependent on which of the two non-calcinated PuO_2 representatives (Mk-8m-V-pH7 or Mk-8m-III-pH8) were used in combination with Pu(III)aq and one finds with this approach that both spectra (Mk-40d-V-pH8 and Mk-8m-III-pH7) are very similar in composition (as, of cause, one would guess from the their visual similarity) and contain about 90 % PuO_2 and 10 % Pu(III) (88 – 92 % PuO_2 and 8 – 13 % Pu(III)). As an example, the LC XANES fit for sample Mk-8m-III-pH7 with references Pu(III)aq and Mk-8m-III-pH8 (as PuO_2) is shown in Fig. 3.3.14. LC fitting of the normalized spectrum of Mk-8m-III-pH7 was repeated in the energy range of 18.105 to 18.330 keV, again with the two different PuO_2 representatives used before (Mk-8m-V-pH7 or Mk-8m-III-pH8). The results are very similar to the LC fit in the XANES region and confirm a PuO_2 content of roughly 90 % for Mk-8m-III-pH7 (Table 3.3.6 and Fig. 3.3.16).

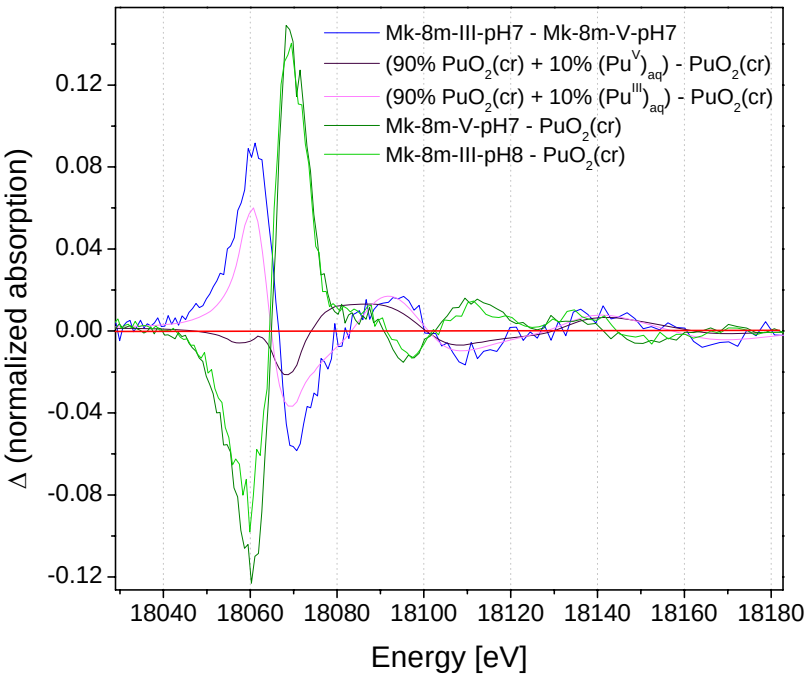

Figure 3.3.13. Comparison of difference spectra resulting from subtraction of PuO_2(cr) from Mk-8m-V-pH7or Mk-8m-III-pH8 with difference spectra from Fig. 3.3.12.

Table 3.3.5. Linear combination fit of sample Mk-40d-V-pH8 and Mk-8m-III-pH7 with Pu(III)aq and non-calcinated PuO_2 (either sample Mk-8m-V-pH7 or Mk-8m-III-pH8) as references in the energy range 18.040 to 18.105 keV. For plot see Fig. 3.3.14.

samples	Pu(III)aq and Mk-8m-III-pH8				Pu(III)aq and Mk-8m-V-pH7			
	Pu(III)	PuO_2	sum [%]	R-factor	Pu(III)	PuO_2	sum [%]	R-factor
Mk-40d-V-pH8	7.9 %	92.3 %	100.2	$1.0 \cdot 10^{-4}$	11.4 %	89.5 %	100.9	$1.4 \cdot 10^{-4}$
Mk-8m-III-pH7	9.3 %	90.9 %	100.2	$5.2 \cdot 10^{-5}$	12.7 %	88.1 %	100.8	$8.2 \cdot 10^{-5}$

Table 3.3.6. Linear combination fit of sample Mk-8m-III-pH7 with Pu(III)aq and non-calcinated PuO_2 (either sample Mk-8m-V-pH7 or Mk-8m-III-pH8) as references in the energy range 18.105 to 18.330 keV. For plot see Fig. 3.3.15.

references	Pu(III)	PuO_2	sum [%]	R-factor
Pu(III)aq and Mk-8m-III-pH8	7.2 %	92.8 %	100.0	$8 \cdot 10^{-6}$
Pu(III)aq and Mk-8m-V-pH7	11.0 %	89.1 %	100.1	$8 \cdot 10^{-6}$

Before reporting shell fitting results of the PuO_2-like Pu-mackinawite spectra, I would like to consider the influence of a Pu(III) or Pu(V) add-mixture to PuO_2(cr) by comparing artificially created mixture spectra with pure PuO_2(cr). Apart from comparing the resulting EXAFS spectra, the influence of such admixtures on shell fitting results will be considered.

In figure 3.3.16, the influence of increasing Pu(III) or Pu(V) contents on PuO_2(cr) spectra is shown. In as far as real mixture spectra would not have the same degree of structural order as PuO_2(cr) and as non-calcinated PuO_2 is characterized by higher WL intensities, these kind of artificially created mixture spectra are not true representatives of spectra acquired from samples containing Pu(IV) as

PuO_2 and either tri- or penta-valent Pu. However, it is instructive to observe the changes induced by the presence of Pu(III) or Pu(V) on the XANES and EXAFS region of X-ray absorption spectra.

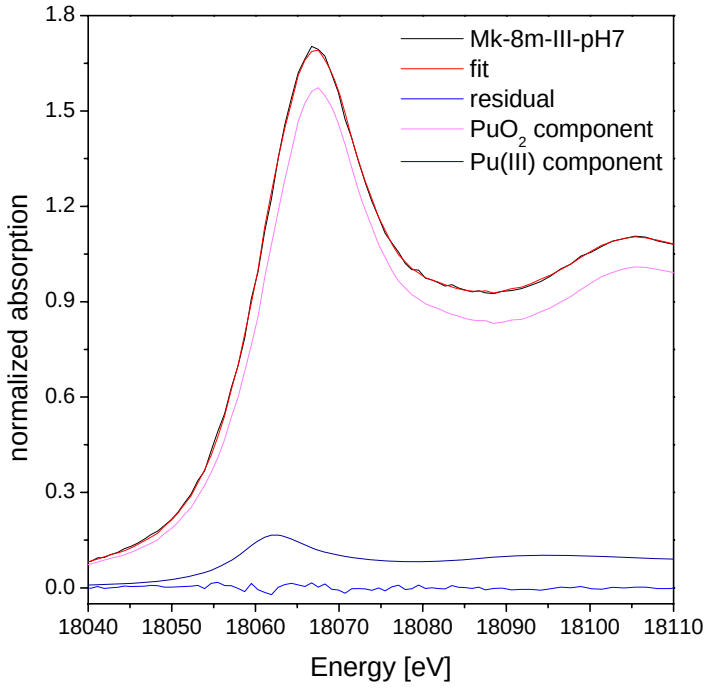

Figure 3.3.14. LC fit of sample Mk-8m-III-pH7 in the range 18040 to 18105 eV using Pu(III)aq and sample Mk-8m-III-pH8 (as representative of non-calcinated PuO_2) as references. For fit results see Table 3.3.5.

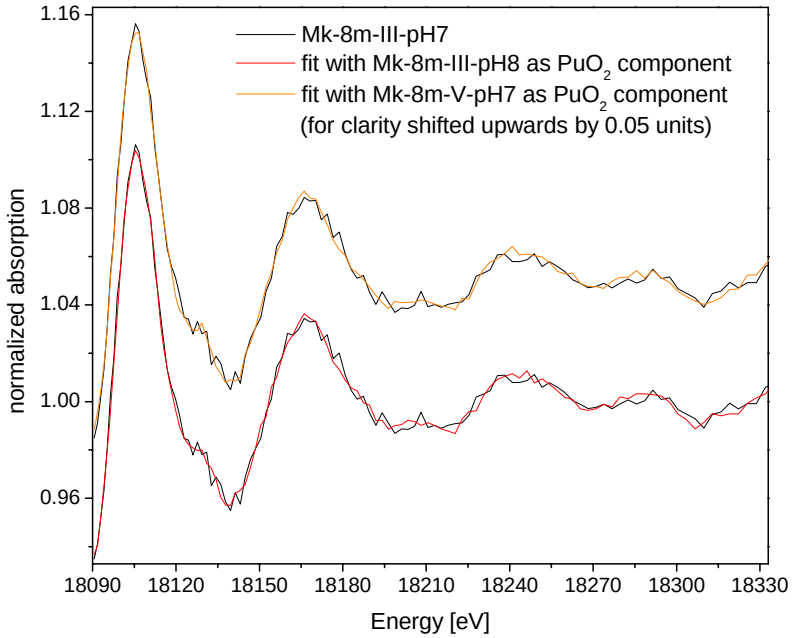

Figure 3.3.15. LC fit of sample Mk-8m-III-pH7 in the range 18105 to 18330 eV using Pu(III)aq and either Mk-8m-III-pH8 or Mk-8m-V-pH7 (as representatives of non-calcinated PuO_2) as references. For fit results see Table 3.3.6

As we see in Fig. 3.3.16 (and as was shown in Fig. S11, chap. 3.2), add-mixtures of Pu(III) to PuO_2(cr) spectra induce considerable changes in the position of the inflection point, the WL maximum and in WL intensity. Also the position and shape of the post-WL minimum and following maximum is strongly affected. The presence of Pu(V) in the spectra has only almost no effect on the position of the inflection point and a far smaller effect on the WL maximum position than Pu(III). Similarly to Pu(III), considerable changes on WL intensity and shape of the post-WL maximum result from Pu(V) add-mixtures. If a suitable PuO_2 reference exists, it is thus possible to detect even small add-mixtures of Pu(III) or Pu(V). To be suitable as a reference, a PuO_2 phase is ideally required to be free of other oxidation states and to have a similar particle size and degree of structural disorder (as these influence the WL intensity) as the samples under investigation. As we cannot know to what extent the PuO_2 samples, used as references for the LC fits whose results are reported in Tables 3.3.5 and 3.3.6, fulfill these requirements, the found Pu(III) contents are subject to some uncertainty. If the intensity of the post-WL maximum is taken as a point of reference for a "oxidation state purity estimation" (Fig. 3.3.11) (not considering any other spectral features), one could assume that the PuO_2 containing Pu-mackinawite samples used as PuO_2 references (e.g. Mk-8m-V-pH7) contain at maximum 10 % Pu(III) (for Mk-8m-V-pH7 the intensity is 0.92, for a mixed sample containing 90 % PuO_2(cr) and 10 % Pu(III)aq it is also 0.92 and for PuO2(cr) it is 0.91). If the standard itself contains some Pu(III), the Pu(III) content of the sample whose Pu(III) content one might try to assess by LC fitting is underestimated. If c = x*a + y*b (with c= composition of sample under investigation, a = $PuO_{2reference}$ and b = Pu(III)) and if a = t*b + u*PuO_{2pure}, it follows that c= x*(t*b + u*PuO_{2pure}) + y*b = (x*t+y)*b + x*u*PuO_{2pure}. For a sample for which x was found equal to 0.9 (the sample consists to 90 % of $PuO_{2reference}$) and y = 0.1 (10 % Pu(III)) and assuming that t = 0.1 (Pu(III) content of $PuO_{2reference}$ itself) and thus u= 0.9 (PuO2 content of $PuO_{2reference}$) a real Pu(III) content of the sample of 19 % instead of the 10 % found with $PuO_{2reference}$ would result.
The LC fit results from Tables 3.3.5 and 3.3.6 are thus subject to an uncertainty of about ± 10 %.

EXAFS spectra of some of the mixtures from Fig. 3.3.16 are shown in Fig. 3.3.17. The presence of Pu(III) or Pu(V) in PuO_2 spectra results in a reduction of the amplitude of most of the maxima and minima while their position is hardly affected. For example, the amplitude reduction effect of Pu(III) on the maxima and minima at k = 4.5, 5.3 and 10.3 $Å^{-1}$ is somewhat stronger than the one caused by Pu(V) but otherwise similar. Only a few spectra features are affected differently by the presence of Pu(III) or Pu(V) and are circled in grey in Fig. 3.3.17. Pu(III) decreases the amplitude of the minima at 6.1, 6.5 and 9 $^{-1}$ while Pu(V) leaves the intensity of the 6.1 and 9 $Å^{-1}$ minima quasi unaffected. Inversely, Pu(III) does not affect the amplitude of the minimum at 7.5 Å-1 while Pu(V) has a decreasing effect. Compared to the influence of Pu(III) or Pu(V) on the shape and position of the XANES, the spectral changes induced in the EXAFS are minor. In addition, most spectral changes due

to the presence of Pu(III) or Pu(V) in the EXAFS are similar while their influences on the XANES differ markedly.

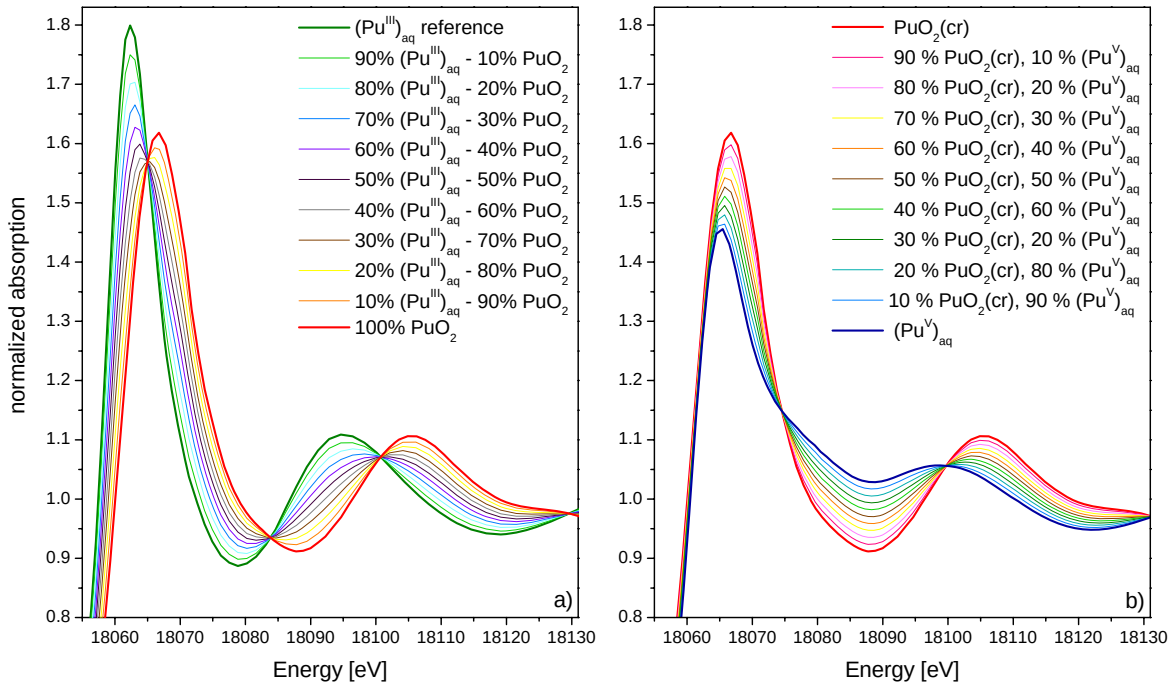

Figure 3.3.16. XANES spectra of artificially created PuO_2(cr)-Pu(III) (a) and PuO_2(cr)-Pu(V) mixtures.

How Pu(III) or Pu(V) induced changes of the EXAFS translate into changes of the Fourier transformed spectra and back-transforms of the first peaks is shown in figures 3.3.18 and 3.3.19. As shown in Fig. 3.3.18, spectra containing 10 % of Pu(III) or 10 % of Pu(V) can hardly be distinguished, irrespective of whether we look at the EXAFS spectra, the FT or the BT of the oxygen shell.

When considering shell fitting results, as I will do in the next paragraphs, it should be remembered that, as for the XANES, these artificial mixture spectra are non-ideal representations of samples containing PuO_2 and another oxidation states. Apart from the fact that Pu(V) might be part of the structure, or at least surface layer, of PuO_2,[101, 102] Pu(III) might be sorbed to a PuO_2 surface or a mineral surface and its spectrum might thus slightly or even strongly differ from aqueous Pu(III). In addition, the Pu(V)aq and Pu(III)aq spectra used here for the creation of mixture files were measured at RT while PuO_2 was measured at 15 K, which means that they display a higher thermal disorder. I estimate that most of the effects found during shell fitting would also occur when Pu(III) and Pu(V) measured at 15 K were used, but to a somewhat greater or smaller extent. For example, a DW might be increased due to the presence of Pu(III). If the thermal disorder of the added Pu(III) was smaller, the DW might be less influenced by this addition. Apart from reducing the overall amplitude of a PuO_2-mixture spectrum, the disorder imported by a Pu(III) or Pu(V) spectrum might itself influence fitted DW. The extent of these thermal disorder related effects is difficult to estimate. As the approach of considering artificial oxidation state mixture spectra is somewhat tentative and non-ideal in many

ways, I will report the results of this approach as I found them, knowing, and herewith clearly announcing to the reader, that they are not to fully transposable to real spectra.

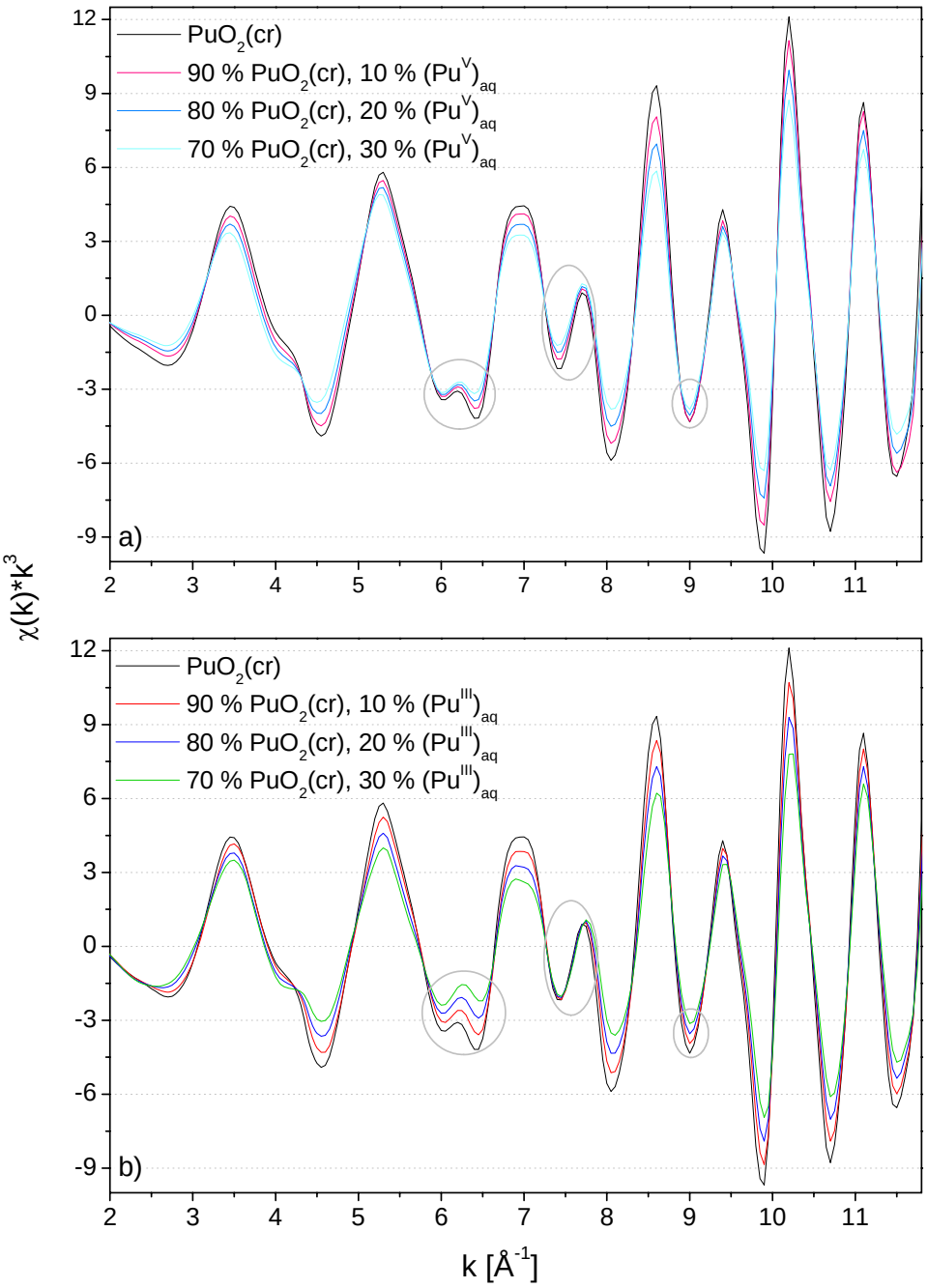

Figure 3.3.17. k^3-weighted EXAFS spectra of a) PuO_2(cr) + Pu(V)aq and of b) PuO_2(cr) + Pu(III)aq mixtures. Spectral features differently affected by the presence of Pu(III) or Pu(V) are circled in grey.

Keeping in mind the afore mentioned "mise en garde", one finds that in a shell fit with adjustable CN, the mixture spectra with 10 % Pu(III) and 10 % Pu(V) yield very similar results. In both cases, the DW of the oxygen shell is slightly increased (by 0.0004 $Å^2$ for Pu(III) and by 0.001 $Å^2$ for Pu(V)) and the CN for Pu-Pu at 3.83 Å is slightly reduced (by 13 % for Pu(III) by 5 % for 10 % Pu(V)). That addition of Pu(V) leads to a greater increase of the DW of the oxygen coordination shell than addition of

Pu(III) is understandable in view of the two Pu-O distances in Pu(V)aq (Pu-O_{ax} at 1.8 Å and Pu-O_{eq} at 2.48 Å) and one Pu-O distance (at least in the EXAFS fit) for Pu(III)aq (Pu-O at 2.49 Å). Interestingly (and strangely), these 10 % contents of Pu(III) and Pu(V) result in a reduction of the DW fitted for the Pu-O shell at 4.43 Å. In addition, 10 % Pu(III) result in a smaller CN for Pu-O at 2.33 Å while 10 % Pu(V) do not. Would sample spectra yield fit results similar to the ones shown in Table 3.3.7 for PuO_2 + Pu(III) and PuO_2 + Pu(V) spectra, it would, at least taking into account the uncertainty of fitted EXAFS parameters (up to 25 % for CN and 0.02 Å for distances[100]), not be possible to decide whether the differences in comparison to PuO_2(cr) result from higher structural disorder in the samples or from the presence of another oxidation state. Much less would it be possible to decide whether the other oxidation state possible present in a sample was Pu(III) or Pu(V).

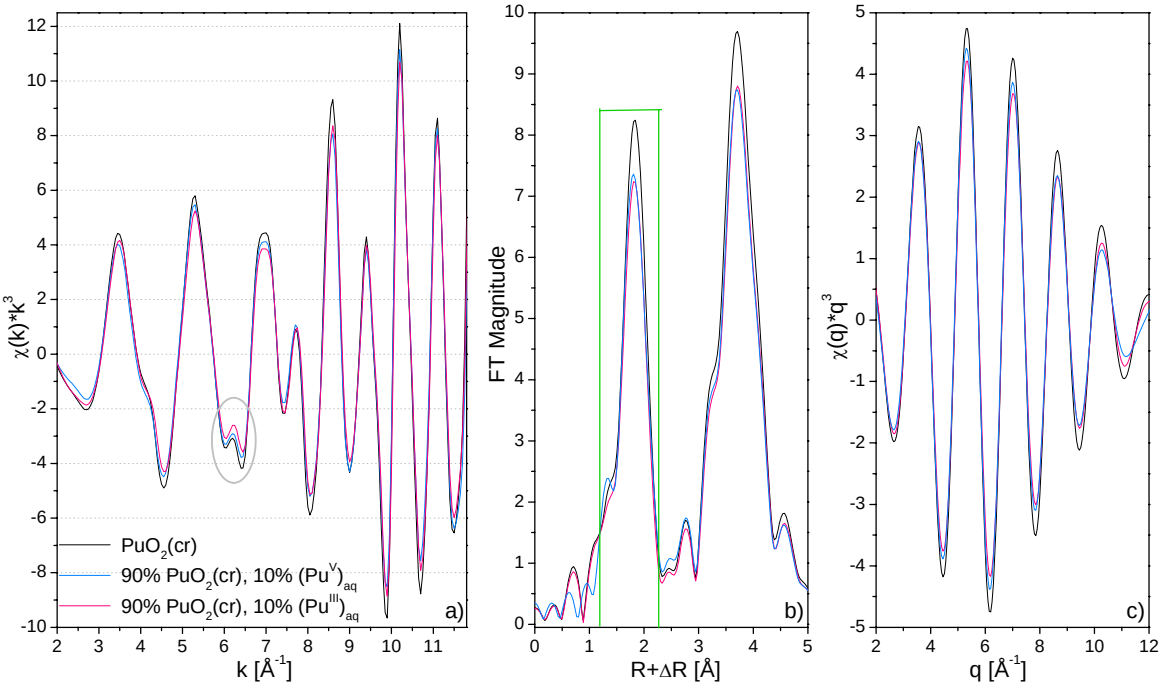

Figure 3.3.18. Comparison of PuO_2 spectra consisting of 90 % PuO_2(cr) and either 10 % Pu(III) or 10 % Pu(V). a) k^3 – weighted EXAFS spectrum; b) FT (based on $2 \leq k \leq 11.8$ Å^{-1}, hanning window, dk1) with window for BT shown in c) marked in green; c) Back-transform of the first oxygen shell ($1.3 \leq R+\Delta R \leq 2.35$). The split minimum at 6.3 Å^{-1} is circled in grey as it is affected differently by the presence of Pu(III) and Pu(V).

EXAFS spectra, FT and BT of the oxygen coordination shell of samples containing 80 % PuO_2(cr) and 20 % of either Pu(III) or Pu(V) are shown in Fig. 3.3.19. At k values above 8 Å^{-1} the impact of Pu(III) and Pu(V) on the spectra is very similar while a stronger amplitude reduction effect of Pu(III) on the maxima and the minimum at k = 5.3, 6.3 and 7 Å^{-1} is apparent. In the FT and BT of the oxygen coordination shell, Pu(III) also results in a stronger amplitude reduction than Pu(V).

For the spectrum containing 20 % Pu(III), the fitted CN for Pu-O at 2.33 Å and for Pu-Pu at 3.82 Å are considerably lower than for PuO_2(cr) (20 % smaller for Pu-O and 31 % for Pu-Pu). Similarly to the fit of the spectrum containing 10 % Pu(III) the DW of Pu-O at 2.33 Å is not much augmented compared to PuO_2(cr) while the DW of Pu-O at 4.43 Å is considerably reduced. In the case of a 20 % Pu(III)

content, the fit does not converge if the DW of Pu-O at 4.43 Å is not set to be equal to DW of the Pu-O path at 2.33 Å. Presence of 20 % Pu(V) also reduced the CN for Pu-Pu (by 17 %) but does not reduce CN of Pu-O at 2.33 Å. Again it can be noted that Pu(V) increases the DW of the Pu-O shell at 2.33 Å more than Pu(III) (0.0082 $Å^2$ vs 0.0064 $Å^2$).

Table 3.3.7. Shell fit comparison between PuO_2(cr), 90 % PuO_2 + 10 % Pu(III), and 90 % PuO_2 + 10 % Pu(V). Mixture spectra were created from normalized files according to: $y = 0.9 \cdot PuO_2(cr) + 0.1 \cdot (Pu^{III})_{aq}$ or $y = 0.9 \cdot PuO_2(cr) + 0.1 \cdot (Pu^{V})_{aq}$.

paths and parameters	PuO_2(cr)			90 % PuO_2+10 % Pu(III)			90 % PuO_2+10 % Pu(V)			PuO_2 structure	
	CN	R [Å]	σ^2 [$Å^2$]	CN	R [Å]	σ^2 [$Å^2$]	CN	R [Å]	σ^2 [$Å^2$]	CN	R [Å]
Pu - O	8.2	2.33	0.0056	7.4	2.33	0.0060	8.2	2.33	0.0066	8	2.34
Pu - Pu	10.9	3.83	0.0026	9.5	3.82	0.0025	10.3	3.82	0.0028	12	3.82
Pu - O	35	4.42	0.0118	22	4.43	0.0075	27	4.42	0.009	24	4.48
Pu-O MS	8.2[c]	4.66[c]	0.0056[c]	7.4[c]	4.66[c]	0.0060[c]	8.2[c]	4.66[c]	0.0066[c]	8	4.68
R range [Å]	1.39 – 4.42			1.37 – 4.45			1.37 – 4.42				
k range [$Å^{-1}$]	3.0 – 11.8			3.0 – 11.8			3.0 – 11.8				
Residual [%]	5.1			5.6			5.7				
E_0-shift [eV]	7.5			7.2			7.0				

c: correlated to SS path

[a]fit carried out in R, FT of $\chi(k)*k^3$ with Bessel window function (window parameter: 3), fit mode k^3+k^2, S_0^2=0.95

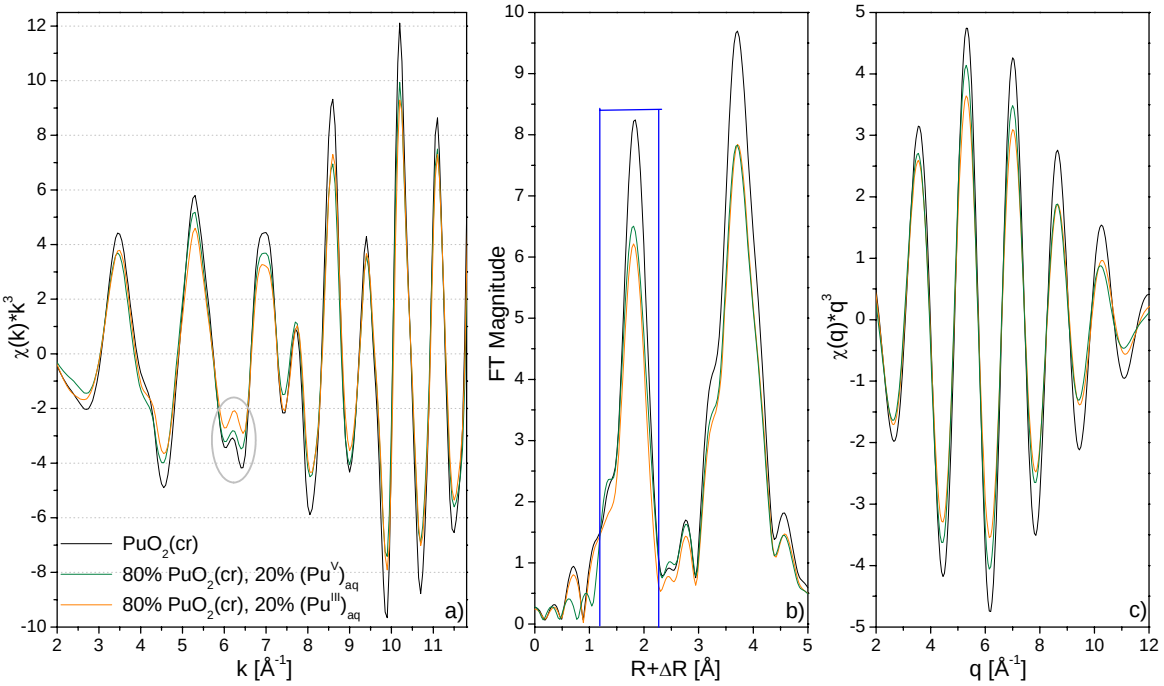

Figure 3.3.19. Comparison of PuO_2 spectra consisting of 80 % PuO_2(cr) and either 20 % Pu(III) or 20 % Pu(V). a) k^3 – weighted EXAFS spectrum; b) FT (based on $2 \leq k \leq 11.8 Å^{-1}$, hanning window, dk1) with window for BT shown in c) marked in green; c) Back-transform of the first oxygen shell ($1.3 \leq R+\Delta R \leq 2.35$). The split minimum at 6.3 $Å^{-1}$ is circled in grey as it is affected differently by the presence of Pu(III) and Pu(V).

Table 3.3.8. Shell fit comparison between PuO_2(cr), 80 % PuO_2 + 20 % Pu(III), and 80 % PuO_2 + 20 % Pu(V). Mixture spectra were created from normalized files according to: $y = 0.8 \cdot PuO_2(cr) + 0.2 \cdot (Pu^{III})_{aq}$ or $y = 0.8 \cdot PuO_2(cr) + 0.2 \cdot (Pu^{V})_{aq}$.

paths and parameters	PuO_2(cr)			80 % PuO_2+20 % Pu(III)			80 % PuO_2+20 % Pu(V)			PuO_2 structure	
	CN	R [Å]	σ^2 [Å^2]	CN	R [Å]	σ^2 [Å^2]	CN	R [Å]	σ^2 [Å^2]	CN	R [Å]
Pu - O	8.2	2.33	0.0056	6.6	2.33	0.0064[d]	8.6	2.33	0.0082	8	2.34
Pu - Pu	10.9	3.83	0.0026	7.5	3.82	0.0021	9.0	3.82	0.0029	12	3.82
Pu - O	35	4.42	0.0118	16	4.43	0.0064[d]	20	4.43	0.0064	24	4.48
Pu - O MS	8.2[c]	4.66[c]	0.0056[c]	6.6[c]	4.66[c]	0.0064[c]	8.6[c]	4.66[c]	0.0082[c]	8	4.68
R range [Å]	1.39 – 4.42			1.39 – 4.45			1.31 – 4.43				
k range [Å^{-1}]	3.0 – 11.8			3.0 – 11.8			3.0 – 11.7				
Residual [%]	5.1			5.5			6.8				
E_0-shift [eV]	7.5			6.5			6.0				

c: correlated to SS path, d: correlated

[a]fit carried out in R, FT of $\chi(k)*k^3$ with Bessel window function (window parameter: 3), fit mode k^3+k^2, S_0^2=0.95

Thus, both add-mixtures of Pu(III) and Pu(V) to PuO_2(cr) result in smaller CN for Pu-Pu at 3.83 Å and in a reduced value for the DW of Pu-O at 4.43 but, at least up to a relative content of 20 %, only Pu(III) also reduces the CN for Pu-O at 2.33 while Pu(V) leads to a greater increase in the DW for this paths than Pu(III) does. If it cannot be recognized from the XANES that another oxidation state than Pu(IV) is present in a spectrum dominated by PuO_2 (which is to say, a spectrum that visually strongly resembles PuO_2(cr) and will be recognized as such before even a shell fit is undertaken), the reduced CN for Pu-Pu at 3.83 might mislead into thinking that the recorded spectrum is that of nano-particulate PuO_2-solid phase. In the absence of a spectrum of pure PuO_2 nanoparticles (PuO_2(coll, hyd)) to compare with, it is not possible to know if features exist that differentiate a particle size induced decrease of the CN for Pu-Pu at 3.83 from an oxidation state mixture induced decrease.

If the presence of another oxidation state in a PuO_2 spectrum is not expected, the approach of fitting with CN fixed to the crystallographic values of PuO_2(cr) can be taken to estimate the increased structural disorder. As in this case differences to PuO_2(cr) cannot be attributed to differing CN they will be fitted as due to structural disorder and thus both Pu(III) and Pu(V) lead to higher DW factors for Pu-O at 2.33 Å and for Pu-Pu at 3.83 Å (Table 3.3.9). A graphic representation of the structural disorder as a function of the Pu-O distance is given in Fig. 3.3.20, where σ (the square root of the tabulated σ^2 value) is plotted as a function of r for values obtained by fitting with adjustable (a) or fixed (b) CN.

Table 3.3.9. Shell fit comparison between PuO_2(cr), 80 % PuO_2 + 20 % Pu(III), and 80 % PuO_2 + 20 % Pu(V); coordination numbers are fixed to the crystallographic values of PuO_2(cr). Mixture spectra were created from normalized files according to:
$y = 0.8 \cdot PuO_2(cr) + 0.2 \cdot (Pu^{III})_{aq}$ or $y = 0.8 \cdot PuO_2(cr) + 0.2 \cdot (Pu^{V})_{aq}$.

paths and parameters	PuO_2(cr)			80 % PuO_2+20 % Pu(III)			80 % PuO_2+20 % Pu(V)			PuO_2 structure	
	CN	R [Å]	σ^2 [Å^2]	CN	R [Å]	σ^2 [Å^2]	CN	R [Å]	σ^2 [Å^2]	CN	R [Å]
Pu - O	8	2.33	0.0054	8	2.33	0.0086	8	2.33	0.0074	8	2.34
Pu-Pu	12	3.83	0.0031	12	3.82	0.0045	12	3.82	0.0043	12	3.82
Pu-O	24	4.43	0.0058	24	4.43	0.0050	24	4.43	0.0055	24	4.48
Pu-O-Pu-O	8	4.66[c]	0.0054[c]	8	4.66[c]	0.0086[c]	8	4.66[c]	0.0074[c]	8	4.68
R range [Å]	1.39 – 4.41			1.37 – 4.44			1.34 – 4.44				
k range [Å^{-1}]	3.0 – 11.8			3.0 – 11.8			3.0 – 11.8				
Residual [%]	6.1			5.6			7.2				
E_0-shift [eV]	7.1			6.3			6.2				

c: correlated to SS path,
[a]fit carried out in R, FT of $\chi(k)*k^3$ with Bessel window function (window parameter: 3), fit mode k^3+k^2, S_0^2=0.95

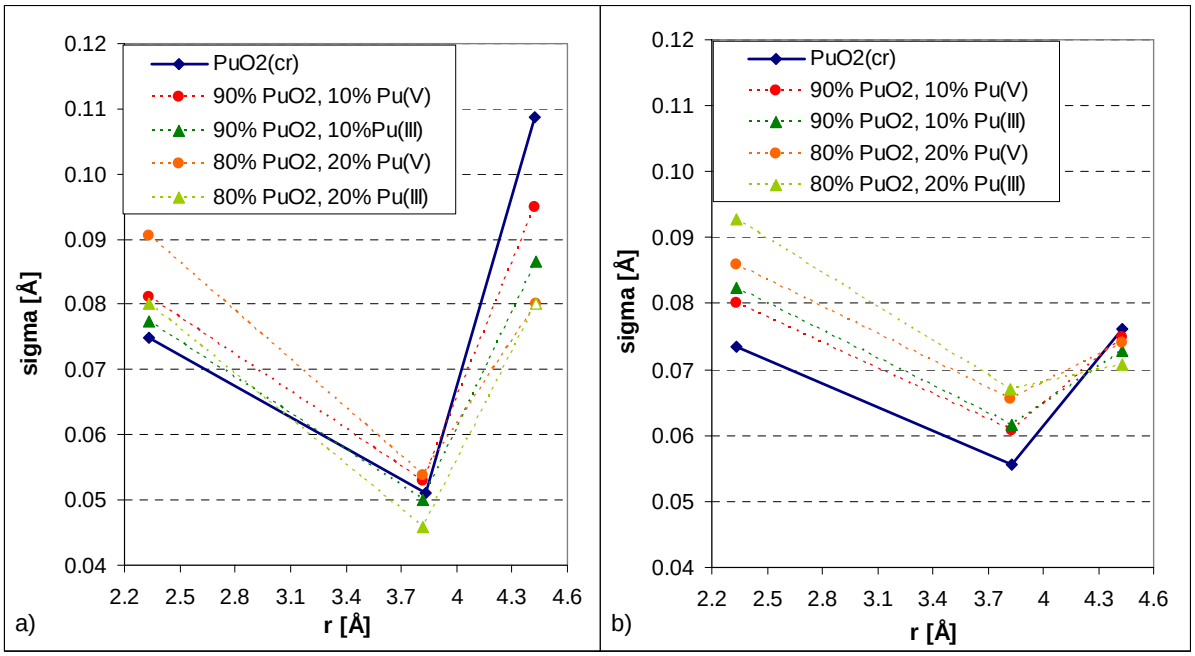

Figure 3.3.20. The structural disorder of Pu-O shells as indicated by σ (σ = sqrt(σ^2)) as a function of distance. a) σ as obtained by fitting with adjustable CN; b) σ as obtained by fitting with CN fixed to the crystallographic values of PuO_2. The corresponding σ^2 values are tabulated in Tables 3.3.7, 3.3.8 and 3.3.9 (apart from values for a fit with fixed CN for spectra with 10 % Pu(III) or Pu(V) which are not reported in tabulated form). Lines between data points are drawn only as a guide to the eye and to facilitate pattern recognition.

The k^3-weighted EXAFS spectra of all six Pu-mackinawite samples are shown in figure 3.3.21. Only spectra of samples Mk-8m-V-pH8 and Mk-8m-III-pH8 were measured up to k = 20 $Å^{-1}$ while spectra of Mk-8m-V-pH7 and Mk-8m-III-pH7 had been acquired up to k = 16 $Å^{-1}$. As fitting of the Mk-40d-V-pH8 spectrum has been discussed in extension in chapter 3.2 and as it was measured only up to k = 13 $Å^{-1}$, it will not be included into the following discussion.

At first glance, a strong resemblance of all six spectra to the PuO_2(cr) spectrum is apparent. However, some spectra and, in particular the one from Mk-8m-III-pH7, appear quite noisy. The noise level of the χ(k) spectra was characterized by calculating the root mean square (r.m.s) noise amplitude in k-space, ε_k. This value is accessible through Parseval's theorem according to which ε_k can be calculated from the r.m.s. amplitude of the "R-space transform in a region devoid of structural features" that, "if the statistical noise is truly white", can be approximated by a single number, ε_R.[103]

$$\varepsilon_k = \varepsilon_R \sqrt{\frac{\pi(2\omega+1)}{\delta k\left(k_{\max}^{2\omega+1} - k_{\min}^{2\omega+1}\right)}} \qquad (3.3.1)$$

ε_R – r.m.s. noise amplitude in the k-weighted R-space spectrum
ε_k – r.m.s. noise amplitude in the unweighted k-space spectrum
ω – k-weight of the Fourier transformed spectrum,
k_{min}, k_{max} – minimum and maximum k-values of the k-range over which the FT is carried out
δk – spacing of data points in k-space

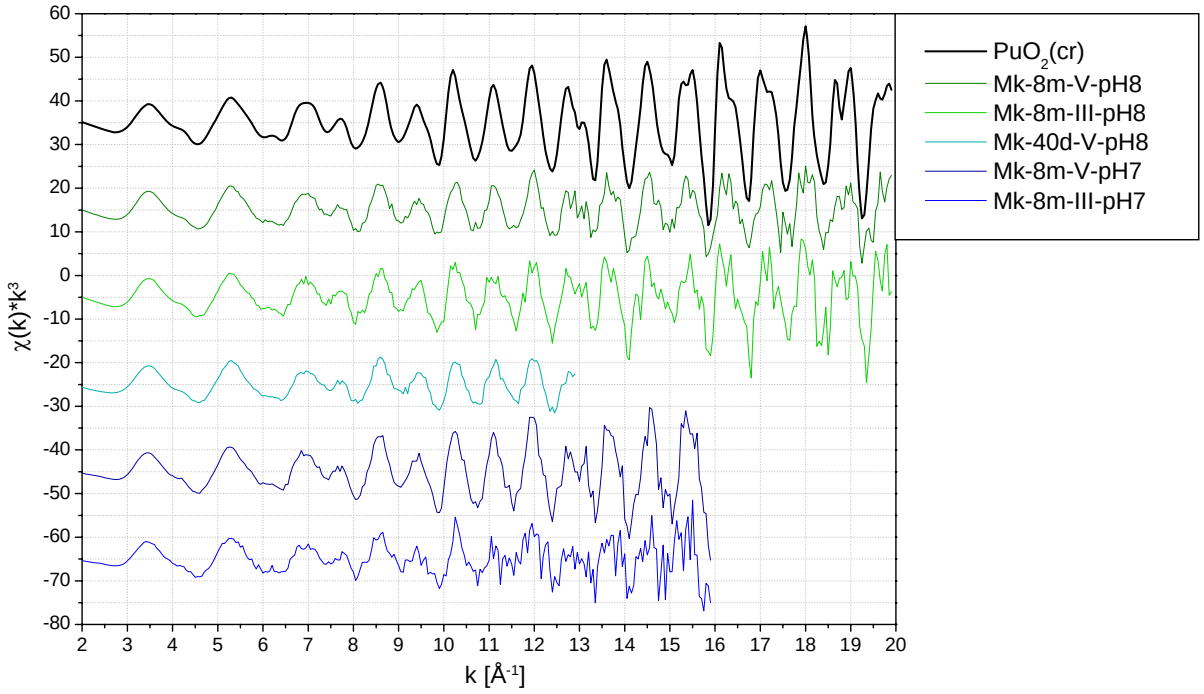

Figure 3.3.21. k^3-weighted EXAFS spectra of Pu-mackinawite samples and PuO_2(cr) for reference.

For the calculation of ε_R, a FT of k^3-weighted spectra (thus ω = 3) based on a k-range of 3.0 ≤ k ≤ 15.15 $Å^{-1}$ was carried out (hannig window, dk = 0) and ε_R was calculated according to:

ε_R = sqrt(Σ_i (y_i^2)/N) with y = FT amplitude of the i-th point, N = total number of data points in the R-range used. The R-space used for the calculation of ε_R was 15 Å ≤ R ≤ 30 Å. Data spacing in k-space (δk) was 0.05 $Å^{-1}$.

In this way, the ε_k values reported in Table 3.3.10 were obtained. As could be expected, the samples measured in fluorescence mode display a higher noise level than the spectrum from PuO_2(cr) that was measured in transmission mode. This difference in noise level between Pu-mackinawite samples and reference (PuO_2(cr)) is represented graphically in Fig. 3.3.24, where the FT is shown up to R + ΔR 25 Å. Some of the variation between the sample spectra noise levels can be explained as being due to higher Pu mass loadings for some minerals compared to others. Another important factor in determining the noise level of the final averaged spectrum is the number of scans acquired per spectrum. It would have been possible to exclude the influence of this factor by considering the noise level of averaged files based on the same number of spectra. This was, however, not done for two reasons, these being the time it takes to reaverage a large number of spectra and that it will often happen that unequal numbers of scans are acquired for samples from one set that will afterwards be compared with each other. The number of scans factor is however not further discussed.

Table 3.3.10. R.m.s. noise amplitude in k-space, ε_k, calculated for a k-range of 3.0 - 15.15 $Å^{-1}$ based on an R-space of 15 - 30 Å using Parseval's theorem. Also reported is the nb of scans per spectrum in fluorescence (Fl) or transmission (T) mode.

sample	εk*1000	nb of scans
$PuO_{2(}$cr)	0.21	1, T
Mk-8m-V-pH8	0.60	9, Fl
Mk-8m-III-pH8	0.67	7, Fl
Mk-8m-V-pH7	0.90	6, Fl
Mk-8m-III-pH7	1.46	6, Fl
Chuk-8m-V	0.47	9, Fl
Chuk-8m-III	0.48	9, Fl

In figure 3.3.22 the edge jump[vi] is plotted as a function of the Pu mass loading (a) and the noise level ($\varepsilon_k \cdot 1000$) as a function of the edge jump (b).

It appears that the edge jump for sample Mk-8m-III-pH7 (blue diamond with an edge jump of similar intensity as the red triangles, Fig. 3.3.22 a) is only about half of what would be expected from the Pu mass loading, suggesting that during either measurement or sample holder filling something for this sample went less well than for the others. In figure 3.3.22 b) the noise level of the six samples from Table 3.3.10 that all contain PuO_2 and that all were measured at least up to k = 16$Å^{-1}$ (thus not including the hematite, maghemite and magnetite samples from a) is compared to the edge jump. It appears that a strong inverse correlation exist between the edge jump, and thus mass loading, and the

[vi]The "edge jump" is the increase in absorption at the edge and is calculated as the difference between the pre-edge and post-edge background functions at the edge, at or close to E0 which in these spectra was set to the inflection point. After normalization, the edge jump is 1. The height of the edge jump depends on the intensity of the fluorescence signal. The higher the Pu loading in a sample, the more intensive will the fluorescence signal be.

noise level up to an edge jump of about 0.5 (corresponding to a mass loading of about 3000 ppm) above which the noise level does not decrease further. This kind of dependence of noise level over edge jump and edge jump over mass loading is interesting to keep in mind for the preparation of Pu and other actinide XAS samples as the experimental conditions are always a trade off between an attempt to produce samples as similar to what can be expected to occur under natural conditions (e.g. samples with a low Pu-mineral loading resulting from Pu contamination in streams and sediments) and the necessity to obtain "measurable samples" with not too low a signal-to-noise ratio. If the noise level does not decrease further beyond a certain mass loading exceeding this value means to loose "naturality" for no gain in signal-to-noise ratio.

Based on a shorter k-range, all 22 Pu samples could be included into this kind of comparison and it might be interesting to include them in the future and see if the trend shown in Fig. 3.3.22 (and in particular in 3.3.22 b) is confirmed.

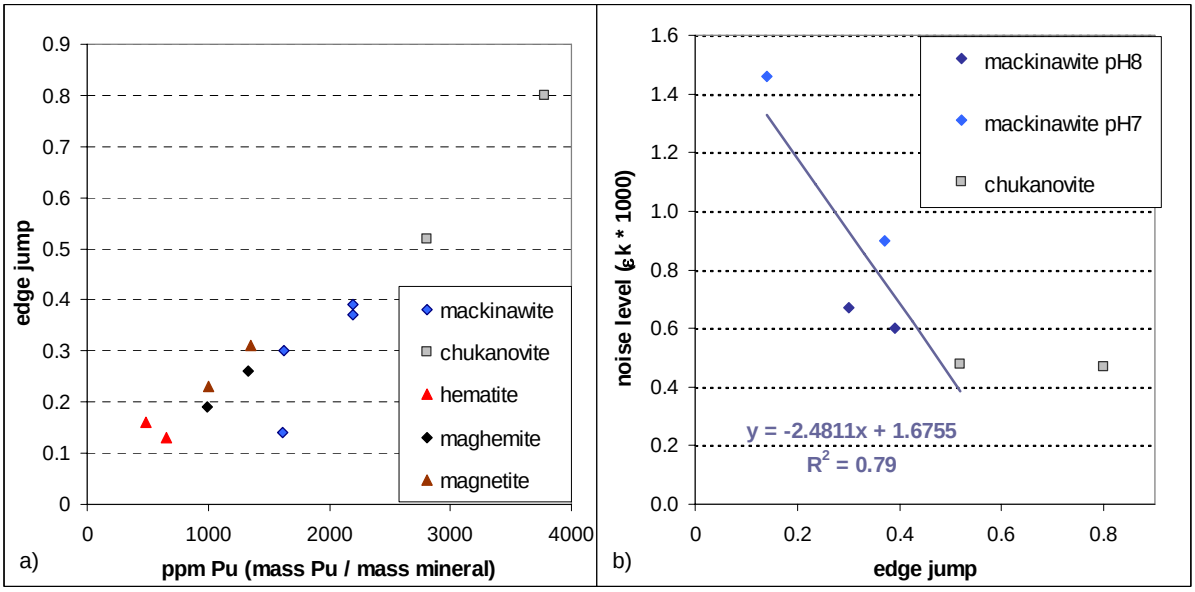

Figure 3.3.22. Edge jump of XAS spectra as a function of Pu mass loadings (a) and noise level of the unweighted k-spectra as a function of edge jump (b).

Fourier Transforms of the mackinawite spectra from Fig. 3.3.21 are shown in figures 3.3.23 and 3.3.24; the first is based on a shorter k-range (3 – 12.6 $Å^{-1}$) and includes all PuO_2-like Pu-mackinawite spectra, the second includes only the eight month samples and uses a longer k-range (3 – 15.2 $Å^{-1}$).

In both EXAFS and FT (Fig. 3.3.21, 23, 24), Mk-8-V-pH7 is the sample that most strongly resembles PuO_2(cr) in amplitude (EXAFS) and peak (FT) intensity. Whether the FT is based on a shorter or longer k-range, the other three 8-months samples have very similar peak intensities with regard to the Pu-O coordination shell (at R + ΔR = 1.9 Å) while for the Pu-Pu peak at R + ΔR = 3.7 Å a decrease in intensity is observed according to Mk-8m-III-pH8 > Mk-8m-V-pH8 > Mk-8m-III-pH7.

Shell fits in R-space (R + ΔR = 1.3 – 4.2 Å) were carried out for all four Pu-mackinawite 8 months samples and PuO_2(cr) with fixed and adjustable CN based on a k-range of 3.0 to 15.2 $Å^{-1}$ (Tables A3.23–26). Based on the same k-range, a longer R-range (R + ΔR = 1.3–6.9 Å) was fitted for PuO_2(cr) and samples Mk-8m-V-pH7 and Mk-8m-V-pH8 (Tables A3.27–28). For one of the samples measured

up to k = 20 Å^{-1} (Mk-8m-V-pH8), fits based on a k-range of 3.0 to 19.2 Å^{-1} were carried out for both R-ranges used above and with fixed or adjustable CN (Tables A3.29–32).

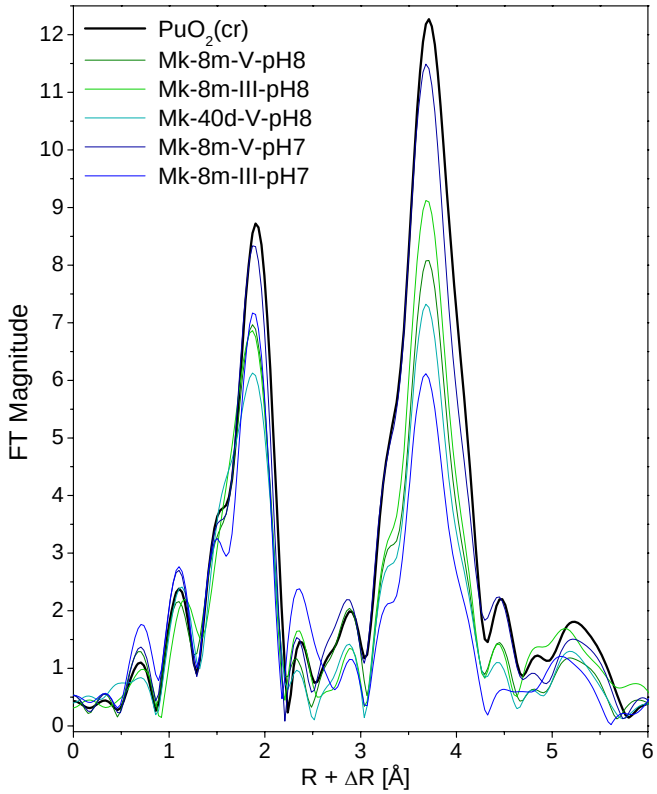

Figure 3.3.23. FT of Pu-mackinawite samples from Fig. 3.3.21.
FT parameters: 3 ≤ k ≤ 12.6, hannig window, dk1.

Before looking at these shell fit results, it might be useful to reformulate the questions we want to answer by carrying out shell fits on these PuO_2-like spectra. We see visually that all spectra resemble the PuO_2(cr) reference spectrum and we know from the XANES, that one sample (Mk-8m-III-pH7) might contain some 10 % Pu(III), while in the others only traces of it can be expected. However, as we saw above, tracking the presence of Pu(III) in the shell fitting is not straightforward (Fig. 3.3.20) and in spectra with potentially different degrees of structural disorder it will be even more complicated to find reliable indications for its presence.

What we may still try to obtain from the shell fit is then: firstly, a confirmation that the Pu–O and Pu–Pu distances in the samples are similar to the ones of PuO_2(cr) and secondly, the shell fit will yield Pu–O and Pu–Pu coordination numbers that may be similar to, or different from, PuO_2(cr). If they are different, the question will be whether the difference is due to the presence of Pu(III) in the sample or to particle size effects and/or structural disorder.

Methodically, it might be interesting to see if fitting based on a longer k-range yields substantially different coordination numbers or DW for the main scattering paths. If not, measuring spectra up to k = 20 Å might not be necessary as it would not yield additional information compared to a fit up to e.g. k = 16 Å^{-1}.

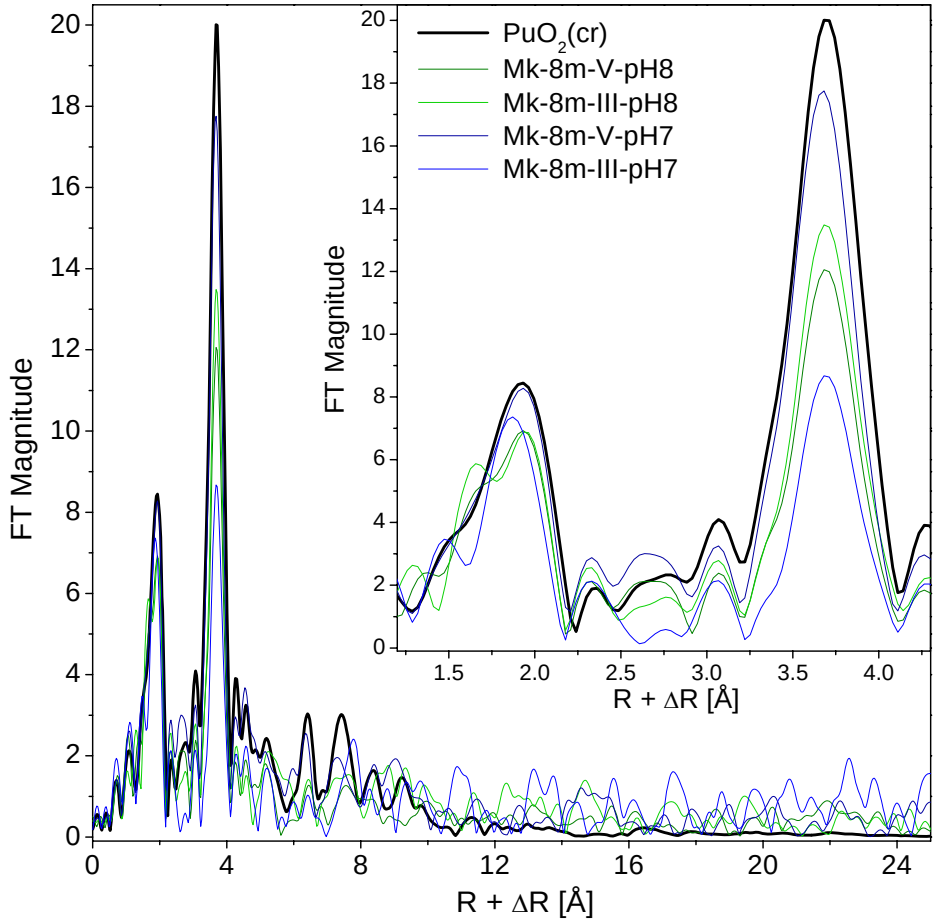

Figure 3.3.24. FT of 8 months Pu-mackinawite samples from Fig. 3.3.21. FT parameters: $3 \leq k \leq 15.15$ Å^{-1}, hannig window, dk1. Large graph: overview up to R + ΔR 25 Å. The noise level is indicated by the amplitude of peaks above ca. 12 Å. Inset: zoom of the on the 1.2 to 4.3 Å region.

To start with, one can observe that the fit residual[vii] depends quite strongly on the the noise level of the fitted spectrum (Fig. 3.3.25). A higher fit residual for a sample than for the PuO_2(cr) reference spectrum is thus most probably neither an indication for the fact that structural information different from PuO_2(cr) is present in the spectrum nor for the fact that the fitting approach (e.g. the selected feff paths) might be less suitable for the sample than for the standard.

Much of the information contained in Tables A3.23–26 is summerized in figure 3.3.26 where, (similarly to Fig. 3.3.20) σ (the square root of the DW) is plotted as a function of r (the fitted distance) and in Table 3.3.11, where the fitted CN for Pu–O 2.33 Å and Pu–Pu 3.83 Å are listed for different fitting ranges. Due to the measurements having been carried out at 15 K, the DW is thought of as resulting to a far greater extent from structural than from thermal disorder and differences in DW are

[vii] The fit residual in % (defined as stated in chapter 3.2) is given here as a goodness of fit parameter as it is provided by the WinXAS software and even though it may not be the best value to indicate the goodness of a fit. It is not equal to the *R*-factor that is proposed in the error reporting recommendations (ERR) from the IXS standars and criteria committee from 2000. Both the *R*-factor (ERR) and the residual (WinXAS) are not weighted over the experimental error while the parameter minimized during the fit (χ^2 in WinXAS and $(\Delta\chi)^2$ in the ERR) are.

thought of as representing differing degrees of structural (dis)order in the samples (and possibly from the presence of other oxidation states and artefacts).

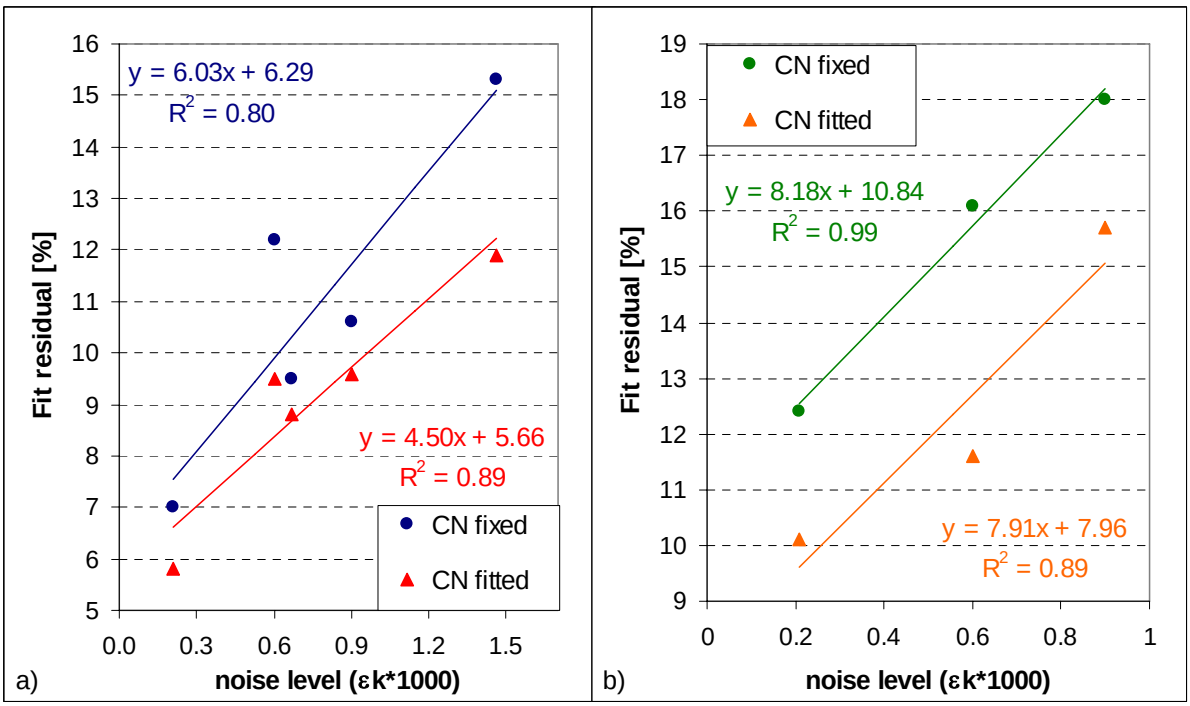

Figure 3.3.25. Fit residual as a function of the spectral noise level in k-range (same values as tabulated in Table 3.3.10) for fits with fixed and adjustable CN; FT based on $3.0 \leq k \leq 15.2$ Å^{-1}. Fit range in R-space was a) $1.3 \leq R \leq 4.1$ Å, b) $1.3 \leq R \leq 6.7$ Å. Apart from PuO_2(cr) in a) all four 8 months Pu-mackinawite sample appear (data from Tables 3.3.11 – 14). In b) only Mk-8m-V-pH7 and Mk-8m-V-pH7 were included (data from Tables 3.3.15, 16).

Probably the main result from all the different shell fits is that the fitted Pu-O (2.33 Å and 4.42 Å) and Pu-Pu (3.83 Å) distances for all four 8-months Pu-mackinawite samples correspond very well to the ones obtained for PuO_2(cr) (Fig. 3.3.26). Formation of a solid phase with PuO_2-structure is thus confirmed.

The two samples resulting from reaction at pH8 (Mk-8m-V-pH8 and Mk-8m-III-pH8) are similar to each other with respect to the fitted (though not necessary real) structural disorder both when a fit with fixed or adjustable CN is undertaken (Fig. 3.3.26). With adjustable CN the radial displacement σ for the Pu-O and Pu-Pu paths (at 2.33 and 3.83 Å) is for both samples fitted as being about 20 % higher than for PuO_2(cr) or Mk-8m-V-pH7. Their Pu-O coordination numbers do not significantly differ from PuO_2(cr), whatever the fit-conditions are (k-range, R-range) (Table 3.3.11). If a k-range of 3 to 15 Å^{-1} is used, the Pu-Pu CN differ somewhat between these two samples, the CN for Mk-8m-V-pH8 being significantly (30 %) lower than for PuO_2(cr) but the one for Mk-8m-III-pH8 being only slightly lower (Table 3.3.11). For a longer k-range (3 to 19 Å^{-1}) 20 to 30 % lower Pu-Pu CN are obtained for both samples. As the XANES gave no indication for the presence of Pu(III) in these samples, it is very unlikely that the presence of another oxidation state is responsible for the lowered Pu-Pu CN, and it might be indicative of a particle size effect. However, the correlation factor between the Pu-Pu CN and the DW is quite high (0.975 to 0.96) and I am thus not sure how reliable the fitted CN for Pu-Pu

backscattering are. As in the XANES, where it is slightly shifted to lower energy, the Mk-8m-III-pH7 spectrum differs somewhat from the other three 8-months sample spectra. Compared to PuO_2(cr) and Mk-8m-V-pH7, its σ-value for Pu-O at 2.33 Å is constant, while the one for the Pu-Pu paths at 3.83 Å is increased by about 40 % (Fig. 3.3.26 a). It is not obvious where this behavior (increase of σ only for Pu-Pu at 3.83 Å but not for Pu-O at 2.33 Å) originates in as the presence of Pu(III) alone (and of up to 20 % at maximum) should not result in an increase of the DW for Pu-Pu at 3.83 Å (Fig. 3.3.20) and should, in contrast, somewhat increase the DW of Pu-O. Again, and due to the higher noise level probably more so than for the two pH 8 samples, it is not sure to what extent the Pu-Pu CN and the DW are correctely resolved. Nonetheless, the shell fits suggests that this sample is more disordered than the other three samples.

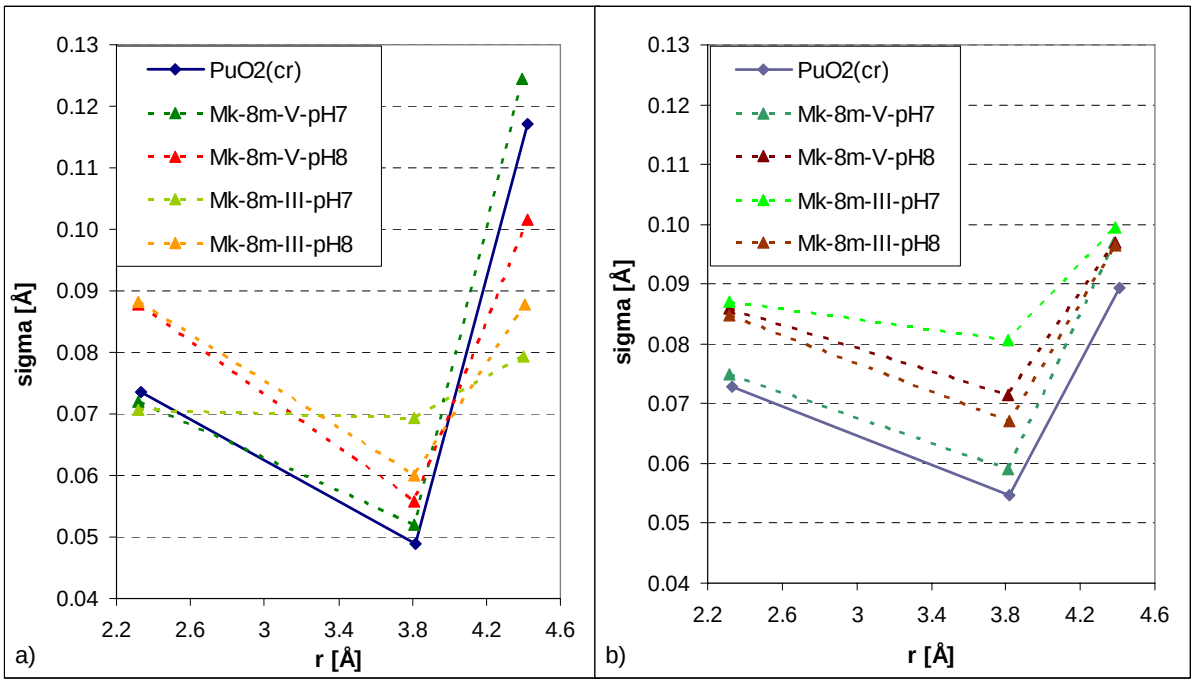

Figure 3.3.26. The structural disorder of Pu-O (2.33 and 4.42 Å) and Pu-Pu (3.83 Å) paths as indicated by σ (σ = sqrt(σ^2)) as a function of distance. a) σ as obtained by fitting with adjustable CN; b) σ as obtained by fitting with CN fixed to the crystallographic values of PuO_2. The corresponding σ^2 values are tabulated in Tables A3.23–26. Fits based on $3 \leq k \leq 15.2$ Å^{-1} and $1.3 \leq R \leq 4.1$ Å. Lines between data points are drawn only as a guide to the eye and to facilitate pattern recognition.

For Mk-8m-V-pH7, the shell fit confirms, as EXAFS amplitude and FT magnitude suggested, that it is the sample with the highest degree of order and that it closely ressembles PuO_2(cr). In particular, it is noteworthy that the DW for Pu-O at 4.42 Å for the three other samples is reduced compared to the value one might expect based on PuO_2(cr) (that is a σ value about 0.035 Å higher than for Pu-Pu) while for this sample all σ values follow closely the PuO_2(cr) pattern. As one can see in Tables A3.28 and A3.32 (given in the annex to this chapter), the DW for the two other Pu-Pu paths (at 5.40 and 6.61 Å) mostly have to be correlated to the DW of the 3.83 Å Pu-Pu paths, which means that the CN obtained for these paths will not be very reliable. Integrating them into the fitting scheme usually does not shift the values for the first Pu-O and Pu-Pu paths, which at least suggest that not taking them into

account does not falsify the fit for the closer shells. Fitting based on a longer k-range slightly reduces the correlation between the DW and CN for Pu-Pu at 3.83 Å, but, nonetheless, these values continue to be highly correlated (0.975 vs 0.96) (e.g. the correlation factor between CN and DW for Pu-O at 2.33 Å is approx. 0.9–0.93). Fitting based on a longer k-range also results in slightly lower CN for Pu-Pu (at 3.83 Å). One would expect this effect to occur similarly for sample spectra and the relative difference between the Pu-Pu CN ((CN(PuO_2(cr)) - CN(sample)) / CN(PuO_2(cr)) to be stable.

Table 3.3.11. Summary of fitted coordination numbers for Pu–O and Pu–Pu paths at 2.33 Å and 3.83 Å for fits based on different k and R-ranges. Values from Tables 3.3.12, 14, 16, 18, 20. Also given is the correlation factor between the DW and CN for the Pu–Pu paths at 3.83 Å.

fit range in k-space	fit range in R-space	Sample	CN (Pu-O) at 2.33 Å	Δ CN (Pu–O) = CN (sample) – CN (PuO_2(cr))	CN (Pu-Pu) at 3.83 Å	Δ CN (Pu–Pu) = CN (sample) – CN (PuO_2(cr))	Correlation between CN (Pu–Pu) and σ^2
3 - 15.2	1.3 - 4.2	**PuO_2(cr)**	**8.1**		**10.4**		**0.977**
3 - 15.2	1.3 - 4.2	Mk-8m-V-pH7	7.6	- 6 %	9.7	- 7 %	0.979
3 - 15.2	1.3 - 4.2	Mk-8m-V-pH8	8.3	2 %	7.3	- 30 %	0.975
3 - 15.2	1.3 - 4.2	Mk-8m-III-pH8	8.5	5 %	9.2	- 12 %	0.975
3 - 15.2	1.3 - 4.2	Mk-8m-III-pH7	6.1	- 25 %	7.9	- 24 %	0.974
3 - 15.2	1.3 - 6.9	**PuO_2(cr)**	**8.1**		**9.6**		-*
3 - 15.2	1.3 - 6.9	Mk-8m-V-pH7	7.6	- 6 %	8.7	- 9 %	-*
3 - 15.2	1.3 - 6.9	Mk-8m-V-pH8	8.1	0 %	6.7	- 30 %	-*
3 - 15.2	1.3 - 6.9	Mk-8m-III-pH8	8.3	2 %	8.7	- 9 %	-*
3 - 19.2	1.4 - 4.0	**PuO_2(cr)**	**7.6**		**9.6**		0.965
3 - 19.2	1.4 - 4.0	Mk-8m-V-pH8	7.6	0 %	6.8	- 29 %	0.960
3 - 19.2	1.4 - 4.0	Mk-8m-III-pH8	8.4	11 %	7.5	- 21 %	0.962
3 - 19.2	1.4 - 6.6	**PuO_2(cr)**	**7.6**		**9.0**		-*
3 - 19.2	1.4 - 6.6	Mk-8m-V-pH8	7.6	0 %	6.6	- 27 %	0.957
3 - 19.2	1.4 - 6.6	Mk-8m-III-pH8	8.2	8 %	7.0	- 22 %	-*

*no correlation factor available as for the fit to to converge the σ^2 value of the Pu-Pu paths at 3.83 Å had to be coupled to the one of the 5.4 Å Pu-Pu paths.

However, for one (out of only two) sample, the Pu-Pu CN of the sample was relatively more reduced, thus indicating a considerable (though not "significant" with respect to the maximum uncertainty of 25 % for CN) difference in CN Pu-Pu between PuO_2(cr) and this sample (Mk-8m-III-pH8). It is thus not entirely clear, if a k-range beyond 15 $Å^{-1}$ or 16 $Å^{-1}$ helps to improve significantly the information to be gained from a sample spectrum consisting to a large part of PuO_2. If the question to be answered is mainly if PuO_2 is present in a given sample and if other oxidation states are present as well, a spectrum with a good resolution at the edge (0.8 eV or better) and k up to 13 $Å^{-1}$ might be a good choice and if a little more beamtime is available, k up to 16 $Å^{-1}$ can probably provide a little more confidence about fitted Pu-Pu CN even though conclusions on particle size based solely on XAS data are not very reliable if the difference to PuO_2(cr) is not very large (which is to say that for very small colloids XAS spectra differ significatly from PuO_2(cr).[76]

3.3.3. Conclusions

Thermodynamically, formation of PuO_2(am,hyd) was, according to measured pe-pH pairs, expected to occur for all Pu-mackinawite samples. In five out of six samples, PuO_2 could be identified by XAS while for the remaining samples, corresponding to the lowest pH (Mk-40d-III-pH6), only Pu(III) was found associated with the mineral phase. In two samples, one resulting from reaction at pH 7, the other from reaction at pH 8, a noticeable amount of Pu(III) was present along with PuO_2. These results are summerized in Table 3.3.12.

Table 3.3.12. Pu(III) content in the Pu-mackinawite samples

sample	% Pu(III)	pH_{final}	Pu_{final} [nmol/L]	FeS conc. [g/L]	Pu loading [µmol/g]
Mk-40d-III-pH6	90 - 100	6.4	202	3.4	3.6
Mk-8m-III-pH7	10	7.1	25	1.7	6.8
Mk-8m-V-pH7	traces	6.9	2.5	1.7	9.2
Mk-40d-V-pH8	10	8.0	≤ 1	3.4	3.9
Mk-8m-III-pH8	traces	8.0	≤ 0.04	1.7	6.8
Mk-8m-V-pH8	traces	8.4	≤ 0.04	1.7	9.2

These results might be explained by a combination of PuO_2(am,hyd) (or PuO_2(coll,hyd)) solubility and stabilization of Pu(III) through adsorption to the FeS surface.

If PuO_2(am,hyd) is present, dissolved Pu(III) is expected to be in equilibrium with this solid phase, its concentration, $[Pu(III)_{eq/PuO2}]$, being a function of pe, pH and ionic strength. If, through adsorption of Pu(III) to a mineral surface, [Pu(III)] is decreased to below the value for $[Pu(III)_{eq/PuO2}]$, formation of a PuO_2 solid phase is not expected. This is most likely the mechanism explaining the absence of PuO_2 in sample Mk-40d-III-pH6.

Of course, in the other five samples, sorption of Pu(III) to the mineral surface may have occurred. To what extent this is the case, that is, what Pu(III) loading on the mackinawite surface will result and what percentage of the total added Pu will exist adsorbed to the mineral, depends on $[Pu(III)_{eq/PuO2}]$ and on the mineral solid/solution ratio as $[Pu(III)_{eq/PuO2}]$ must be equal to $[Pu(III)_{eq/Pu(III)adsFeS}]$, the Pu(III) equilibrium concentration for a certain Pu(III) loading on the mineral. How $[Pu(III)_{eq/Pu(III)adsFeS}]$ is related to a Pu(III) surface loading on mackinawite depends on the general affinity between Pu(III) and mackinawite surface sites. The relation between surface (or mass) loadings and the corresponding solution concentrations they are in equilibrium with can typically be described by sorption isotherms.

As $[Pu(III)_{eq/PuO2}]$ decreases sharply with increasing pH (e.g. from $\approx 10^{-6}$ M at pH 6.4, pe -4.1 to $\approx 10^{-8}$ M at pH 7, pe -4.3 and to $\approx 5 \cdot 10^{-11}$ M at pH 8, pe -5 for PuO_2(am,hyd) at I = 0) and since the concentration of negatively charged surface sites on FeS increases comparatively less (by a factor of about 50) between pH 6.4 and pH 8, a much lower Pu(III) loading on the FeS surface must be expected at pH 7 or pH 8 compared to pH 6. $[Pu(III)_{eq/PuO2}]$, the Pu(III) concentration in equilibrium with PuO_2, is, not only dependent on pe, pH and ionic strength, but also dependent on the particle size and degree of structural order in the PuO_2 formed. Thus a more disordered or more nano-crystalline

PuO_2-phase is expected to be in equilibrium with a higher [$Pu(III)_{eq/PuO2}$] which will then also be in equilibrium with a higher Pu(III) loading on the FeS surface. And the greater the surface area of FeS present (the smaller the FeS particles or the higher the FeS solid/solution ratio), the higher will be the percentage of the total Pu present in the form of Pu(III) bound to FeS in an outer-sphere surface complex.
Keeping in mind the factors influencing [$Pu(III)_{eq/PuO2}$], it makes sense that at pH 7, one sample (Mk-8m-III-pH7) was found to contain about 10 % Pu(III) while the other (Mk-8m-V-pH7) contains only traces: For Mk-8m-III-pH7, the final Pu concentration is about an order of magnitude higher, the degree of disorder apparent in the EXAFS is much greater, and the loading Pu loading is about 25 % lower than for Mk-8m-V-pH7. A similar relation of higher structural disorder and lower Pu-mineral loading explains probably the Pu(III) content of about 10 % in Mk-40d-V-pH8 as opposed to a trace content in the two 8-months samples at pH 8.

It is surprising and remains unresolved by the considerations of the preceding paragraphs why PuO_2 solids with different degrees of structural order and different solubilities form at pH 7 from added Pu(III) and Pu(V) but not at pH 8. In the first about thirty days, both pH 7 samples behave very similarly according to pe, pH and [Pu], but, as the rates of Pu sorption between days 33 and 210 differ by one order of magnitude (Table 3.3.2), a seizable difference in the solubility controlling solid phases is likely. In the absence of XAS data (or data from another solid state investigation method), it cannot be elucidated in what this difference consists. For both samples, it is possible that the decrease in [Pu] over time is related to an increase in order and/or particle size of PuO_2.
These experiments do not provide indications for the mechanisms of reduction of Pu(V) to PuO_2 and Pu(III) or of oxidation of Pu(III) to PuO_2. As the reduction of PuO_2 to Pu(III) by Fe(II) has been demonstrated,[104, 105] it is likely that, through dissolution, FeS can act as an Fe(II) source for this process. Similarly, in the absence of an inner-sphere surface complex between Pu(V) and FeS, Fe(II)aq is the most likely electron source for reduction of Pu(V) to PuO_2. Electrons from Pu(III) might either reduce sites of surface oxidation on FeS that, as discussed above, can be expected even under glove-box anoxic conditions or otherwise might lead to the formation of H_2(g). The amounts of H_2(g) potentially produced are, however, too small to be detected considering the Pu concentrations used.
As it is somewhat surprising that at pH 7 PuO_2 with the lowest and highest degree of disorder was formed and as it is particle size and crystallinity of PuO_2 that ultimately control Pu solubility, it would be interesting to further investigate the dependence of PuO_2 crystallinity on reaction pH and possibly mineral surface/solution ratio.
The total dissolved [Pu] cannot be higher in the presence of FeS than in its absence as in both cases PuO_2(am,hyd) (or PuO_2(coll, hyd)) provide an upper limit. To assess what environmental implications might result from the stabilization of Pu(III) with mackinawite, it should be considered in how far the mobility of Pu bound to FeS differs, if it does, for that of PuO_2 (nano-) particle.

In summary of this conclusion, it can be said that, while under reducing conditions Pu(III) is expected as a solution species in equilibrium with PuO_2(am,hyd), these Pu-mackinawite samples have permitted to observe that, even in the absence of inner-sphere complexation, Pu(III) can be associated with the FeS surface and can be stabilized against oxidation to PuO_2. For a given system, the amount of surface associated Pu(III) is expected to depend on the available mineral surface area and PuO_2 crystallinity and/or particle size.

At mildly acidic pH where negatively charged surface sites are still present on FeS and where dissolved Pu(III) concentrations in equilibrium with PuO_2(am,hyd) are relatively high ($\approx 10^{-6}$M to 10^{-4} M at I = 0.1), surface sorption of Pu(III) on FeS can considerably decrease dissolved Pu concentrations.

While the presence of PuO_2 is readily detectable in the EXAFS spectra of these Pu-mackinawite samples, detection of solid phase associated Pu(III) is largely dependent on the XANES and its presence can easily be overlooked.

3.4. Reaction of plutonium with chukanovite

In this chapter, the reaction of plutonium with chukanovite will be discussed considering all three plutonium-chukanovite samples (Table 3.4.1) (thus including a short reconsideration of Chuk-40d-V that was discussed in chapter 3.2). As in the preceding chapter, a graphic overview of the reaction conditions (pH, pe, [Pu]) will be given (Fig 3.4.1, Tables A3.7–9), followed by results from X-ray absorption spectroscopy.

Table 3.4.1. List of Pu-chukanovite samples to be discussed in this chapter.

Mineral	sample abbreviation	reaction time	Pu added as*	pH $_{final}$**	$[Pu]_{start}$ [µmol/L]	$[Pu]_{final}$ [nmol/L]	% Pu sorbed	Pu/mineral loading m/m [ppm]	[µmol/g]	[nmol/m^2]
Chukanovite	Chuk-40d-V	40 d	Pu(V)	8.4	13.4	≤ 1	99.993	1638	6.8	61
	Chuk-8m-V	7.6 m	Pu(V)	8.5	27.0	≤ 0.04	100.000	3957	16.4	147
	Chuk-8m-III	7.6 m	Pu(III)	8.6	20.1	0.04	100.000	2945	12.2	109

* Initial Pu oxidation state
** pH measured in suspension at the end of the reaction period
# The values preceded by a ≤ sign correspond to the detection limit for Pu concentrations by LSC. As the detection limit changed with the amount of sample solution used, different detection limits (1 vs 0.04 nM) were obtained at the end of the 40 d and 6 m experiments.

3.4.1. Overview of the reaction conditions

The three Pu-chukanovite samples were prepared at slightly differing solid/solution ratios (2.0 in the 40 d vs. 1.7 g/L in the 8 m experiment) and with three different Pu concentrations. To the samples with the highest and lowest Pu loadings Pu(V) had been added, while Pu(III) had been used for the intermediate concentration (Table 3.4.1). The reaction pH was rather stable over the period of observation and close to 8.5 for all three samples (8.3 to 8.7); pe values acquired in suspension vary between -6 and -4 (Fig. 3.4.1 a,b, Tables A3.7–9). Compared to the redox potential measured in Pu-mackinawite samples (Fig. 3.3.2) this variation is huge and no reason to explain this difference between mackinawite and chukanovite samples is obvious.

Pu solution concentrations decreased for all three samples very rapidly to the detection limit. For the two 8-months samples, the Pu concentration increased again, to about 10^{-6} M at day 11 for the Pu(III) sample and to 10^{-8}M at day 96 for the Pu(V) sample (Fig. 3.4.1.c). As for both samples the intervals for concentration measurements were rather large, the time dependence of [Pu] is not well described. Based on the scarcity of solution data and the fact that XAS was done only at the end of the reaction period, any explanation for these concentration increases would be very hypothetical. Compared to other samples where no such "jumpy" behavior of the Pu concentration was observed, it is quite unlikely that artefacts are responsible for these concentration increases but cannot be ruled out completely.

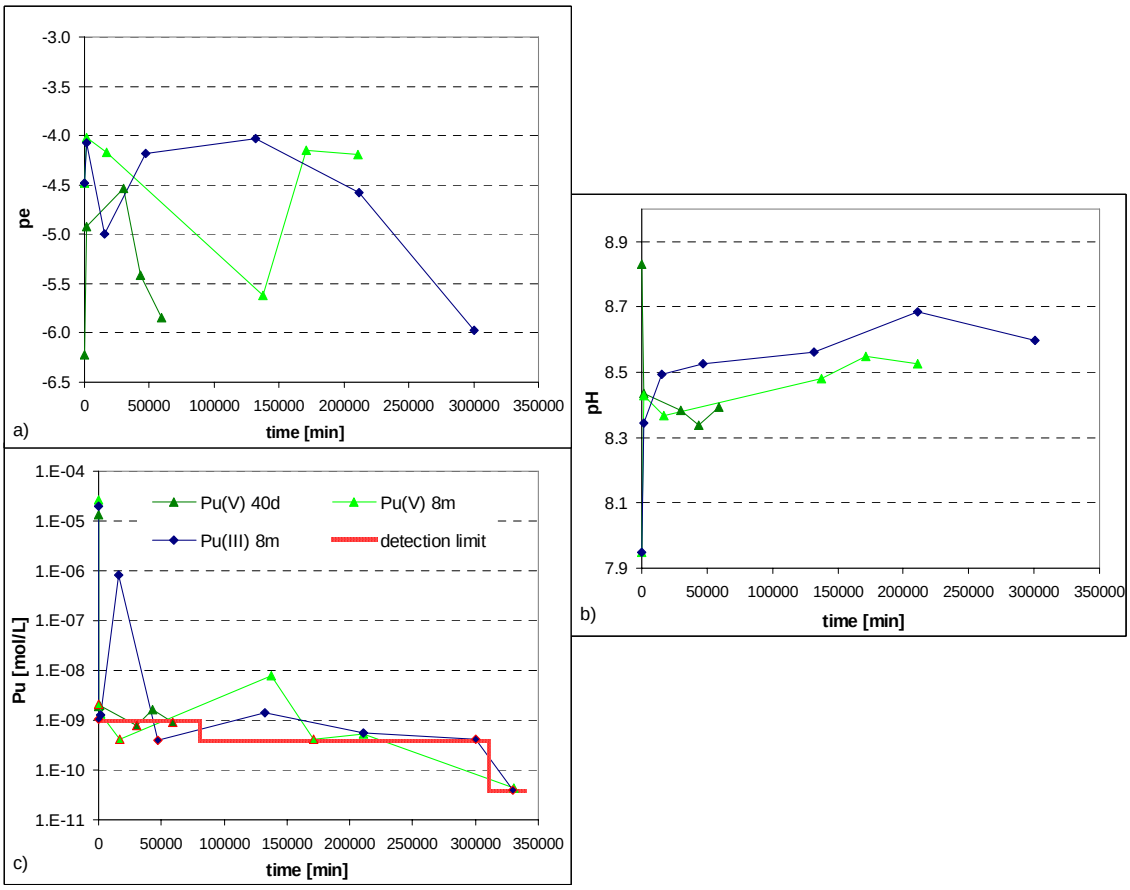

Figure 3.4.1. pe_{sus} (a) and pH_{sus} (b) values and total dissolved Pu concentrations (c) over time for Pu-chukanovite samples. Data points corresponding to values at or below the detection limit are marked by red outer line. The samples are designated by the initial Pu oxidation state and reaction time.

3.4.2. Results from X-ray absorption spectroscopy

The XANES spectra of Chuk-40d-V and Chuk-8m-III are very similar to each other and are shifted to lower energy compared to Chuk-8m-V and to the two Pu-mackinawite spectra that are shown for reference (Fig. 3.4.2). Chuk-8m-V strongly resembles the Mk-8m-III-pH7 spectrum. All Pu-chukanovite spectra thus seem to contain some Pu(III). Quantification by LC fitting was carried out similarly to what was done for Pu-mackinawite samples, that is, by using Pu(III)aq as Pu(III) reference and Mk-8m-V-pH7 or Mk-8m-III-pH8 as reference for non-calcinated PuO_2. Using normalized spectra, the XANES (18040 to 18105 eV) (Table 3.4.2) and early EXAFS regions (18105 to 18330 eV) (Table 3.4.3) were fitted. For Chuk-8m-III, LC fitting was also applied to k^3-weighted EXAFS spectra (Table 3.4.4). As before for samples Mk-8m-III-pH7 and Mk-40d-V-pH8 (Table 3.3.5), using Mk-8m-III-pH8 as PuO_2 reference for Pu-chukanovite spectra results in a 2–3 % smaller Pu(III) contents than if Mk-8m-V-pH7, the PuO_2 spectrum with the WL maximum at the highest energy (Fig. 3.3.6), is used. According to the XANES, the different Pu-chukanovite spectra thus contain about 40, 45 and 15 % Pu(III) (Table 3.4.2). As for the Pu-mackinawite LC fits, fitting in the early EXAFS region of the normalized Pu-chukanovite spectra yields slightly (2–3 %) lower Pu(III) contents than fitting in the XANES region does, whether Mk-8m-III-pH8 or Mk-8m-V-pH7 was used as PuO_2 reference.

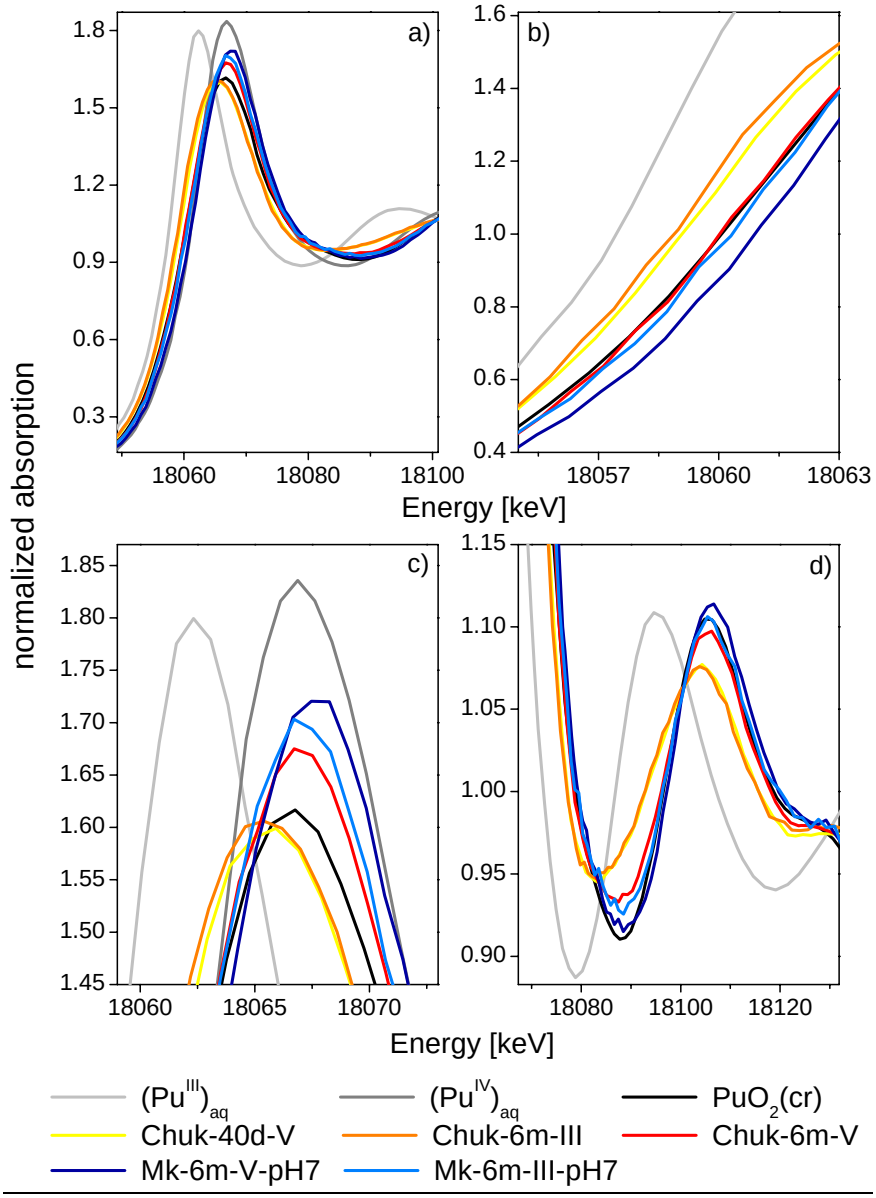

Figure 3.4.2. XANES region of Pu-L_{III}-edge X-ray absorption spectra of Pu-chukanovite samples (red, orange and yellow) and PuO_2(cr), Pu(III)aq, Pu(IV)aq and two Pu-mackinawite samples for comparison. a) Overview of the XANES region, b) zoom on the edge region, c) WL-maximum region, d) post-WL minimum region.

Table 3.4.2. Linear combination fit of samples Chuk-40d-V, Chuk-8m-III, Chuk-8m-V with Pu(III)aq and non-calcinated PuO_2 (either sample Mk-8m-V-pH7 or Mk-8m-III-pH8) as references in the energy range 18.040 to 18.105 keV. For exemplary plot see Fig. 3.4.3.

samples	Pu(III)aq and Mk-8m-III-pH8				Pu(III)aq and Mk-8m-V-pH7			
	Pu(III)	**PuO_2**	**sum [%]**	**R-factor**	**Pu(III)**	**PuO_2**	**sum [%]**	**R-factor**
Chuk-40d-V	38.4 %	61.7 %	100.1	$9.5 \cdot 10^{-5}$	40.7 %	59.8 %	100.5	$1.0 \cdot 10^{-4}$
Chuk-8m-III	42.6 %	58.1 %	100.7	$1.2 \cdot 10^{-4}$	44.8 %	56.3 %	101.1	$1.5 \cdot 10^{-4}$
Chuk-8m-V	14.1 %	86.1 %	100.2	$3.4 \cdot 10^{-5}$	17.3 %	83.2 %	100.5	$5.5 \cdot 10^{-5}$

If spectra of the very components of the Pu-chukanovite spectra could be used as references, an LC fit should yield the same result whatever the region of the fit was. That the fit behavior of the samples with the reference spectra used is not totally ideal is than an indication for the fact that the references are not 100 % appropriate. At close inspection, a small deviance between data and fit in the XANES region at 18080 to 18100 eV is also apparent, visually confirming this non-ideality.

Table 3.4.3 Linear combination fit of samples Chuk-8m-III and Chuk-8m-V with Pu(III)aq and non-calcinated PuO_2 (either sample Mk-8m-V-pH7 or Mk-8m-III-pH8) as references in the energy range 18.105 to 18.330 keV. For exemplary plot see Fig. 3.4.3.

sample	references	Pu(III)	PuO_2	sum [%]	R-factor
Chuk-40d-V	Pu(III)aq and Mk-8m-III-pH8	35.2 %	64.8 %	100.0	$3{\cdot}10^{-6}$
	Pu(III)aq and Mk-8m-V-pH7	37.7 %	62.3 %	100.0	$2{\cdot}10^{-6}$
Chuk-8m-III	Pu(III)aq and Mk-8m-III-pH8	37.1 %	62.9 %	100.0	$4{\cdot}10^{-6}$
	Pu(III)aq and Mk-8m-V-pH7	39.6 %	60.5 %	100.1	$4{\cdot}10^{-6}$
Chuk-8m-V	Pu(III)aq and Mk-8m-III-pH8	13.2 %	86.8 %	100.0	$3{\cdot}10^{-6}$
	Pu(III)aq and Mk-8m-V-pH7	16.5 %	83.5 %	100.0	$3{\cdot}10^{-6}$

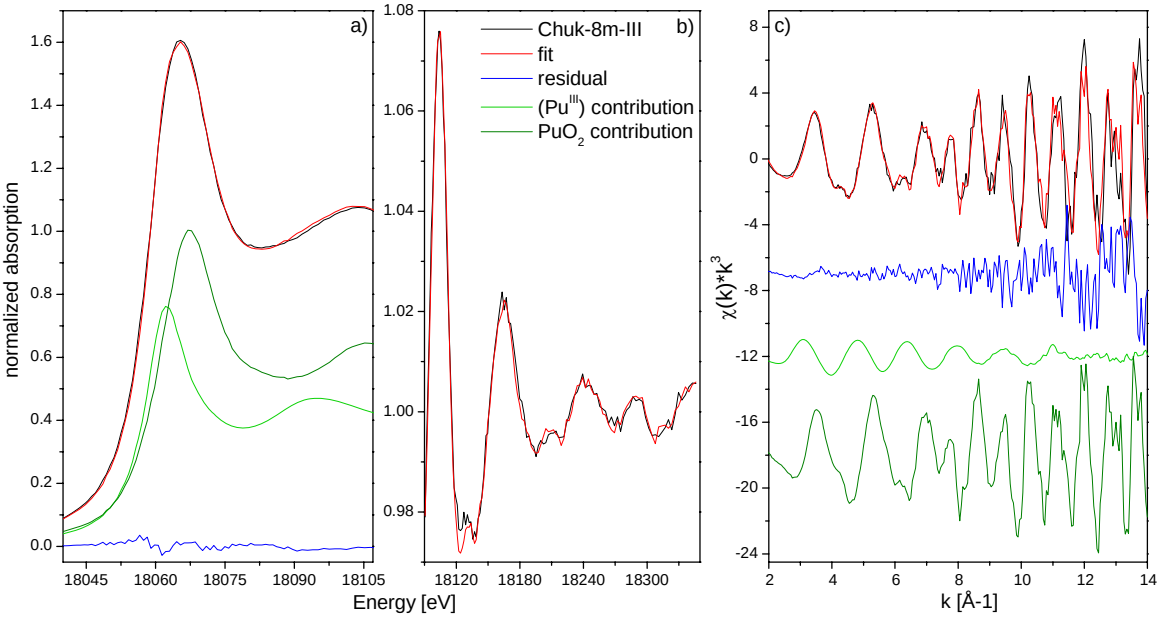

Figure 3.4.3. LC fit of sample Chuk-8m-III using Pu(III)aq and Mk-8m-III-pH8 as references. a) XANES (fit range: 18.040 to 18.105 keV), b) early EXAFS region (normalized spectrum) (fit range: 18.105 to 18.33 keV), c) EXAFS (fit range 3.0–12.3 $Å^{-1}$, E_0 of sample and reference spectra set to 18.060 keV).

If one wants to carry out an LC fit using EXAFS spectra, it is important to chose the same value of E_0 (the value with respect to which the conversion from energy into k-space is performed according to ($k = \sqrt{((2m_e/\hbar^2) * (E-E_0))}$[viii]) for all spectra (sample and references), otherwise the sum of the components deviates strongly from 100 % and the found contributions are not correct. This is exemplified for a LC fit of k^3-weighted spectra for Chuk-8m-III. If for each spectrum the inflection point of the absorption edge is used as E_0 (18057 eV for Pu(III)aq, 18059.5 eV for Chuk-8m-III and

[viii] m_e – rest mass of the electron, $\hbar = h/2\pi$, h – Plank's constant

18061.5 eV for Mk-8m-III-pH8), the sum of the components reaches only 73 % and the found percentages of Pu(III) and PuO_2 deviate strongly from the XANES fit results (Table 3.4.4., first line). If E_0 is set to the same value for all three spectra, the fit residual decreases and the sum of the components comes closer to 100 %. Which E_0 value is chosen has a slight effect on the R-factor but hardly affects the found percentages (Table 3.4.4).

Comparison between results from the fit of the early EXAFS region (normalized spectra) and the EXAFS shows that a fit using k^3-weighted EXAFS spectra yields a lower Pu(III) content (33.5-34.5 %) while the PuO_2 content is only slightly changed (from 62.9 % to between 61.1 and 64 %) (Table 3.4.3, 4). This is another indication for the non-ideality of the reference spectra.

Table 3.4.4. LC fit of samples Chuk-8m-III with Pu(III)aq and non-calcinated PuO_2 (Mk-8m-III-pH8) in k-space in the range 3.0–8.85 and 3.0–12.3 $Å^{-1}$. For exemplary plot see Fig. 3.4.3.

E_0	fit range	Pu(III)	PuO_2	sum [%]	R-factor
infl. point	k = 3.0 – 8.85 $Å^{-1}$	16.6 %	56.3 %	72.9	0.063
18060 eV	k = 3.0 – 8.85 $Å^{-1}$	32.6 %	61.7 %	94.3	0.035
	k = 3.0 – 12.3 $Å^{-1}$	32.5 %	64.0 %	96.5	0.138
18059 eV	k = 3.0 – 8.85 $Å^{-1}$	32.3 %	61.1 %	93.4	0.041
	k = 3.0 – 12.3 $Å^{-1}$	31.7 %	62.6 %	94.3	0.159
18061 eV	k = 3.0 – 8.85 $Å^{-1}$	32.3 %	61.3 %	93.6	0.044
	k = 3.0 – 12.3 $Å^{-1}$	32.2 %	63.8 %	96.0	0.153

If different k-weightings are tested, one finds that the lower the k-weight used the higher is the Pu(III) content found. For the 3.0-8.85 $Å^{-1}$ range (with E0 = 18060 eV), a Pu(III) content of 36.9 % is found for k^0-, 35.9 % for k^1- and 34.5 % for k^2- weighting while PuO_2 changes only from 61.0 % at k^0- to 62.0 % at k^2-weighting. This behavior suggests that small variations exist between Pu(III)aq and Pu(III) contained in Chuk-8m-III. For example, a higher DW factor for Pu(III) in the Chuk-8m-III spectrum could result in such a fitting behavior as differences in DW more strongly affect spectra at higher k-values and as, at higher k-weighting, parts of the spectrum at higher k-values are given a greater importance than at lower k-weighting.[106, p.42]

Assigning a precise Pu(III) content to the Pu-chukanovite spectra is thus difficult. However, one might assume that by assigning the average of what was found by fitting of the early EXAFS region (Table 3.4.3) and adding an uncertainty of about 5 %, the potential Pu(III) content for each sample is correctly described. The advantage of fitting directly with the early EXAFS region of the normalized spectrum, and not with a $\chi(k)$ spectrum, is that in this case all potential errors introduced by assigning an E_0 value (which is better suited for one spectrum than for another if the same must be chosen for all spectra), through background subtraction, the spline and k-weighting are avoided.

Pu(III) contents in the Pu-chukanovite spectra might thus be summarized as 37 ± 5 % for Chuk-40d-V, 38 ± 5 % for Chuk-8m-III and 15 ± 5 % for Chuk-8m-V.

If one assumed the Pu(III) in the Pu-chukanovite samples to be sorbed to the chukanovite surface, the resulting $Pu(III)_{adsChuk}$ loadings would be 22.6, 41.4 and 22.1 nmol/m^2 for Chuk-40d-V, Chuk-8m-III and Chuk-8m-V, respectively.

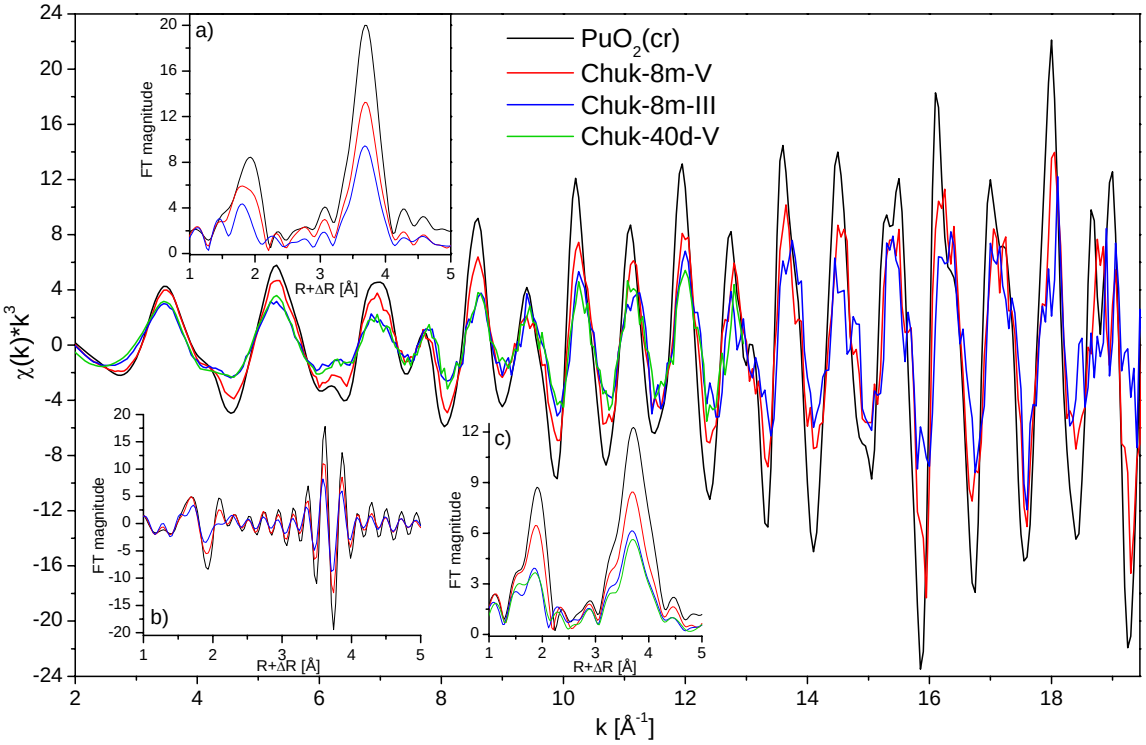

Figure 3.4.4. EXAFS spectra acquired at the Pu-L_{III}-edge (large picture) and FT of Pu-chukanovite spectra and PuO_2(cr) for reference. Insets: a) FT of k^3-weighted spectra (k-range of $3 \leq k \leq 15.2$ Å^{-1}) (only 8-months spectra), b) Imaginary part of the FT in a), c) FT over $3 \leq k \leq 12.6$ Å^{-1} (including Chuk-40d-V).

Pu-chukanovite k^3-weighted EXAFS spectra and FT over two different k-ranges are shown in Fig. 3.4.4. In the EXAFS and short k-range FT, the resemblance (Fig. 3.4.4 c) of Chuk-8m-III and Chuk-40d-V is clearly visible. Over the longer k-range, the magnitude of the first peak (Pu-O at 2.33 Å) of the Chuk-8m-III spectrum is very small, but in the imaginary part of the FT clearly follows the pattern of the other two spectra, though with lower amplitude (Fig. 3.4.4 a and b).

It is somewhat surprising, that the two samples to which Pu(V) had been added, have very different Pu(III) contents (37 vs 15 %) but very similar Pu(III) surface loadings while the sample to which Pu(III) had been added, has a final Pu(III) content similar to one of the Pu(V) samples but a much higher Pu(III) surface loading. The main difference between the two Pu(V) samples are slightly different solid/solution ratios and that to the second sample with lower final Pu(III) content a higher Pu(V) concentration had been added.

That with a smaller surface area and higher Pu(V) concentration less Pu(III) is formed might suggest that contact with the surface is necessary for the transformation of Pu(V) or PuO_2 to Pu(III). But as also with mackinawite, where inner-sphere complexation probably does not occur, Pu(V) is reduced to both Pu(III) and PuO_2 and as PuO_2 can be reduced by Fe(II) alone,[105] this higher final Pu(III) content in presence of a greater surface area is not necessarily an indication for a surface reaction.

Supposing, as for mackinawite, that surface adsorbed (inner or outer-sphere) Pu(III), $Pu(III)_{adsChuk}$, is in equilibrium with a certain Pu(III) solution concentration, $[Pu(III)_{eq/Pu(III)adsChuk}]$, that is in equilibrium with PuO_2 and thus equals $[Pu(III)_{eq/PuO2}]$, one might suppose that then a surface Pu(III) surface loading on chukanovite is in equilibrium with the PuO_2 formed. If this is the case, then why is the surface loading in one sample about twice as high as for the two others?

One possible explanation would be, that starting from Pu(III), thermodynamic equilibrium has not been attained yet and that for this reason, the sample has a higher Pu(III) content. Another explanation could lie in the solubility of the PuO_2 formed. In the presence of more disordered or smaller sized PuO_2 particles, $[Pu(III)_{eq/PuO2}]$ would be greater than for a more ordered PuO_2 phase and higher $[Pu(III)_{eq/PuO2}]$ would be in equilibrium with a higher surface loading. Different possibilities exist to try and differentiate between these explanations. The simplest option would be to determine Pu solution concentrations and see if they differ from each other. As in this experiment concentrations for all three samples were at or below the detection limit, a similar experiment with lower detection limit using another Pu-isotope would be necessary for this kind of comparison. A second option to differentiate between non-attained thermodynamic equilibrium and more disordered PuO_2 resulting from addition of Pu(III) to chukanovite, would be to re-measure the samples after a relatively long amount of time to see if the Pu(III) contents change over time. But even if they were not subject to change, this would not necessarily constitute a proof for thermodynamic equilibrium as the time of waiting could still have been too short. The third option would then be to characterize the degree of order in the PuO_2 contained in these samples. As was shown before, the fit parameters obtained from a mixed PuO_2(cr)-Pu(III) spectrum vary from those of pure PuO_2(cr). However, the influence of Pu(III) is not easily differentiated from that of disorder itself and particle size effects and it is far from sure, that, knowing a sample's Pu(III) content, the degree of structural disorder of the contained PuO_2 could be assessed.

The other options not being accessible, one might thus try to explore this third possibility, even though it may appear as some kind of reading in "coffee grounds".

As for Pu-mackinawite spectra, shell fit results for Chuk-8m-III and Chuk-8mV with fixed and adjustable CN are shown in figure 3.4.5 in the form of σ over r for the first two Pu-O paths (2.33 and 4.43 Å) and first Pu-Pu paths (3.83 Å) (for CN and other parameters, see Tables A3.33, 34). For both fits (CN adjustable or fixed), the apparent structural disorder, σ, is much greater for Chuk-8m-III than for Chuk-8m-V as can be expected from its much higher Pu(III) content (38 vs. 15 %).

For comparison with theoretical PuO_2(cr)-Pu(III) mixture spectra, sigma-over-r plots for fitting with fixed or adjustable CN are shown in figure 3.4.6 for spectra consisting of up to 50 % of Pu(III). As before (Fig. 3.3.20), the corresponding fits are based on a shorter k-range than for Pu-mackinawite and Pu-chukanovite spectra, which somewhat limits the comparability of obtained σ values (in addition to the fact, that, as explained above, artificial mixture spectra are not in all aspects comparable to real mixed samples).

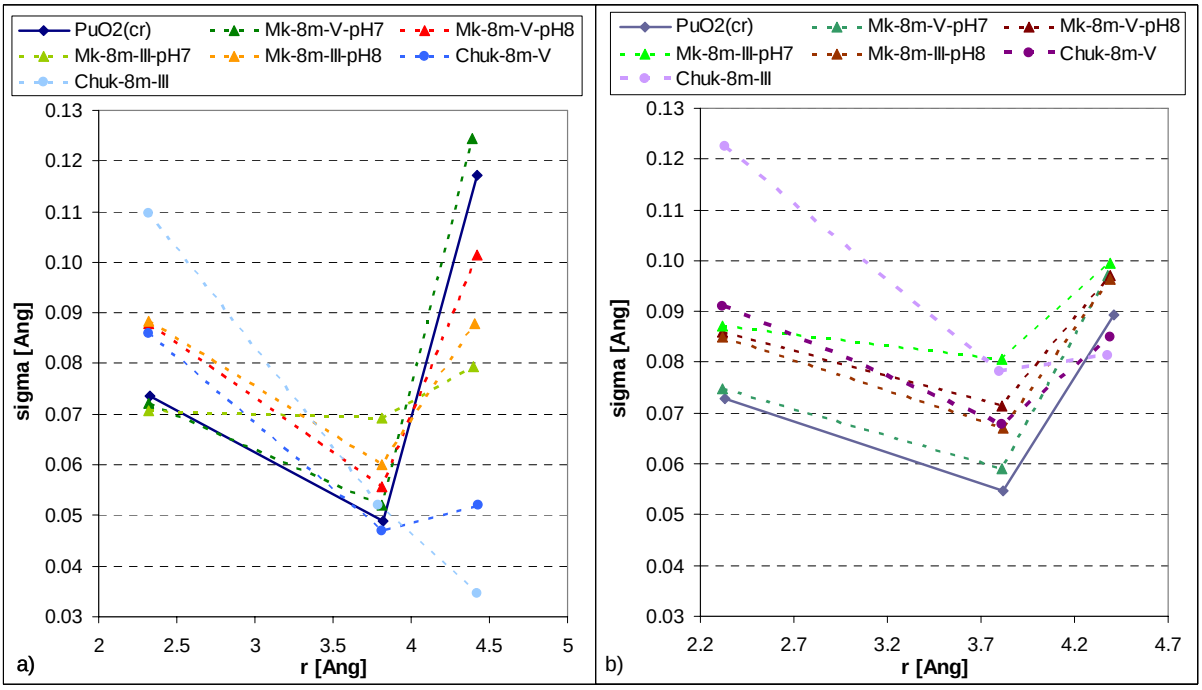

Figure 3.4.5. The structural disorder of Pu-O (2.33 and 4.42 Å) and Pu-Pu (3.83 Å) paths as indicated by σ (σ = sqrt(σ^2)) as a function of distance. a) σ as obtained by fitting with adjustable CN; b) σ as obtained by fitting with CN fixed to the crystallographic values of PuO_2. The corresponding σ^2 values are tabulated in Tables A.3.23–26, 33, 34. Fits based on $3 \leq k \leq 15.2$ Å^{-1} and $1.3 \leq R \leq 4.1$ Å. Lines between data points are drawn only as a guide to the eye.

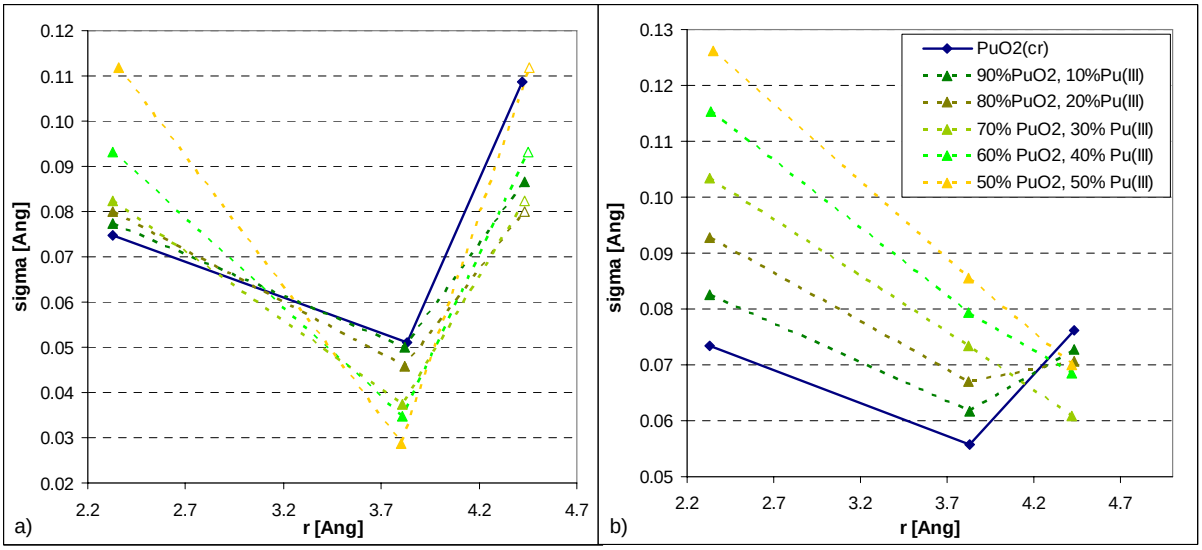

Figure 3.4.6. The structural disorder of Pu-O shells as indicated by σ (σ = sqrt(σ^2)) as a function of distance. a) σ as obtained by fitting with adjustable CN (open triangle for second Pu-O shell (4.4.3 Å) signify values that had to be correlated to the first Pu-O shell); b) σ as obtained by fitting with CN fixed to the crystallographic values of PuO_2. Lines between data points are drawn only as a guide to the eye.

Only if the increase in σ(Pu-O) and increase (CN fixed) or decrease (CN adjustable) of σ(Pu-Pu) follows a regular pattern and can be described by an equation, would it be possible to extract σ-values for PuO_2 contained in the chukanovite samples. In figure 3.4.6 b, the changes in σ(Pu-O) and σ(Pu-Pu) induced by the presence of Pu(III) in the mixture spectra, appear quite regularly spaced and indeed can be described by linear equation (Fig. 3.4.7 b). For fits with adjustable CN, changes in σ(Pu-O) do not

confirm to a linear equation and the decrease in σ(Pu-Pu) (Fig. 3.4.7 a) is less well described by a linear equation than for a fit with fixed CN.

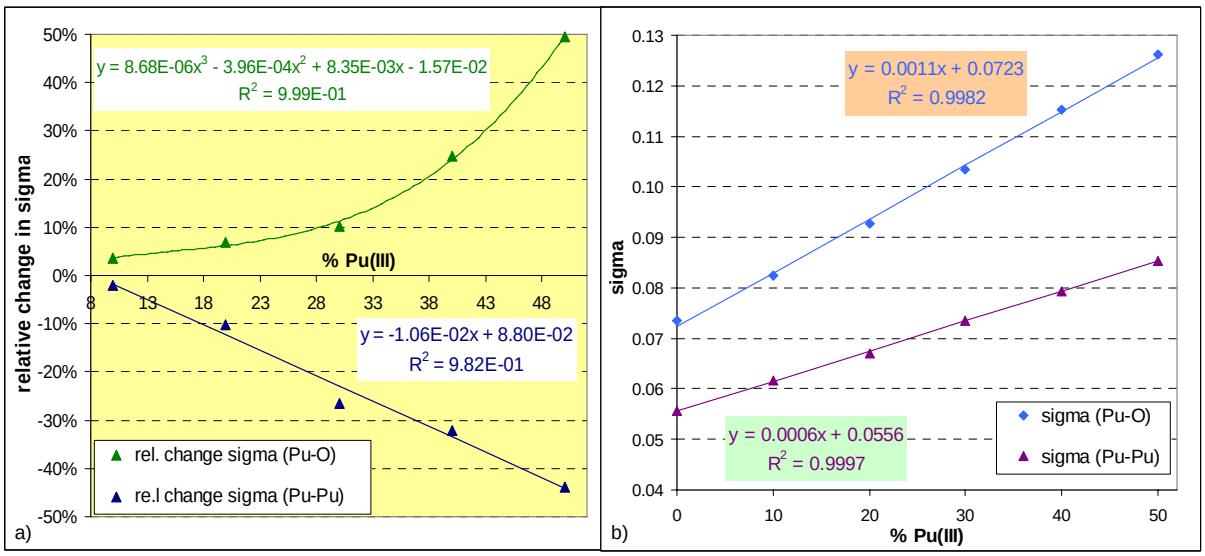

Figure 3.4.7. a) Relative increase (positive values) or decrease (negative values) of σ(PuO_2+Pu(III)) vs σ(PuO_2(cr)) calculated as: Δσ/σ(PuO_2(cr)) = (σ(PuO_2+Pu(III))-σ(PuO_2(cr)) / σ(PuO_2(cr) for fits with adjustable CN. b) σ(Pu-O) and σ(Pu-Pu) over Pu(III) content for fits with fixed CN calculated from data points in Fig. 3.4.5.

Supposing the Pu-chukanovite samples contain 15, 37 and 38 % of Pu(III) as found by LC fitting, one might then try to extract sigma-values for the PuO_2 contained in these samples. As Chuk-40d-V was measured only up to k = 12.9 $Å^{-1}$, a fit with fixed and adjustable CN was repeated for all three samples based on a shorter k-range (Fig. A3.1). Parameters obtained for PuO_2 contained in the Pu-chukanovite spectra by using the equations from Fig. 3.4.7 and applying them to the values shown in Fig. 3.4.5 and A3.1, are plotted in figure 3.4.8.

From fits with fixed CN (Fig. 3.4.8 b), the hypothetical PuO_2 components derived for all three Pu-chukanovite spectra are lying relatively close to each other according to the sigma parameters. The PuO_2 hypothetically contained in Chuk-8m-III would be characterized by the greatest sigma value for Pu-O and the smallest for Pu-Pu, which appears somewhat strange. But no sample can be said to be clearly more disordered than any of the other two. From fits with adjustable CN, it appears, in contrast, that PuO_2 in Chuk-8m-III would be far more disordered than in the other two Pu-chukanovite samples. In figure 3.4.8 a) the values contained for Chuk-8m-V were obtained from fitting both at a longer and shorter k-range, for Chuk-40d-V only the shorter k-range was available and for Chuk-8m-III, the fit in the shorter k-range did not converge as the value for σ(Pu-Pu) became too small, so that only values based on the longer k-range could be plotted. Both the higher sigma value for the longer fit range and the fact that the fit for the shorter k-range did not converge for Chuk-8m-III, would be in agreement with a more disordered structure for the PuO_2 contained in this sample. However, other explanations might exist, such as a smaller PuO_2 particle size, for example. It is also possible, that yet other factors are responsible for this higher apparent structural disorder in Chuk-8m-III.

A fit with fixed CN imposes constraints on the samples that are less and less justified the higher the Pu(III) content is. If the disorder in a sample is quite high and a large amount of Pu(III) is present in

addition, it is not certain that the "real" structural disorder and the apparent structural disorder (increase in the sigma value as a function of Pu(III) content) are additive (meaning: behave in an additive manner in the fit with fixed CN). Such a non-additivity of disorder might explain why in the fit with fixed CN, Chuk-8m-III has rather a lower than a higher σ-parameter for the Pu-Pu path at 3.83 Å than the other two Pu-chukanovite samples.

To test if this kind of calculation could correctly characterize the structural disorder of PuO_2 contained in PuO_2+Pu(III) mixture spectra, reference samples consisting of PuO_2 of different degrees of order and particle size and containing different amounts of Pu(III) would have to be measured and analyzed. The outcome of this try to retrieve a disorder parameter for the PuO_2 contained in the Pu-chukanovite samples is thus only that the found σ(Pu-Pu) values are not in disagreement with the possibility that the PuO_2 contained in Chuk-8m-III could be more disordered than in the two samples that resulted from reaction with Pu(V)aq.

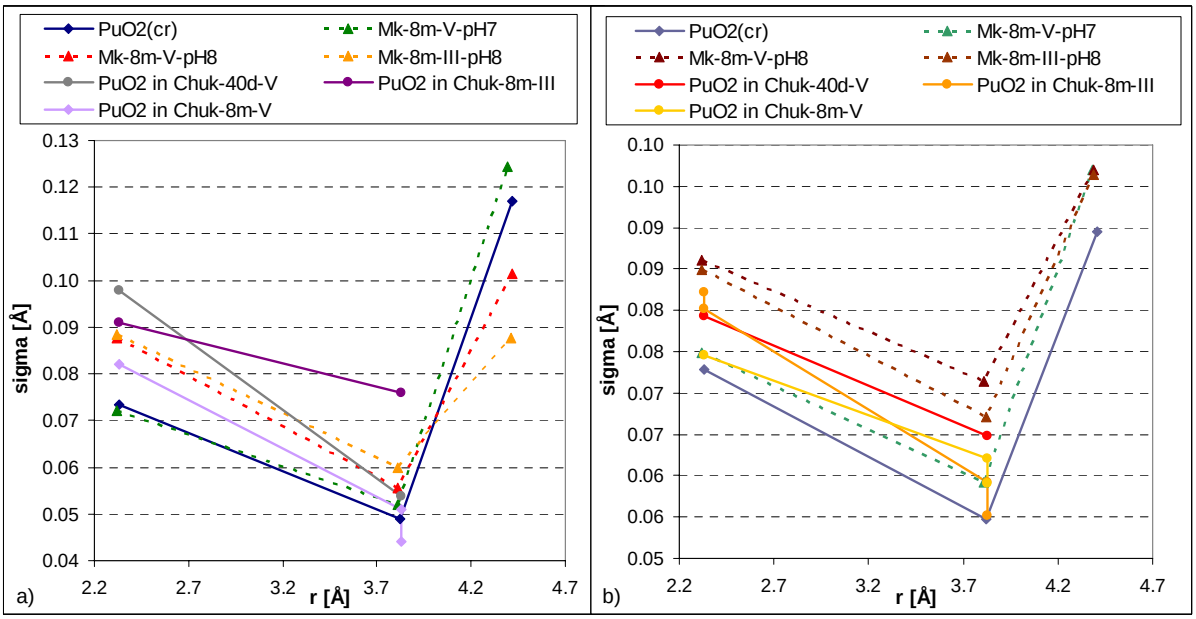

Figure 3.4.8. Sigma as a function of r obtained for the hypothetical PuO_2 component in mixed Pu(III)-PuO_2 Pu-chukanovite samples obtained by applying the equations from Fig. 3.4.7 to data plotted in Fig. 3.4.5 and Fig. A3.1. a) Fits with adjustable CN. Pu-mackinawite samples, Chuk-8m-III, Chuk-8m-V and PuO_2(cr): $3 \leq k \leq 15.2$ Å^{-1}. For Chuk-40d-V and Chuk-8m-V: $3 \leq k \leq 12.1$ Å^{-1}. b) Fits with fixed CN. Pu-mackinawite samples, Chuk-8m-III, Chuk-8m-V and PuO_2(cr): $3 \leq k \leq 15.2$ Å^{-1}. Chuk-40d-V, Chuk-8m-V and Chuk-8m-III: $3 \leq k \leq 12.1$ Å^{-1} For all: fit range in R-space: $1.3 \leq R \leq 4.1$ Å.

3.4.3. Conclusions

Similarly to the reaction of aqueous Pu(V) and Pu(III) with mackinawite, for Pu-chukanovite samples reduction of Pu(V)aq to Pu(III) and PuO_2 and partial oxidation of Pu(III)aq to PuO_2 were observed. The found Pu(III) contents are higher with chukanovite than with mackinawite. This might be due to Pu(III) carbonate complexation. As no sample contained only Pu(III) after reaction, it could not be elucidated if Pu(III) forms inner-sphere or outer-sphere complexes on chukanovite surfaces and to what extent it might be complexed by carbonate. Also, it cannot be excluded that Pu(III) was adsorbed to the surfaces of the PuO_2 formed.

From the present data, it is not completely clear why in two samples almost 40 % Pu(III) are found after reaction with chukanovite and only 15 % in the other sample. Supposing that Pu(III) was adsorbed to the chukanovite surface and taking into account the resulting surface loadings, one possible explanation for the different Pu(III) contents of the three samples would be that the PuO_2 formed in the sample with the highest surface loading is characterized by a lower degree of structural order or by a smaller particle size. As for all three samples Pu solution concentrations were at or below the detection limit, [Pu] cannot be used to support or refute this hypothesis based on potential solubility differences of the PuO_2 phase. Shell fit results are not sufficient to proof this explanation but are not in disagreement with it, either.

As the PuO_2 in Mk-8m-III-pH7 also appeared more disordered than the one resulting from reaction with Pu(V) at the same pH, a question arising from these experiments would thus be if reaction of Pu(III) with minerals under anoxic reducing conditions leads to smaller and/or more disordered PuO_2 particles than reaction of Pu(V) (or Pu(IV)) under the same conditions does. As Pu(III), at least as long as it predominantly exists as Pu^{3+} and $Pu(OH)^{2+}$ (that is up to pH 8.2 at I=0), has a higher charge than PuO_2^+, it might be expected to interact more strongly with charged sites on mineral surfaces. If, when Pu(III) comes into contact with a mineral surface under conditions where thermodynamically PuO_2 is predicted to form, no PuO_2 is present at the beginning of the reaction, the nucleation of PuO_2(coll,hyd) will at first lead to very small particles characterized by a much higher solubility than PuO_2(am,hyd).[8] If with Pu(III), due to its higher surface adsorption tendency, nucleation of PuO_2 started from a smaller solution concentrations and thus smaller oversaturation, nucleation of PuO_2 might set in later and the growth of particles might be slower compared to a situation where Pu(V) is present. However, if growth is slowed and takes places at a smaller supersaturation than for Pu(V), PuO_2 particles would rather be expected to be less amorphous/better crystallized. If it was found that PuO_2 particles formed from Pu(III) were at first smaller than those formed from Pu(IV) or Pu(V), it would be important to investigate the timescale of transformation to more ordered PuO_2 as the particle size might impact the migration behavior of the resulting PuO_2 colloids.

As was stated before for Pu-mackinawite reactions, the persistance of non-negligible amounts of Pu(III) in the presence of PuO_2 does probably not affect the Pu solution concentration that is imposed by PuO_2, but it might affect Pu migration behavior if mineral particles are transported or dissolved. The biological availability to microorganisms and thus the toxicity of surface sorbed Pu(III) might also be different from that of PuO_2 (nano-) particles. As much as complexation reaction of Pu with dissolved complexing ion are investigated to be taken into account for the prediction of the long term behavior of Pu in the context of nuclear waste disposal or environmental contamination, it might thus be important to also consider the specific form in which non-dissolved Pu is present under specific conditions (pH, pe, ionic strength, dissolved complexing ions, water saturation, type of minerals present, mineral surface areas and accessibilities of these surfaces, microbial communities, etc.).

3.5. Reaction of plutonium with magnetite and maghemite

Following the reactions of plutonium with an iron(II)-sulfide (chap. 3.3) and an iron(II)-hydroxycarbonate (chap. 3.4), in this chapter the reaction of plutonium with magnetite and maghemite will be discussed (Table 3.5.1). As three of the five Pu-magnetite spectra were considered in detail in chapter 3.2, the discussion will mainly focus on the comparison of the two remaining samples with 8-months reaction time with the 40 day reaction time samples. The reaction conditions (pH, pe, [Pu]) are summarized in figures 3.5.1, 2 (Tables A3.10-18).

Table 3.5.1. List of Pu-magnetite and Pu-maghemite samples to be discussed in this chapter.

Mineral	sample abbreviation	reaction time	Pu added as*	pH $_{final}$**	$[Pu]_{start}$ [µmol/ L]	$[Pu]_{final}$ [nmol/ L]	% Pu sorbed	Pu/mineral loading		
								m/m [ppm]	[µmol/ g]	[nmol/ m^2]
Magnetite	Mg-40d-V-pH8	40d	Pu(V)	7.9	13.4	≤ 1	99.993	584	2.4	32
	Mg-8m-V-pH8	7.6 m	Pu(V)	8.4	15.7	≤ 0.04	100.000	1367	5.6	75
	Mg-40d-III-pH6	40d	Pu(III)	6.1	12.2	3.5	99.971	532	2.2	29
	Mg-40d-III-pH8	40d	Pu(III)	7.9	12.2	≤ 1	99.992	532	2.2	29
	Mg-8m-III-pH8	7.6 m	Pu(III)	8.3	11.7	≤ 0.04	100.000	1017	4.2	56
Maghemite	Mh-40d-V	40d	Pu(V)	5.8	13.4	≤ 1	99.993	575	2.4	24
	Mh-8m-V	7.6 m	Pu(V)	5.9	15.7	0.05	100.000	1347	5.6	77
	Mh-40d-III	40d	Pu(III)	5.8	12.2	0.9	99.993	523	2.2	22
	Mh-8m-III	7.6 m	Pu(III)	5.7	11.7	0.08	99.999	1002	4.1	57

* Initial Pu oxidation state
** pH measured in suspension at the end of the reaction period
# The values preceded by a ≤ sign correspond to the detection limit for Pu concentrations by LSC. As the detection limit changed with the amount of sample solution used, different detection limits (1 vs 0.04 nM) were obtained at the end of the 40 d and 6 m experiments.

3.5.1. Overview of the reaction conditions

After the first three Pu-magnetite samples that were reacted for 40 days, we attempted to prepare two more samples at the higher of the two pH values of this first experiment. As we did not completely succeed in reaching the same pH again, the Pu-magnetite sample set is constituted by five samples prepared at three different pH values (pH ≈ 6.2, pH ≈ 7.8 and pH ≈ 8.4). Apart from pH, the later two samples diverge from the other three in reaction time (8 months vs 40d) and Pu/mineral loadings as a smaller solid/solution ratio and slightly higher Pu concentration had been used for their preparation.

As can be seen in figure 3.5.1a and c, the pH was relatively stable over the time of reaction and very similar for samples pairs prepared from one magnetite stock suspension by adding Pu(III) or Pu(V) (blue and green data points in Fig. 3.5.1 a). Similarly, measured pe values for samples prepared from Pu(V) or Pu(III) at the same pH were quasi identical (Fig. 3.5.1 b).

For all samples, 99.9 % of the added Pu were sorbed very quickly (i.e. until the first sample was taken after 15 to 20 minutes). For Mg-40d-III-pH6, [Pu] oscillates between 10^{-8} M and 10^{-9} M above the detection limit. I am not sure if this slight oscillation of [Pu] is real or is within the uncertainty of the

concentration values. For the 40d pH 8 samples dissolved Pu is at or below the detection limit for the whole 40d reaction period. For the 8-months samples, the detection limit was slightly lower ($4\text{-}5\cdot10^{-10}$ M instead of about $1\cdot10^{-9}$ M) and for both samples [Pu] reaches this level very quickly. For Mg-8m-III-pH8, two concentration values are above the detection limit after about 95 and 147 days of reaction before being at the detection limit for the last two measurements. Again, I am not sure if the one value close to 10^{-9} M for this sample after 147 days of reaction is significantly higher than the preceding and subsequent data points. At the end of the observation period, [Pu] for Mg-8m-III-pH8 and Mg-8m-V-pH8 is at the detection limit below 10^{-10} M.

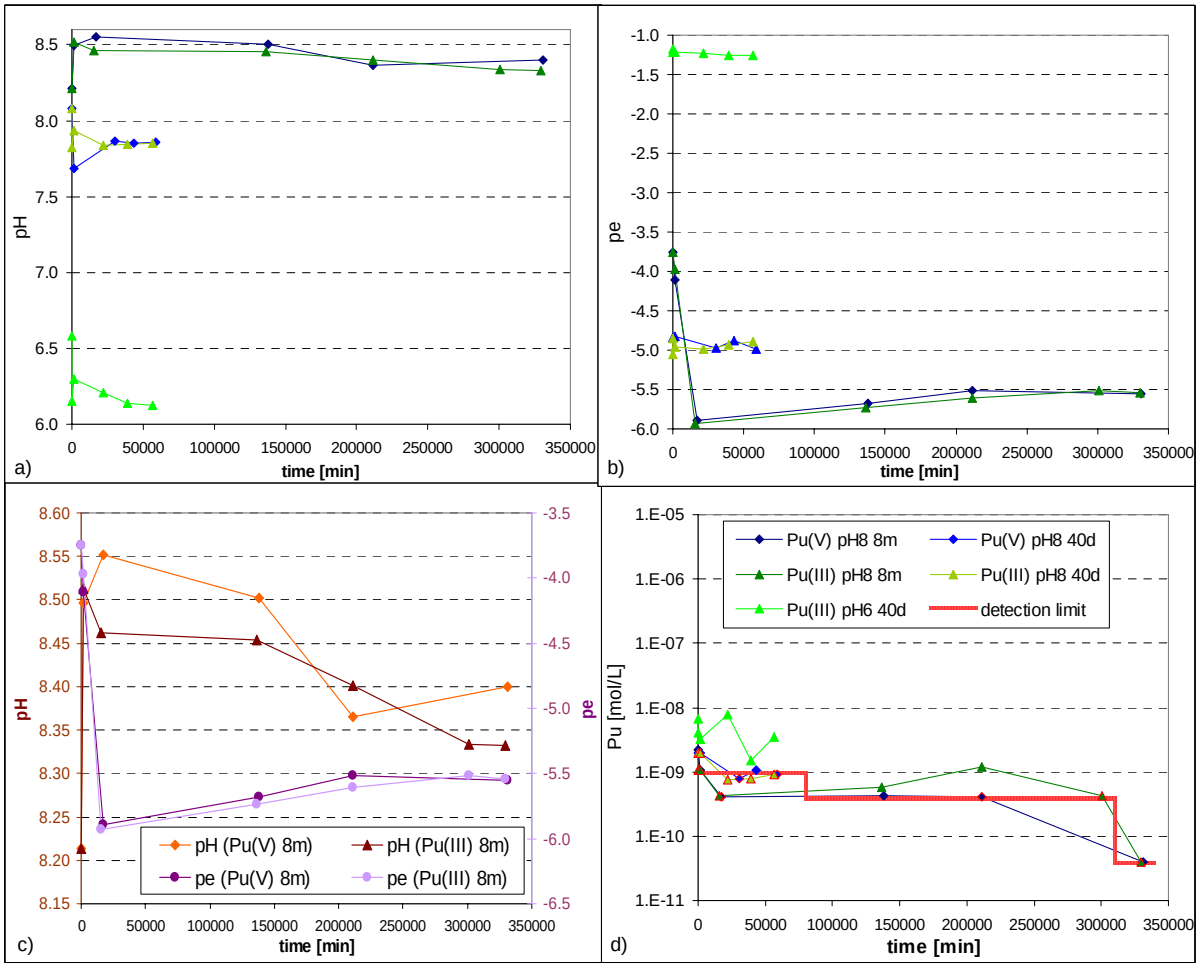

Figure 3.5.1. pH_{sus} (a), pe_{sus} (b), zoom on pH_{sus} (left ordinate) and pe_{sus} (right ordinate) for 8m samples (c), and total dissolved Pu concentrations (d) over time for Pu-magnetite samples. Legend for a, b and d given in d. In d) data points corresponding to values at or below the detection limit are marked by red outer line. The samples are designated by the initial Pu oxidation state and reaction time. Lines between data points are plotted as guide to the eye.

The four Pu-maghemite samples are close to each other in pe and pH, the discrepancy in pH between the two 8-months samples (about 0.3 pH units) being larger than between any of the two and the 40 day samples. Most of the pe values of the 40 d samples are situated between 2 and 3 while the pe of the 8-months samples oscillates between 2 and 4 and seems to increase slightly over the duration of the experiment. For three of the four samples, Pu sorption was fast, [Pu] being at or below the detection limit already at the first measurement. For Pu(V) in the 8-months experiment, sorption was

considerably slower. Only two thirds of Pu had been removed from solution in the first 15 minutes and after 1 day, [Pu] was still about 10^{-6} M, corresponding to a Pu removal from solution of 92 %. Despite a faster sorption with Pu(III), [Pu] for Mh-8m-III-pH6 was in the later reaction period slightly above the values from Mh-8m-V-pH6 and, as for Pu-magnetite samples, I am not sure if this discrepancy is significant or is within the uncertainty range of the concentration values themselves. For both 8-months samples, [Pu] at the end of the observation period was below 10^{-10} M and slightly above the detection limit.

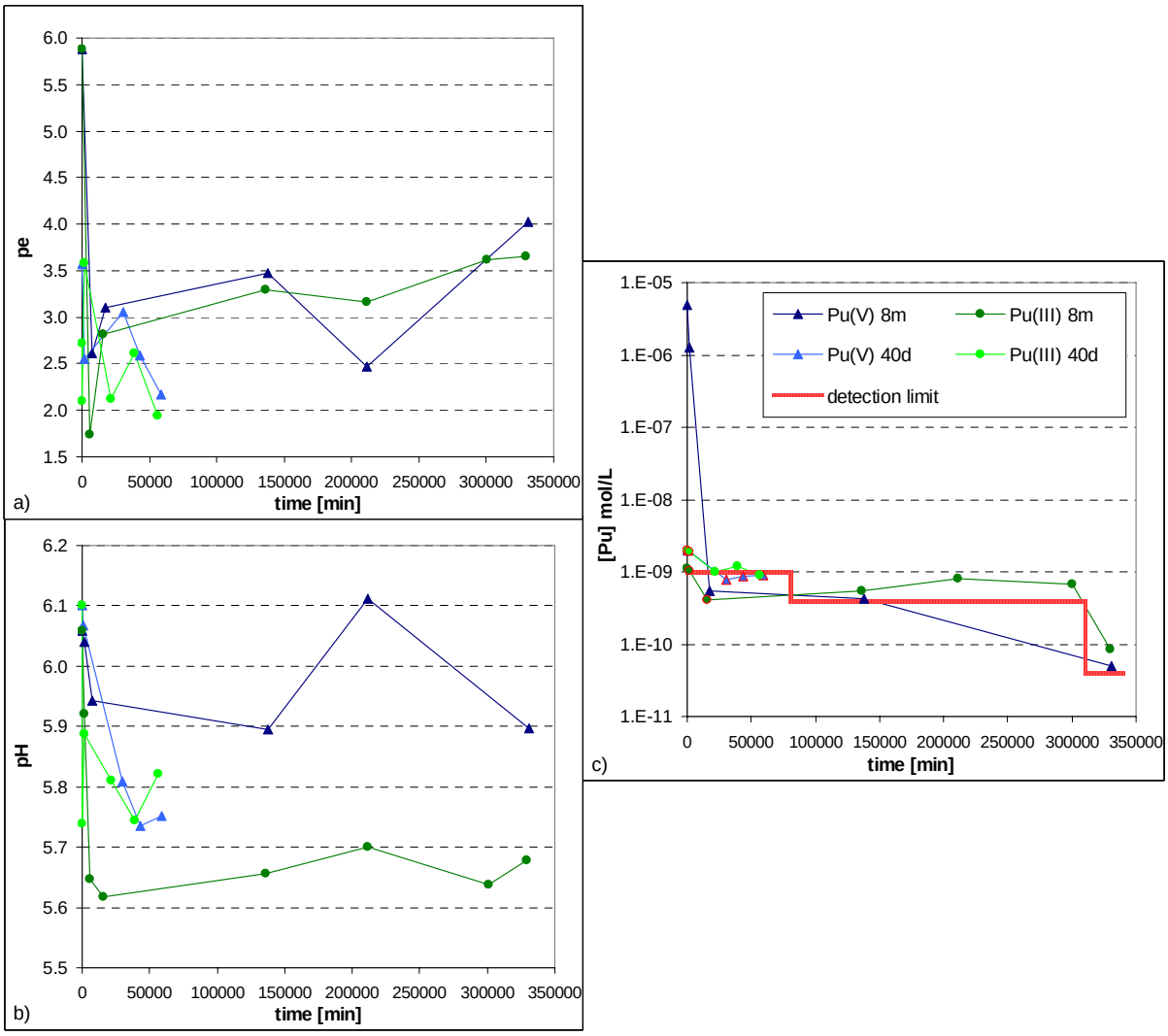

Figure 3.5.2. pe_{sus} (a), pH_{sus} (b) and total dissolved Pu concentrations (c) over time for Pu-maghemite samples. Legend for a, b and d given in c. In c) data points corresponding to values at or below the detection limit are marked by red outer line. The samples are designated by the initial Pu oxidation state and reaction time. Lines between data points are plotted as guide to the eye.

3.5.2. Results from X-ray absorption spectroscopy

As was shown in chapter 3.2, the three 40 d Pu-magnetite samples contain predominantly Pu(III) in the form of a tridentate hexanuclear inner-sphere surface complex. How the XANES of the two 8-months samples (Mg-8m-V-pH8 and Mg-8m-III-pH8) compares to these three 40 d samples and Pu(III)aq and Pu(IV)aq for reference is shown in Fig. 3.5.3a. While the WL position of both 8-months

spectra appears to coincide with the one from Pu(III)aq and Pu(III)ads-Mg, the absorption peak of the Mg-8m-V-pH8 samples appears slightly widened. This impression is confirmed when the five Pu-magnetite spectra are shown superimposed on each other (Fig. 3.5.3 b). That the spectrum of Mg-8m-V-pH8 goes through the crossing points of PuO_2 with $Pu(III)_{ads\text{-}Mg}$ suggests that this sample might contain PuO_2 in addition to the Pu(III) surface complex.

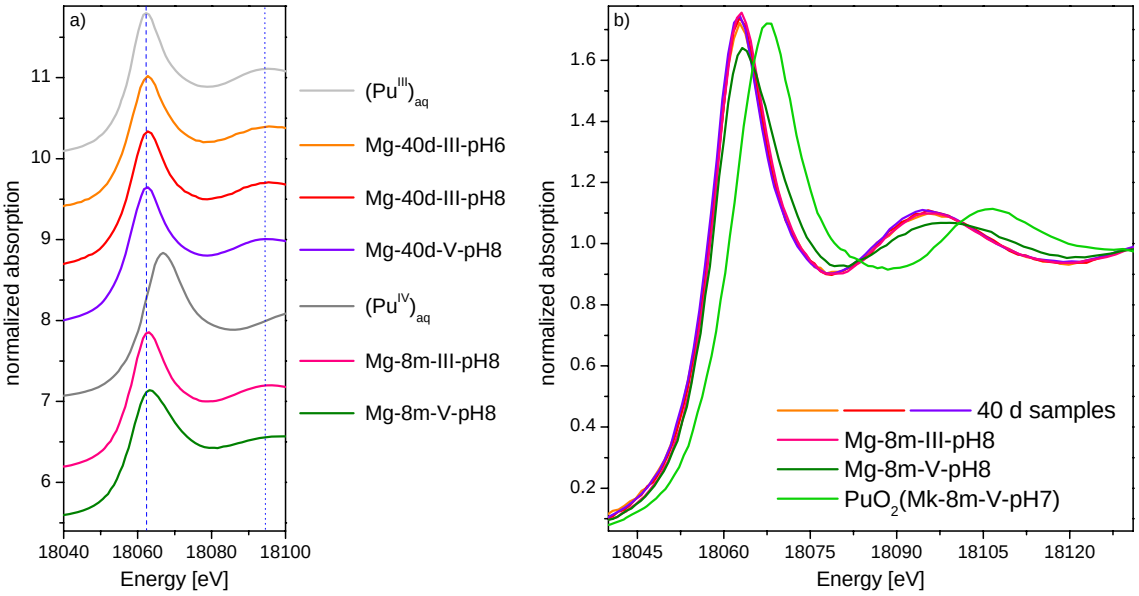

Figure 3.5.3. XANES region of Pu-L_{III}-edge X-ray absorption spectra of Pu-magnetite samples and Pu(III)aq and Pu(IV)aq references for comparison. a) Spectra shifted in height for clarity, dotted lines marking positions of Pu(III) WL maximum and first post-WL maximum, b) Overlay of five Pu-magnetite spectra and Mk-8m-V-pH7 as representative of non-calcinated PuO_2.

Comparison of the EXAFS spectra and FT of $Pu(III)_{ads\text{-}Mg}$, Mk-8m-V-pH8 and PuO_2 confirms this first impression from the XANES (Fig. 3.5.4). All three spectra share the same crossing points in the EXAFS and over the whole k-range the dark green spectrum (Mk-8m-V-pH8) is situated in between the other two. Through the negative interference between the $Pu(III)_{ads\text{-}Mg}$ and PuO_2 spectrum seen in the EXAFS, the peak of the oxygen coordination shell in the FT at about 2 Å (not corrected for phase shift) (Fig. 3.5.4 b) is for Mg-8m-V-pH8 much reduced. Also, in addition to the Pu-Fe peak at 3.2 Å, another peak that coincides in position with the Pu-Pu scattering in PuO_2 at about 3.7 Å in Fig. 3.5.4 b is present in Mg-8m-V-pH8.

To quantify the $Pu(III)_{ads\text{-}Mg}$ and PuO_2 contents in Mg-8m-V-pH8, LC fitting was applied to the XANES region and to k^3-weighted EXAFS spectra (Fig. 3.5.5, Tables 3.5.2). Irrespective of whether Mk-8m-III-pH8 or Mk-8m-V-pH7 is chosen as PuO_2 reference and irrespective of whether the fit is carried out in the XANES or EXAFS regions, a PuO_2 content of about 30 % is identified. That XANES and EXAFS fits yield very similar results suggests that the used reference spectra well represent the Pu(III) and PuO_2 contained in the fitted sample.

Similarly to Pu-chukanovite spectra, the influence of the choice of E_0 for the EXAFS LC fit was tested by setting E_0 to the inflection point for each spectrum and by assigning the same E_0 value to all three

spectra. For this second option, either an intermediate value (18060 eV) or one corresponding to the inflection point of Pu(III) (18057.6) or PuO_2 (18061.4 eV) was used (Table 3.5.2, 3). As for Chuk-8m-III (Table 3.4.4.), choice of E_0 has little influence on the found percent contents of Pu(III) and PuO_2 but somewhat affects the R-factors and sum of percentages. Using its inflection point for each spectrum again leads to results with the lowest sum of percent contents compared to the other options.

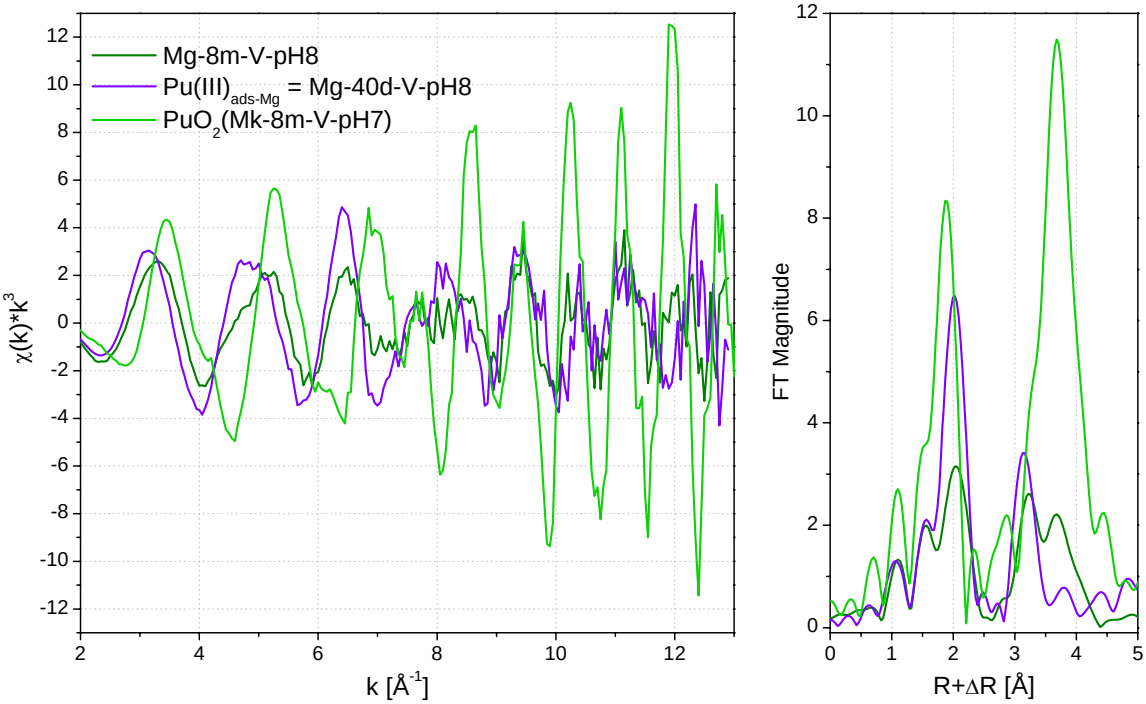

Figure 3.5.4. EXAFS region (a) and FT (b) of Pu-L_{III}-edge X-ray absorption spectra of two Pu-magnetite samples (Mg-40d-V-pH8 and Mg-8m-V-pH8) and PuO_2 (sample Mk-8m-V-pH7). FT based on $3 \leq k \leq 12.6$ Å^{-1}, hannig window, dk1.

Table 3.5.2. LC fit of sample Mg-8m-V-pH8 with $Pu(III)_{ads\text{-}Mg}$ (= Mg-40d-V-pH8) and non-calcinated PuO_2 (either sample Mk-8m-V-pH7 or Mk-8m-III-pH8) as references in the energy range 18040 to 18100 eV and in k-range 2.8–6.8 and 2.8–9.7 Å^{-1}. For fit in k-space E_0 was set to 18060 eV for all spectra. For plot see Fig. 3.5.5.

fit range	references	Pu(III)	PuO_2	sum [%]	R-factor
18040 – 18100 eV	$Pu(III)_{ads\text{-}Mg}$, Mk-8m-III-pH8	71.2 %	28.8 %	100.0	$5.3 \cdot 10^{-5}$
	$Pu(III)_{ads\text{-}Mg}$, Mk-8m-V-pH7	72.3 %	27.8 %	100.1	$7.3 \cdot 10^{-5}$
k = 2.8 – 6.8 Å^{-1}	$Pu(III)_{ads\text{-}Mg}$, Mk-8m-III-pH8	69.9 %	31.6 %	101.5	0.017
	$Pu(III)_{ads\text{-}Mg}$, Mk-8m-V-pH7	70.3 %	29.8 %	100.1	0.019
k = 2.8 – 9.7 Å^{-1}	$Pu(III)_{ads\text{-}Mg}$, Mk-8m-III-pH8	66.2 %	27.9 %	94.1	0.096
	$Pu(III)_{ads\text{-}Mg}$, Mk-8m-V-pH7	66.4 %	24.5 %	90.9	0.102

Shell fitting was not applied as it cannot be expected to yield additional information for a sample like Mg-8m-V-pH8 that contains of a mixture of some 70 % Pu(III) and 30 % PuO_2.

In the 40 d experiments at pH 7.8, reaction with both Pu(V) and Pu(III) had resulted in formation of the Pu(III) inner-sphere surface complex identified in chapter 3.2 and for both initial oxidation states was the only reaction product with magnetite. In the 8-months samples at slightly higher pH, this is the

case only for the the sample to which Pu(III) had been added (Mg-8m-III-pH8) as in the sample to which Pu(V) had been added (Mg-8m-V-pH8) PuO_2 is present in addition to $Pu(III)_{ads\text{-}Mg}$. As was shown in Fig. 3.5.1c, the two 8-months samples reacted under very similar pH and pe conditions and the reaction conditions can thus not account for the difference in reaction products, i.e. the presence of about 30 % PuO_2 in one sample but not in the other.

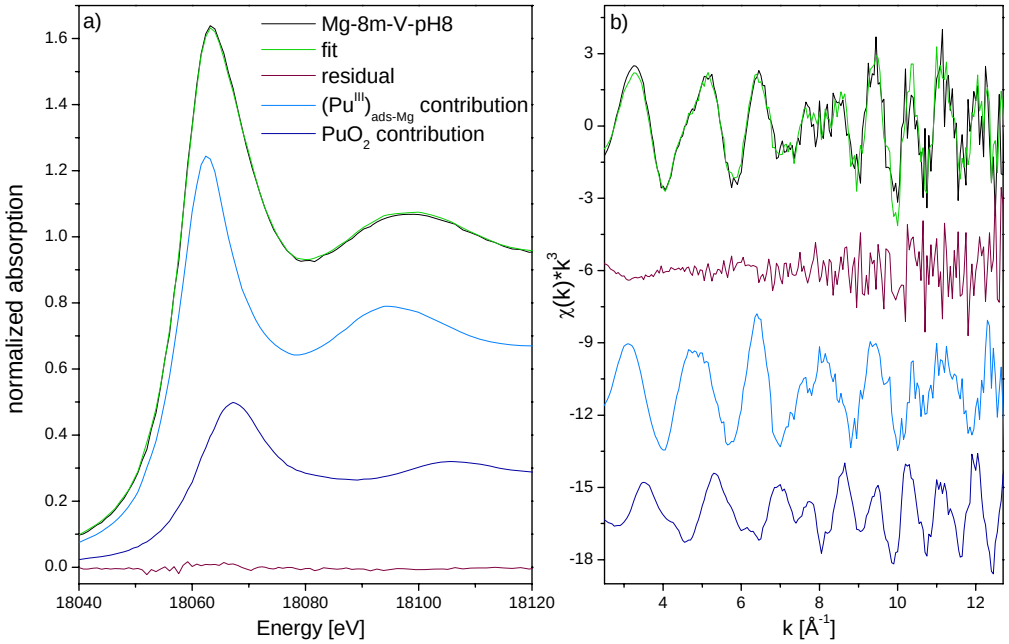

Figure 3.5.5. LC fit of Pu-L_{III}-edge XAS spectrum of sample Mg-8m-V-pH7 using $Pu(III)_{ads\text{-}Mg}$ (sample Mg-40d-V-pH8) and PuO_2 (Mk-8m-III-pH8) as references. a) XANES (fit range: 18040 to 18100 eV), b) EXAFS (fit range 2.8–9.7 $Å^{-1}$, E_0 of sample and reference spectra set to 18060 eV).

Table 3.5.3. LC fit of samples Mg-8m-V-pH8 with $Pu(III)_{ads\text{-}Mg}$ (= Mg-40d-V-pH8) and non-calcinated PuO_2 (Mk-8m-III-pH8) in k-space in the range 2.8–6.8 and 2.8–9.7 $Å^{-1}$. E0 was chosen as the inflection point of each spectrum or was for all three spectra set to the value of one of the reference spectra.

E_0	fit range	Pu(III)	PuO_2	sum [%]	R-factor
infl. point	k = 2.8 – 6.8 $Å^{-1}$	59.9 %	28.6 %	88.5	0.032
	k = 2.8 – 9.7 $Å^{-1}$	57.4 %	25.9 %	83.3	0.102
18057.6 eV	k = 2.8 – 6.8 $Å^{-1}$	69.1 %	30.0 %	99.1	0.027
	k = 2.8 – 9.7 $Å^{-1}$	64.1 %	26.0 %	90.1	0.110
18061.4 eV	k = 2.8 – 6.8 $Å^{-1}$	69.5 %	31.5 %	101.0	0.023
	k = 2.8 – 9.7 $Å^{-1}$	64.4 %	26.8 %	91.2	0.104

When the reaction conditions of the 40 d and 8-months samples (pH 7.8, pe -5 vs pH 8.4, pe -5.5) are compared with respect to the Pu(III) concentration in equilibrium with PuO_2(am,hyd), one can see that for the first pe-pH pair $[Pu(III)_{eq/PuO2}]$ is about one order of magnitude higher than for the second ($5 \cdot 10^{-10}$ vs $3 \cdot 10^{-11}$ M). It is thus not surprising as such that some PuO_2 formed at the higher pH. It is, however, not clear why this occurred only in one of the two samples. One explanation, assuming that thermodynamic equilibrium has not been reached, would be that upon addition to the magnetite

suspension part (or all) of the added Pu(V) was very quickly reduced to Pu(IV) and precipitated as PuO_2 and that further reduction of this PuO_2 to the Pu(III) surface complex is a very slow process. Or, inversely, sorption of Pu(III) happened very fast and oxidation of the Pu(III) surface complex to PuO_2 is a very slow process.

Another explanation can be given taking into account the Pu loading and assuming that equilibrium has been reached. The initial Pu concentration in the sample in which about 30 % PuO_2 were present after reaction (Mg-8m-V-pH8) was about 34 % higher than for the sample in which only Pu(III) was present (Mg-8m-III-pH8). It is well possible that for Pu loadings of 30 nmol/m^2, as in the 40 d samples, and 55 nmol/m^2, as in Mg-8m-III-pH8, the equilibrium concentration of the sorption complex is below the Pu(III) concentration that would be expected to be in equilibrium with PuO_2 while a 30 % higher loading (75 nmol/m^2) would result in an Pu(III) equilibrium concentration above this limit and would thus lead to precipitation of PuO_2.

As it is not known which percentage of the total magnetite surface area is constituted of (111) faces on which the tridentate Pu(III) complex is formed, it is also possible that the number of sorption sites for Pu(III) somewhat limited.

XANES spectra of the four Pu-maghemite samples clearly fall into 2 groups(Fig. 3.5.6): The two 40 d samples are situated roughly half-way between Pu(III)aq and Pu(IV)aq while both 8-months samples have a lower WL intensity but are not shifted compared to Pu(IV)aq. As samples to which initially Pu(III) or Pu(V) had been added yield quasi identical XANES spectra, it is likely that thermodynamic equilibrium has been attained, i.e. that, at the time of sampling, the oxidation state of Pu is governed by the redox conditions of the system and not by the starting conditions.

Quantification by LC fitting using aqueous Pu(III), Pu(IV) and Pu(V) as references yields a Pu(III) content of about 60 % Pu(III) for both 40 d samples and a Pu(IV) content of about 80 % for the 8-months samples (Table 3.5.4). While there is no doubt concerning the mixed oxidation state of the 40 d samples that fall clearly between Pu(III) and Pu(IV), it is not sure if the 8-months samples contain another oxidation state in addition to Pu(IV). The lower WL intensity and heightened post-WL minimum might indicate presence of Pu(V) while the absorption edge at slightly lower energy than Pu(IV)aq might indicate presence of Pu(III). However, also the WL intensity of Pu(III) adsorbed on magnetite (sample Mg-40d-V-pH8, Fig. 3.5.6) is characterized by both a lower WL intensity and an adsorption edge at slightly lower energy than Pu(III)aq. For this reason and as the WL intensity of PuO_2 spectra (or rather of Pu(IV) polymers in general) is lower than that of Pu(IV)aq,[76] it is not excluded that the 8-month Pu-maghemite samples contain Pu(IV) to a higher degree than indicated by LC fitting using aqueous oxidation state references.

The EXAFS spectra of the four Pu-maghemite samples and of two Pu-magnetite samples are shown in figure 3.5.7. Generally, the Pu-maghemite spectra show some similarity to the Pu-magnetite spectra, but also some notable differences are apparent. E.g., the broad oscillation at 5 Å^{-1} changes in shape

when going from Pu(III) adsorbed to magnetite (green) to Pu(IV) on maghemite (dark blue) and the broad oscillation at 8 $Å^{-1}$ apparently splits in two in the 40 d maghemite samples (cyan) and decreases in intensity in the 8-months maghemite spectra. Also, the signal to noise ratio above 10 $Å^{-1}$ is in all five other spectra higher than in Mg-40d-V-pH8. In the Fourier Transform, the Pu-O peak of the Pu-maghemite spectra is strongly reduced in magnitude compared to Pu(III) on magnetite and, at least for the Mh-40d-III, the Pu-Fe peak is considerably increased. Shell fitting results based on a k-range up to 10 $Å^{-1}$ for all spectra in figure 3.5.7 and for Mg-40d-V-pH8 up to 12 $Å^{-1}$ are given in Table 3.5.5 and are shown in figures 3.5.9, 10.

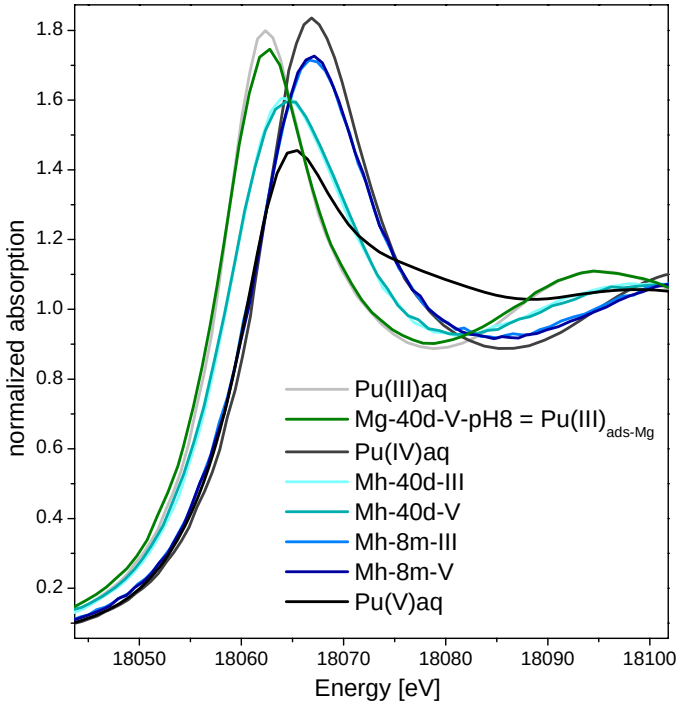

Figure 3.5.6. XANES region of Pu-L_{III}-edge X-ray absorption spectra of Pu-maghemite samples, of Pu(III) adsorbed to magnetite and of Pu(III)aq, Pu(IV)aq, Pu(V)aq references for comparison.

Table 3.5.4. LC fitting of XANES region of Pu-maghemite spectra using Pu(III)aq, Pu(IV)aq and Pu(V)aq as references.

sample	% Pu(III)	% Pu(IV)	% Pu(V)	Sum %
Mh-40d-III	57.6	31.6	10.7	99.9
Mh-40d-V	57.4	34.4	8.1	99.9
Mh-8m-III	7.1	76.5	16.6	100.2
Mh-8m-V	5.7	78.8	15.5	100.0

Firstly, it is surprising to find that the Pu-O distance obtained for the 40 d Pu-maghemite samples is with 2.47 to 2.48 Å very similar to a Pu(III)-O distance (e.g. 2.49 Å in Pu(III) adsorbed to magnetite). In an artificial Pu(III)-Pu(IV) mixture spectrum containing 60 % Pu(III), the fitted distance of 2.44 Å lies clearly in between the Pu(IV)aq and the Pu(III)aq distances (2.39 Å vs 2.49 Å). As according to the XANES these samples must contain both Pu(III) and Pu(IV), it is not clear why the fitted distance

does not indicate this mixture of oxidation states. That the fitted Pu-O coordination number is lower than that of Pu(III) and Pu(IV) (5.8 and 6.3 compared to 8.0 for Pu(III)aq and 7.5 to 7.7 for Pu(III) on magnetite) provides, however, an indication for the fact that Pu-O coordination sphere in the 40 d Pu-maghemite samples is different from Pu(III) on magnetite. Most likely, disorder and negative interference of different Pu-O distances in one sample lead to this decreased in the fitted CN. In addition, if two oxidation states are present and are characterized by different degrees of disorder, the fitted distance will more strongly represent the distance corresponding to the less disordered oxidation state. In such a case, the fitted DW and the fitted correlation numbers are not reliable. For the 40 d maghemite samples this could mean that Pu(III) is present in a well ordered complex while Pu(IV) would be present in more disordered form. Thus the fitted distance would be very close to a pure Pu(III) distance even though only little more than half of the plutonium was present in the Pu(III) complex.

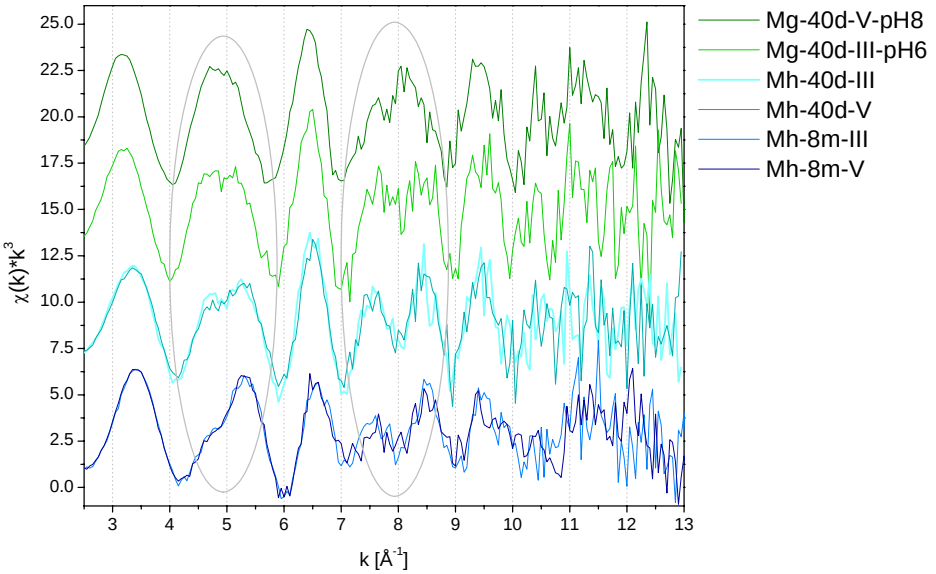

Figure 3.5.7. Comparison of Pu-magnetite (green) and Pu-maghemite (blue) EXAFS spectra.

The 8-months Pu-maghemite spectra are characterized by very large σ^2 values for the Pu-O shell and a mean Pu-O distance of 2.42 Å. This mean distance is slightly larger than what would be expected for Pu(IV) (2.39 Å). The potential Pu(III) or Pu(V) contents of up to 10 and 20 %, respectively, can in themselves not be responsible for this increase in the average Pu-O distance. As can be seen in Table 3.5.5, 20 % Pu(V) hardly affect the mean Pu(IV) distance and 40 % Pu(III) are necessary to raise a Pu-O distance above 2.40 Å. As for the 40 d samples, it is possible that what little Pu(III) might be present in these samples has a less disordered oxygen coordination shell than Pu(IV) and thus influences the fitted distance beyond its percent contribution. Thus the main feature of the oxygen shell of the 8-months maghemite spectra remains the high degree of disorder. It results that,

concerning the oxidation state distribution in all four Pu-maghemite samples, the shell fit does not provide insights beyond what is apparent in the XANES.

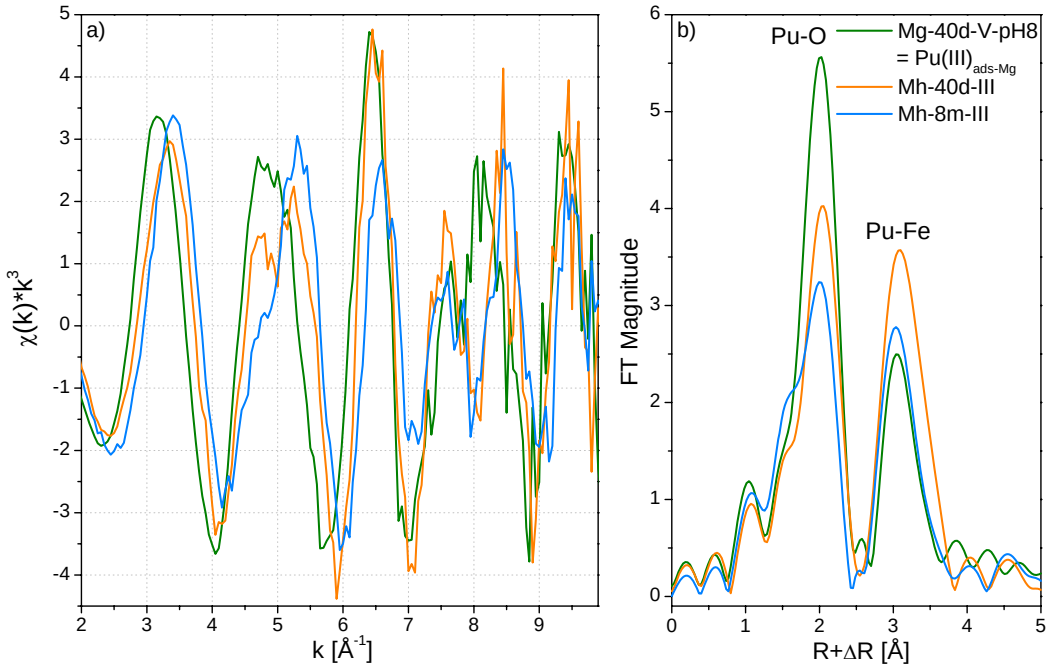

Figure 3.5.8. a) EXAFS and b) Fourier Transform of Pu(III) on magnetite (green) and of Pu(III) reacted with maghemite (40 d light blue vs 8 m, blue) (FT based on $3 \leq k \leq 10$ Å^{-1}, Kaiser-Bessel window, dk1).

Table 3.5.5. Shell fitting results of Pu-maghemite samples, 2 Pu-magnetite samples and 2 artificial oxidation state mixture spectra. Also given is the correlation factor between CN and DW for Pu-O and Pu-Fe paths.*

sample	paths	CN	dist	DW	Δ E	Res [%]	k-range	R-range	corr**
Mg-40d-V-pH8	Pu-O	7.7	2.49	0.0060	8.5	8.3	2.72-12.20	1.35-3.61	0.929
	Pu-Fe	3.3	3.54	0.0067					0.968
Mg-40d-V-pH8	Pu-O	7.7	2.49	0.0061	8.6	5.9	2.71-9.84	1.41-3.93	0.955
	Pu-Fe	5.1	3.54	0.0108					0.974
Pu(III)aq	Pu-O	8.0	2.49	0.0076	10.0	4.4	2.82-10.0	1.44-2.54	0.958
Mg-40d-III-pH6	Pu-O	7.5	2.49	0.0070	8.7	5.2	2.68-9.83	1.39-3.80	0.954
	Pu-Fe	8	3.52	0.0111					0.978
Mh-40d-III	Pu-O	6.3	2.48	0.0085	12.3	7.8	2.83-9.77	1.46-3.89	0.957
	Pu-Fe	9.4	3.54	0.0115					0.980
Mh-40d-V	Pu-O	5.8	2.47	0.0097	12.1	6.3	2.86-9.78	1.50-3.88	0.962
	Pu-Fe	7.5	3.54	0.0102					0.980
60%Pu(III)aq,40%Pu(IV)aq	Pu-O	7.7	2.44	0.0120	10.7	6.2	2.91-10.04	1.31-2.48	0.959
Mh-8m-III	Pu-O	8.7	2.42	0.0163	8.7	9.5	2.91-10.0	1.29-3.69	0.963
	Pu-Fe	7	3.49	0.0123					0.980
Mh-8m-V	Pu-O	9.1	2.42	0.0167	8.3	6.3	2.90-10.0	1.28-3.61	0.965
	Pu-Fe	11.7	3.49	0.0195					0.981
80%Pu(IV)aq,20%Pu(V)aq	Pu-O	10.6	2.38	0.0120	5.4	5.0	2.98-9.70	1.32-2.53	0.964
60%Pu(IV)aq,40%Pu(III)aq	Pu-O	8.3	2.41	0.0119	8.0	3.9	2.91-10.02	1.33-2.56	0.958

*Fit in R-space, $S_0^2 = 0.95$, k^3+k^2 fit mode, Bessel window function, window parameter 3
**corr: correlation between CN with σ^2

Also fitting of the Pu-Fe peak (Fig. 3.5.8) does not yield very clear results. When starting with Pu(III) on magnetite at pH8 (Mg-40d-V-pH8), one can see how the length of the spectrum influences the fitted CN for the Pu-Fe path. When the spectrum is fitted based on a k-range up to 12.2 $Å^{-1}$, a CN that corresponds to the Pu(III) sorption complex identified by MC simulation is found. However, when the spectrum is only fitted up to 10 $Å^{-1}$, the DW increases considerably (from 0.0067 to 0.011) and the CN increases from 3 to 5. The correlation factor between DW and CN is, however, hardly affected. For this kind of sorption complex a k-range up to 10 $Å^{-1}$ is thus not sufficient to obtain a reliable Pu-Fe CN. As in the Pu-maghemite spectra the noise level above 10 $Å^{-1}$ is high, a fit can only be carried out based on a k-range up to 10 $Å^{-1}$. Due to this short fit range in itself and due to the fact that the 40 d do not and that 8-months samples possibly do not contain pure oxidation states it is unlikely to obtain reliable Pu-Fe CN.

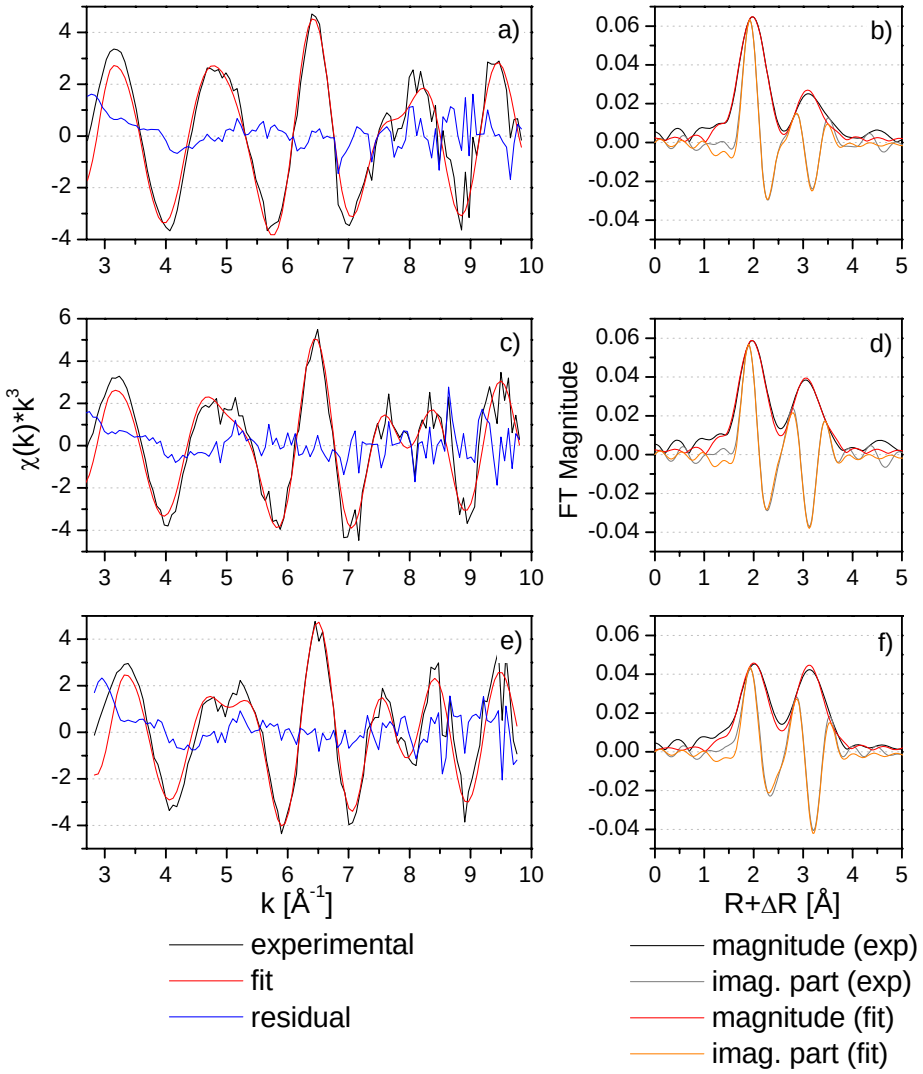

Figure 3.5.9. Shell fits of Pu-magnetite and Pu-maghemite samples from Table 3.5.5. a), b) Mg-40d-V-pH8, c), d) Mg-40d-III-pH6, e), f) Mh-40d-III. a, c, e EXAFS, b, d, f Fourier Transform.

How unreliable the fitted CN for Pu-Fe is becomes apparent when comparing the two 8-months and 40 d samples among themselves. Despite their visually very similar spectra, the fitted CN for the 8-months samples are with values of 7 and almost 12 largely different from each other. Also for the 40 d samples, the difference between 7.5 and 9.4 is large for spectra so similar to each other. The uncertainty associated with the fitted value is thus huge. If CN obtained by fitting a backtransform of the Pu-Fe peak are compared, the difference between the two 8-months samples is reduced to a value of 2 and all maghemite and the Pu-magnetite sample reacted at pH 6 have Pu-Fe coordination numbers of 8 to 11 (Table 3.5.6). For fits in R-space, the Pu-Fe distances for the 8-months samples appear with 3.49 Å to be considerably shorter than 3.54 Å obtained for most of the other samples. When BT fits are carried out, the Pu-Fe distances for all samples are not significantly different.

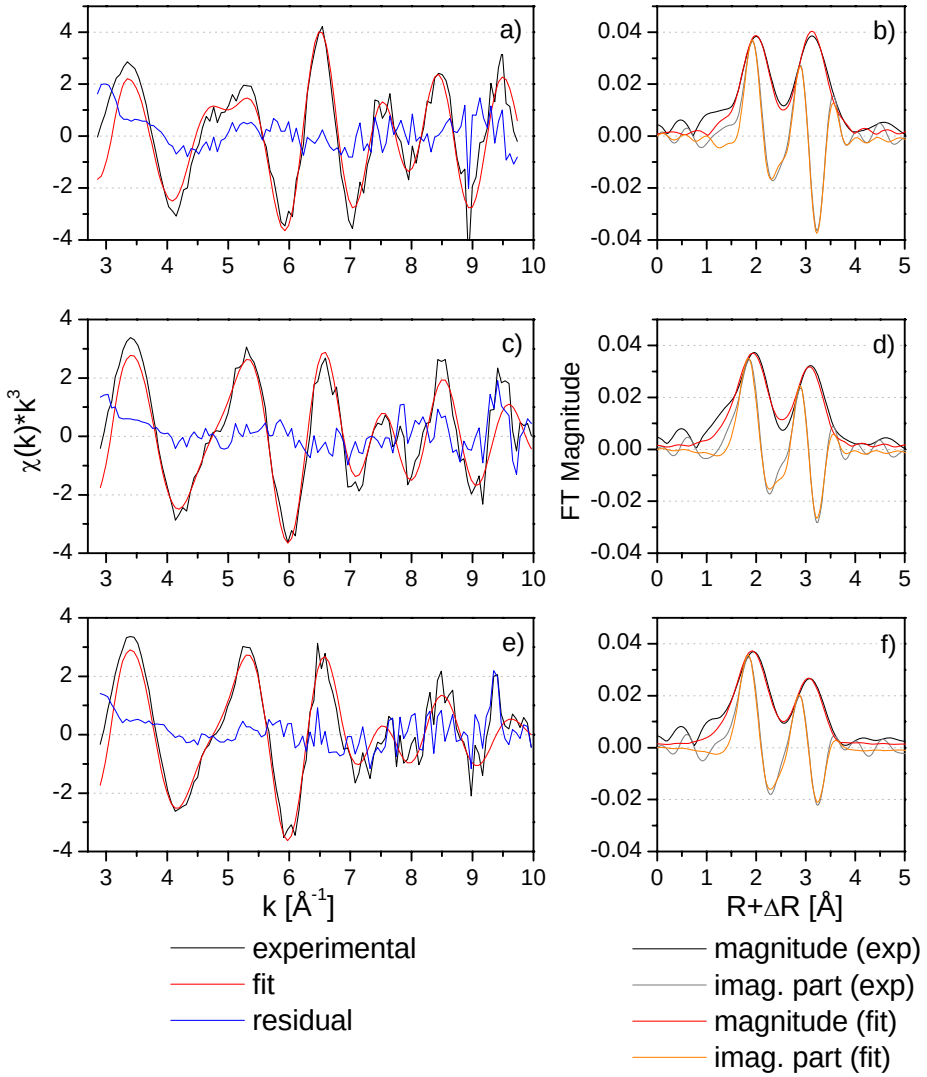

Figure 3.5.10. Shell fits of Pu-magnetite and Pu-maghemite samples from Table 3.5.5. a),b) Mh-40d-V, c), d) Mh-8,-III e), f) Mh-8m-V. a, c, e EXAFS, b, d, f Fourier Transform.

From this it appears that the splitting of the oscillation at 7-9 $Å^{-1}$ visible in the EXAFS spectrum is accompanied by fitted Pu-Fe CN significantly higher than for Pu(III) on magnetite at pH8. But, it is

not clear to what extent the fitted CN, DW and mean Pu-Fe distance are reliable. In the case of an oxidation state mixture as in the 40 d Pu-maghemite samples the same hold true as what was said for Pu-O distances in mixed oxidation state samples. If several Pu oxidation states are present that are characterized by different Pu-Fe distances and if these complexes are differently disordered, the fitted distance will not correctly represent the content in each oxidation state and the fitted DW will not correctly represent the degree of disorder either. In the case of the 8-months maghemite and the pH6 magnetite samples this explanation is less valid as one set of samples contains mainly Pu(IV) and the other predominantly Pu(III). But, similarly, if for samples containing one oxidation state several Pu-Fe distances were present in complexes characterized by different degrees of order, the average distance, DW and CN would not correspond to the weighted geometric average values resulting from the different complexes and their distances, CN and DW.

Table 3.5.6. Shell fitting results after back transforms of the Pu-Fe peak for Pu-maghemite and 2 Pu-magnetite samples.*

sample	paths	CN	dist	DW	Δ E	Res [%]	k-range	corr**
Mg-40d-V-pH8	Pu-Fe	3.4	3.55	0.0068	9.63	12.2	2.78-12.17	0.927
Mg-40d-V-pH8	Pu-Fe	5.5	3.56	0.0119	10.25	14.4	2.78-9.90	0.944
Mg-40d-III-pH6	Pu-Fe	9.3	3.52	0.0129	8.66	11.8	2.70-9.83	0.945
Mh-40d-III	Pu-Fe	10.6	3.54	0.0132	12.43	11.7	2.87-9.68	0.945
Mh-40d-V	Pu-Fe	9.2	3.54	0.0127	12.39	12.1	2.92-9.80	0.946
Mh-8m-III	Pu-Fe	8.0	3.52	0.0126	13.7	12.4	3.00-10.00	0.941
Mh-8m-V	Pu-Fe	10.4	3.52	0.0185	11.8	15.5	3.00-9.93	0.941

*Fit in k-space of k^3-weighted BT spectra, $S_0^2 = 0.95$
corr**: correlation between CN with σ^2

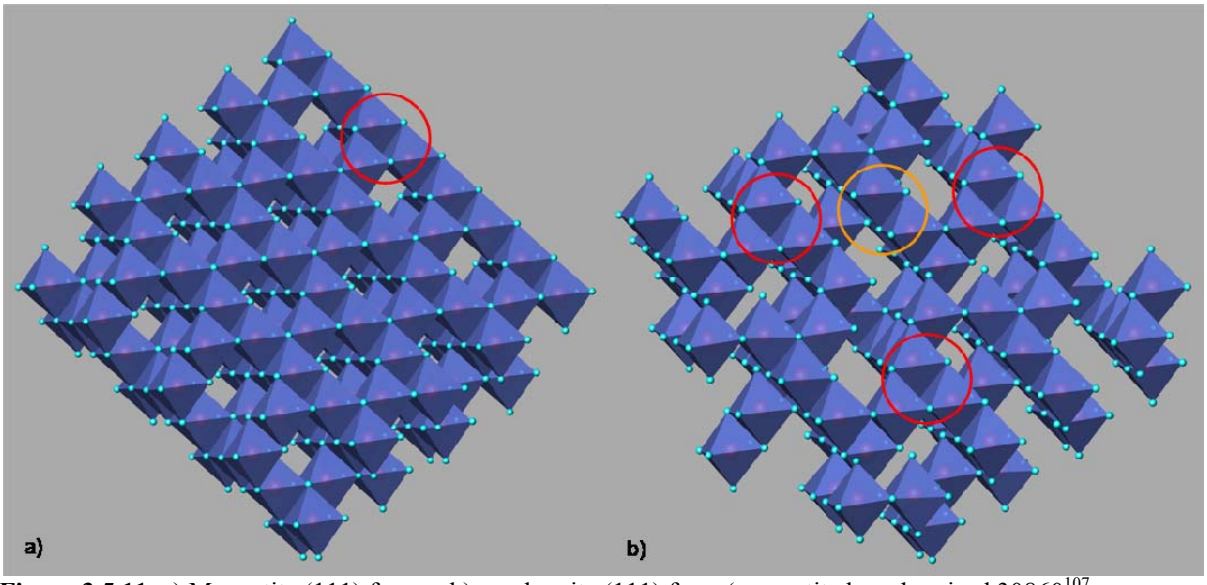

Figure 3.5.11. a) Magnetite (111) face vs b) maghemite (111) face. (magnetite based on icsd 30860[107], maghemite based on icsd 79196[108]).

Assuming that the fitted CN are higher than the in the samples existing, average Pu-Fe coordination numbers, an explanation based on structural disorder might be given. The structure of maghemite is

very similar to that of magnetite but is characterized by vacancies in the octahedral sites of the spinel structure; ideally maghemite can be described as $Fe^{3+}_{tetr}[Fe^{3+}_{5/3}\ \square_{1/3}]_{oct}O_4$ (□ represents a cationic vacancy on the octahedral sublattice).[109] On maghemite surfaces the potential binding sites for Pu(III) and Pu(IV) are thus not necessarily the same as on magnetite and, as can be seen in Fig. 3.5.11, the number of tridentate trinuclear sites for Pu(III) on (111) faces is reduced. If tridentate complexes can still be formed with the oxygen atoms of the remaining FeO_6-octahedra (orange circle in Fig. 3.5.11), the CN for Pu-Fe would be reduced compared to tridentate trinuclear complexes and would result in a lower average CN. However, on a surface characterized by vacancies also bi- or monodentate binding sites might be created that go along with different Pu-Fe distances compared to the tridentate complex. Also, for Pu(IV) sorption complexes with similar structure slightly shorter Pu-Fe distances than in Pu(III) complexes are to be expected due to the shorter Pu-O distance in Pu(IV) compared to Pu(III). Thus the higher fitted CN in maghemite samples would be the result of a DW that does not correctly represent the overall disorder in the samples. However, looking at figure 3.5.8 a) this explanation appears to be somewhat counter-intuitive as disorder rather tents to lead to negative interference in the spectra. But the amplitude of the 7-9 $Å^{-1}$ region of sample Mh-40-III is not reduced compared to Mg-40d-V-pH8.
Another possibility would then be to assume that even though the fitted CN may not be exact they might, indeed, indicate an increased Pu-Fe CN in the samples. A CN higher than three is, however, not easy to explain through a sorption complex characterized by a higher Pu-Fe CN but by the same Pu-Fe distance as was found for the Pu(III) complex on magnetite. For example, would Pu be situated on top of the six-membered FeO_6-octahedra ring on a magnetite (111) face (or a five-membered open ring on maghemite) the complex would be corner and not edge-sharing and a longer Pu-Fe distance would result. Thus the question may be raised if Pu is somehow incorporated into the maghemite structure or if this, compared to magnetite, more open structure undergoes some rearrangement of FeO_6-octahedra around Pu. E.g., by Moessbauer spectrometry, incorporation of Pu into goethite or potentially formation of a Pu-iron oxide was observed.[110]

Throughout this chapter the terms magnetite and maghemite have been used. However, as has been outlined in the materials and methods section, maghemite had been synthesized using H_2O_2 and it is likely that magnetite ($Fe^{II}Fe^{III}_2O_4$) was not completely oxidized to $Fe^{III}_2O_3$ but retained some divalent iron. Thus the solid called maghemite would be rather "partially oxidized magnetite". That partially oxidized magnetite reduces more slowly than stoichiometric magnetite (i.e. with an Fe(II)/Fe(III) ratio of 0.5) has been shown[88] and that a solid with a higher Fe(II) content would be in equilibrium with a higher Pu(III) content in the Pu sorbed to its surface is likely. A higher Fe(II) content in the "maghemite" used for the 40 d experiment is very likely considering the differences in synthesis for the two "maghemite" batches. With respect to its surface, it may, however, be somewhat justified to call the partially oxidized magnetite "maghemite" as oxidation in an acid medium or with oxygen starts by dissolving or oxidizing Fe(II) from the surface, resulting in a surface characterized by

octahedral vacancies typical of maghemite.[111, 112] Thus a magnetite core can be covered by a more or less thick maghemite outer-layer. As under acidic, anoxic conditions Fe(II) is leached from magnetite and maghemite is formed, magnetite at pH 6 will have rather a maghemite than a magnetite surface even though its core may still be retain the stoichiometric Fe(II)/Fe(III) ratio and may thus be sufficient to stabilize Pu(III) on its surface. This explains why concerning the Pu-Fe shell fit the Mg-40d-III-pH6 samples clusters with the maghemite samples.

In this way the presence of Pu(III) at pH 8 and pH 6 with "magnetite" and of Pu(III/IV) and Pu(IV) with "maghemite" can be explained qualitatively. For a quantitative and thermodynamic description the exact Fe(II) contents of all solids would be needed.

3.5.3. Conclusions

In magnetite suspensions under anoxic conditions, Pu(V) can be reduced to Pu(III) and Pu(III) can be stabilized against oxidation to PuO_2 by inner-sphere surface complexation on magnetite (111) faces. However, for the sample with the highest surface coverage and at the highest pH, formation of PuO_2 was observed and accounted for about 30 % of the total Pu. As was shown for Pu sorption on goethite by Zhao et al.(2011),[113] it is quite likely that a similar mechanism can explain formation of PuO_2 in the presence of magnetite once a certain, pH specific, Pu(III) surface loading has been exceeded. This hypothesis could be tested by performing sorption and EXAFS experiments at higher loadings starting from Pu(III), that, if the hypothesis was true, should also result in PuO_2 precipitation.

In line with the Pu-mackinawite and Pu-chukanovite results and with the findings of Zhao et al. (2011), simultaneous presence of Pu(III) and PuO_2 with magnetite could be explained by assuming that the Pu(III) surface complex is in equilibrium with dissolved Pu(III) and that, once, as a function of surface loading, the Pu(III) concentration becomes higher than the equilibrium concentration for PuO_2, PuO_2 starts precipitating.

With maghemite (or rather partially or strongly oxidized magnetite), Pu(III) and Pu(IV) mixtures and predominantly Pu(IV) were found associated with the solid phase. As addition of Pu(III) and Pu(V) led to the same oxidation state distribution in the samples, it can be assumed that Pu is in thermodynamic equilibrium with the solid phase and that the Pu(III) and Pu(IV) contents reflect the redox potential (or "electron pressure") of the solid. Formation of PuO_2 was not observed at the given conditions at pH 6 and surface loadings of up to 80 nmol/m^2. Pu-Fe distances with maghemite are similar to Pu-Fe distances in the Pu(III)-magnetite surface complex. According to the shell fit, Pu-Fe coordination numbers appear higher than for Pu(III) on magnetite. Incorporation of Pu into maghemite or formation of a Pu-iron oxide phase can, therefore, not be excluded.

3.6. Reaction of plutonium with hematite and goethite

3.6.1. Overview of the reaction conditions

In this chapter, the focus will be on the interaction of plutonium with hematite (α-Fe_2O_3) and goethite (α-FeOOH), two iron-(III)-(oxyhydr)oxides whose interaction with plutonium has been investigated numerous times under oxic conditions.[72-75, 114-117] Despite the nominal absence of a reductant in these Fe(III) minerals, reduction of Pu(V) to Pu(IV) and/or formation of Pu(IV) polymers has been observed through or inferred from e.g. a shift of the pH-edge over time,[75] by leaching Pu off the mineral suface and performing speciation analysis by solvent extraction[72] and through the time dependence of sorption.[74] Pu(IV) or Pu(IV)-Pu(V) mixtures were also observed on goethite and Mn-substituted goethite by XANES after reaction with Pu(V) or Pu(VI).[116, 118] It was found, that this reduction reaction was surface mediated and that it could be photo-catalyzed[72] and in many cases, reduction was explained through traces of Fe(II) that were sufficient to reduce nanomolar concentrations of Pu(V). In preparing these samples, our objective was to investigate under anoxic conditions the oxidation state and local structure of plutonium associated with the solid phase. By adding either Pu(III) or Pu(V), we attempted to have an indicator for whether thermodynamic equilibrium has been attained or not, supposing that if the result observed from both initial oxidation states was the same, equilibrium had been established. As it is and as will be shown in detail in this chapter, these samples are raising numerous questions. The reaction conditions (pH, pe, [Pu]) are summarized in figure 3.6.1 (Tables A3.19-22).

Table 3.6.1. List of Pu-hematite and Pu-goethite samples to be discussed in this chapter.

Mineral	sample abbreviation	reaction time	Pu added as*	pH $_{final}$**	$[Pu]_{start}$ [µmol/L]	$[Pu]_{final}$ [nmol/L]	% Pu sorbed	Pu/mineral loading m/m [ppm]	[µmol/g]	[nmol/m^2]
Hematite	He-40d-V	40 d	Pu(V)	7.5	13.4	$\leq 1^{\#}$	99.993	282	1.2	28
	He-8m-V	7.6 m	Pu(V)	7.5	15.7	6.1	99.961	662	2.7	65
	He-8m-III	7.6 m	Pu(III)	7.2	11.7	0.2	99.998	492	2.0	49
Goethite	Go-40d-V	40d	Pu(V)	7.9	13.4	1.9	99.986	1617	6.7	32

* Initial Pu oxidation state

** pH measured in suspension at the end of the reaction period

The values preceded by a ≤ sign correspond to the detection limit for Pu concentrations by LSC. As the detection limit changed with the amount of sample solution used, different detection limits (1 vs 0.04 nM) were obtained at the end of the 40 d and 6 m experiments.

During reaction the pH of the Pu-hematite and Pu-goethite samples was somewhat less stable than in most of the other mineral suspensions, dropping, e.g., from initial pH values of about 7.9 to pH 7.5 and 7.2 for the 8-months Pu-hematite samples (Fig. 3.6.1 a). Experimental redox potentials varied by up to 5 pe units, but no clear drift over time is apparent. (Fig. 3.6.1 b). As can be expected from its high charge, sorption of Pu(III) was fastest, more than 99.9 % having been adsorbed in the first 20

minutes of reaction (Fig. 3.6.1 c). In the Pu(V)-hematite samples, about 91 % and 86 % of Pu(V) were adsorbed in the first 15 minutes (40 d and 8 m sample). With goethite, almost 99 % were adsorbed in the first 16 minutes. In this experiment, the surface area was by a factor of 2.5 to 5 higher than the highest surface area used by Powell et al. (2005)[72] but the Pu concentrations used were about three orders of magnitude greater. If the equation describing the time dependence of Pu sorption in their experiments ($df^{Pu(V)}/dt = -k\, f^{Pu(V)}\, [\alpha\text{-}Fe_2O_3]^{2.08 \pm 0.32}\, [H+]^{-0.39 \pm 0.05}$, with $k = 1.75 \pm 2.05 \cdot 10^{-10}$ $(m^{-2}\, L)^{2.08}$ $(mol^{-1}L)^{-0.39}$ (s^{-1})) is applied to our experimental conditions (480 and 240 m^2/L, Pu start concentrations, pH), the first data point can be made to lie on the resulting [Pu]-over-time curve if the uncertainty of the equation parameters is taken into account. Thus, with a value for k of $5 \cdot 10^{-11}$ for the 40 d and of $1.3 \cdot 10^{-10}$ in the 8-month experiment and using the lowest possible power for the surface area ($[\alpha\text{-}Fe_2O_3]^{2.08\text{-}0.32\, =\, 1.76}$), the light and dark violet curves going through the first data point in Fig. 3.6.1 d result. The sorption process described by these curves would lead to concentrations below the detection limit in less than 2 hours.

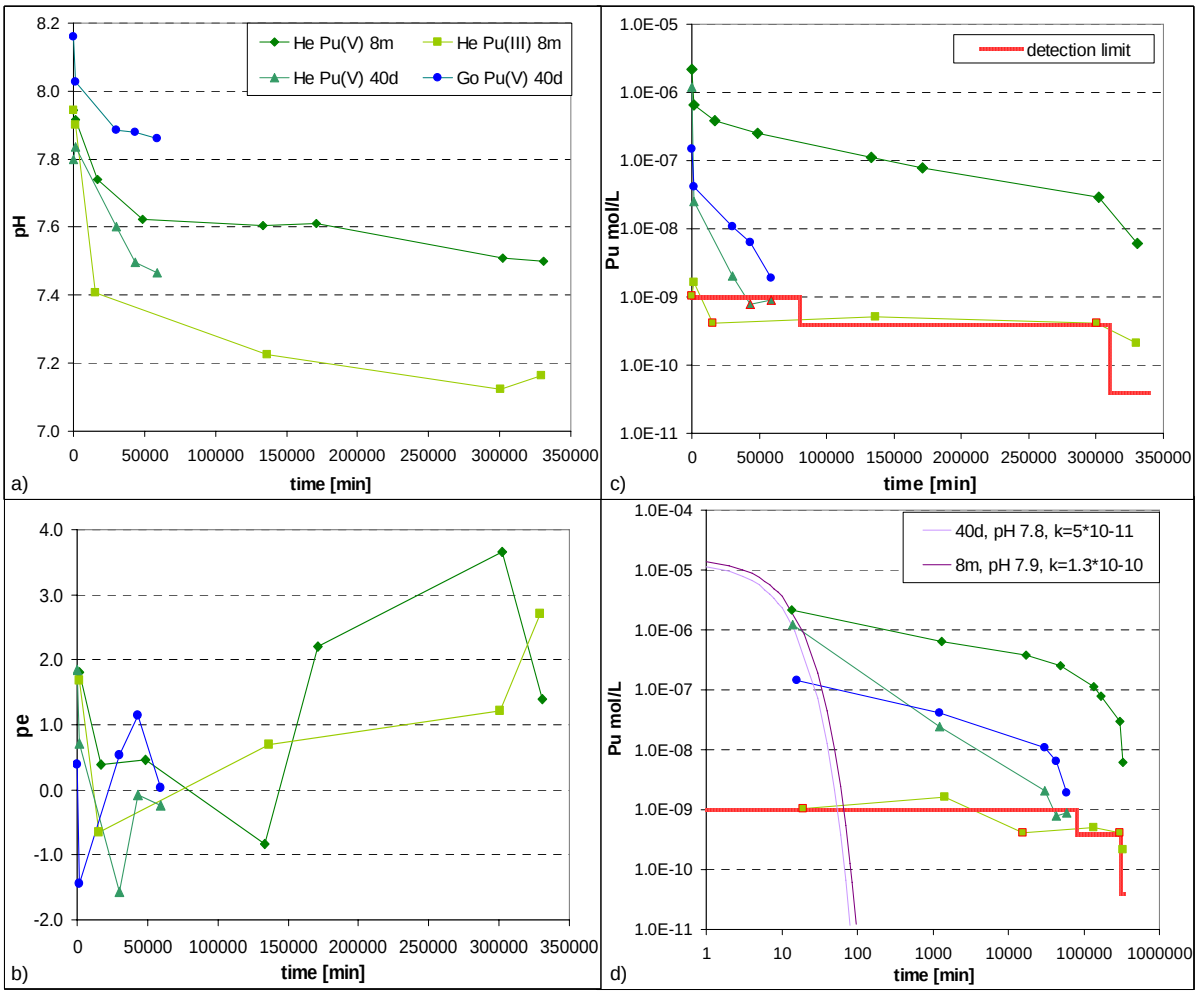

Figure 3.6.1.. . pH_{sus} (a), pe_{sus} (b), total dissolved Pu concentrations over time for Pu-hematite and Pu-goethite samples (c) and comparison with Pu-sorption as a function of time using the formula published by Powell et al. (2005)[72]. Key to samples for b, c, d given in a. In c) and d) data points corresponding to values at or below the detection limit are marked by red outer line. Samples are designated by the initial Pu oxidation state and reaction time. Lines between data points are plotted as guide to the eye.

The observed time dependence of Pu(V) sorption is, however, very different: in the 8-month sample the Pu concentration decreases very slowly over the whole period of investigation and is, after almost 8-months of reaction, still $\geq 10^{-9}$ M. Such a slow decrease over time after initially fast sorption might suggest that the number of sorption sites is limited and in our experiments probably exceeded. Linearisation of the time dependent decrease of the Pu concentration according to a pseudo-first order reaction yields rate constants of $1.4 \cdot 10^{-6}$ s^{-1} for the 40 d and of $1.6 \cdot 10^{-7}$ s^{-1} for the 8-months experiment (Fig. 3.6.2). These constants are similar to the ones observed, e.g., in the Mk-8m-V-pH7 ($k = 1.4 \cdot 10^{-7}$ s^{-1}) and Mk-8m-III-pH8 samples ($k = 1.6 \cdot 10^{-6}$ s^{-1}). As in these Pu-mackinawite samples PuO_2 has formed and as growth or ripening of PuO_2 might be related to the observed rate constants, one might expect that the slow decrease of Pu solution concentrations in the Pu-hematite samples is due to formation and growth (or ripening) of PuO_2 particles. By TEM formation of PuO_2 nanoparticles has recently been observed under oxic conditions with both goethite and hematite.[113, 117, 119]

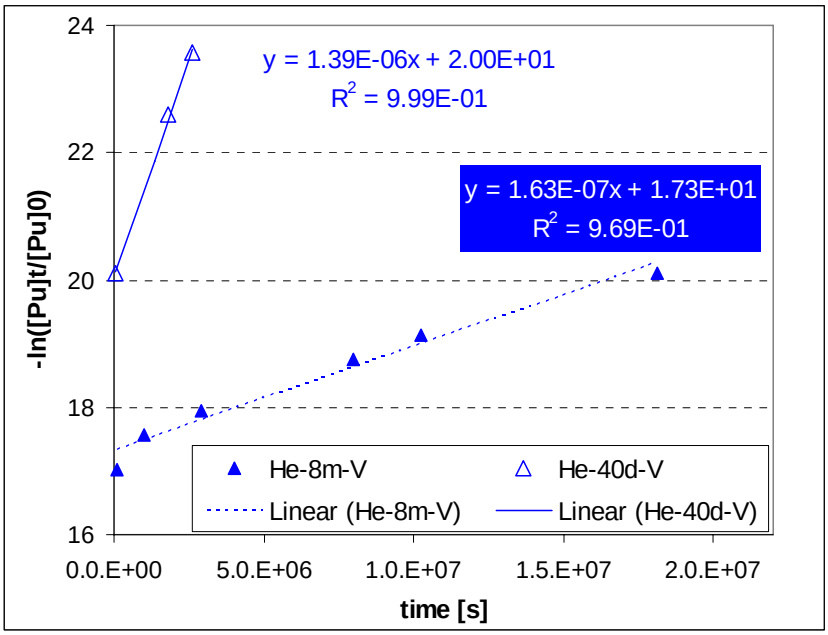

Figure 3.6.2. Plot of $-\ln([Pu]_t/[Pu]_0)$ over time and resulting apparent rate constants according to (pseudo)-first order kinetics.

3.6.2. Results from X-ray absorption spectroscopy

In 3.6.3, the XANES region of Pu-hematite and goethite spectra is compared to aqueous Pu(IV) and Pu(V) reference spectra, one maghemite 8-month sample and two Pu-mackinawite samples in which formation of PuO_2 occurred. The WL position and intensity of the of the He-8m-III sample coincides with that of Mh-8m-III and is very close to the two Pu-mackinawite samples. The WL intensities of the other two Pu-hematite spectra and of the goethite sample are somewhat lower. The Go-40d-V spectrum has the lowest WL intensity and is also the most shifted upwards in the post-WL minimum region (18075 to 18093 eV). It is interesting to note, that all sample spectra seem to share one crossing point with the Pu(IV)aq spectrum at about 18073 eV and the hematite, goethite and maghemite spectra again share a crossing point with the Pu(IV)aq spectrum at about 18094 eV. As the Pu(V)aq spectrum

does not go through the same crossing points, it is clear that Pu(IV)aq and Pu(V)aq cannot be perfect references for the Pu(IV) and/or Pu(V) contained in the hematite and goethite samples. Up to 18088 eV, the hematite, goethite and maghemite spectra cluster more or less closely around the two Pu-mackinawite PuO_2-like spectra. From this point on, they are shifted to higher absorption values and thus seem to constitute a group of spectra whose XANES region is noticeably different from PuO_2-like spectra. If, nonetheless, aqueous Pu(III), Pu(IV) and Pu(V) are used as references for oxidation state analysis by LC fitting and iterative target testing (Fig. 3.6.4, 5), Pu(IV) contents of 65 to 75 % for Pu-hematite spectra and about 60 % for the Pu-goethite spectrum are found (Tables 3.6.2, 3). Thus the spectrum with the most intensive WL (He-8m-III) is assigned the highest Pu(IV) content and the spectrum with the lowest WL (Go-40d-V) the highest Pu(V) content. As one can see in Fig. 3.6.4, 3.6.5 and Table 3.6.4, the LC fit results in rather large standard deviations between data and fit and the factors identified by ITT and representing the oxidation states do not completely coincide with the aqueous species.

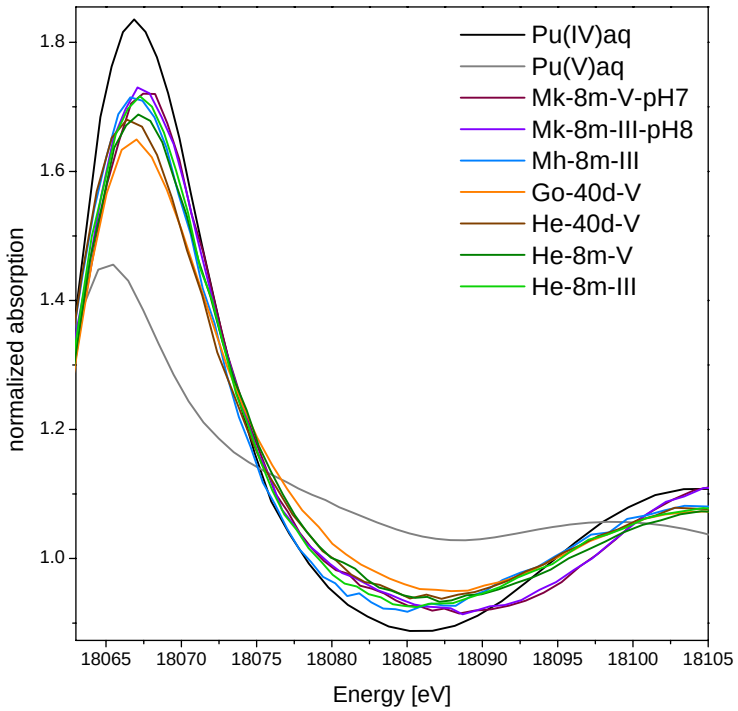

Figure 3.6.3. XANES region of Pu-L_{III}-edge X-ray absorption spectra of Pu-hematite and Pu-goethite samples, of Pu(IV)aq and Pu(V)aq for reference and of one Pu-maghemite sample and two Pu-mackinawite samples for comparison.

Thus, for Pu-hematite and goethite spectra, the situation concerning oxidation state analysis of the XANES region is similar to that of the Pu-maghemite 8-months samples: If polymerisation of Pu(IV) can occur (or if sorption to a mineral surface can potentially have a similar effect), the WL intensity can be lowered and the post-WL minimum intensity heightened compared to acqueous Pu(IV). This effect is not easily differenciated from presence of Pu(V) and by ITT or LC fitting the Pu(V) content can be easily overestimated.

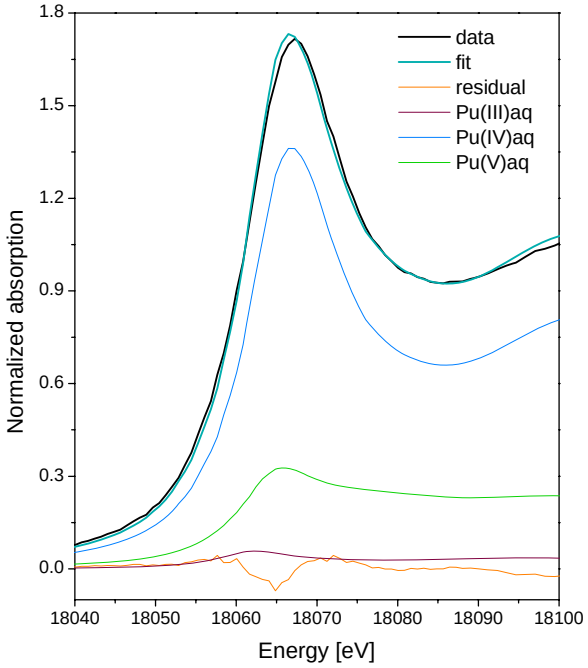

Figure 3.6.4. XANES region linear combination fit of sample He-8m-III using aqueous Pu references.

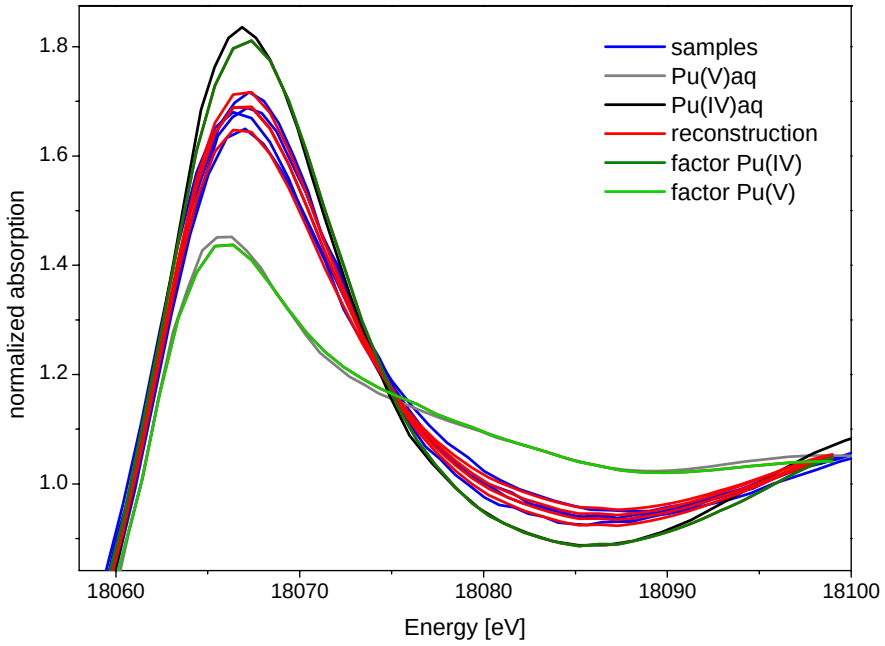

Figure 3.6.5. Pu(IV)aq and Pu(V)aq references, Pu-hematite and Pu-goethite spectra (blue), reconstruction of samples spectra (red) and Pu(IV) and Pu(V) factors (green) found by ITT analysis of the XANES region (18040 – 18100 eV) (plot corresponds to data in Table 3.6.3 b).

In the EXAFS and Fourier Transform, the Pu-hematite and goethite spectra largely ressemble each other; only the spectrum of sample He-8m-III is slightly different in showing a stronger peak at about 2.9 Å (R+ΔR) in the FT and in showing an additional oscillation at 8 $Å^{-1}$ in a k-range (7.5 to 10 $Å^{-1}$) where the other three spectra appear void of any oscillation apart from the more or less high background noise.

Table 3.6.2. Oxidation state analysis of the XANES region of Pu-hematite and Pu-goethite spectra using linear combination (LC) fitting in the range 18040 – 18100 eV. Aqueous Pu(III), Pu(IV) and Pu(V) species are used as references.

sample	Pu(III)	Pu(IV)	Pu(V)	% total
He-40d-V	8.7 ± 1.1 %	64.1 ± 1.9 %	27.9 ± 2.2 %	100.7 ± 5.2
He-8m-V	0.0 ± 0.0 %	67.8 ± 0.0 %	32.5 ± 0.0 %	100.3 ± 0.0
He-8m-III	3.2 ± 1.0 %	74.4 ± 1.8 %	22.5 ± 2.0 %	100.1 ± 4.8
Go-40d-V	0.0 ± 0.0 %	56.1 ± 0.0 %	44.3 ± 0.0 %	100.4 ± 0.0

Table 3.6.3. Oxidation state distribution in Pu-hematite and Pu-goethite samples according to analysis of the XANES region (18040 – 18100 eV) by Iterative Target Testing (ITT) using a) Pu(III)aq, Pu(IV)aq and Pu(V)aq or b) Pu(IV)aq and Pu(V)aq as references.

sample	Pu(III)	Pu(IV)	Pu(V)	% total
a)				
He-40d-V	9.4 %	64.5 %	26.9 %	100.8
He-8m-V	0.5 %	68.6 %	31.2 %	100.3
He-8m-III	3.7 %	75.2 %	21.2 %	100.1
Go-40d-V	0.0 %	56.5 %	44.4 %	100.9
b)				
He-40d-V	-	66.7 %	34.1 %	100.8
He-8m-V	-	68.9 %	31.3 %	100.2
He-8m-III	-	76.0 %	24.1 %	100.1
Go-40d-V	-	56.8%	43.7 %	100.4

Table 3.6.4. Standard deviation (SD) of Pu-hematite and goethite spectra fits (LC) and reproductions (ITT) and of reference spectra reproductions (ITT).

spectrum	SD ITT	SD LC fit
$Pu(III)_{aq}$	0.014	
$Pu(IV)_{aq}$	0.020	
$Pu(V)_{aq}$	0.009	
He-40d-V	0.009	0.020
He-8m-V	0.009	0.024
He-8m-III	0.007	0.021
Go-40d-V	0.008	0.020

Compared to the aqueous Pu species (Pu(IV), Pu(V)) and to a Pu(IV) containing samples with strong iron-backscattering (Mh-8m-III), such an absence of oscillation is probably indicative of negative interference, that is of backscattered electron waves that cancel out with each other. The question is then what might be the cause of this negative interference.

If PuO_2 formed in the presence of hematite and/or goethite, one might expect this to be visible in the EXAFS as, on the one hand, the pH is quite high and even PuO_2 nano-colloids formed at pH 2 display a clearly PuO_2 – like spectrum (e.g. Fig. 3 in Rothe et al., 2004)[76] and as, on the other hand, the presence of PuO_2 in sample Mg-8m-V-pH8 was well apparent in addition to the Pu(III) sorption complex, indicating that in the presence of an iron oxide PuO_2 well discernable in an EXAFS spectrum can form. In the shell fit (Table 3.6.5), the peak at 2.9 Å in the FT in figure 3.6.6. can be fitted with a

Pu-Fe backscattering path and a Pu-Fe distance of 3.36 Å is found. A Pu-Pu path corresponding to a distance of 3.82 Å (as present in PuO_2) and a Pu-Fe path corresponding to 3.36 Å do not cancel out with each other (not shown). That Pu-Pu from PuO_2 and the longer Pu-Fe distance of 3.54 Å do not cancel out, could be observed in the spectrum of Mg-8m-V-pH8. Presence of a sorption complex and of PuO_2, thus, cannot account for the observed negative interference resulting in the cancelling of oscillation in the mentioned k-range.

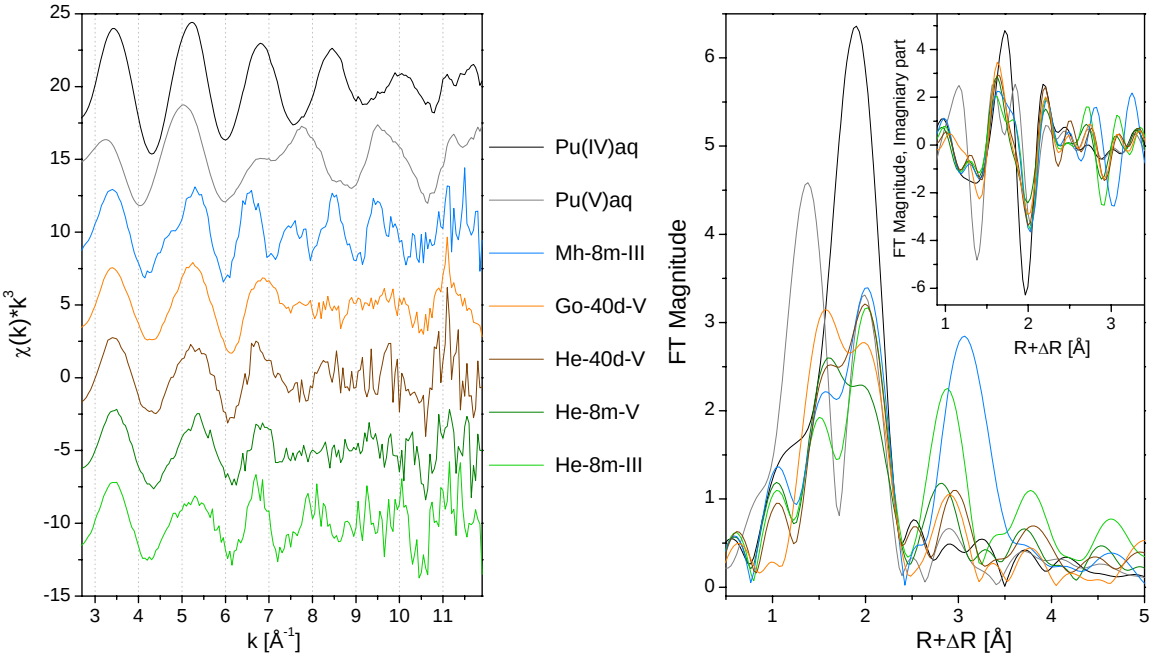

Figure 3.6.6. EXAFS spectra (left), FT Magnitude (right) and imaginary part of the FT (right, inset) of Pu-hematite and goethite spectra, of Mh-8m-III for comparison and of Pu(IV)aq and Pu(V)aq for reference. FT based on $2.9 \leq k \leq 10.7$ Å^{-1}, hannig window, dk1.

If PuO_2 is formed in the Pu-hematite and goethite samples, is would be surprising that this was not visible in the EXAFS spectrum. However, in the case of goethite, formation of a plutonium oxide with bcc and not fcc structure of the oxygen lattice and resulting from epitaxial growth on goethite was identified.[117] One might thus speculate if formation of such a distorted Pu oxide or interference between the Pu-Pu paths in such a structure and a Pu-Fe paths might be responsible for the observed absence of oscillations between 7.5 to 10 Å^{-1} in the Pu-hematite and goethite EXAFS spectra (Fig. 3.6.6). In the Fourier Transform, the oxygen shell of all Pu-hematite and goethite spectra is reduced in magnitude compared to Pu(IV)aq and Pu(V)aq and appears split. Thus, for a fit based on a k-range beyond 8 Å^{-1}, two Pu-O shells need to be implemented to obtain a good reproduction. The Pu-hematite and goethite spectra were fitted based on several k-ranges (Table 3.6.5) depending on the signal intensity. As can be seen from the fits of sample He-8m-III, the fit range has an influence on the Pu-O distances found for the two Pu-O shells while the Pu-Fe distance is left (almost) unaffected (for an exemplary fit of He-8m-III, see Fig. A3.2 in the annex). Whether the DW factores of the two Pu-O paths are correlated to be equal to each other or not also affects the found distances. However, for these spectra, the fits did not converge when the DWs were not correlated. Compared to an artificial

mixture spectrum containing 30 % Pu(V)aq and 70 % Pu(IV)aq, the found Pu-O distances are quite similar based on the longest k-range, but when the fits based on a k-range up to 7 $Å^{-1}$ is considered, the different noise levels become apparent and put the comparability of these spectra (He-8m-III vs 80 % Pu(IV)aq-30 % Pu(V)aq) into question. Also for PuO_2-colloids, Pu-O distances close to 2.20 Å and 2.40 Å were found (albeit with non-correlated DW). Thus the shell fit, in this case, does not help to identify the presence of Pu(V) in the He-8m-III spectrum and does not allow to differenciate between a disordered Pu(IV) surface complex and a PuO_2 nano-particle either.

For all samles, the fitted Pu-Fe distance of 3.36 Å is similar to the path identified for Pu(IV) sorbed to Mn-goethite (Hu et al.)[116] but differs from the distance attributed by Kersting et al. (2003)[118] to a Pu-Fe scattering paths on goethite (3.43 Å).

Table 3.6.5. Shell fitting results of Pu-hematite and Pu-goethite and of 2 artificial oxidation state mixture spectra. Also given is the correlation factor between CN and DW for Pu-O and/or Pu-Fe paths.*

sample	paths	CN	dist	DW	Δ E	Res [%]	k-range	R-range	corr**
He-8m-III	Pu-O	2.8	2.19	0.0062[c]	6.5	10.3	2.94-10.71	1.24-3.26	
	Pu-O	5.7	2.41	0.0062[c]					
	Pu-Fe	3.8	3.35	0.0109					0.9790
	Pu-O	2.6	2.17	0.0038[d]	5.9	1.3	2.94-8.75	1.15-3.43	
	Pu-O	5.3	2.40	0.0038[d]					
	Pu-Fe	4.6	3.36	0.0131					0.9900
	Pu-O	11.0	2.38	0.0233	5.7	2.4	2.94-7.03	1.00-3.48	0.9871
	Pu-Fe	2.7	3.37	0.006[f]					
	Pu-O	2.3	2.14	0.0147[e]	5.5	1.0	2.94-7.03	0.00-3.53	
	Pu-O	8.7	2.37	0.0147[e]					
	Pu-Fe	2.9	3.36	0.0071					0.9997
He-8m-V	Pu-O	8.5	2.33	0.0179	4.1	3.2	2.97-7.13	0.93-3.49	
	Pu-Fe	3.6	3.36	0.0176					0.9876
He-40d-V	Pu-O	7.7	2.35	0.0140	5.0	2.6	2.94-8.1	1.12-3.51	
	Pu-Fe	3.9	3.37	0.0164					0.9852
Go-40d-V	Pu-O	3.0	2.21	0.0006[g]	4.8	7.5	2.94-10.89	1.18-3.23	
	Pu-O	3.8	2.40	0.0006[g]					
	Pu-Fe	2.0	3.36	0.0125					0.9718
	Pu-O	5.6	2.31	0.0066	1.52	2.3	2.94-7.25	1.02-2.54	
60%Pu(IV)aq, 40%Pu(V)aq	Pu-O	3.7	2.20	0.0051[h]	5.4	8.1	2.96-10.96	1.05-2.44	
	Pu-O	7.4	2.39	0.0051[h]					
	Pu-O	0.5	1.76	0.0025[f]	9.1	1.9	2.96-10.96	1.05-2.44	
	Pu-O	2.6	2.26	0.0034[i]					
	Pu-O	5.0	2.42	0.0034[i]					
	Pu-O	9.5	2.35	0.0108	4.0	6.2	2.96-7.2	0.93-2.60	
70%Pu(IV)aq, 30%Pu(V)aq	Pu-O	3.3	2.21	0.0048[j]	6.3	6.2	2.97-10.34	0.99-2.42	
	Pu-O	7.2	2.39	0.0048[j]					
	Pu-O	9.9	2.36	0.0109	4.5	4.4	2.97-7.22	0.98-2.57	0.9842

*Fit in R-space, $S_0^2 = 0.95$, k^3+k^2 fit mode, Bessel window function, window parameter 3
**corr: correlation between CN with σ^2
a, b, c, d, e, g, h, i, j: values correlated to be equal to each other, f: value fixed during the fit

Based on the mean Pu-O distances of 2.33 Å and 2.35 Å, it is likely that in the two Pu(V)-hematite samples either formation of PuO_2 occurred or that Pu(V) is, indeed, present, as these fitted distances are not characteristic of Pu(IV)aq. Similarly, for the goethite sample, a mean Pu-O distance of 2.31 Å is too short for Pu(IV)aq or for what can be expected for a Pu(IV) sorption complex.

To differentiate between a Pu(IV) or Pu(V) sorption complex on hematite and goethite and formation of PuO_2, it would probably be useful to collect EXAFS spectra of samples to which either Pu(III), Pu(IV) and Pu(V) have been freshly added. Also, TEM is likely to provide information on the presence or absence of PuO_2 formation under the given conditions.

3.6.3. Conclusions

Through addition of Pu(III) and Pu(V) to hematite and of Pu(V) to goethite, we could spectroscopically confirm that Pu(IV) is the dominant oxidation state associated with the solid phase. Initial sorption of Pu was fast under all conditions but in the Pu(V) 8-months hematite sample a very slow decrease of the dissolved Pu concentration was observed over the whole reaction period. The mechanism behind this slow Pu-removal could not be elucidated from the spectroscopical data. Whether formation of PuO_2 occurred with either hematite or goethite was not visible in the EXAFS spectra. In the Pu-hematite sample to which Pu(III) had been added, a Pu-Fe scattering paths at 3.36 Å was clearly visible. In the other spectra, a smaller peak could be fitted with the same Pu-Fe path. Due to negative interference in a large part of the EXAFS spectrum, it could not be elucidated to what extent Pu is present as a sorption complex in these samples.

Annex to chapter 3

Parameters acquired during sample preparation and reaction to characterize the reaction conditions (pe and pH measured in suspension (susp) or after centrifugation (cen), [Pu] after 10 kD ultrafiltration, Fe(II) and Fe(II) after ultrafiltration) are tabulated in the following Tables (A3.1 to A3.22).
Samples are tabulated in the order Pu-mackinawite (Table A3.1-6), Pu-chukanovite (Table A3.7-9), Pu-magnetite (Table A3.10-14), Pu-maghemite (Table A3.15-18), Pu-hematite (Table A3.19-21), Pu-goethite (Table A3.22). Table order for each mineral is Pu(III)-40d, Pu(III)-8m, Pu(V)-40d, Pu(V)-8m.

Table A3.1. Reaction conditions for sample Mk-40d-III-pH6

Mk-40d-III-pH6							
time* [min]	pH_{susp}	pe_{susp}	pH_{cen}	pe_{cen}	Fe(II) [mol/L]	Fe(III) [mol/L]	Pu [mol/L]
0	6.18	- 4.04	6.09		$1.13 \cdot 10^{-3}$	$5.60 \cdot 10^{-4}$	$1.22 \cdot 10^{-5\#}$
22							$2.02 \cdot 10^{-6}$
272	5.73	- 4.29					$2.04 \cdot 10^{-6}$
1507	6.00	- 4.28	6.20	- 0.31	$2.04 \cdot 10^{-3}$	≤ det. limit	$2.03 \cdot 10^{-6}$
21772	6.15	- 4.21	6.53	- 0.11	$7.23 \cdot 10^{-4}$	$7.42 \cdot 10^{-5}$	$1.84 \cdot 10^{-7}$
39217	6.32	- 4.16	7.60	- 0.76	$8.90 \cdot 10^{-4}$	$3.62 \cdot 10^{-5}$	$4.42 \cdot 10^{-7}$
56452	6.42	- 4.11	7.50	- 0.60	$7.48 \cdot 10^{-4}$	$5.37 \cdot 10^{-5}$	$9.93 \cdot 10^{-8}$

*time after addition of Pu, #$[Pu]_{start}$ – calculated from $[Pu]_{stock\ solution}$ and V_{sample}

Table A3.2. Reaction conditions for sample Mk-8m-III-pH7

Mk-8m-III-pH7							
time* [min]	pH_{susp}	pe_{susp}	pH_{cen}	pe_{cen}	Fe(II) [mol/L]	Fe(III) [mol/L]	Pu [mol/L]
0	7.52	- 4.02	7.41	- 1.01			$1.17 \cdot 10^{-5\#}$
14							$2.86 \cdot 10^{-6}$
1428				- 2.84			$2.72 \cdot 10^{-6}$
5843	6.32	- 3.97					
15713	6.88	- 4.50	6.91	- 1.51			$1.79 \cdot 10^{-6}$
47213	6.80	- 4.41	6.53	3.23			$2.48 \cdot 10^{-6}$
132113	7.18	- 4.43					$2.21 \cdot 10^{-6}$
169613	7.04	- 4.38					$2.21 \cdot 10^{-6}$
300653	7.01	- 4.29	5.50	- 2.17			$1.85 \cdot 10^{-6}$
329513	7.07	- 4.26			$3.65 \cdot 10^{-4}$	$6.79 \cdot 10^{-6}$	$2.50 \cdot 10^{-8}$

*time after addition of Pu, #$[Pu]_{start}$ – calculated from $[Pu]_{stock\ solution}$ and V_{sample}

Table A3.3. Reaction conditions for sample Mk-8m-III-pH8

Mk-8m-III-pH8							
time* [min]	pH_{susp}	pe_{susp}	pH_{cen}	pe_{cen}	Fe(II) [mol/L]	Fe(III) [mol/L]	Pu [mol/L]
0	8.64	- 4.73	8.35	- 2.33			$1.17 \cdot 10^{-5\#}$
14							$9.69 \cdot 10^{-7}$
1428	7.75	- 3.53					$2.33 \cdot 10^{-7}$
15713	7.43	- 5.09	7.52	- 2.68			$4.35 \cdot 10^{-8}$
47213	7.54	- 5.18	7.71	3.11			$2.57 \cdot 10^{-9}$
132113	7.79	- 5.20					*$4.10 \cdot 10^{-10}$*
211253	8.05	- 4.97	8.05	- 1.57	$9.28 \cdot 10^{-5}$	$1.10 \cdot 10^{-6}$	*$4.07 \cdot 10^{-10}$*
300653	7.80	- 5.18					$5.45 \cdot 10^{-10}$
329513	7.97	- 4.83			$9.05 \cdot 10^{-6}$	$1.36 \cdot 10^{-7}$	*$3.93 \cdot 10^{-11}$*

*time after addition of Pu, #$[Pu]_{start}$ – calculated from $[Pu]_{stock\ solution}$ and V_{sample},
[Pu] values in red italics are ≤ detection limit

Table A3.4. Reaction conditions for sample Mk-40d-V-pH8

Mk-40d-V-pH8							
time* [min]	pH_{susp}	pe_{susp}	pH_{cen}	pe_{cen}	Fe(II) [mol/L]	Fe(III) [mol/L]	Pu [mol/L]
0	7.80	- 5.48	8.44	- 5.76	$1.11 \cdot 10^{-5}$	≤ det. limit	$1.34 \cdot 10^{-5\#}$
17							*$1.94 \cdot 10^{-9}$*
1250	8.22	- 5.24			$1.66 \cdot 10^{-5}$	≤ det. limit	*$1.94 \cdot 10^{-9}$*
30270	8.08	- 5.13	8.45	- 1.81	$8.78 \cdot 10^{-6}$	≤ det. limit	*$7.80 \cdot 10^{-10}$*
43260	8.04	- 4.97	8.33	- 3.65	$1.49 \cdot 10^{-5}$	≤ det. limit	$1.93 \cdot 10^{-9}$
59025	8.02	- 4.90	8.38	- 2.13	$7.99 \cdot 10^{-6}$	≤ det. limit	*$8.93 \cdot 10^{-10}$*

*time after addition of Pu, #$[Pu]_{start}$ – calculated from $[Pu]_{stock\ solution}$ and V_{sample},
[Pu] values in red italics are ≤ detection limit

Table A3.5. Reaction conditions for sample Mk-8m-V-pH7

Mk-8m-V-pH7							
time* [min]	pH_{susp}	pe_{susp}	pH_{cen}	pe_{cen}	Fe(II) [mol/L]	Fe(III) [mol/L]	Pu [mol/L]
0	7.52	- 4.02	7.41	- 1.01			$1.57 \cdot 10^{-5\#}$
14							$3.63 \cdot 10^{-6}$
1354	6.53	- 3.77					$3.14 \cdot 10^{-6}$
17141	7.16	- 4.42	7.29	- 0.92			$2.04 \cdot 10^{-6}$
48641	7.02	- 4.28	6.46	3.33			$2.19 \cdot 10^{-6}$
133541	6.81	- 4.36					$1.08 \cdot 10^{-6}$
171041	7.15	- 4.29					$7.74 \cdot 10^{-7}$
302081	6.77	- 4.29	6.84	0.56			$2.57 \cdot 10^{-7}$
330941	6.85	- 4.14			$3.68 \cdot 10^{-4}$	$2.49 \cdot 10^{-6}$	$2.51 \cdot 10^{-9}$

*time after addition of Pu, #$[Pu]_{start}$ – calculated from $[Pu]_{stock\ solution}$ and V_{sample}

Table A3.6. Reaction conditions for sample Mk-8m-V-pH8

Mk-8m-V-pH8							
time* [min]	pH_{susp}	pe_{susp}	pH_{cen}	pe_{cen}	Fe(II) [mol/L]	Fe(III) [mol/L]	Pu [mol/L]
0	8.64	- 4.73	8.35	- 2.33			$1.57 \cdot 10^{-5\#}$
14							$9.56 \cdot 10^{-10}$
1354	8.53	- 4.53					*$1.05 \cdot 10^{-9}$*
17141	8.42	- 5.29	7.70	- 1.79			*$4.15 \cdot 10^{-10}$*
137801	8.35	- 5.32					*$4.00 \cdot 10^{-10}$*
211241	8.25	- 5.16	8.10	- 1.82	$2.799 \cdot 10^{-5}$	≤ det. limit	$1.10 \cdot 10^{-9}$
330941	8.37	- 5.23			$4.24 \cdot 10^{-6}$	$5.77 \cdot 10^{-7}$	*$3.98 \cdot 10^{-11}$*

*time after addition of Pu, #$[Pu]_{start}$ – calculated from $[Pu]_{stock\ solution}$ and V_{sample},
[Pu] values in red italics are ≤ detection limit

Table A3.7. Reaction conditions for sample Chuk-8m-III

Chuk-8m-III							
time* [min]	pH_{susp}	pe_{susp}	pH_{cen}	pe_{cen}	Fe(II) [mol/L]	Fe(III) [mol/L]	Pu [mol/L]
0	7.95	- 4.48	8.04	- 2.62			$2.01 \cdot 10^{-5\#}$
13							$1.05 \cdot 10^{-9}$
1427	8.34	- 4.07					$1.30 \cdot 10^{-9}$
15712	8.49	- 4.99	8.38	- 4.30			$8.15 \cdot 10^{-7}$
47212	8.53	- 4.18	7.46	1.61			$4.01 \cdot 10^{-10}$
132112	8.56	- 4.03					$1.39 \cdot 10^{-9}$
211252	8.69	- 4.58	7.52	- 2.84	$1.86 \cdot 10^{-4}$	≤ det. limit	$5.59 \cdot 10^{-10}$
300652	8.60	-5.98					$4.19 \cdot 10^{-10}$
329512					$1.56 \cdot 10^{-5}$	$2.92 \cdot 10^{-7}$	$4.03 \cdot 10^{-11}$

*time after addition of Pu, #$[Pu]_{start}$ – calculated from $[Pu]_{stock\ solution}$ and V_{sample},
[Pu] values in red italics are ≤ detection limit, Fe(II) below quantification limit

Table A3.8. Reaction conditions for sample Chuk-40d-V

Chuk-40d-V							
time* [min]	pH_{susp}	pe_{susp}	pH_{cen}	pe_{cen}	Fe(II) [mol/L]	Fe(III) [mol/L]	Pu [mol/L]
0	8.83	- 6.22	8.67	- 4.97	$2.01 \cdot 10^{-5}$	$2.05 \cdot 10^{-6}$	$1.34 \cdot 10^{-5\#}$
27							$1.94 \cdot 10^{-9}$
1252	8.43	- 4.92			$1.39 \cdot 10^{-5}$	$1.53 \cdot 10^{-6}$	$1.95 \cdot 10^{-9}$
30272	8.38	- 4.54	8.11	- 2.19	$5.45 \cdot 10^{-5}$	≤ det. limit	$7.81 \cdot 10^{-10}$
43262	8.34	- 5.41	8.03	- 3.97	$5.18 \cdot 10^{-5}$	≤ det. limit	$1.66 \cdot 10^{-9}$
59027	8.39	- 5.84	8.03	- 3.28	$6.92 \cdot 10^{-5}$	≤ det. limit	$8.92 \cdot 10^{-10}$

*time after addition of Pu, #$[Pu]_{start}$ – calculated from $[Pu]_{stock\ solution}$ and V_{sample},
[Pu] values in red italics are ≤ detection limit

Table A3.9. Reaction conditions for sample Chuk-8m-V

Chuk-8m-V							
time* [min]	pH_{susp}	pe_{susp}	pH_{cen}	pe_{cen}	Fe(II) [mol/L]	Fe(III) [mol/L]	Pu [mol/L]
0	7.95	- 4.48	8.04	- 2.62			$2.70 \cdot 10^{-5\#}$
13							$2.08 \cdot 10^{-9}$
1313	8.43	- 4.02					$1.31 \cdot 10^{-9}$
17100	8.37	- 4.17	7.93	- 2.95			$4.11 \cdot 10^{-10}$
137760	8.48	- 5.62					$7.84 \cdot 10^{-9}$
171000	8.55	- 4.14					$4.08 \cdot 10^{-10}$
211200	8.53	- 4.20	7.65	- 2.55	$2.96 \cdot 10^{-4}$	$4.39 \cdot 10^{-6}$	$5.29 \cdot 10^{-10}$
330900					$7.30 \cdot 10^{-5}$	$8.66 \cdot 10^{-7}$	$4.26 \cdot 10^{-11}$

*time after addition of Pu, #$[Pu]_{start}$ – calculated from $[Pu]_{stock\ solution}$ and V_{sample},
[Pu] values in red italics are ≤ detection limit

Table A3.10. Reaction conditions for sample Mg-40d-III-pH6

Mg-40d-III-pH6							
time* [min]	pH_{susp}	pe_{susp}	pH_{cen}	pe_{cen}	Fe(II) [mol/L]	Fe(III) [mol/L]	Pu [mol/L]
0	6.58	- 1.17	6.04		$2.56 \cdot 10^{-3}$	$1.38 \cdot 10^{-3}$	$1.22 \cdot 10^{-5\#}$
23							$6.65 \cdot 10^{-9}$
273	6.15	- 1.21					$4.06 \cdot 10^{-9}$
1483	6.29	- 1.22	6.07	- 0.18	$4.94 \cdot 10^{-3}$	$1.99 \cdot 10^{-4}$	$3.24 \cdot 10^{-9}$
21758	6.21	- 1.23	5.24	2.71	$2.45 \cdot 10^{-3}$	$1.81 \cdot 10^{-4}$	$7.93 \cdot 10^{-9}$
39203	6.14	- 1.26	5.50	2.90	$3.01 \cdot 10^{-3}$	$1.88 \cdot 10^{-5}$	$1.49 \cdot 10^{-9}$
56438	6.12	- 1.26	5.48	2.89	$3.13 \cdot 10^{-3}$	≤ det. limit	$3.51 \cdot 10^{-9}$

*time after addition of Pu, #$[Pu]_{start}$ – calculated from $[Pu]_{stock\ solution}$ and V_{sample},
[Pu] values in red italics are ≤ detection limit

Table A3.11. Reaction conditions for sample Mg-40d-III-pH8

Mg-40d-III-pH8							
time* [min]	pH_{susp}	pe_{susp}	pH_{cen}	pe_{cen}	Fe(II) [mol/L]	Fe(III) [mol/L]	Pu [mol/L]
0	8.08	- 5.05	7.90		$9.21 \cdot 10^{-6}$	$5.33 \cdot 10^{-6}$	$1.22 \cdot 10^{-5\#}$
19							*$1.95 \cdot 10^{-9}$*
269	7.82	- 4.86					*$1.94 \cdot 10^{-9}$*
1504	7.94	- 4.96	7.66	- 2.46	$2.27 \cdot 10^{-5}$	≤ det. limit	*$1.93 \cdot 10^{-9}$*
21769	7.84	- 4.99	6.61	1.95	$1.99 \cdot 10^{-5}$	$1.59 \cdot 10^{-6}$	*$7.70 \cdot 10^{-10}$*
39214	7.85	- 4.93	7.48	2.06	$2.15 \cdot 10^{-5}$	≤ det. limit	*$7.71 \cdot 10^{-10}$*
56449	7.85	- 4.89	7.36	2.14	$2.18 \cdot 10^{-5}$	≤ det. limit	*$9.00 \cdot 10^{-10}$*

*time after addition of Pu, #$[Pu]_{start}$ – calculated from $[Pu]_{stock\ solution}$ and V_{sample},
[Pu] values in red italics are ≤ detection limit

Table A3.12. Reaction conditions for sample Mg-8m-III-pH8

Mg-8m-III-pH8							
time* [min]	pH_{susp}	pe_{susp}	pH_{cen}	pe_{cen}	Fe(II) [mol/L]	Fe(III) [mol/L]	Pu [mol/L]
0	8.21	- 3.75	7.64	- 1.10			$1.17 \cdot 10^{-5\#}$
18							$1.05 \cdot 10^{-9}$
1458	8.51	- 3.97					$1.06 \cdot 10^{-9}$
15743	8.46	- 5.93	8.12	- 3.37			$4.18 \cdot 10^{-10}$
136403	8.45	- 5.74					$5.87 \cdot 10^{-10}$
211283	8.40	- 5.61			$4.98 \cdot 10^{-5}$	≤ det. limit	$1.21 \cdot 10^{-9}$
300683	8.33	- 5.51					$4.21 \cdot 10^{-10}$
329543	8.33	- 5.55			$3.75 \cdot 10^{-6}$	$2.98 \cdot 10^{-7}$	$3.96 \cdot 10^{-11}$

*time after addition of Pu, #$[Pu]_{start}$ – calculated from $[Pu]_{stock\ solution}$ and V_{sample},
[Pu] values in red italics are ≤ detection limit, Fe(II) below quantification limit

Table A3.13. Reaction conditions for sample Mg-40d-V-pH8

Mg-40d-V-pH8							
time* [min]	pH_{susp}	pe_{susp}	pH_{cen}	pe_{cen}	Fe(II) [mol/L]	Fe(III) [mol/L]	Pu [mol/L]
0	8.08	- 4.83	7.85	1.47	$1.33 \cdot 10^{-5}$	$1.30 \cdot 10^{-6}$	$1.34 \cdot 10^{-5\#}$
15							*$1.93 \cdot 10^{-9}$*
1238	7.69	- 4.82			$1.51 \cdot 10^{-5}$	≤ det. limit	*$1.96 \cdot 10^{-9}$*
30268	7.86	- 4.98	7.39	2.32	$1.63 \cdot 10^{-5}$	≤ det. limit	*$7.83 \cdot 10^{-10}$*
43258	7.85	- 4.88	7.44	0.52	$1.84 \cdot 10^{-5}$	≤ det. limit	$1.05 \cdot 10^{-9}$
59023	7.86	- 4.98	7.21	2.41	$1.93 \cdot 10^{-5}$	≤ det. limit	*$9.09 \cdot 10^{-10}$*

*time after addition of Pu, #$[Pu]_{start}$ – calculated from $[Pu]_{stock\ solution}$ and V_{sample},
[Pu] values in red italics are ≤ detection limit

Table A3.14. Reaction conditions for sample Mg-8m-V-pH8

Mg-8m-V-pH8							
time* [min]	pH_{susp}	pe_{susp}	pH_{cen}	pe_{cen}	Fe(II) [mol/L]	Fe(III) [mol/L]	Pu [mol/L]
0	8.21	- 3.75	7.64	- 1.10			$1.57 \cdot 10^{-5\#}$
15							$2.21 \cdot 10^{-9}$
1328	8.50	- 4.11					$1.05 \cdot 10^{-9}$
17115	8.55	- 5.90	7.15	1.14			$4.08 \cdot 10^{-10}$
137775	8.50	- 5.68					$4.28 \cdot 10^{-10}$
211215	8.37	- 5.51	6.26	3.33	$2.39 \cdot 10^{-6}$	≤ det. limit	$4.06 \cdot 10^{-10}$
330915	8.40	- 5.55			$2.43 \cdot 10^{-6}$	$9.33 \cdot 10^{-7}$	4.00E-11

*time after addition of Pu, #$[Pu]_{start}$ – calculated from $[Pu]_{stock\ solution}$ and V_{sample},
[Pu] values in red italics are ≤ detection limit

Table A3.15. Reaction conditions for sample Mh-40d-III

Mh-40d-III							
time* [min]	pH_{susp}	pe_{susp}	pH_{cen}	pe_{cen}	Fe(II) [mol/L]	Fe(III) [mol/L]	Pu [mol/L]
0	6.1	2.72	6.04		≤ det. limit	≤ det. limit	$1.22 \cdot 10^{-5\#}$
21							*$1.95 \cdot 10^{-9}$*
271	5.74	2.09					*$1.94 \cdot 10^{-9}$*
1481	5.89	3.58	6.07	0.84	≤ det. limit	≤ det. limit	*$1.93 \cdot 10^{-9}$*
21756	5.81	2.12	5.92	2.55	≤ det. limit	≤ det. limit	$9.98 \cdot 10^{-10}$
39201	5.74	2.61	5.78	2.60	≤ det. limit	≤ det. limit	$1.18 \cdot 10^{-9}$
56436	5.82	1.94	5.78	2.55	$2.94 \cdot 10^{-6}$	≤ det. limit	$9.06 \cdot 10^{-10}$

*time after addition of Pu, #$[Pu]_{start}$ – calculated from $[Pu]_{stock\ solution}$ and V_{sample},
[Pu] values in red italics are ≤ detection limit

Table A3.16. Reaction conditions for sample Mh-8m-III

Mh-8m-III							
time* [min]	pH_{susp}	pe_{susp}	pH_{cen}	pe_{cen}	Fe(II) [mol/L]	Fe(III) [mol/L]	Pu [mol/L]
0	6.06	5.88	6.35	3.19			$1.17 \cdot 10^{-5\#}$
18							$1.11 \cdot 10^{-9}$
1458	5.92						*$1.05 \cdot 10^{-9}$*
5873	5.65	1.74					
15743	5.62	2.82	5.95	2.17			*$4.15 \cdot 10^{-10}$*
136403	5.66	3.30					$5.47 \cdot 10^{-10}$
211283	5.70	3.16	5.82	3.51	$1.063 \cdot 10^{-6}$	≤ det. limit	$8.05 \cdot 10^{-10}$
300683	5.64	3.62					$6.68 \cdot 10^{-10}$
329543	5.68	3.66			$3.18 \cdot 10^{-6}$	$1.07 \cdot 10^{-7}$	$8.39 \cdot 10^{-11}$

*time after addition of Pu, #$[Pu]_{start}$ – calculated from $[Pu]_{stock\ solution}$ and V_{sample},
[Pu] values in red italics are ≤ detection limit, Fe(II) below quantification limit

Table A3.17. Reaction conditions for sample Mh-40d-V

Mh-40d-V							
time* [min]	pH_{susp}	pe_{susp}	pH_{cen}	pe_{cen}	Fe(II) [mol/L]	Fe(III) [mol/L]	Pu [mol/L]
0	6.1	3.57	6.06	4.26			$1.34 \cdot 10^{-5\#}$
11							*1.95E-09*
1241	6.07	2.55			≤ det. limit	≤ det. limit	*1.94E-09*
30256	5.81	3.06	5.87	3.34	≤ det. limit	≤ det. limit	*7.80E-10*
43246	5.73	2.59	5.79	3.18	$2.25 \cdot 10^{-6}$	≤ det. limit	*8.77E-10*
59011	5.75	2.18	5.78	3.37	≤ det. limit	≤ det. limit	*8.96E-10*

*time after addition of Pu, #$[Pu]_{start}$ – calculated from $[Pu]_{stock\ solution}$ and V_{sample},
[Pu] values in red italics are ≤ detection limit

Table A3.18. Reaction conditions for sample Mh-8m-V

Mh-8m-V							
time* [min]	pH_{susp}	pe_{susp}	pH_{cen}	pe_{cen}	Fe(II) [mol/L]	Fe(III) [mol/L]	Pu [mol/L]
0	6.06	5.88	6.35	3.19			$1.57 \cdot 10^{-5\#}$
15							$4.89 \cdot 10^{-6}$
1328	6.04						$1.24 \cdot 10^{-6}$
7245	5.94	2.61					
17115	7.27	3.10	6.31	2.39			$5.40 \cdot 10^{-10}$
137775	5.90	3.47					$4.29 \cdot 10^{-10}$
211215	6.11	2.47	6.34	3.74	$1.372 \cdot 10^{-6}$	≤ det. limit	
330915	5.90	4.03			$7.62 \cdot 10^{-7}$	$7.46 \cdot 10^{-7}$	$4.94 \cdot 10^{-11}$

*time after addition of Pu, #$[Pu]_{start}$ – calculated from $[Pu]_{stock\ solution}$ and V_{sample},
[Pu] values in red italics are ≤ detection limit, Fe(II) below quantification limit

Table A3.19. Reaction conditions for sample He-8m-III

He-8m-III							
time* [min]	pH_{susp}	pe_{susp}	pH_{cen}	pe_{cen}	Fe(II) [mol/L]	Fe(III) [mol/L]	Pu [mol/L]
0	7.94	4.69	8.10	0.74			$1.17 \cdot 10^{-5\#}$
19							*$1.05 \cdot 10^{-9}$*
1459	7.90	1.69					$1.62 \cdot 10^{-9}$
15744	7.41	- 0.66	7.52	6.31			*$4.12 \cdot 10^{-10}$*
136404	7.23	0.69					$5.08 \cdot 10^{-10}$
300684	7.12	1.21	7.24	3.03			*$4.17 \cdot 10^{-10}$*
329544	7.16	2.71			≤ det. limit	≤ det. limit	$2.13 \cdot 10^{-10}$

*time after addition of Pu, #$[Pu]_{start}$ – calculated from $[Pu]_{stock\ solution}$ and V_{sample},
[Pu] values in red italics are ≤ detection limit

Table A3.20. Reaction conditions for sample He-40d-V

He-40d-V							
time* [min]	pH_{susp}	pe_{susp}	pH_{cen}	pe_{cen}	Fe(II) [mol/L]	Fe(III) [mol/L]	Pu [mol/L]
0	7.80	1.84	7.77	4.17	≤ det. limit	≤ det. limit	$1.34 \cdot 10^{-5\#}$
14							$1.21 \cdot 10^{-6}$
1234	7.84	0.71			≤ det. limit	≤ det. limit	$2.48 \cdot 10^{-8}$
30259	7.60	- 1.58	7.66	2.45	≤ det. limit	≤ det. limit	$2.05 \cdot 10^{-9}$
43249	7.50	- 0.07	7.69	4.42	≤ det. limit	≤ det. limit	*$7.69 \cdot 10^{-10}$*
59014	7.46	- 0.24	7.48	2.16	≤ det. limit	≤ det. limit	*$9.01 \cdot 10^{-10}$*

*time after addition of Pu, #$[Pu]_{start}$ – calculated from $[Pu]_{stock\ solution}$ and V_{sample},
[Pu] values in red italics are ≤ detection limit

Table A3.21. Reaction conditions for sample He-8m-V

He-8m-V							
time* [min]	pH_{susp}	pe_{susp}	pH_{cen}	pe_{cen}	Fe(II) [mol/L]	Fe(III) [mol/L]	Pu [mol/L]
0	7.94	4.69	8.10	0.74			$1.57 \cdot 10^{-5\#}$
13							$2.2 \cdot 10^{-6}$
1313	7.92	1.81					$6.5 \cdot 10^{-7}$
17100	7.74	0.38	7.72	1.28			$3.8 \cdot 10^{-7}$
48600	7.62	0.46	7.50	4.82			$2.5 \cdot 10^{-7}$
133500	7.61	- 0.82					$1.1 \cdot 10^{-7}$
171000	7.61	2.21					$7.8 \cdot 10^{-8}$
302040	7.51	3.66	7.57	2.69			$2.9 \cdot 10^{-8}$
330900	7.50	1.39			≤ det. limit	≤ det. limit	$6.1 \cdot 10^{-9}$

*time after addition of Pu, #$[Pu]_{start}$ – calculated from $[Pu]_{stock\ solution}$ and V_{sample},
[Pu] values in red italics are ≤ detection limit

Table A3.22. Reaction conditions for sample Go-40d-V

Go-40d-V							
time* [min]	pH_{susp}	pe_{susp}	pH_{cen}	pe_{cen}	Fe(II) [mol/L]	Fe(III) [mol/L]	Pu [mol/L]
0	8.16	0.39	8.07	2.85	≤ det. limit	≤ det. limit	$1.34 \cdot 10^{-5\#}$
16							$1.46 \cdot 10^{-7}$
1229	8.03	- 1.44			≤ det. limit	≤ det. limit	$4.15 \cdot 10^{-8}$
30254	7.89	0.54	7.97	1.70	≤ det. limit	≤ det. limit	$1.09 \cdot 10^{-8}$
43244	7.88	1.14	7.95	2.08	≤ det. limit	≤ det. limit	$6.32 \cdot 10^{-9}$
59009	7.86	0.03	7.95	2.10	≤ det. limit	≤ det. limit	$1.88 \cdot 10^{-9}$

*time after addition of Pu, #$[Pu]_{start}$ – calculated from $[Pu]_{stock\ solution}$ and V_{sample},
[Pu] values in red italics are ≤ detection limit

Shell fitting results for Pu-mackinawite samples fitted in chapter 3.3 are reported in the following tables (Table A3.23-32.).

Table A3.23. Shell fit results* for PuO_2(cr) and samples Mk-8m-V-pH7 and Mk-8m-V-pH8 for four paths fits with coordination numbers fixed to the crystallographic values of the PuO_2 structure.

	PuO_2(cr)			Mk-8m-V-pH7			Mk-8m-V-pH8			PuO_2 - structure	
path	**CN**	**R [Å]**	**σ^2 [Å^2]**	**CN**	**R [Å]**	**σ^2 [Å^2]**	**CN**	**R [Å]**	**σ^2 [Å^2]**	**nb**	**dist [Å]**
Pu - O	8	2.33	0.0053	8	2.32	0.0056	8	2.32	0.0074	8	2.34
Pu - Pu	12	3.82	0.0030	12	3.81	0.0035	12	3.81	0.0051	12	3.82
Pu - O	24	4.41	0.0080	24	4.38	0.0094	24	4.39	0.0094	24	4.48
Pu - O MS	8	4.66^c	0.0052^c	8	4.64^c	0.0056^c	8	4.65^c	0.0074^c	8	4.68
	E_0-shift [eV]		6.5	E_0-shift [eV]		5.6	E_0-shift [eV]		6.5		
	Res [%]		7.0	Res [%]		10.6	Res [%]		12.2		
	k range [Å^{-1}]		3.0 – 15.2	k range [Å^{-1}]		3.0 – 15.2	k range [Å^{-1}]		3.0 – 15.1		
	R range [Å]		1.33 – 4.15	R range [Å]		1.35 – 4.1	R range [Å]		1.27 – 4.14		
	c: correlated to SS paths										
*Fitted in R-space, FT with bessel window function (window parameter = 3). Fit mode $k^3 + k^2$.											

Table A3.24. Shell fit results* for PuO_2(cr) and samples Mk-8m-V-pH7 and Mk-8m-V-pH8 for four paths fits with adjustable coordination numbers.

	PuO_2(cr)			Mk-8m-V-pH7			Mk-8m-V-pH8			PuO_2 - structure	
path	**CN**	**R [Å]**	**σ^2 [Å^2]**	**CN**	**R [Å]**	**σ^2 [Å^2]**	**CN**	**R [Å]**	**σ^2 [Å^2]**	**nb**	**dist [Å]**
Pu - O	8.1	2.33	0.0054	7.6	2.32	0.0052	8.3	2.32	0.0077	8	2.34
Pu - Pu	10.4	3.82	0.0024	9.7	3.81	0.0027	7.3	3.81	0.0031	12	3.82
Pu - O	35	4.42	0.0137	28	4.39	0.0155	11.5	4.42	0.0103	24	4.48
Pu - O MS	8.1^c	2.33^c	0.0054^c	7.6^c	2.32^c	0.0052^c	8.3	4.65^c	0.0077^c	8	4.68
	E_0-shift [eV]		6.9	E_0-shift [eV]		5.8	E_0-shift [eV]		6.1		
	Res [%]		5.8	Res [%]		9.6	Res [%]		9.5		
	k range [Å^{-1}]		3.0 – 15.2	k range [Å^{-1}]		3 – 15.2	k range [Å^{-1}]		3.0 – 15.1		
	R range [Å]		1.33 – 4.15	R range [Å]		1.35 – 4.1	R range [Å]		1.27 – 4.14		
	c: correlated to SS paths										

Table A3.25. Shell fit results* for PuO_2(cr) and samples Mk-8m-III-pH8 and Mk-8m-III-pH7 for four paths fits with coordination numbers fixed to the crystallographic values of the PuO_2 structure.

	PuO_2(cr)			Mk-8m-III-pH8			Mk-8m-III-pH7			PuO_2 - structure	
path	**CN**	**R [Å]**	**σ^2 [Å^2]**	**CN**	**R [Å]**	**σ^2 [Å^2]**	**CN**	**R [Å]**	**σ^2 [Å^2]**	**nb**	**dist [Å]**
Pu - O	8	2.33	0.0053	8	2.32	0.0072	8	2.32	0.0076	8	2.34
Pu - Pu	12	3.82	0.0030	12	3.82	0.0045	12	3.81	0.0065	12	3.82
Pu - O	24	4.41	0.0080	24	4.39	0.0093	24	4.39	0.0099	24	4.48
Pu - O MS	8	4.66^c	0.0052^c	8	4.65^c	0.0072^c	8	2.32^c	0.0076^c	8	4.68
	E_0-shift [eV]		6.5	E_0-shift [eV]		6.05	E_0-shift [eV]		6.1		
	Res [%]		7.0	Res [%]		9.5	Res [%]		15.3		
	k range [Å^{-1}]		3.0 – 15.2	k range [Å^{-1}]		3.0 – 15.2	k range [Å^{-1}]		3.0 – 15.1		
	R range [Å]		1.33 – 4.15	R range [Å]		1.41 – 4.15	R range [Å]		1.32 – 4.11		
	c: correlated to SS paths										

Table A3.26. Shell fit results* for PuO_2(cr) and samples Mk-8m-III-pH8 and Mk-8m-III-pH8 for four paths fits with adjustable coordination numbers.

	PuO_2(cr)			Mk-8m-III-pH8			Mk-8m-III-pH7			PuO_2 - structure	
path	**CN**	**R [Å]**	**σ^2 [Å^2]**	**CN**	**R [Å]**	**σ^2 [Å^2]**	**CN**	**R [Å]**	**σ^2 [Å^2]**	**nb**	**dist [Å]**
Pu - O	8.1	2.33	0.0054	8.5	2.32	0.0078	6.1	2.32	0.0050	8	2.34
Pu - Pu	10.4	3.82	0.0024	9.2	3.81	0.0036	7.9	3.81	0.0048	12	3.82
Pu - O	35	4.42	0.0137	14.2	4.41	0.0077	8.6	4.40	0.0063	24	4.48
Pu - O MS	8.1[c]	2.33[c]	0.0054[c]	8.5[c]	4.65[c]	0.0078[c]	6.1[c]	4.65[c]	0.0050[c]	8	4.68
	E_0-shift [eV]	6.9		E_0-shift [eV]	5.5		E_0-shift [eV]	5.7			
	Res [%]	5.8		Res [%]	8.8		Res [%]	11.9			
	k range [Å^{-1}]	3.0 – 15.2		k range [Å^{-1}]	3.0 – 15.2		k range [Å^{-1}]	3.0 – 15.1			
	R range [Å]	1.33 – 4.15		R range [Å]	1.41 – 4.15		R range [Å]	1.32 – 4.11			
	c: correlated to SS paths										

Table A3.27. Shell fit results* for PuO_2(cr) and samples Mk-8m-V-pH7 and Mk-8m-V-pH8 for six paths fits with coordination numbers fixed to the crystallographic values of the PuO_2 structure.

	PuO_2(cr)			Mk-8m-V-pH7			Mk-8m-V-pH8			PuO_2 - structure	
path	**CN**	**R [Å]**	**σ^2 [Å^2]**	**CN**	**R [Å]**	**σ^2 [Å^2]**	**CN**	**R [Å]**	**σ^2 [Å^2]**	**nb**	**dist [Å]**
Pu - O	8	2.33	0.0053	8	2.32	0.0056	8	2.32	0.0074	8	2.34
Pu - Pu	12	3.82	0.0030	12	3.81	0.0034	12	3.81	0.0051	12	3.82
Pu - O	24	4.41	0.0087	24	4.38	0.0100	24	4.39	0.0099	24	4.48
Pu - O MS	8	4.66[c]	0.0053[c]	8	4.65[c]	0.0056[c]	8	4.65[c]	0.0074[c]	8	4.68
Pu - Pu	6	5.39	0.0047	6	5.39	0.0050	6	5.37	0.0067	6	5.40
Pu- Pu	24	6.65	0.0076	24	6.63	0.0093	24	6.66	0.0134	24	6.61
	E_0-shift [eV]	6.4		E_0-shift [eV]	5.6		E_0-shift [eV]	6.4			
	Res [%]	12.4		Res [%]	18.0		Res [%]	16.1			
	k range [Å^{-1}]	3.0 – 15.2		k range [Å^{-1}]	1.35 – 6.69		k range [Å^{-1}]	3.0 – 15.2			
	R range [Å]	1.33 – 6.8		R range [Å]	3.0 – 15.2		R range [Å]	1.32 – 6.71			
	c: correlated to SS paths										

Table A3.28. Shell fit results* for PuO_2(cr) and samples Mk-8m-V-pH7 and Mk-8m-V-pH8 for six paths fits with adjustable coordination numbers.

	PuO_2(cr)			Mk-8m-V-pH7			Mk-8m-V-pH8			PuO_2 - structure	
path	**CN**	**R [Å]**	**σ^2 [Å^2]**	**CN**	**R [Å]**	**σ^2 [Å^2]**	**CN**	**R [Å]**	**σ^2 [Å^2]**	**nb**	**dist [Å]**
Pu - O	8.1	2.33	0.0053	7.6	2.32	0.0052	8.1	2.32	0.0075[e]	8	2.34
Pu - Pu	9.6	3.82	0.0021[d]	8.7	3.81	0.0023[d]	6.7	3.81	0.0029[d]	12	3.82
Pu - O	32	4.42	0.0137	24	4.39	0.0162	7.8	4.43	0.0075[e]	24	4.48
Pu - O MS	8.1[c]	4.66[c]	0.0053[c]	7.6[c]	4.64[c]	0.0052[c]	8.1[c]	4.65[c]	0.0075[c]	8	4.68
Pu - Pu	3.2	5.40	0.0021[d]	3.2	5.39	0.0023[d]	2.4	5.37	0.0029[d]	6	5.40
Pu- Pu	8.2	6.64	0.0028	5.4	6.62	0.0023[d]	3.6	6.64	0.0029[d]	24	6.61
	E_0-shift [eV]	6.5		E_0-shift [eV]	5.5		E_0-shift [eV]	5.9			
	Res [%]	10.1		Res [%]	15.7		Res [%]	11.6			
	k range [Å^{-1}]	3.0 – 15.2		k range [Å^{-1}]	1.35 – 6.69		k range [Å^{-1}]	3.0 – 15.2			
	R range [Å]	1.34 – 6.8		R range [Å]	3.0 – 15.2		R range [Å]	1.32 – 6.71			
	c: correlated to SS paths, d: correlated										

Table A3.29. Shell fit results* for PuO_2(cr) and sample Mk-8m-V-pH8 for four paths fits based on a k-range up to 19 and with coordination numbers fixed to the crystallographic values of the PuO_2 structure.

	PuO_2(cr)			**Mk-8m-V-pH8**			**PuO_2 - structure**	
path	**CN**	**R [Å]**	**σ^2 [Å^2]**	**CN**	**R [Å]**	**σ^2 [Å^2]**	**nb**	**dist [Å]**
Pu - O	8	2.33	0.0052	8	2.32	0.0072	8	2.34
Pu - Pu	12	3.82	0.0027	12	3.81	0.0045	12	3.82
Pu - O	24	4.39	0.0084	24	4.37	0.0087	24	4.48
Pu - O MS	8	4.66[c]	0.0052[c]	8	4.66[c]	0.0072[c]	8	4.68
	E_0-shift [eV]	6.2		E_0-shift [eV]	6.7			
	Res [%]	6.9		Res [%]	17.3			
	k range [Å^{-1}]	3.0 – 19.1		k range [Å^{-1}]	3.0 – 19.2			
	R range [Å]	1.45 – 3.97		R range [Å]	1.42 – 3.99			
	c: correlated to SS paths							

Table A3.30. Shell fit results* for PuO_2(cr) and sample Mk-8m-V-pH8 for four paths fits based on a k-range up to 19 and with adjustable coordination numbers.

	PuO_2(cr)			**Mk-8m-V-pH8**			**PuO_2 - structure**	
path	**CN**	**R [Å]**	**σ^2 [Å^2]**	**CN**	**R [Å]**	**σ^2 [Å^2]**	**nb**	**dist [Å]**
Pu - O	7.6	2.33	0.0049	7.6	2.32	0.0067	8	2.34
Pu - Pu	9.6	3.82	0.0022	6.8	3.81	0.0029	12	3.82
Pu - O	31	4.42	0.0156	14.7	4.43	0.0187	24	4.48
Pu - O MS	7.6[c]	4.66[c]	0.0049[c]	7.6[c]	4.65[c]	0.0067[c]	8	4.68
	E_0-shift [eV]	6.4		E_0-shift [eV]	6.4			
	Res [%]	4.9		Res [%]	10.5			
	k range [Å^{-1}]	3.0 – 19.1		k range [Å^{-1}]	3.0 – 19.2			
	R range [Å]	1.45 – 3.97		R range [Å]	1.43 – 3.97			
	c: correlated to SS paths							

Table A3.31. Shell fit results* for PuO_2(cr) and sample Mk-8m-V-pH8 for six paths fits based on a k-range up to 19 and with coordination numbers fixed to the crystallographic values of the PuO_2 structure.

	PuO_2(cr)			**Mk-8m-V-pH8**			**PuO_2 - structure**	
path	**CN**	**R [Å]**	**σ^2 [Å^2]**	**CN**	**R [Å]**	**σ^2 [Å^2]**	**nb**	**dist [Å]**
Pu - O	8	2.32	0.0051	8	2.32	0.0072	8	2.34
Pu - Pu	12	3.82	0.0028	12	3.81	0.0046	12	3.82
Pu - O	24	4.41	0.0084	24	4.37	0.0094	24	4.48
Pu - O MS	8	4.66[c]	0.0051[c]	8	4.65[c]	0.0072[c]	8	4.68
Pu - Pu	6	5.49	0.0032	6	5.38	0.0060	6	5.40
Pu - Pu	24	6.62	0.0060	24	6.65	0.0126	24	6.61
	E_0-shift [eV]		5.6	E_0-shift [eV]		6.5		
	Res [%]		14.0	Res [%]		22.4		
	k range [Å^{-1}]		3.0 – 19.1	k range [Å^{-1}]		3.0 – 19.1		
	R range [Å]		1.49 – 6.69	R range [Å]		1.39 – 6.56		
	c: correlated to SS paths							

Table A3.32. Shell fit results* for PuO_2(cr) and sample Mk-8m-V-pH8 for six paths fits based on a k-range up to 19 and with adjustable coordination numbers.

	PuO_2(cr)			**Mk-8m-V-pH8**			**PuO_2 - structure**	
path	**CN**	**R [Å]**	**σ^2 [Å^2]**	**CN**	**R [Å]**	**σ^2 [Å^2]**	**nb**	**dist [Å]**
Pu - O	7.6	2.32	0.0048	7.6	2.32	0.0067	8	2.34
Pu - Pu	9.0	3.82	0.0021[d]	6.6	3.81	0.0029	12	3.82
Pu - O	17	4.44	0.0066	6.6	4.44	0.0064	24	4.48
Pu - O MS	7.6[c]	4.66[c]	0.0048[c]	7.6[c]	4.65[c]	0.0067[c]	8	4.68
Pu - Pu	3.82	5.40	0.0021[d]	2.6	5.38	0.0033[d]	6	5.40
Pu - Pu	6.8	6.61	0.0021[d]	3.1	6.6	0.0033[d]	24	6.61
	E_0-shift [eV]		5.7	E_0-shift [eV]		6.1		
	Res [%]		10.1	Res [%]		15.8		
	k range [Å^{-1}]		3.0 – 19.1	k range [Å^{-1}]		3.0 – 19.2		
	R range [Å]		1.49 – 6.69	R range [Å]		1.40 – 6.58		
	c: correlated to SS paths, d: correlated							

Table A3.33. Shell fit results* for PuO_2(cr) and samples Chuk-8m-V and Chuk-8m-III for four paths fits with coordination numbers fixed to the crystallographic values of the PuO_2 structure.

	PuO_2(cr)			**Chuk-8m-V**			**Chuk-8m-III**			**PuO_2 - structure**	
path	**CN**	**R [Å]**	**σ^2 [Å^2]**	**CN**	**R [Å]**	**σ^2 [Å^2]**	**CN**	**R [Å]**	**σ^2 [Å^2]**	**nb**	**dist [Å]**
Pu - O	8	2.33	0.0053	8	2.32	0.0083	8	2.33	0.0150	8	2.34
Pu - Pu	12	3.82	0.0030	12	3.81	0.0046	12	3.80	0.0061	12	3.82
Pu - O	24	4.41	0.0080	24	4.39	0.0072	24	4.38	0.0067	24	4.48
Pu - O MS	8	4.66^c	0.0052^c	8	4.64^c	0.0083^c	8	4.66^c	0.0150^c	8	4.68
	E_0-shift [eV]	6.5		E_0-shift [eV]	6.2		E_0-shift [eV]	5.4			
	Res [%]	7.0		Res [%]	8.5		Res [%]	20.1			
	k range [Å^{-1}]	3.0 – 15.2		k range [Å^{-1}]	3.0 – 15.2		k range [Å^{-1}]	3.0 – 15.3			
	R range [Å]	1.33 – 4.15		R range [Å]	1.3 – 4.2		R range [Å]	1.30 – 4.16			
	c: correlated to SS paths										
*Fitted in R-space, FT with bessel window function (window parameter = 3). Fit mode $k^3 + k^2$.											

Table A3.34. Shell fit results* for PuO_2(cr) and samples Chuk-8m-V and Chuk-8m-III for four paths fits with adjustable coordination numbers.

	PuO_2(cr)			**Chuk-8m-V**			**Chuk-8m-III**			**PuO_2 - structure**	
path	**CN**	**R [Å]**	**σ^2 [Å^2]**	**CN**	**R [Å]**	**σ^2 [Å^2]**	**CN**	**R [Å]**	**σ^2 [Å^2]**	**nb**	**dist [Å]**
Pu - O	8.1	2.33	0.0054	7.4	2.32	0.0074	6.5	2.32	0.0120	8	2.34
Pu - Pu	10.4	3.82	0.0024	6.1	3.81	0.0022	5.1	3.80	0.0027	12	3.82
Pu - O	35	4.42	0.0137	6.5	4.43	0.0027	15.2	4.42	0.0120^c	24	4.48
Pu - O MS	8.1^c	2.33^c	0.0054^c	7.4^c	4.64^c	0.0074^c	6.5^c	4.66^c	0.0120^c	8	4.68
	E_0-shift [eV]	6.9		E_0-shift [eV]	5.8		E_0-shift [eV]	5.2			
	Res [%]	5.8		Res [%]	4.7		Res [%]	14.9			
	k range [Å^{-1}]	3.0 – 15.2		k range [Å^{-1}]	3.0 – 15.2		k range [Å^{-1}]	3.0 – 15.3			
	R range [Å]	1.33 – 4.15		R range [Å]	1.3 – 4.2		R range [Å]	1.30 – 4.16			
	c: correlated to SS paths										

if (based on the same k- and R-range as in Table A3.34) the first peak of Chuk-8m-III is fit with two oxygen shells and with DW correlated for all Pu-O path, it results

	CN	R[Å]	s2[Å^2]
Pu-O_1	4.1	2.30	0.0048^c
Pu-O_2	2.3	2.47	0.0048^c
Pu-Pu	4.9	3.80	0.0025
Pu-O	7.6	4.40	0.0048^c
Res [%]	9.1	ΔE_0	6.1

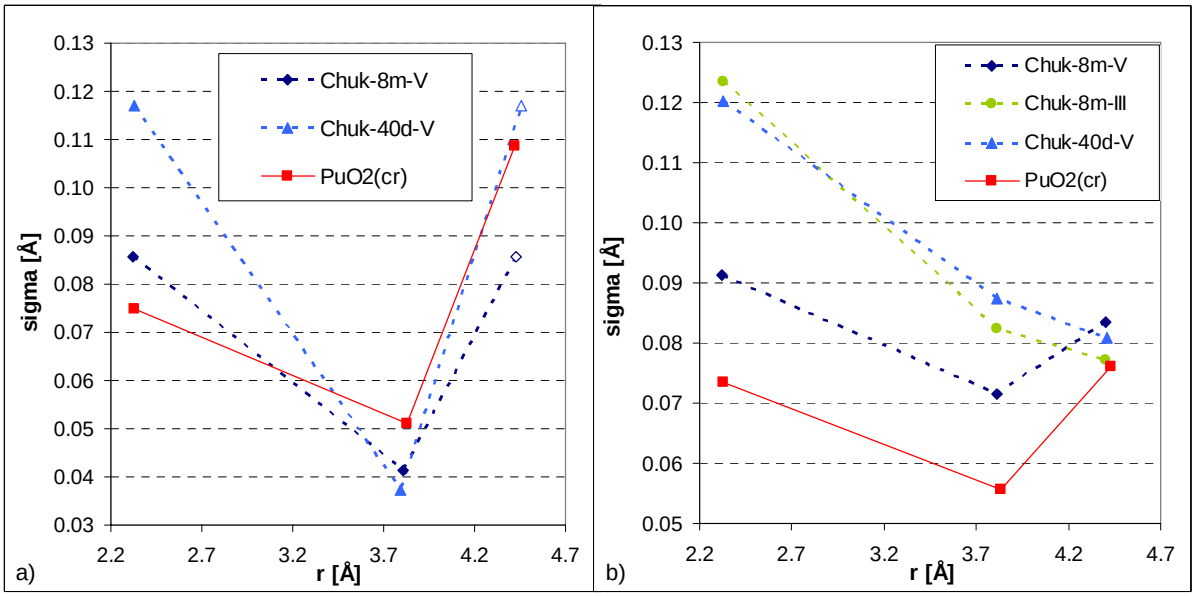

Figure A3.1. The structural disorder of Pu-O (2.33 and 4.42 Å) and Pu-Pu (3.83 Å) paths as indicated by σ (σ = sqrt(σ^2)) as a function of distance. a) σ as obtained by fitting with adjustable CN; b) σ as obtained by fitting with CN fixed to the crystallographic values of PuO_2. Fits based on $3 \leq k \leq 12.1$ Å^{-1} for Pu-chukanovite samples and on $3 \leq k \leq 11.8$ Å^{-1} for PuO_2(cr). R-space: $1.3 \leq R \leq 4.1$ Å. Non-filled triangles in a) indicate data points obtained from correlating the σ^2 value of the 4.43 Å Pu-O paths to the σ^2 value of the Pu-O paths at 2.33 Å. Lines between data points are drawn only as a guide to the eye.

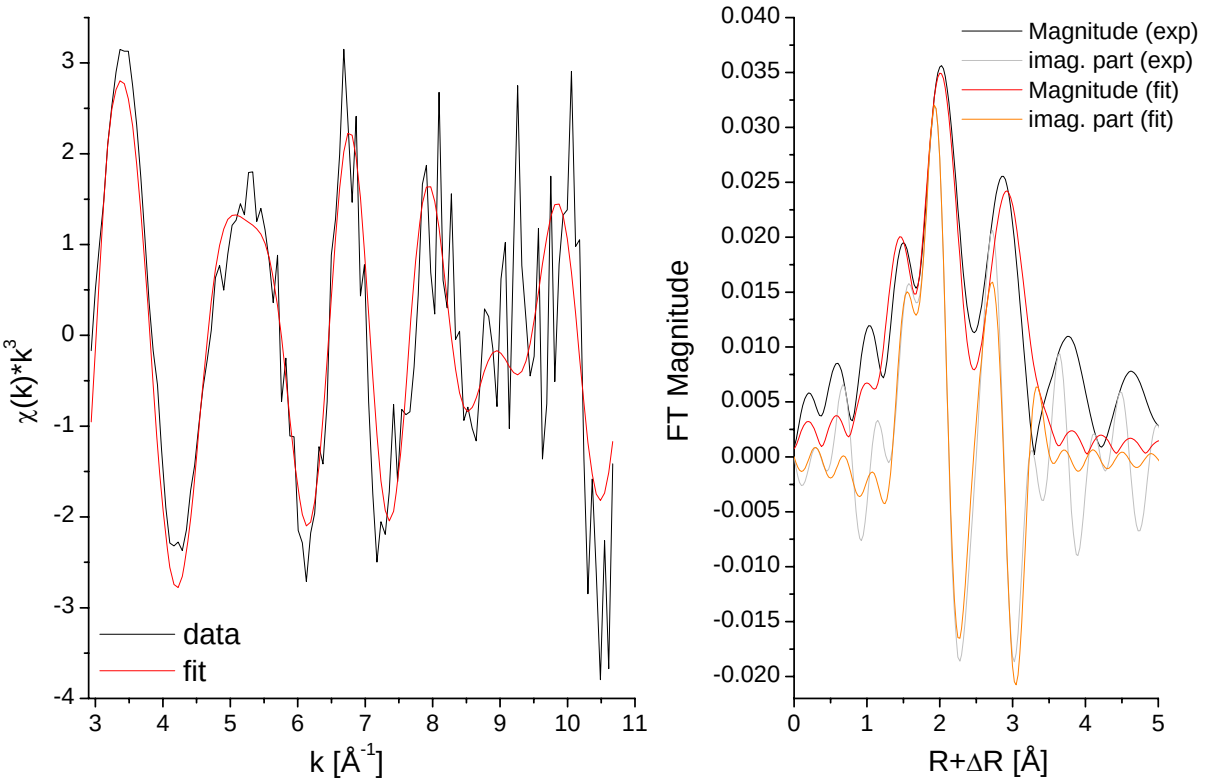

Figure A3.2. Shell fit EXAFS spectrum of sample He-8m-III. Fit carried out in R-space, based on k-range $3 \leq k \leq 10.7$ Å^{-1}, fit parameters given in Table 3.6.5.

4. Reactions of antimony with mackinawite

All experiments to investigate sorption and redox reactions of antimony with mackinawite under anoxic conditions we carried out in a N2 glove box with oxygen levels of 0-5 ppmv. For sorption experiments, solution pH, ionic strength of the background electrolyte ($CaCl_2$), and antimony concentrations were varied. To investigate antimony mackinawite redox reactions, XAS samples were prepared at different pH values, solid/liquid ratios, and Sb concentrations.

4.1. Experimental setup

For all experiments, mackinawite synthesized as explained above (chapter 3.2) was used. Mackinawite was washed with deionized water (once) and 25 mM CaCl2 (Riedel de Haën, puriss.) (three times) by centrifugation-decantation cycles and thereafter stored in 25 mM CaCl2. 0.01 M Sb(V) stock solution was prepared by dissolving the corresponding amount of KSb(OH)6 (Sigma-Aldrich) in MilliQ water (18.2 M□). As Sb(III) stock solution, Sb2O3 dissolved in 2 M HCl (Certipur, Merck) was used. pH and Eh were measured in suspension using a glass combination electrode (Sentix HW, WTW or Methrom 6.0233) and Pt combination electrode (Crison 5261), respectively, connected to a Orion (525A) or Mettler Toledo (MA235) pH-meter.

For analysis of [Sb]tot and [Fe]tot by ICP-MS, aliquots of the samples were filtered through 0.45 µm syringe filters (Minisart, Sartorius Stedium Biotech (cellulose acetate membrane) or Millex® -HA filters, Millipore, (mixed cellulose esters membrane)). The filtered solutions were acidified with concentrated HNO3 (14.4 M) (100 µL HNO3 for 1 mL sample) and stored at 4°C. For ICP-MS measurements, samples were diluted (1/10, 1/100 or 1/1000) with 2 % HNO3 and 2 % HNO3 spiked with Ge, In, Be, Tm, and Bi as internal standards.

a) Sorption of Sb(V) on mackinawite was investigated as a function of time (Stime), of pH and ionic strength (SpH), and of Sb concentration (Siso) (Table 4.1.1). Samples with a volume of 40mL were prepared in 60 mL bottles and were continuously shaken on a Vibramax shaker (900 rpm) during the periods of pH conditioning (i.e.mackinawite suspension to which NaOH or HCl had been added prior to Sb addition) and Sb sorption. No pH buffer was added to the mackinawite suspensions and during the time of Sb sorption, no acid or base was added to keep the pH stable. Total Sb concentrations were obtained from ICP-MS analysis of filtered solutions. For experiments Stime (ac and bas), SpH_a, and Siso (ac and bas) (Table 4.1.1), Sb speciation was analyzed using HG-AFS (for method descriptions see chapter 2).

At the same conditions at which sorption experiments were carried out (1.7 g/L FeS, 1.9 or 25 mM $CaCl_2$), Sb free samples were prepared in which the redox potential was monitored as a function of pH.

Table 4.1.1. Overview of experiments undertaken to investigate the sorption of Sb(V) to mackinawite as a function of time, pH and initial Sb concentration.

solid/liquid ratio for experiment 1 to 3			1.73 g FeS/L = 19.6 mmol/L					
Experiment 1								
Stime	Sb(V) sorption as a function of reaction time						reaction time	3 days
	Background electrolyte		25 mM $CaCl_2$					
samples	Sb(V) [M] start	Sb(V) [M] end	pH start	pH end	Sb sorption	loading [mol Sb/g FeS]	FeS dissolution end	$[Fe]_{tot}$ end [mM]
Stime_ac	$1.0 \cdot 10^{-4}$	$4.3 \cdot 10^{-8}$	5.6	6.4	100 %	$6.1 \cdot 10^{-5}$	5.2 %	1.0
Stime_bas	$1.0 \cdot 10^{-4}$	$8.6 \cdot 10^{-5}$	8.1	8.1	15 %	$8.8 \cdot 10^{-6}$	0.3 %	0.05
Experiment 2								
SpH	Sb(V) sorption as a function of pH and ionic strength							
Background electrolyte	25 mM $CaCl_2$ (SpH_a) 1.9 mM $CaCl_2$ (SpH_b)			reaction time	25.3 ± 0.5 h for SpH_a 28.1 ± 1.2 h for SpH_b			
pH range investigated	pH 3.5 to pH 10.5			Sb(V) start [M]	$1.02 \cdot 10^{-5}$			
Experiment 3								
Siso	Sorption of Sb(V) as a function of [Sb] initial							
Background electrolyte	25 mM $CaCl_2$ for Siso_ac 1.9 mM $CaCl_2$ for Siso_bas			reaction time	28.25 ± 0.5 h for Siso_ac 34 ± 0.3 h for Siso_bas			
[Sb] initial [M]	$1.0 \cdot 10^{-5}$ to $6.1 \cdot 10^{-4}$							
samples	pH start	pH end	Sb sorption	loading [mol Sb/g FeS]	FeS dissolution end	$[Fe]_{tot}$ end [mM]		
Siso_ac	5.7	6.0 to 7.8	99.7 to 11.9 %	$6 \cdot 10^{-6}$ to $4.3 \cdot 10^{-5}$	2.8 to 3.1 %	$(5.5 \text{ to } 6.0) \cdot 10^{-4}$		
Siso_bas	7.7	7.9 to 8.3	6.3 to 21.9 %	$4 \cdot 10^{-7}$ to $7.3 \cdot 10^{-5}$	0.2 to 0.0 %	$(3.8 \text{ to } 0.9) \cdot 10^{-5}$		

b) Samples for XAS measurements were prepared at two different mackinawite solid/liquid ratios. In experiment A mackinawite was reacted with either Sb(III) or Sb(V) at relatively low Sb/FeS ratios resulting in Sb loadings of $2.3 \cdot 10^{-7}$ to $4.4 \cdot 10^{-6}$ mol Sb/g FeS; in experiment B the mackinawite solid/liquid ratio was much lower than in A (1/25th) and four different initial Sb concentrations were used, resulting in Sb loadings of $1.06 \cdot 10^{-5}$ to $1.14 \cdot 10^{-3}$ mol Sb/g FeS) (Tables 4.1.2, 4.1.3).

Samples for experiment A were prepared in 50 mL acid washed (3 % HCl) centrifuge tubes that were wrapped with aluminum foil to protect the samples against light. Samples were manually shaken directly after addition of Sb and then once daily until the end of the reaction period. The pH of the mackinawite suspension was adjusted one (15 d, 30 d samples) or two days prior to addition of Sb(V). The pH was not adjusted over time. Blank samples without added mackinawite were prepared by adding Sb(III) or Sb(V) stock solutions to 25 mM $CaCl_2$ preadjusted to pH 4.5, pH 6 and pH 8. Due to the fact that Sb(III) was dissolved in 2 M HCl, addition of Sb(III) resulted in a pH drop down to pH 1.8. Total Sb in these FeS free blanks was stable over time and neither reduction of Sb(V) nor oxidation of Sb(III) was observed by HG-AFS. 25 mM $CaCl_2$ blanks were prepared to monitor loss of Sb from the bottles over time. After 30 d, [Sb]tot was below the detection limit, in this case $8.2 \cdot 10^{-8}$ M.

Samples for experiment B were prepared in 250 or 500 mL bottles (PEHD, VWR) and were continuously shaken on a Heidolph Vibramax 100 shaker (1200rpm). For samples without Sb (control samples), the total volume was 200 mL; for samples with added Sb, the total volume was 400 mL. The pH of the mackinawite suspension was adjusted two days prior to addition of Sb(V) and was adjusted over time by adding 1 M, 0.1 M or 0.01 M NaOH or HCl. However, the attempt to keep the pH stable over time failed somewhat for the pH 5 samples (see Fig. A4.3)

Table 4.1.2. Experimental conditions for XAS-experiment A

solid/liquid ratio: 25 g FeS / L = 0.28 mol/L								Background electrolyte: 25 mM $CaCl_2$			
sample name	Sb(V) [mM] start	Sb(V) [mM] end	pH start	pH end	Eh start [mV]	Eh end [mV]	% Sb sorbed	loading* [mol Sb/ g FeS]	loading* [mol Sb/ mol FeS]	FeS dissolution end [%]	reaction time
Xa_p1hpH5	$1\cdot10^{-4}$	$2.1\cdot10^{-7}$	4.5	4.5	-240	-240	99.8	$4.0\cdot10^{-6}$	$3.5\cdot10^{-4}$	1.3	1.00 h
Xa_p1hpH6	$1\cdot10^{-4}$	$8.3\cdot10^{-5}$	6.0	6.3	-290	-290	16.6	$6.6\cdot10^{-7}$	$5.8\cdot10^{-5}$	0	1.00 h
Xa_p1hpH8	$1\cdot10^{-4}$	$9.4\cdot10^{-5}$	7.9	8.1	-340	-330	5.8	$2.3\cdot10^{-7}$	$2.0\cdot10^{-5}$	0	1.00 h
Xa_p22hpH5	$1\cdot10^{-4}$	$2.1\cdot10^{-7}$	4.5	5.4	-240	-240	99.8	$4.0\cdot10^{-6}$	$3.5\cdot10^{-4}$	1.3	22.25 h
Xa_p22hpH6	$1\cdot10^{-4}$	$1.5\cdot10^{-5}$	6.0	7.3	-290	-290	82.5	$3.3\cdot10^{-6}$	$2.9\cdot10^{-4}$	0	22.33 h
Xa_p22hpH8	$1\cdot10^{-4}$	$9.4\cdot10^{-5}$	7.9	8.3	-340	-330	39.6	$1.6\cdot10^{-6}$	$1.4\cdot10^{-4}$	0	22.25 h
Xa_p13dpH6	$1\cdot10^{-4}$	$<10^{-7}$	5.9	5.6	-	-	100.0	$4.0\cdot10^{-6}$	$3.5\cdot10^{-4}$	0.9	13.33 d
Xa_p13dpH7	$1\cdot10^{-4}$	$<10^{-7}$	7.0	6.7	-	-	100.0	$4.0\cdot10^{-6}$	$3.5\cdot10^{-4}$	0.1	13.32 d
Xa_p13dpH8	$1\cdot10^{-4}$	$9\cdot10^{-7}$	8.0	8.3	-	-	97.0	$4.0\cdot10^{-6}$	$3.5\cdot10^{-4}$	0.0	13.28 d
Xa_p30dpH4	$1\cdot10^{-4}$	$<10^{-8}$	4.2	4.3	-	-	100.0	$4.2\cdot10^{-6}$	$3.6\cdot10^{-4}$	4.3	30.00 d
Xa_p30dpH5	$1\cdot10^{-4}$	$<10^{-8}$	5.0	5.3	-	-	100.0	$4.0\cdot10^{-6}$	$3.5\cdot10^{-4}$	1.1	29.98 d
Xa_p30dpH8	$1\cdot10^{-4}$	$3\cdot10^{-7}$	8.0	8.4	-	-	99.2	$4.0\cdot10^{-6}$	$3.5\cdot10^{-4}$	0.0	29.94 d
sample name	Sb(III) [M] start	Sb(III) [M] end	pH start	pH end	Eh start [mV]	Eh end [mV]	% Sb sorbed	loading* [mol Sb/ g FeS]	loading* [mol Sb/ mol FeS]	FeS dissolution end [%]	reaction time
Xa_t13dac1	$1\cdot10^{-4}$	$<10^{-7}$	5.6	4.1	-	-	100.0	$4.2\cdot10^{-6}$	$3.7\cdot10^{-4}$	4.9	13.28 d
Xa_t13dac2	$1\cdot10^{-4}$	$<10^{-7}$	7.9	4.2	-	-	100.0	$4.1\cdot10^{-6}$	$3.6\cdot10^{-4}$	3.3	13.23 d
Xa_t30dac1	$1\cdot10^{-4}$	$<10^{-8}$	4.2	3.9	-	-	100.0	$4.4\cdot10^{-6}$	$3.8\cdot10^{-4}$	8.4	29.91 d
Xa_t30dac2	$1\cdot10^{-4}$	$<10^{-8}$	8.0	4.2	-	-	100.0	$4.1\cdot10^{-6}$	$3.6\cdot10^{-4}$	3.4	29.88 d

* mol Sb sorbed / undissolved FeS at the end of the experiment

Table 4.1.3. Experimental conditions for XAS-experiment B.

solid/liquid ratio: 0.94 g FeS / L = 0.01 mol/L			reaction time: 7 d				Background electrolyte: 0.94 mM $CaCl_2$			
sample name	Sb(V) [M]		pH start	pH end	Eh start [mV]	Eh end [mV]	% Sb sorbed	loading* [mol Sb/ g FeS]	loading* [mol Sb/ mol FeS]	FeS dissolution end [%]
	start	end								
Xb_ac_0	$2.0 \cdot 10^{-8}$	$2.2 \cdot 10^{-8}$	5.9	5.1	-140	-55	-	-	-	17.8
Xb_ac_1	$1.1 \cdot 10^{-4}$	$5.7 \cdot 10^{-8}$	5.6	5.3	-80	-80	99.95	$1.22 \cdot 10^{-4}$	1.2 %	11.7
Xb_ac_2	$3.1 \cdot 10^{-4}$	$3.1 \cdot 10^{-8}$	5.5	5.3	-80	-70	99.99	$3.49 \cdot 10^{-4}$	3.5 %	17.3
Xb_ac_3	$6.6 \cdot 10^{-4}$	$7.6 \cdot 10^{-8}$	5.4	5.0	-110	-80	99.99	$8.72 \cdot 10^{-4}$	8.7 %	29.5
Xb_ac_4	$8.4 \cdot 10^{-4}$	$1.2 \cdot 10^{-7}$	5.3	4.9	-120	-80	99.99	$1.14 \cdot 10^{-3}$	11.4 %	31.5
Xb_bas_0	$1.1 \cdot 10^{-8}$	$4.5 \cdot 10^{-8}$	8.8	8.7	-260	-190	-	-	-	0.06
Xb_bas_1	$1.1 \cdot 10^{-4}$	$1.0 \cdot 10^{-4}$	8.6	8.7	-250	-230	10.00	$1.06 \cdot 10^{-5}$	0.1 %	0.07
Xb_bas_2**	$3.3 \cdot 10^{-4}$	$2.9 \cdot 10^{-4}$	8.5	8.8	-290	-260	11.74	$3.65 \cdot 10^{-5}$	0.4 %	0.83
Xb_bas_3	$6.6 \cdot 10^{-4}$	$5.7 \cdot 10^{-4}$	8.5	8.5	-290	-250	13.78	$8.48 \cdot 10^{-5}$	0.9 %	0.13
Xb_bas_4	$8.6 \cdot 10^{-4}$	$7.4 \cdot 10^{-4}$	8.7	8.6	-290	-260	13.16	$1.06 \cdot 10^{-4}$	1.1 %	0.11

* mol Sb sorbed / undissolved FeS at the end of the experiment
** during centrifugation, the centrifuge tube containing this sample broke and the sample could therefore not be analysed by XAS

4.2. The Fe – S – H_2O system

Whenever a redox potential is measured in a suspension containing mineral particles, the question arises, if the acquired value accurately represents the redox potential in the system. E.g., Sylvester et al. (2005)[120] found that for hydrous ferric oxide and nanoparticulate ferric oxide hydrate onto which Fe(II) had been adsorbed, calculated and experimental Eh were in good agreement. For goethite and lepidocrocite suspension, the recorded rest potential values were higher than predicted and were explained as potentially caused by a bigger particle size and smaller Fe(II) concentrations in solution, factors that could hinder establishmend of redox equilibrium between the Pt-electrode and the suspension.

Mackinawite particles resulting from precipitation of Fe(II) with sulfide are usually small;[121, 122] the mackinawite used here has previously been shown to have a diameter of 5 nm as determined by PDF analysis,[123] though over time its size and/or crystallinity must not necessarily have been stable. This small size and consequently high surface area might facilitate equilibration with the surface of the Pt-electrode. To calculated theoretical values to compare with the experimentally acquired redox potentials, one needs to know what species might constitute the oxidized and reduced redox partners that interact with the electrode surface.

It has previously been claimed by Gallegos et al. (2008) that in a mackinawite containing Fe-S-H_2O system pe values decreased linearly as a function of pH and that the line representing the resulting pe-pH relation paralled the lower water stability line.[124] From this, the authors deduced that "the redox of the system could be poised by the H_2/H^+ redox couple through a surface controlled reaction with mackinawite".[124] Further, it was found that higher solid concentrations resulted in lower pe values, e.g. the pe-pH line for a 10 g/L suspension was found to be 0.8 pe units below the line corresponding to 1 g/L and 1.4 pe units below the 0.5 g/L line.

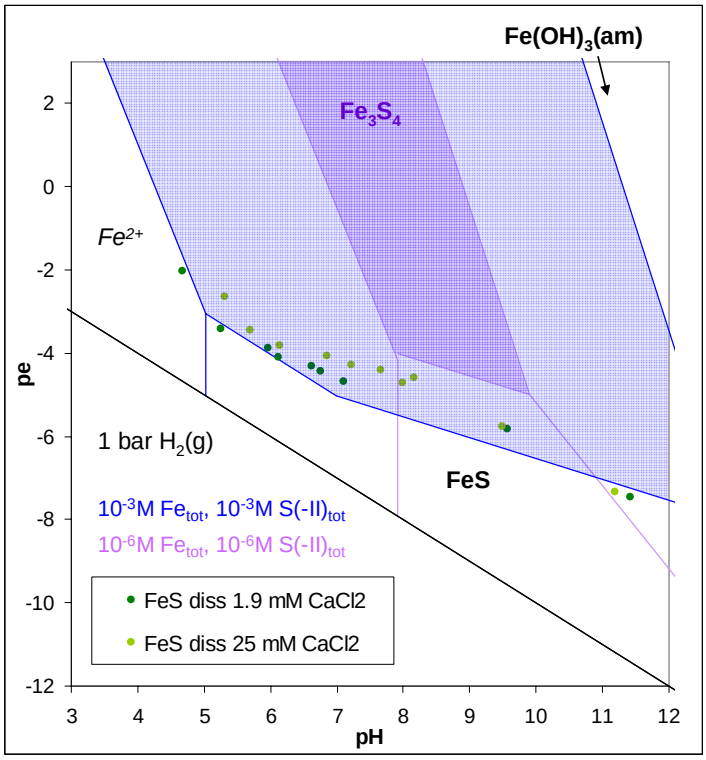

Figure 4.2.1. pe-pH predominance diagram for the Fe – S – H_2O system, considering equilibria between mackinawite (FeS(am)), greigite (Fe_3S_4), ferri-hydroxide ($Fe(OH)_3$(am)), and dissolved ferrous iron. Sulfide oxidation is neglected. Concentrations of dissolved iron and sulfide are fixed to 10^{-3} M (blue) or 10^{-6} M (violet). Data points from FeS dissolution (1,7 g/L) in 1.9 or 25 mM $CaCl_2$.

As in Gallegos et al. (2008), a mackinawite suspension was prepared and the pH adjusted by addition of HCl or NaOH. In contrast, pH buffers were not used and measurements were carried out at more pH values and over a greater range. Data points resulting from mackinawite dissolution at two ionic strengths are shown in figure 4.2.1 and compared to a pe-pH diagram calculated for two different, fixed ΣFe(II) and ΣS(-II) concentrations. A linear pe-pH relationship is in this case not evident and the position between the two given FeS-Fe_3S_4 equilibrium lines suggest that it might be the mackinawite-greigite equilibrium that controls the redox potential in the system. But a pe-pH diagram with a single fixed iron and sulfide concentration over the whole pH range does necessarily not accurately model experimental conditions where pH dependent FeS dissolution controls ΣFe(II) and ΣS(-II).

For this reason, a pe-pH diagram was computed using iron and sulfide concentrations resulting from FeS dissolution.

It was assumed that $\Sigma Fe(II) = \Sigma S(-II)$.

Assigning aqueous species to ΣFe(II) and ΣS(-II), this results in:

$$\{Fe^{2+}\} + \{FeOH^{+}\} + \{Fe(OH)_2\} + \{Fe(OH)_3^{-}\} + \{FeCl^{+}\} = \{H_2S\} + \{HS^{-}\} + \{S^{2-}\}.$$

Thus the diagram in Fig. 4.2.2 was obtained (for details see Tables 4.2.1, 4.2.2). The impression, that the data points might follow the FeS-Fe_3S_4 equilibrium line is confirmed at least between pH 6 and 8.5. Below pH 6, a number data points are significantly shifted to higher pe values. Also the four data

points at pH 9.5 and 11.5 appear somewhat more distant from the FeS-Fe_3S_4 line. As in these dissolution experiments no attempt was made to keep the (H_2S)aq concentration stable and to prevent H_2S from going into the gasphase at low pH, it is well possible that a considerable H_2S loss occurred at pH values below 7 where (H_2S)aq is the dominant solution species. A line indicating how H_2S loss shifts the FeS-Fe_3S_4 line has been added in figure 4.2.2. Comparing to data points from the Pu-mackinawite and Sb-mackinawite experiments, it appears that a small influence of the FeS solid concentration on the apparent redox potential might exist. But considering the scatter of the data points, it is not easy to quantify this effect. In addition, it might originate rather in the suspension effect on the reference electrode than in a real lowering of the systems redox potential.

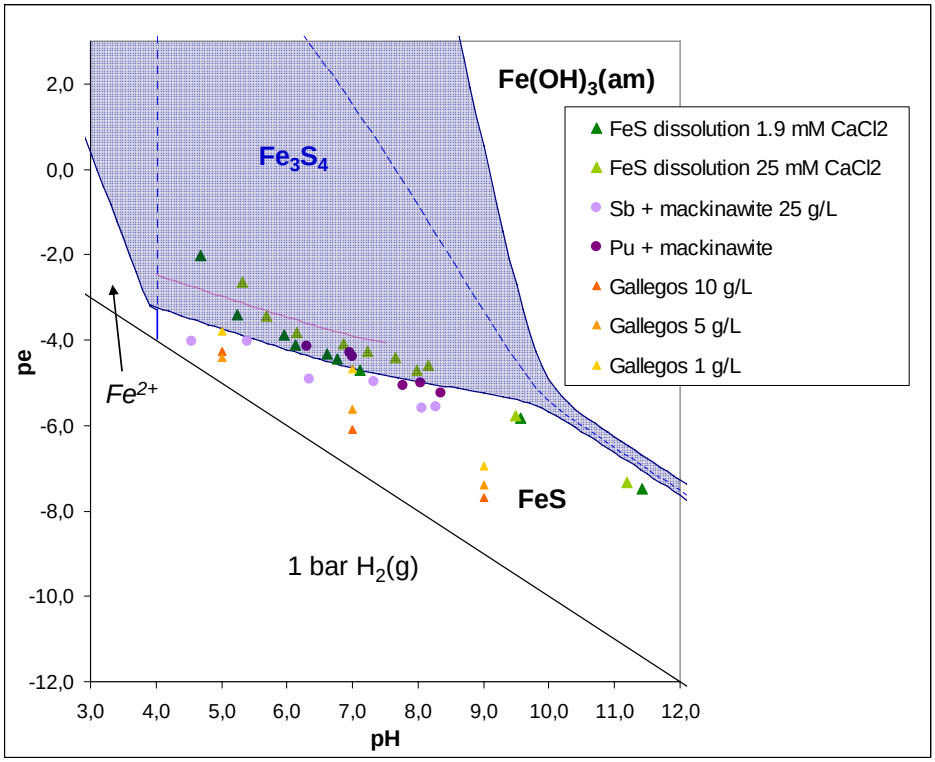

Figure 4.2.2. pe-pH predominance diagram for the Fe – S – H_2O system, considering equilibria between mackinawite (FeS(am)), greigite (Fe_3S_4), ferrihydroxide ($Fe(OH)_3$(am)), and dissolved ferrous iron. Sulfide oxidation and precipitation of $Fe(OH)_2$(s) is neglected. Concentrations of dissolved iron and sulfide result from dissolution of FeS as a function of pH. Solid phase names are printed in bold, solution species in italics. Dotted lines in the centre of the greigite field represent equilibria between FeS(am) and $Fe(OH)_3$(am) in the absence of greigite formation. Rose line in the greigite field results when a lower $\{H_2S\}$aq activity is assumed, e.g. through loss of H_2S(g); in this case, a decrease by 97 % of $\{H_2S\}$aq is assumed. Data points from FeS dissolution (green), from FeS + Sb(V) redox (light violet), and from FeS + Pu redox experiments from chapter 3.3 (purple). Triangles represent data are from the supporting information of Gallegos et al. (2008).[124]

Considering that apparently similar experimental approaches for the FeS dissolution experiments were used, it is surprising that very different redox potentials were obtained in this study and by Gallegos et al. (2008). However, one crucial difference existed between their and our study: their experiments were carried out in a glove box with 95 % N_2 and 5 % H_2 atmosphere, whereas ours were carried out in an N_2-glovebox (or Ar-glovebox for Pu-mackinawite). Thus, indeed, their system might be poised by the H_2/H^+ redox couple for which mackinawite functions as a catalytic surface. Whereas in our

system, in the absence of H_2, it would be the FeS-greigite or FeS vs partially oxidized FeS (i.e. accomdating some Fe(III) in its structure: $Fe^{II}S$ - $Fe^{II}_{1-x}Fe^{III}_{x}S$) that controls the redox potential. If this was true, the applicability of redox experiments carried out in the presence of $H_2(g)$ and a catalytic surface to natural settings where no such considerable amounts of $H_2(g)$ are present would be questionable. As N_2/H_2 glove boxes are common in many laboratories this issue should certainly be further investigated.

The greigite field above pH 10 in figure 4.2.2 is very small and whether it is found present at high pH values or not depends on the Δ_fG values assigned to Fe_3S_4 and $Fe(OH)_3$(am). If a more negative Δ_fG value is assigned to $Fe(OH)_3$(am), as done in the calculation on which figure 4.2.3 is based, it appears that, at high pH, it might be rather the FeS-$Fe(OH)_3$ equilibrium that control the redox potential. If another sulfide source in addition to FeS dissoltuion was present, this situation might change again and result in a larger greigite field even at high pH.

If modeling FeS dissolution and calculating a pe-pH diagram based on the resulting concentrations does not represent natural settings, it might, at least, be useful to understand results from laboratory studies, whose experimental conditions can be taken into account quite accurately.

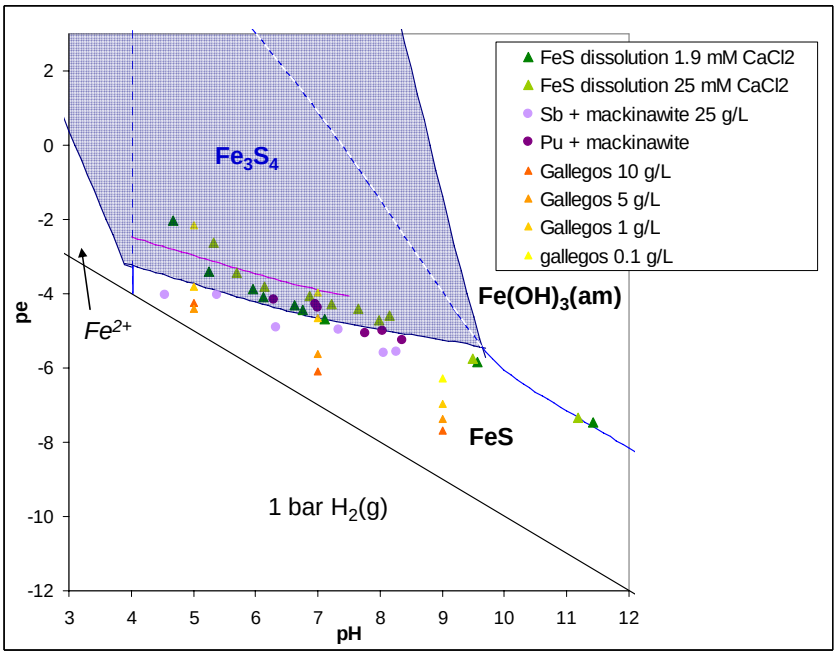

Figure 4.2.3. Same as Fig. 4.2, but using a Δ_fG value of -692 kJ/mol for $Fe(OH)_3$(am) instead of -688.35 kJ/mol.

Table 4.2.1. Gibbs free energies of formation for species used to calculate the diagrams in figures 4.1 to 4.3.

species	$\Delta_f G$ [kJ/mol]	source	species	$\Delta_f G$ [kJ/mol]	source
H_2O	-237.14	NEA-TDB[80]	FeS(am)	-83.68	L, TA12.1
OH-	-157.22	NEA-TDB	FeS(am)	-78.9	Wolthers, 2005[98]
Fe^{2+}	-78.87	L, TA12.1*	FeS(am)	-81.5	Fig. 4.2, 4.3
$FeOH^+$	-258.4	L, TA12.1	Fe_3S_4	-273.63	L, TA12.1
$Fe(OH)_2$	-436.18	L, TA12.1	$Fe(OH)_3$(am)	-688.35	L, TA12.1
$Fe(OH)_3^-$	-622.58	L, TA12.1	$Fe(OH)_3$(am)	-692	Stumm**
$FeCl^+$	-207.11	L, TA12.1			
Fe^{3+}	-4.6	L, TA12.1			
H_2S(aq)	-27.648	NEA-TDB			
HS^-	-12.243	NEA-TDB			
S^{2-}	120.7	NEA-TDB			
Cl^-	-131.21	L, TA12.3			

*L: Langmuir, Aqueous environmental geochemistry[79]
**Stumm: Aquatic chemistry[125]

Table 4.2.2. Equations and logK values used to compute diagrams in Fig. 4.1 to 4.3. logK values are based on $\Delta_f G$ values from Table 4.4; for equilibria containing FeS(am) and $Fe(OH)_3$am logK are based on $\Delta_f G$ = -81.5 kJ/mol and -692 kJ/mol, respectively. The equations in the bottom row indicates how, for each pH value, a H_2S(aq) concentration was computed. Based on this concentration, concentrations for HS^- and S^{2-} and Fe^{2+} were computed. Based on Fe^{2+} obtained as a function of H_2S(aq), concentrations for all other Fe(II) species were calculated. pH steps of 0.1 unit were used. No ionic strength correction was carried out for the calculation of the diagrams in Fig. 4.1 to 4.3. As for each pH, all sulfide species have a specific value corresponding to the H_2S - HS^- - S^{2-} equilibria, equations based on either of them yield the same pe for a given pH. Thus only equilibria including HS^- are given.

reaction		index	logK
$FeS(am) + 2H^+ \rightleftarrows Fe^{2+} + H_2S(aq)$	based on $\Delta_f G$ von -81.5 kJ/mol for FeS	K3	4.41
	based on $\Delta_f G$ von -83.68 kJ/mol for FeS	K3	4.03
$Fe^{2+} + H_2O \rightleftarrows FeOH^+ + H^+$		Ka	-10.09
$Fe^{2+} + 2\,H_2O \rightleftarrows Fe(OH)_2(aq) + 2\,H^+$		Kb	-20.49
$Fe^{2+} + 3\,H_2O \rightleftarrows Fe(OH)_3^- + 3\,H^+$		Kc	-29.38
$Fe^{2+} + Cl^- \rightleftarrows FeCl^+$			-0.52
$Fe^{3+} + e^- \rightleftarrows Fe^{2+}$			13.01
$H_2S(aq) \rightleftarrows HS^- + H^+$		K1	-6.99
$H_2S(aq) \rightleftarrows S^{2-} + 2\,H^+$		K2	-25.99
$Fe(OH)_3(am) + e^- + 3\,H^+ \rightleftarrows Fe^{2+} + 3\,H_2O$			17.22
$Fe^{3+} + 3\,H_2O \quad Fe(OH)_3(am) + 3\,H^+$			- 4.21
$Fe_3S_4 + 8\,H^+ + 2\,e^- \rightleftarrows 3\,Fe^{2+} + 4\,H_2(aq)$			12.89
$3\,Fe^{3+} + e^- + 4\,H_2S(aq) \rightleftarrows Fe_3S_4 + 8\,H^+$			26.15
$Fe_3S_4 + 2\,e^- + H^+ \rightleftarrows 3\,FeS(am) + HS^-$			-7.25
$Fe(OH)_3(am) + e^- + HS^- \rightleftarrows FeS(am) + H_2O + 2\,OH^-$			-8.18
$3\,Fe(OH)_3(am) + e^- + 4\,HS^- \rightleftarrows Fe_3S_4 + 4\,H_2O + 5\,OH^-$			-3.28
$O_2(g) + 4\,e^- + 4\,H^+ \rightleftarrows 2\,H_2O(l)$, pe = ¼ logK - pH			83.09
$H^+ + e^- \rightleftarrows ½\,H_2(g)$, pe = -pH – ½ log $pH_2(g)$			0
$\{H_2S(aq)\} = sqrt((K3\,\{H+\}^2\,(1 + Ka/\{H+\} + Kb/\{H+\}^2 + Kc/\{H+\}^3 + Kd\{Cl-\}) / (1 + K1 / \{H+\} + K2/ \{H+\}^2)$			

4.3. Sorption of antimony to mackinawite

In experiments Stime_ac and Stime_bas (Table A4.2), the time dependence of sorption, or rather, removal from solution, of Sb(V) by mackinawite was investigated ([Sb]initial = 1 10^{-4} M, 1.73 g/L FeS in 25 mM $CaCl_2$). As will be seen from the XAS data, removal of Sb(V) from solution is, at acidic pH, a coupled adsorption-reduction and ligand exchange process and is (or can be), at basic pH, a coupled adsorption-reduction-coprecipitation process. One can thus not expect to obtain a reaction order for any single process from these data. A further complication results from the fact that the sorption-reduction-ligand exchange process of Sb(V) at acidic pH goes along with a considerable increase in pH (from pH 5.6 to 6.4 during the first day, period wherein 99.4 % of Sb were removed from solution), sorption does thus not take place at a constant pH.

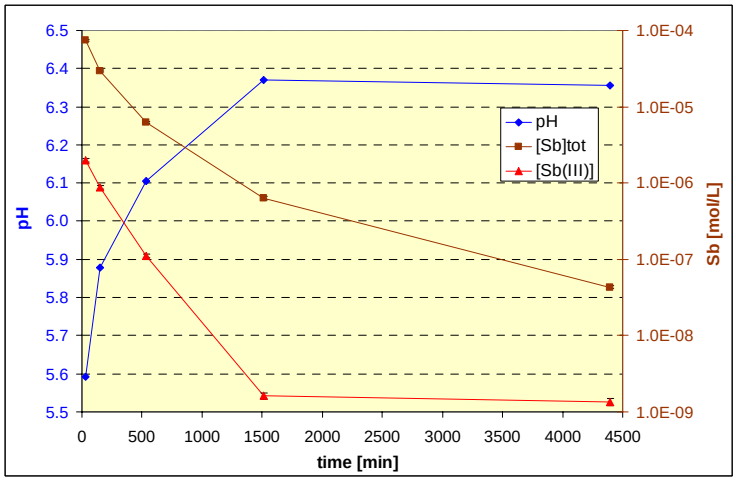

Figure 4.3.1. pH suspension, $[Sb]_{total}$, and [Sb(III)] plotted over time for sample Stime_ac.

At acidic pH (experiment Stime_ac, Fig. 4.3.1), removal of Sb(V) from solution is relatively fast and an uptake level of 99.4 % is attained within one day (Fig. 4.3.2 b). However, within the first thirty minutes and in contrast to "simple" adsorption reactions[126] only about 25 % of $[Sb]_{total}$ are removed, indicating that the removal process of Sb(V) is somewhat complex and not only constituted by direct surface complexation of the Sb(V) solution species. Sb(III) accounted for up to 3 % of total dissolved antimony and its concentration decreased more rapidly than $[Sb]_{total}$ (3 orders of magnitude over the first day compared to 2 orders of magnitude for $[Sb]_{total}$), reaching nano-molar concentration levels within 1 day. Over the duration of the experiment, $[Sb]_{total}$ decreased to a concentration of 43 nmol/L, but as steady state had not been reached, the data do not provide an equilibrium concentration at the obtained mackinawite loadings of 5.4 mmol Sb/mol FeS (= 61 µmol Sb/g FeS). The Sb concentration after three days, 43 ± 2 nmol/L (= 5.3 ± 0.3 µg/L Sb), corresponds to the WHO drinking water guideline value of 5 µg/L. Under mildly acidic conditions (pH range 5.5 – 6) sediments containing nano-particular mackinawite can thus be expected to effectively retain antimony and reduce dissolved Sb concentrations to drinking water standard levels.

Compared to the Sb uptake under acidic pH conditions, antimony removal from solution is very slow at alkaline pH (experiment Stime_bas, Fig. 4.3.2 b), only 15 % of total antimony having been removed from solution within 3 days. In contrast to the uptake reaction at acidic pH, the suspension pH is very stable at pH 8.1 and, while at acidc pH the highest Sb(III) concentration occurred at the beginning of the reaction period, at alkaline pH the highest Sb(III) concentration was recorded after 1 day of reaction, accounting for 0.5 % of dissolved antimony (Fig. 4.3.2a).

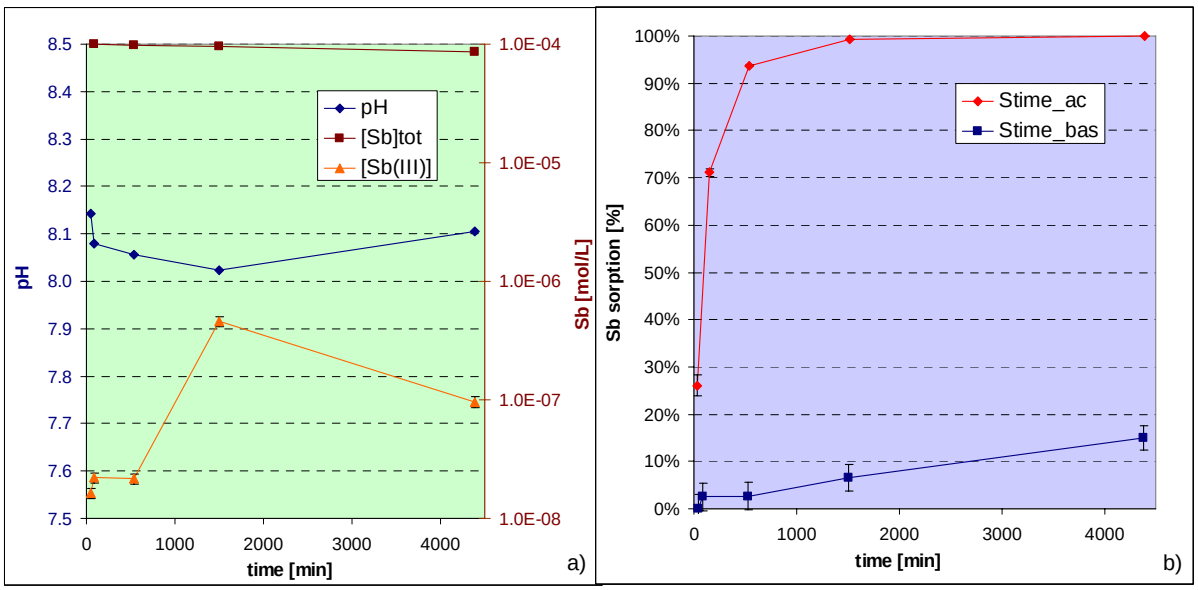

Figure 4.3.2. a) Stime_bas experiment: pH, $[Sb]_{total}$ and Sb(III) over time, b) Sb sorption [%] over time for pH 5.6 to 6.4 (Stime_ac) and at pH 8.1 (Stime_bas).

Despite the fact, that several processes occur simultaneously during the removal of Sb(V) from mackinawite suspensions and despite the fact, that in sample Stime_ac the pH was not stable, it might still be possible to get an order of magnitude idea to what extent the rate of Sb removal varies with pH. As the data from Stime_bas are well fitted assuming a pseudo-first order process (Fig. 4.3.3 b), the first order linearisation was also applied to Stime_ac (Fig. 4.3.3 a) and the slope for pairs of two points was determined and assigned to the average pH value for this pair. Plotting logk of Stime_ac and Stime_bas as a function of the proton activity, it appears that the rate of Sb removal from solution changes by about one order of magnitude per pH unit (Fig. 4.3.3 c).

As the experiment lasted only 3 days, it can, of course, not be known from it how the reaction at pH 8 would proceed, i.e. how long it would take to reach equilibrium and how many percent Sb would then be adsorbed. In addition, it is possible be that, were more data available, it became clear that the rate of Sb sorption is not adequately modelled by a pseudo-first order reaction. In addition, as the mackinawite solid/solution ratio in this experiment was between the one of the first and the second XAS experiment (A and B), it is not clear, whether the process occuring during Sb removal is similar to the first experiment, in which only one process was apparent over the whole pH range or if more than one process is occuring as is apparent in the second experiment at lower FeS concentrations. The

found pH dependence of the rate constant of Sb removal from solution is thus only a rough, overall approximation of a complex process with a strong pH dependence.

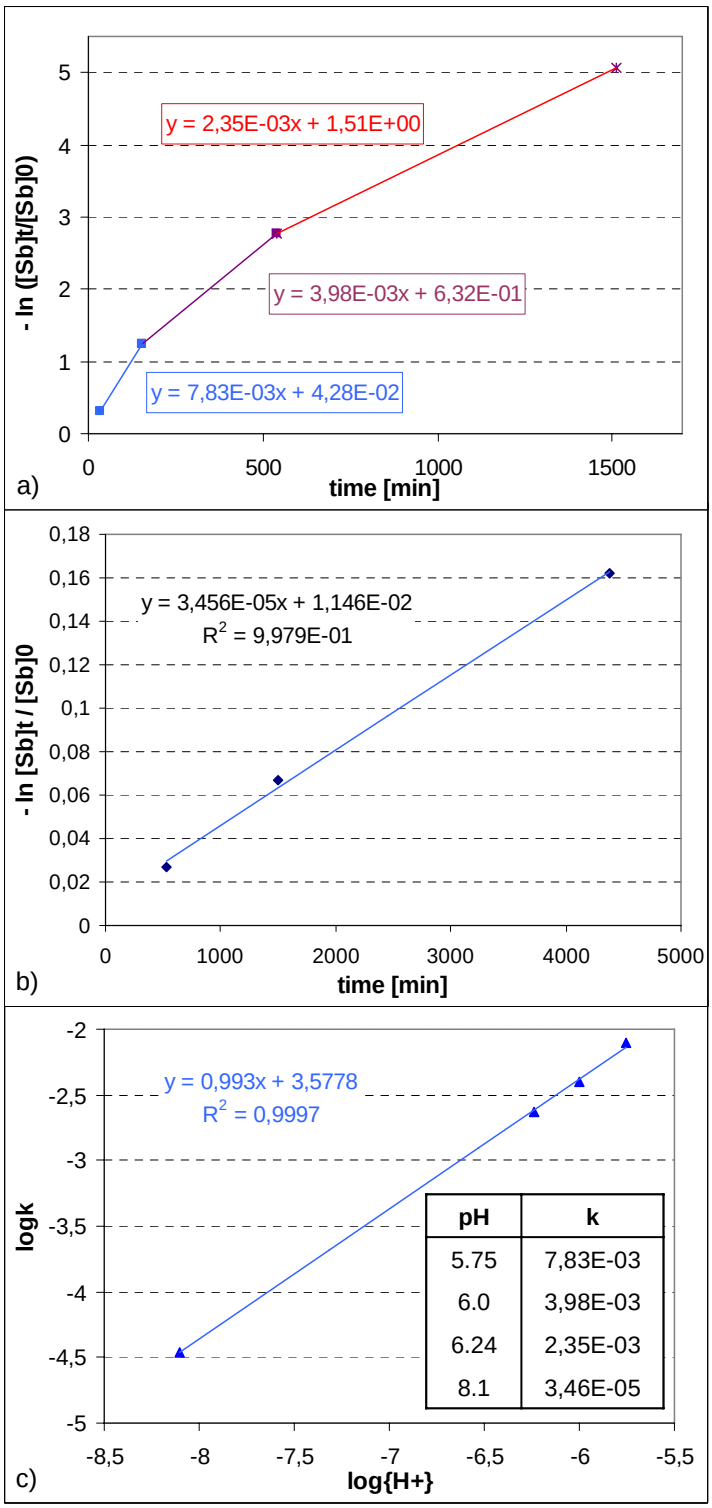

Figure 4.3.3. Plot of - $\ln([Sb]_t/[Sb]_0)$ over time for samples Stime_ac (a) and Stime_bas (b) and pseudo-first order rate constant as a function of proton activity (c).

Sorption of Sb(V) to mackinawite as a function of pH is shown in figure 4.3.4. From the lowest tested pH value of about 3.7 (and despite considerable FeS dissolution) up to pH 5.7, sorption of Sb(V) is

complete within the reaction time of about one day. Above pH 8.5, it is almost zero. As sorption in 1.9 mM $CaCl_2$ was slightly higher than in 25 mM $CaCl_2$, a slight influence of influence of ionic strength seems to exist. High sorption below the point of zero charge of a mineral surface (when it is positively charged) is common for anions and thus not surprising for Sb(V) that exists predominantly as $Sb(OH)_6^-$ above pH 2.5.

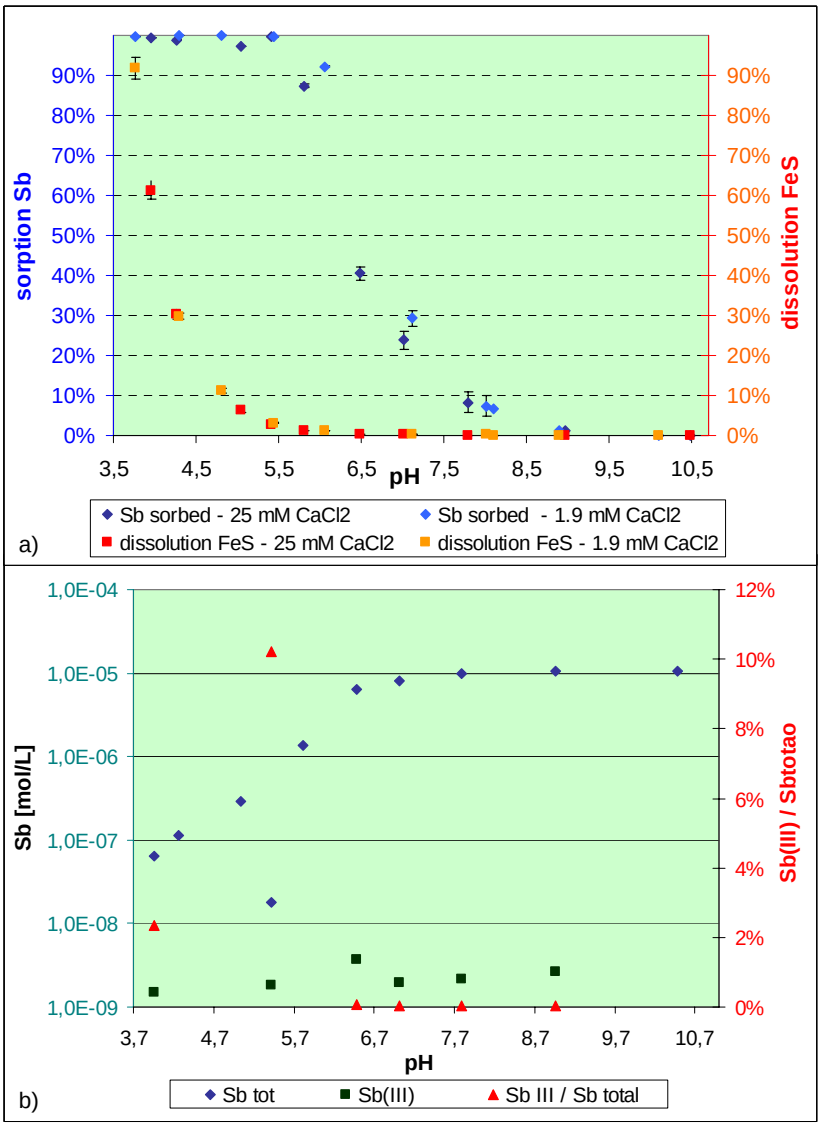

Figure 4.3.4. Sorption of Sb(V) to mackinawite as a function of pH (experiments SpH_a and b). a) % Sb sorption and % FeS dissolution, b) final $[Sb]_{total}$ and [Sb(III)] concentrations as a function of pH and Sb(III) content in percent (in 25 mM $CaCl_2$).

Sb(III) levels in solution were very low (up to $1 \cdot 10^{-8}$ M) and above pH 6 Sb(III) did not represented more than one percent of the total dissolved Sb (Fig. 4.3.4 b). When more than 90 % of Sb(V) had been sorbed, Sb(III) could represent up to about 10 % of dissolved Sb. With HG-AFS Sb(III) was differentiated from Sb(V) but whether Sb(III) is present as a sulfide complex or as $Sb(OH)_3$ has not been investigated.

Two isotherm experiments (Siso_ac and Siso_bas) were undertaken to investigate how the Sb/FeS loading and the equilibrium solution concentration are related. It is clear from the Stime_bas experiment, that the reaction time of 34 hours at alkaline pH was to short to reach equilibrium. None the less, a few insights can be gained from this experiment. As can be seen in figure A4.2a, sorption was accompanied by a 0.2 to 0.6 units increase in pH, the increase being greater for higher initial Sb concentrations. Sorption never exceeded 25 % and was higher for samples with a higher initial Sb concentration, resulting in an almost linear sorption isotherm (Fig. A4.2 d). Such isotherms have been observed, e.g., when sorption occurs through or along with formation of a surface precipitate.[127] Sb(III) increased somewhat with the final pH but was never above 0.5 % of the total dissolved Sb (Fig. A4.2c). During the Siso_ac experiment, the pH increased considerably (by up to two pH units) as a function of the initial Sb(V) concentration (Fig. 4.3.5 a). A sorption isotherm could thus not be obtained. In contrast, it was found that the Sb removal plotted as a function of the final pH closely follows the pH edge observed earlier (Fig. 4.3.4 a, 4.3.5 b). For the four highest start concentrations, Sb(III) reached about $1 \cdot 10^{-5}$ M in solution and represented at maximum about 5 % of the total dissolved Sb (Fig. 4.3.5.c).

In conclusion, these sorption experiments suggest that different mechanisms might be responsible for Sb removal from solution at acidic and basic pH, the process at acidic pH being orders of magnitude faster than at alkaline pH. The process occurring at acidic pH consumes protons and if the pH is not strongly buffered, the suspension pH will increase. It would thus be possible that e.g. acidic mine drainage containing Sb(V) would first interact with mackinawite through the first mechanism and, once enough protons have been consumed, through the second, slower mechanism operating in the alkaline pH range.

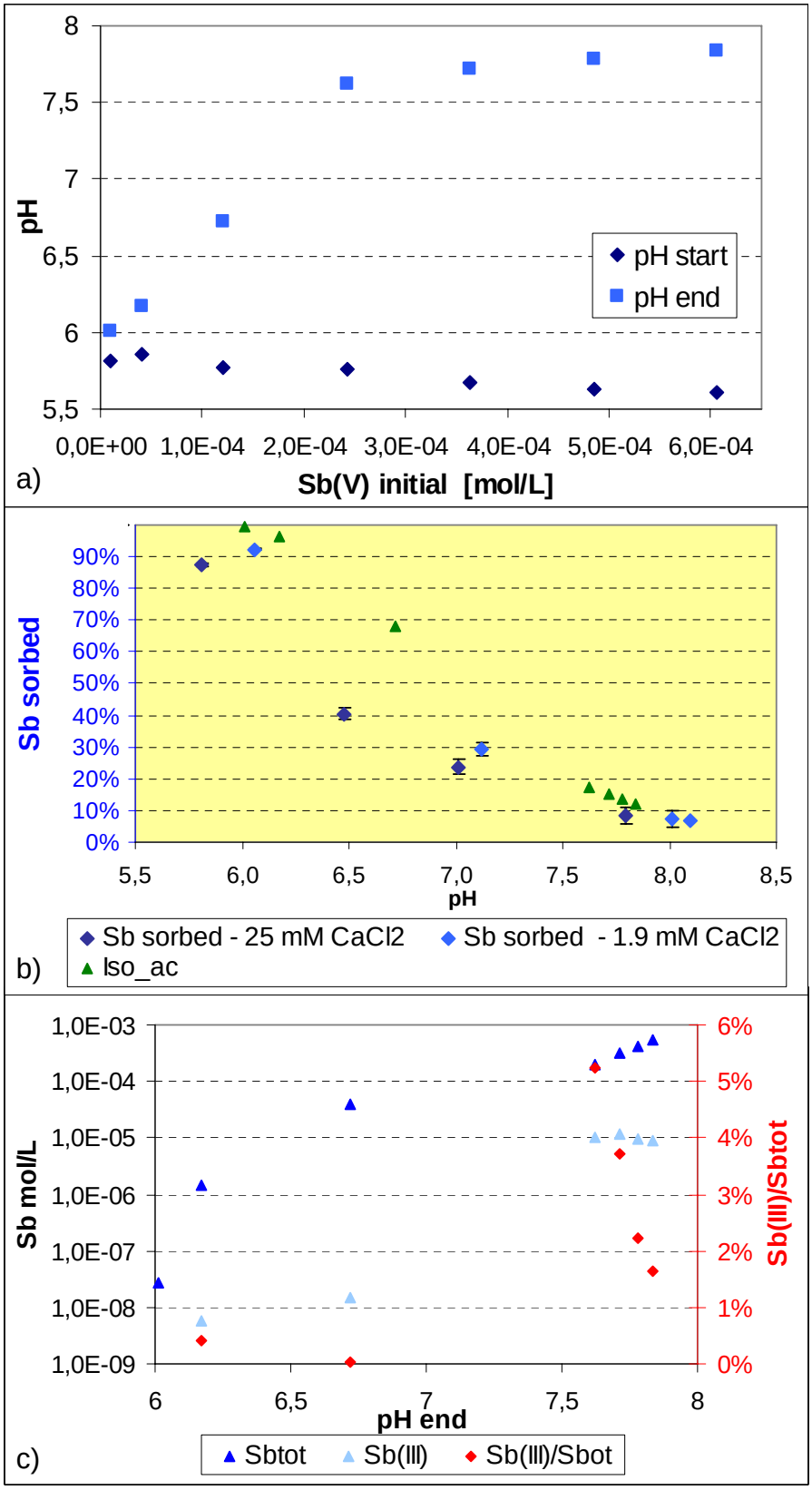

Figure 4.3.5. a) pH increase as a funtion of initial Sb(V) concentration in Siso_ac experiment. b) Comparison of Sb sorption as a function of the final pH in Siso_ac with pH dependent sorption from experiments SpH_a and SpH_b. c) Final total dissolved Sb, Sb(III) and Sb(III) over Sb_{total}.

4.4. Results from X-ray absorption spectroscopy and powder X-ray diffraction

a) Experiment A – low Sb/FeS loadings

As was observed in the sorption experiments in the preceding chapter, the sorption rate of Sb(V) to FeS is strongly pH dependent. This led to a wide range of Sb/FeS loadings for the first series of XAS samples ($2.3 \cdot 10^{-7}$ to $4.4 \cdot 10^{-6}$ mol Sb/g FeS). Dissolved antimony concentrations follow the behavior observed at lower FeS solid/solution ratios (1.7 g/L for sorption experiments vs 25 g/L for the first XAS experimetn) and are higher at higher pH and shorter reaction time (Fig. A4.1).

The position in energy of the XANES region of all spectra obtained from the samples of experiment A suggests that all contain Sb(III) as the main antimony oxidation state after reaction of antimony with mackinawite (not shown). In all samples added Sb(V) was reduced to Sb(III) and added Sb(III) was not further reduced, making its behavior different from As(III), that, with mackinawite, reacts to form realgar (AsS).[124, 128] PCA of the EXAFS-spectra of all samples indicates that only one eigenvector is present. Thus all spectra spectra were averaged. Shell fitting of the resulting average spectrum yields a coordination shell of three sulfur atoms at a distance of 2.46 Å around a central Sb atom.

The threefold coordination in the found SbS_3-complex is typical of Sb(III) which, due to its position in group 15 in the periodic table, has a fully occupied s and three partially filled p orbitals in its outermost electron shell ([Kr] 5s2 5p3), commonly resulting in trigonal pyramidal geometry.[129] Sb(III)-S distances similar to the one found occur in stibnite (Sb_2S_3) (2.53 Å for the first Sb-S shell from XRD[95] and 2.51 Å from EXAFS[40]) and where calculated for Sb(III)-sulfide monomers.[41] For $Sb(SH)_3$ and the fully deprotonated SbS_3^{3-}, the calculated Sb-S distances were 2.42 Å and 2.46 Å, respectively.[41] In contrast, Sb(V) in sulfide complexes exists in fourfold coordination with Sb(V)-S distances of 2.34 Å.[38, 40] XANES and EXAFS data are therefore in agreement with the predominance of Sb(III) in the experiment A samples. At all tested pH values, Sb(V) was thus completely reduced to Sb(III), and the Sb(III)-S_3 complex obtained was identical whether Sb(V) or Sb(III) were initially added. Questions concerning the formed Sb(III)-S_3 complex left unanswered from experiment A are, firstly, whether the identified Sb(III)-S_3 complex is monomeric and, secondly, what the protonation state of the complex might be. Due to the high noise level in the EXAFS data, a second shell of S, Fe or Sb could not be identified, leaving the first question for now unanswered. As far as protonation is concerned, fully deprotonated monomeric SbS_3^{3-} should only be predominant above pH 9.[130] However, $SbS_2(SH)^{2-}$, which should be predominant in the pH range of experiment A, should be characterized by two different Sb-S distances (2 S atoms at 2.355 Å, 1 S atom at 2.677 Å, from which results and average Sb-S distance of 2.46 Å)[41] that, depending on the length of the EXAFS spectrum, should either be resolved by shell fitting or should lead to a high σ^2 value for the coordination shell. The found σ^2 value of 0.0044 $Å^2$ does not suggest that the Sb-S coordination shell might be composed of several Sb-S distances and fitting with two different Sb-S starting distances does not converge.

In the absence of a second shell, we cannot deduce with certainty whether the observed Sb(III)S_3 complex is present as an inner-sphere complex, sharing at least one sulfide atom with the FeS surface,

or as an outer-sphere complex. In the former case, the pKa values of the Sb(III)-S_3 surface complex are likely to be different from the ones of the dissolved $Sb(SH)_3$ species and a completely deprotonated species (such as a surface bound ≡ FeS-Sb(III)S_2^{2-}) might predominate already at lower pH. It is further likely that the two different environments for Sb bound sulfide (surface S(-II) and water coordinated S^{2-}) would yield Sb-S bond lengths different from what is found in dissolved $SbS_2(SH)^{2-}$, and it is possible that the difference in Sb-S bond lengths between the two sulfide environments would be smaller than in $SbS_2(SH)^{2-}$ and might then not be resolved by shell fitting or indicated by a large σ^2 value. Among the dimeric Sb(III)-sulfide complexes, $Sb_2S_4^{2-}$ and $HSb_2S_4^-$ are characterized by several different Sb-S bond lengths (2.32 Å and 2.50 Å for the former and 2.26 Å to 2.57 Å for the latter, with an averaged Sb-S distance of 2.44 Å for both species)[41] and only the two Sb-S distances in $H_2Sb_2S_4$ ((Sb-S) average: 2.43 Å), which, however, becomes important as a solution species only below pH 5,[38] are very close to each other (2.428 vs. 2.437 Å). As explained above for $SbS_2(SH)^{2-}$, the different Sb-S distances in $Sb_2S_4^{2-}$ and $HSb_2S_4^-$ should be resolved by shell fitting or result in large σ^2 values when fitted with a single Sb-S shell.

From the coordination shell fit of the observed SbS_3 species, it cannot clearly be deduced whether the complex is protonated, as one might expect in accordance with data for both mono- and dimeric Sb sulfide complexes, or not, or whether it is present as an inner-sphere complex sharing a surface sulfide atom or not. As the shell fit does not indicate more than one Sb-S distance, a monomeric and fully deprotonated Sb(III)-S_3 surface complex appears, however, to best be agree with the EXAFS data.

b) Experiment B – higher Sb/FeS loadings

As observed before, sorption of Sb(V) to mackinawite was also in this second XAS experiment largely different for samples reacted at acidic or basic pH, leading to very different Sb loadings (Fig. 4.4.1, Table 4.1.3). At acidic pH, sorption was, for all initial Sb concentrations, complete within 4 days, whereas at basic pH only 10 to 14 % of Sb had been sorbed at the end of the reaction time, i.e. after 7 days. Similarly to the Siso_bas experiment, a linear sorption isotherm was obtained from the Xb_bas samples (Fig. A4.4). It can be seen how, over time, the loading increases and the isotherm shifts upwards. As clearly equilibrium had not been attained, no attempt at modelling the resulting isotherm has been made.

According to their XANES (Fig. 4.4.2) and EXAFS spectra (Fig. 4.4.4.), the samples from experiment B clearly fall into two groups corresponding to the pH conditions at which mackinawite was reacted with Sb(V). The samples prepared at an acidic pH are all characterized by a lower X-ray absorption edge position and lower WL intensity compared to the samples prepared at basic pH or to Sb(V) adsorbed to hematite, which is used as Sb(V) reference for composition analysis by ITT (Fig. 4.4.2). Despite some variation in WL intensity and post-WL shape among the Xb_ac samples, PCA with ITFA yielded only one EV for all Xb_ac samples (spectra were analyzed in the energy range from 30460 to 30550 eV). A reconstruction of the Xb_ac samples with one EV is shown in (Fig. A4.6). If the Xb_ac and Xb_bas samples are analyzed together, two eigenvectors are necessary for the

reconstruction of the 7 spectra (Fig. A4.7 a). When $Sb(V)_{ads\text{-}hematite}$ is added for reference, still two EV are sufficient to reconstruct the then 8 spectra (Fig. A4.7 b). As oxidation state and local coordination environment are reflected in the position and shape of the XANES region of the absorption spectrum, the presence of two EV in the Xb_ac and Xb_bas samples and metal oxide adsorbed Sb(V) suggests that the Xb_bas samples are composed by two components: one whose oxidation state and local coordination environment are similar to the Xb_ac samples and another that corresponds to Sb(V) in an octahedral oxygen environment.

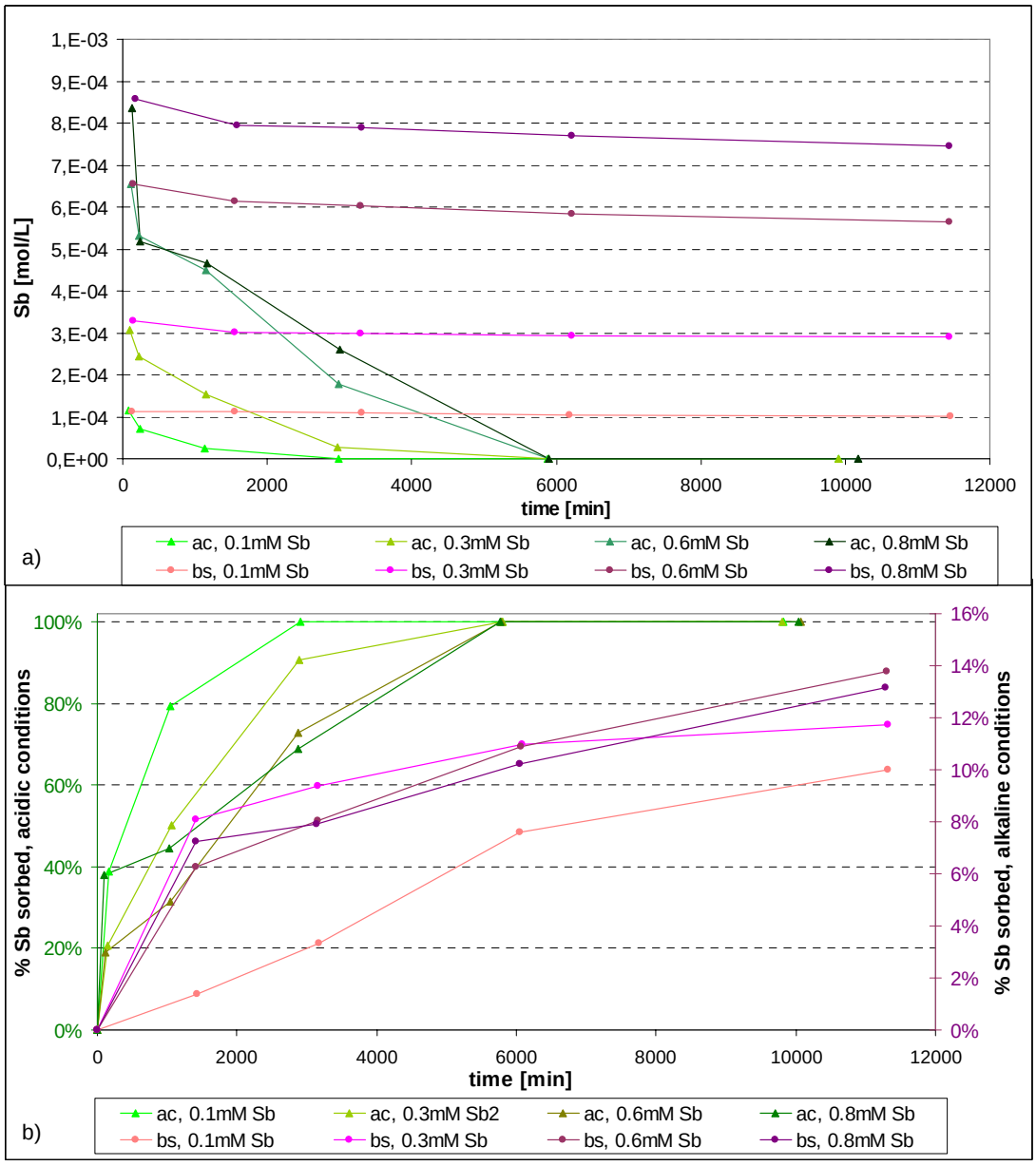

Figure 4.4.1. Dissolved Sb over time (a) and Sb sorption over time (b) for XAS experiment B. Xb_ac_1 to 4 samples are shown in green, Xb_bas_1 to 4 samples in pink-violet. Lines between data points are guide to the eye. In b) Xb_bas samples refer to the right side ordinate.

For a quantitative composition analysis iterative target testing (ITT) with two factors was performed, assigning factor 1 to the Xb_ac_2 spectrum and factor 2 to Sb(V) adsorbed on hematite. The small variation in WL intensity and shape among the Xb_ac samples is reflected in an apparent composition

variation of up to 6 % among the 4 Xb_ac samples, even though, statistically, they consist of only one eigenvector. The Xb_bas samples contain between approximately 50 % and 25 % of factor 1 and a corresponding 50 % to 75 % of factor 2 (Table 4.4.1). A graphic representation of the ITT composition analysis through reconstruction of the sample spectra by two factors is given in figure 4.4.3.

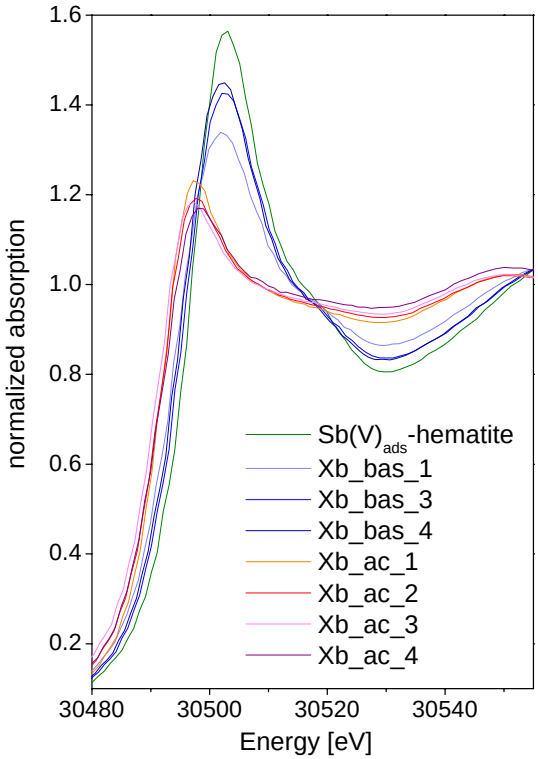

Figure 4.4.2. Sb-K-edge XANES spectra of XAS experiment B, Sb(V) adsorbed to hematite is shown for reference.

Table 4.4.1. Composition analysis by ITT of the Xb_ac and Xb_bas samples using Xb_ac_2 and Sb(V) adsorbed on hematite as references, containing 100 % of factor 1 and factor 2, respectively. Energy range: 30460 eV to 30555 eV.

spectrum	factor 1 [%]	factor 2 [%]	sum [%]
Xb_ac_1	93.8	5.8	99.6
Xb_ac_2	100[f]	0[f]	100[f]
Xb_ac_3	100.0	0.0	100.0
Xb_ac_4	94.5	5.8	100.3
Xb_bas_1	46.9	53.5	100.4
Xb_bas_3	25.5	74.5	100.0
Xb_bas_4	28.5	72.3	100.8
$Sb(V)_{ads}$-hematite	0[f]	100[f]	100[f]

f: fixed

In figure 4.4.4 a) representative Xb_ac sample (Xb_ac_2) is compared to two of the Xb_bas samples with lowest and highest Sb loading (all four Xb_ac samples are shown in the annex, Fig. A4.8). In the EXAFS (Fig. 4.4.4 a) the decrease in intensity of the Sb-S paths when going from Xb_ac_2 (black), to Xb_bas_1 (green) to Xb_bas_4 (red) is clearly apparent. Equally in the Fourier Transform, the Sb-S

peak present in the Xb_ac_2 spectrum decreases considerably (until becoming quasi absent) in the Xb_bas_1 and 4 spectra (Fig. 4.4.4 b). The composition of the Xb_ac and Xb_bas samples was further analyzed by shell fitting of the EXAFS spectra. Results for the samples of figure 4.4.4 are given in Table 4.4.2 whereas plots in k- and R-space and fit parameters for all 7 Xb samples and tripuhyite are given in the annex to this chapter (Fig. A4.9-12, Tables A4.1, 2).

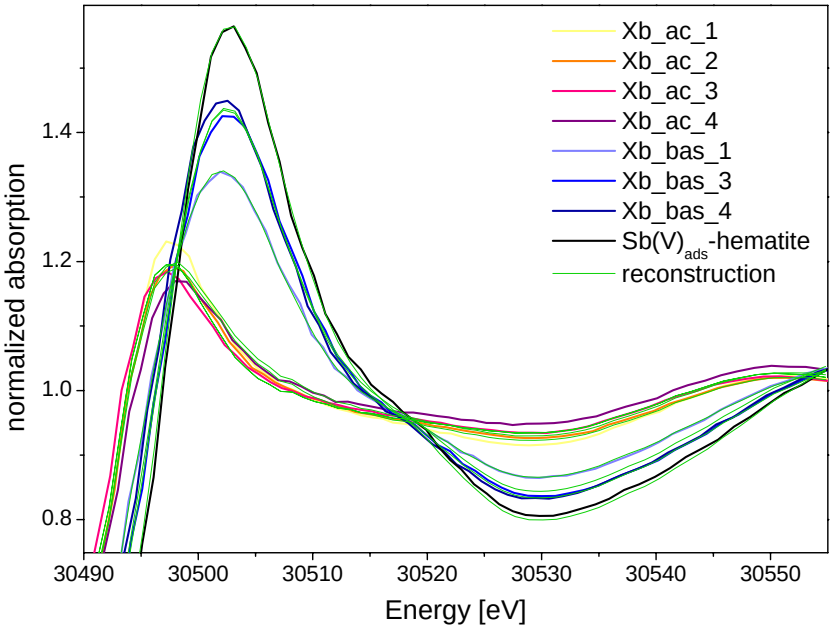

Figure 4.4.3. Experimental spectra and reconstruction of the 8 XANES spectra (Xb_ac, Xb_bas, Sb(V) on hematite) on which composition analysis by ITT with two factors (see text) was performed.

For all Xb_ac samples, a Sb-S distance of 2.47 Å and DW of 0.004 $Å^2$ are found in agreement with the result from the first XAS experiment (Xa). For Xb_ac 2 to 4, a Sb-S CN of 3 is fitted whereas for Xb_ac_1 a slightly higher value is obtained (Table A4.1). As factor analysis yielded only one factor for all Xb_ac spectra, this higher CN is considered not significant and is not further considered. The impact on the shell fit of implementing a Sb-Sb shell in addition to the Sb-S coordination shell was considered (Table 4.4.2 and Table A4.1). The fit residual and standard deviation between fit and experimental EXAFS spectrum are slightly reduced when such a second shell is implemented and the found Sb-Sb distance would correpond quite well to Sb-Sb in Sb_2S_3 of 3.83 Å. However, wavelet analysis gave no indication for the presence of a Sb backscatterer or of any additional backscatter beyond the sulfur coordination shell (not shown). It is thus not completely excluded that a Sb-Sb paths with a similar distance to the one present in Sb_2S_3 exists but, due to the smaller Sb-S distance in the formed Sb-S_3 complex, precipitation of an amourphous metastibnite phase (Sb_2S_3(am)) is unlikely and the hypothesis of a SbS_3-surface complex is maintained.

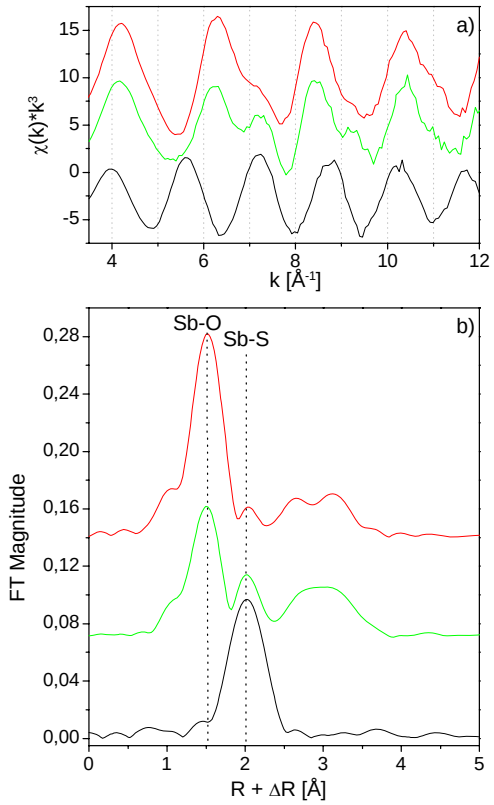

Figure 4.4.4. EXAFS (a) and FT (b) of samples Xb_ac_2 (black), Xb_bas_1 (green) and Xb_bas_4 (red).

Table 4.4.2. Shell fitting results for samples Xb_ac_2, Xb_bas1 and Xb_bas_4.

sample	shell	CN	R(Å)	σ^2(Å^2)	ΔE_0	Res (%)
Xb_ac_2	Sb-S	3.3	2.47	0.0039	11.9	5.6
	Sb-S	3.3	2.47	0.0039	11.9	3.1
	Sb-Sb	1.0	3.81	0.0112		
Xb_bas_1	Sb-O	3.2	1.97	0.0029[c]	11.8	5.3
	Sb-S	0.9	2.45	0.0029[c]		
	Sb-Fe	0.9	3.11	0.0028[d]		
	Sb-Fe	2.0	3.54	0.0028[d]		
Xb_bas_4	Sb-O	4.4	1.97	0.0022[e]	11.6	7.1
	Sb-S	0.1	2.50	0.0022[e]		
	Sb-Fe	0.9	3.10	0.0049[f]		
	Sb-Fe	2.2	3.55	0.0049[f]		
				c, d, e, f - correlated		

	Xb_ac	Xb_bas
k-range	$3.5 \leq k \leq 12.1$ Å^{-1}	$2.6 \leq k \leq 12.6$ Å^{-1}
R-range	$1.6 \leq R \leq 4.1$ Å	$1.1 \leq R \leq 3.9$ Å

To fit the Xb_bas_1 sample, Sb-O, Sb-S and two Sb-Fe paths were necessary whereas for Xb_bas_3 and 4, the Sb-S shell could be implemented but its presence or absence hardly influenced the fit residual and did not change the fit parameters obtained for the other paths.

The found Sb-Fe distances of approx. 3.11 Å and 3.55 Å are characteristic of edge and corner-sharing arrangement between SbO_6 and FeO_6 octahedra as they occur e.g. in the mineral tripuhyite ($FeSbO_4$) and as they have been observed for sorption of Sb(V) onto iron oxides and coprecipitation of Sb(V) with ferrihydrite.[43, 49] The high Sb-Fe coordination numbers of approx 1 for the shorter and approx 2 for the longer Sb-Fe distance are similar to the one obtained by Mitsunobu et al. (2010) for coprecipitation of Sb(V) with ferrihydrite.[49] In their study, CN resulting from surface sorption of Sb(V) onto ferrihydrite were only about 0.7 for the first and 0.9 for the second Sb-Fe distance.

According to the XANES sample Xb_bas_3 and 4 both contain about 70 % of Sb(V) (Table 4.4.1). Reduction of Sb(V) to Sb(III) appears thus be coupled to coprecipitation of Sb(V) with Fe(III), most likely resulting in a Sb containing ferrihydrite. To reach a content of 70 % Sb(V) in the solid phase, 2 Sb(V) molecules have to be precipitated for each Sb(V) that is reduced to Sb(III). As 2 Fe(II) are consumed for this reduction, a Fe/Sb ratio in the coprecipitate of 1 results, similar to the composition of tripuhyite ($FeSbO_4$). In addition, some Sb(V) adsorption to the coprecipitate may occur, further raising the Sb(V) content in the solid phase. In figure A4.13 in the annex, a possible structure for the resulting Sb(V)-Fe(III) coprecipitate is proposed based on the ferrihydrite structure published by Michel et al. (2007)[131] in which some FeO_6 octahedra were substituted by SbO_6 octahedra. In these cluster, the Sb : Fe ratios are close to 1 (4 : 5 for one and 5 : 7 for the second cluster) and the average number of edge (E) and corner sharings (C) per Sb atom are close to what was obtained in the shell fit: E = 0.75, C = 2 for the 4 : 5 cluster and E = 1, C = 2 for the 5 : 7 cluster.

The reduction reaction of Sb(V) with FeS might then tentatively be formulated as:

$$2\ FeS + Sb(OH)_6^- + \equiv FeS^- \rightarrow \equiv FeSSbS_2^{2-} + 2\ Fe(OH)_3 \qquad (4.4.1)$$

If one wants to take coprecipitation of Sb(V) with $Fe(OH)_3$ into account, one might assign the formula of tripuhyite to this coprecipitate and write:

$$2\ FeS + 3\ Sb(OH)_6^- + \equiv FeS^- \rightarrow \equiv FeSSbS_2^{2-} + 2\ FeSbO_4 + 8\ H_2O + 2\ OH^- \qquad (4.4.2)$$

In this case, for each Sb(V) removed from solution 0.66 hydroxide ions would be released to solution. As the mackinawite surface can buffer considerable amounts of protons or hydroxide ions, equation 4.4.2 would be in agreement with the almost stable pH in the Xb_bas samples.

Diffraction pattern of all Xb_ac and Xb_bas samples were acquired by synchrotron powder XRD (Fig. 4.4.5). For the samples reacted at basic pH in the absence of antimony (Xb_bas_0) or in presence of different concentrations of Sb(V) (Xb_bas_1 to Xb_bas_4), all peaks present in the diffraction patterns originate from mackinawite and in the five spectra, no evolution from Xb_bas_0 to Xb_bas_4 can be observed. The solid phase or phases resulting from reaction of Sb(V) with mackinawite at basic pH are therefore either X-ray amorphous and not apparent in the diffraction pattern or are, even though crystalline, not visible in the XRD as they make up only too limited an amount of the total solid. Both explanations can be valid as nanocrystalline ferrihydrite may indeed be X-ray amorphous and as even

in the sample resulting from the highest Sb concentration (Xb_bas_4) the loading was only $1 \cdot 10^{-4}$ mol Sb/g FeS or 1 mol % (mol Sb/ mol FeS).

For the Xb_ac spectra, an evolution from Xb_ac_0 to Xb_ac_4 can be clearly perceived. While only small changes occur between the antimony free sample (Xb_ac_0) and the ones originating from the two lower Sb(V) concentrations (Xb_ac_1 and Xb_ac_2), new peaks are clearly apparent for the two samples originating from the higher Sb(V) concentrations (Xb_ac_3 and Xb_ac_4, light and dark green in Fig. 4.4.5). All peaks occurring in addition to the ones from mackinawite are in agreement with greigite, Fe_3S_4, a mixed valence Fe(II)-Fe(III) iron sulfide with inverse spinel structure. Prominent are, in particular, the peaks at 6.1°, 7.2°, 8.7° and 12.3° 2-theta.

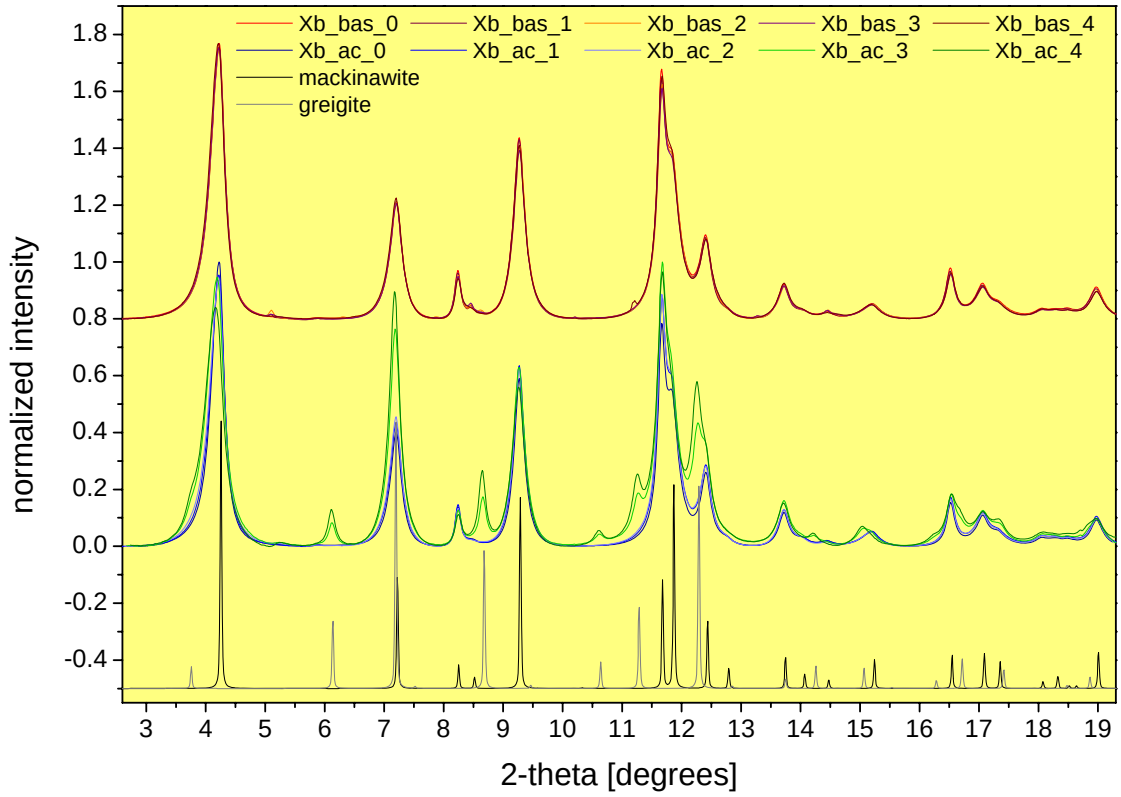

Figure 4.4.5. Diffraction patterns for Xb_ac (red-violet) and Xb_bas (green or blue) samples acquired by synchrotron diffraction at a wavelength of 0.3738 Å compared to greigite (ICSD 42535)[132] (grey) and mackinawite (ICSD 81087)[133] (black) patterns.

It is surprising, that these four peaks are well visible in the Xb_ac_3 diffraction pattern but are absent from the Xb_ac_2 pattern. Possibly, the amount of greigite present in the Xb_ac_2 sample, whose loading in antimony is about 40 % of that of Xb_ac_3, is not sufficient to result in visible diffraction peaks. Considering the size of the peaks at 8.7° and 12.3° 2-theta, one would, however, expect peaks with almost half the area of the light green peaks to still be visible. Another, more likely, possibility is that formation of a separate greigite phase starts only once mackinawite cannot accommodate Fe(III) in its structure any more.[134, 135]

While the exact mechanism of reduction of Sb(V) by mackinawite under acidic conditions cannot be solved, from the observation of greigite as oxidation product of mackinawite and from the observed

SbS_3 (probably surface) complex, the following overall reaction can be formulated:

$$\equiv FeSH_2^+ + 4\,FeS + Sb(OH)_6^- + 2\,H_2S \rightarrow \equiv FeSSbS_2^{2-} + Fe_3S_4 + Fe^{2+} + 6\,H_2O \qquad (4.4.3)$$

If not sufficient dissolved H_2S is present, equation 4.4.3 might be rewritten as:

$$\equiv FeSH_2^+ + 6\,FeS + Sb(OH)_6^- \rightarrow \equiv FeSSbS_2^{2-} + Fe_3S_4 + 3\,Fe^{2+} + 2\,H_2O + 4\,OH^- \qquad (4.4.4)$$

Reduction of Sb(V) by mackinawite would thus be coupled to oxidation of FeS to Fe_3S_4, formation of a Sb(III)-S_3 surface complex and either consumption of H_2S or production of hydroxide ions in line with the observed pH increase during reaction of Sb(V) with FeS under acidic conditions.

Based on a comparison between sample Xb_ac_2, where no greigite formation is apparent in the XRD, and sample Xb_ac_3, where greigite is present, the conditions when greigite formation sets in can be considered if, as done in equation 4.4.3 and 4.4.4, one Fe_3S_4 unit is produced for each $Sb(OH)_6^-$ sorbed and reduced to the SbS_3 surface complex.

In sample Xb_ac_2, $8.88 \cdot 10^{-3}$ M Fe were present in the solid phase at the end of the reaction and $3.08 \cdot 10^{-4}$ M Sb had been sorbed and reduced. Thus, $9.24 \cdot 10^{-4}$ M Fe can be assumed to be present in a hypothetical greigite phase, which would amount to 10.4 % of the total solid phase iron being present as greigite. But at this theoretical greigite content greigite formation does apparently not occur. In Xb_ac_3, dissolution is greater and $7.49 \cdot 10^{-3}$ M Fe are present in the solid phase. According to $6.56 \cdot 10^{-4}$ M sorbed and reduced Sb, $1.97 \cdot 10^{-3}$ M Fe are expected to be present in a greigite phase. In this case, 26.3 % of solid phase Fe would be present as greigite, which, this time, does form and is visible in the XRD. This result is in agreement with Mullet et al. (2002), who found that mackinawite could accommodate up to 20 % Fe(III) in its structure without formation of another phase.[134]

4.5. Comparison to other elements

The reactions of a number of metal and metalloid contaminants such as Pb, Cd, Cr, U and As with mackinawite have been investigated.[124, 126-128, 136-141] While for Cr(VI) and U(VI) mackinawite was found to be an efficient reductant, the situation for As(V) and As(III) is more complicated and the reaction outcome depends strongly on the reaction conditions, in particular As/FeS ratios and pH.

The reactions of Cr, As, and U with mackinawite and their similarities and differences to the reaction of Sb with mackinawite will be considered in detail in the following paragraphs.

Cr(VI) versus Sb(V)

Patterson and Fendorf (1997)[138] and Mullet et al. (2004)[137] agree that chromate is reduced to Cr(III) and that a Fe(III)-Cr(III)-(oxyhydr)oxide layer covering the FeS crystals is formed. There is disagreement between the two studies concerning solid sulfide reaction products (thiosulfate and sulfate in the case of Patterson and Fendorf (1997)[138] and elemental sulfur in the case of Mullet et al. (2004)[137], but both point to a complex reaction mechanism with respect to sulfur and to the likely participation of both Fe(II) and sulfide in the reduction reaction. It is not resolved to what extent Cr(VI) is reduced at the mackinawite surface or by dissolved Fe(II) and sulfide. In addition, Mullet et al. (2004)[137] identified a mackinawite-greigite mixture in the residual iron sulfide. This study also

clearly evidenced a higher chromate removal capacity at lower pH and showed that residual chromate existed in solution only when concentrations of residual ferrous iron approached zero.[137]

Similarities in the reduction of Cr(VI) and Sb(V) by mackinawite lie in the higher removal from solution at lower pH and in the fact that this removal from solution proceeds by reduction to Cr(III) and Sb(III), respectively. Also, in both cases greigite could be identified as an Fe(III) containing solid phase resulting from oxidation of mackinawite.

However, in contrast to chromate reduction, reduction of Sb(V) to Sb(III) is coupled to a sulfur for oxygen ligand exchange and thus leads to sulfur coordinated Sb(III). For the Cr(VI) reduction, the reaction product (Fe(III)-Cr(III)-(oxyhydr)oxide) is not pH dependent and Cr(VI) is at pH 5 to 8 reduced to Cr(III). Sb(V) removal at basic pH is slow and only part of the antimony removed from solution is reduced to Sb(III).

Both Cr(VI) and Sb(V) can be reduced by hydrogen sulfide in aqueous media and in both cases elemental sulfur is the sulfide oxidation product.[142, 143] The absence of zero-valent sulfur in the XRD suggests that reduction of Sb(V) by dissolved hydrogen sulfide does not occur in presence of mackinawite or is minor compared to the reduction by structural Fe(II) from mackinawite. From the experiments performed, it is not clear, whether dissolved Fe(II) acts as a reductant for Sb(V).

As(III) and As(V) versus Sb(III) and Sb(V)

There is considerable variation in the findings reported on reactions of As(III) and As(V) with mackinawite. Four more or less recent articles on the sorption of As(III) or As(V) onto and/or redox reactions with mackinawite (Farquhar et al. (2002)[139], Wolthers et al. (2005)[126] and Gallegos et al. (2007 and 2008)[124, 128] will be discussed and compared to antimony-mackinawite reactions.

Farquhar et al. (2002)[139] investigated the sorption of As(III) and As(V) to mackinawite at pH 5.5 to pH 6.5, reaching loadings of 250 and 1400 ppm (resulting from As concentrations of $4 \cdot 10^{-5}$ M to $2 \cdot 10^{-4}$ M and a mackinawite solid/liquid ratio of 9.6 g/L, samples were reacted over night). From XAS data, it was inferred that interaction between either As(III) or As(V) with mackinawite proceeded by formation of outer sphere complexes wherein both initial As(III), or initial As(V), are coordinated to four oxygen atoms in the coordination shell, with additional shells being composed of sulfur at 3.1 Å and iron at 3.4 to 3.5 Å. As As-O distances for initial As(III) were reduced to 1.72 Å and 1.76 Å (compared to 1.78 Å for As(III) adsorbed onto lepidocrocite and goethite) and as some change in edge position in the XANES was apparent, partial oxidation of As(III) seemed to have occurred while As(V) was not reduced according to fitted As-O distances and edge position.

Coprecipitation of As(III) and As(V) with mackinawite at ratios of 2.5 % to 25 % led to formation of As_2S_3 for low As/FeS ratios and formation of oxygen coordinated As(III) or As(V) sorption complexes and As_2S_3 for higher As/FeS ratios. At the lower As/FeS ratio where only As_2S_3 was observed, As(V) was therefore reduced to As(III).

In the study by Wolthers et al. (2005)[126], the sorption of both As(V) and As(III) to mackinawite was investigated in the range of pH 6 to 8.5 at a solid/solution ratio of 0.044 g/L FeS and at initial [As] of $3 \cdot 10^{-5}$ M (6 h contact time). For both species, sorption was associated with a slight increase in pH and no redox-reactions were observed for either As(III) or As(V). Sorption of As(V) was fast (stable [As]aq in solution within 10 min), decreased at pH values above the pH_{PZC} of mackinawite (pH ~ 7.5) and followed the pH-dependent concentration of positively charged surface species. As(III) sorption was also fast and not strongly pH dependent. Maximum sorption was observed at pH 7.4 for As(V) and at pH 7.2 for As(III). Sorption isotherms were collected for As(III) and As(V) at pH 7.4 to 7.5 and could be expressed by Freundlich isotherms in both cases. If fitted with linear equations, partition coefficient $Kd = ([As(V)]_{ads})([As(V)]_{aq})^{-1}$ or $Kd= ([As(III)]_{ads})([As(III)]_{aq})^{-1}$ values of 9 L g^{-1} for As(V) and 2 L g^{-1} for As(III) were found. From this, a higher mobility of As(III) in anoxic sulfidic waters was inferred. For both species, outer-sphere complexation was concluded to be the sorption mechanism. However, for As(III) sorption, a continuum from sorption to coprecipitation of pourly crystalline As_2S_3 at the surface of mackinawite was postulated as As(III) sorption did not level off at saturation of all surface sites. Despite the different solid/solution ratios used, extensive reference for interpretation of the sorption data was made to the results of Farquhar et al. (2002)[139], since As speciation in the solid phase had not been investigated by XAS or XRD measurements.

In 2007, Gallegos et al.[128] published a study on As(III) uptake by mackinawite at pH 5, 7, and 9 at an FeS solid/solution ratio of 5 g/L and As(III) concentrations of $5 \cdot 10^{-5}$ M and $5 \cdot 10^{-4}$ M using XAS and XRD (the reaction period was 48 h). At the higher As concentration used, reduction of As(III) to a realgar-like phase with As-S distances of 2.26 Å and As-As of 2.54 Å occurred at all pH values. Realgar (As_4S_4) was also identified by XRD for a sample reacted at pH 5 with $1 \cdot 10^{-2}$ M As(III).

At the lower As concentration, a transition from As-O to As-S coordination occurred with decreasing pH, changing from coordination numbers of 2.7 and 0.4 for oxygen and sulfur, respectively, at pH 9 to values of 0.3 for oxygen and 2 for sulfur at pH 5. This study was first in evidencing the influence of the As/FeS ratio and pH on the sorption/reduction reaction of As(III) with mackinawite. Only at the lower tested As concentration, the reaction was pH dependent, adsorption of arsenite being dominant at alkaline pH and precipitation of a realgar-like arsenic sulfide phase prevailing under acidic conditions. Notably, the identified arsenic sulfide was not an orpiment-like phase (As_2S_3) containing trivalent arsenic, but a realgar-like phase, probably α-As_4S_4, containing divalent arsenic. As the authors point out in their following article on model predictions of realgar precipitation by reaction of As(III) with mackinawite (Gallegos et al., 2008)[124], realgar was identified as the primary arsenic-bearing phase in natural shallow aquifer sediments.[144] In this second article on As(III) – mackinawite reactions,[124] sorption of $1.3 \cdot 10^{-5}$ M As(III) on mackinawite was studied at solid/solution ratios of 0.1 to 40 g/L and at pH 5 - 10; the reaction period was 96 h. Removal of As was complete under acidic conditions up to pH 6.5 for all mackinawite concentrations. Above pH 6.5, removal of As(III) depended on both mackinawite solid/solution ratio and pH and, in particular, above pH 8.3, As(III)

removal resembled sorption of As(III) onto iron oxides, exhibiting maximum sorption at the pKa1 of arsenite (pH 9.2). For this reason, a mixed-valence iron solid, $Fe_2(OH)_5$, was included into the fit of the arsenic uptake, following the assumption that when mackinawite reacts with As(III) at alkaline pH to from realgar, Fe(II) is oxidized to Fe(III) and subsequently forms a mixed-valence iron solid. Thus removal of As(III) at high pH is suggested to be due to realgar precipitation and/or adsorption (it is not explicitly stated, whether this adsorption is that of As(III) onto an iron oxyhydroxide resulting from mackinawite oxidation), depending on the As/FeS ratio. As acidic pH, the product of oxidation of mackinawite is predicted to be greigite. At higher mackinawite solid/solution ratios, dissolved As_{total} concentrations are lower, the difference between 10 g/L and 0.1 g/L Fes being about 2 orders of magnitude at pH 5.

Thus results vary considerably concerning the mechanism of removal of As from solution in sorption experiments (outer-sphere complexation versus precipitation). Farquhar et al. (2002)[139] and Wolthers et al. (2005)[126] concluded on outer-sphere complexation of As(III) and As(V) on the mackinawite surface and did not observe reduction of either As(III) or As(V) in the case of sorption experiments (not in the solid phase for Farquhar et al. (2002)[139] and not in the liquid phase for Wolthers et al. (2005)[126]). These results are in opposition to the ones obtained by Gallegos et al. (2007 and 2008)[124, 128], concerning both structural data[128] and pH dependence of As(III) sorption.[124]

If the As concentrations used by Farquhar et al. (2002)[139] and Wolthers et al. (2005)[126] are converted to a mackinawite solid/solution ratio of 5 g/L as used by Gallegos et al. (2007)[128], values of $2.1 \cdot 10^{-5}$ M and $1 \cdot 10^{-4}$ M[139] and $3.4 \cdot 10^{-3}$ M[126] are obtained (the loadings used in the different studies are summarized in Fig. 4.5.1). The concentrations used by Gallegos et al. (2007), $5 \cdot 10^{-5}$ M and $5 \cdot 10^{-4}$ M, are thus very similar to the ones used by Farquhar et al. (2002)[139], while the one used by Wolthers et al. (2005)[126] is about 7 times more concentrated than the higher concentration used by Gallegos et al. (2007)[128] and more than 30 times more concentrated than the higher concentration used by Farquhar et al. (2002)[139]. As results between Gallegos et al. (2007)[128] and Farquhar et al. (2002)[139] differ greatly and as the route of mackinawite synthesis used probably differed between both Farquhar et al. (2002)i and Wolthers et al. (2005)[126] and Farquhar et al. (2002)[139] and Gallegos et al. (2007)[128], it is likely that the conclusions drawn by Wolthers et al. (2005) based on the structural data obtained by Farquhar et al. (2002)[139] at, at minimum, 30 times lower As/FeS ratios, are not the most reliable and thus will not be considered in the following discussion.

Both concentrations used by Farquhar et al. (2002)[139] (converted to 5 g/L FeS: $2.1 \cdot 10^{-5}$ M and $1 \cdot 10^{-4}$ M) are lower than the higher concentration used by Gallegos et al. (2007)[128] ($5 \cdot 10^{-4}$ M), at which the reaction products of the reaction of As(III) with mackinawite were not pH dependent. The lower

[i] Farquhar et al. (2002) write:"Samples of As adsorbed on to mackinawite were prepared by precipitating, as described by Lennie and Vaughan (16, 17)." However, the synthesis route described in reference 16 (Lennie, A. R.; Redfern, S. A.; Schofield, P. F.; Vaughan, D. J. Mineral. Mag. 1995, 59, 677.) does not use precipitation to synthesize mackinawite, or at least not directly, as iron wire is used to generate Fe^{2+}. Thus it is not completely clear in what way mackinawite for adsorption experiments, as opposed to coprecipitation experiments for which the process is described in more detail, was synthesized.

concentration used by Gallegos et al. (2007)[128] ($5 \cdot 10^{-5}$ M), at which the reaction outcome was pH dependent, is in between the concentrations used by Farquhar et al. (2002)[139] and one might thus expect the results at similar pH and similar As/FeS ratios to be similar. This is however, not the case.

While Farquhar et al. (2002)[139] at pH 5.5 to 6.5 finds a first shell composed of four oxygen atoms and sulfur neighbors at a distance of 3.1 Å, Gallegos et al. (2007)[128], at both pH 5 and 7, find only 0.3 oxygen neighbors and one to two sulfur neighbors at about 2.26 to 2.28 Å. These results are interpreted as outer-sphere complexation in the first and a mixture of sorption and realgar precipitation (and thus reduction of As(III) to As(II)) in the second case.

It is possible that a different synthesis route for mackinawite results in different particle sizes and thus differing specific surface areas and possibly different FeS solubilities. As dissolved $[Fe]_{total}$ are not given, FeS solubilities and derived dissolved sulfide concentrations cannot be compared and one cannot know, how these concentrations might influence realgar precipitation differently in the two experiments. In addition, it is not clear if the experiments of Farquhar et al. (2002) were carried out in a glove box or not. As was shown in chapter 4.2, the composition of a glove box atmosphere and in particular if H_2 is present or not might influence the outcome of redox reactions between mackinawite and contaminants such as As or Sb.

In Wolthers et al. (2005)[126] As(III) sorption onto mackinawite was found to be not strongly pH dependent (0.044 g/L FeS, $3 \cdot 10^{-5}$ M As(III)) and maximum sorption was found at pH 7.2. In contrast, Gallegos et al. (2008)[124], who studied the pH dependent sorption of As(III) on mackinawite at different solid/solution ratios ($1.3 \cdot 10^{-5}$ M As(III), 0.1 to 40 g/L FeS, pH 5-10), found that between pH 6.5 and 9 and mackinawite concentrations of 0.1 to 1 g/L, As(III) removal from solution is strongly dependent on pH and mackinawite concentration. Following thermodynamic modeling results, they suggested two different removal mechanisms to be present as a function of pH and mackinawite concentration: precipitation of realgar at acidic pH and realgar precipitation and sorption to an oxidized iron oxyhydroxide phase at basic pH. Comparing reaction conditions, it becomes apparent that the As concentration used by Wolthers et al. (2005)[126] (equivalent to $5.3 \cdot 10^{-5}$ M for 0.1 g/L FeS) was 4 times as high as the one used by Gallegos et al. (2008).[124] Considering the shift in the pH edge between 0.1 and 0.5 g/L mackinawite, it is easily possible that the pH edge corresponding to the conditions of Wolthers et al. (2005)[126] is shifted to the left of the pH range (pH 6 to 8) that they investigated and that their results of non-pH-dependent As(III) sorption to mackinawite are thus not opposed to the ones by Gallegos et al. (2008).[124]

The results obtained by Gallegos et al. (2007 and 2008)[124, 128] show some similarities to the reactions observed between antimony and mackinawite. As the focus of Gallegos et al. (2007 and 2008)[124, 128] lay on reactions of As(III) with mackinawite and I investigated more extensively reactions of Sb(V) with mackinawite, the comparison is, however, not straight forward.

Nonetheless, some similarities exist: Firstly, a strong pH dependence in As(III) and Sb(V) uptake by mackinawite is apparent, that, in both cases, does not result solely from surface complexation reactions

to the mackinawite surface. In both cases a reduction reaction and change from oxygen to sulfur coordination of arsenic (As(III)-O to As(II)-S) and antimony (Sb(V)-O to Sb(III)-S or Sb(III)-O to Sb(III)-S) take place and are favored by acidic pH and high mackinawite solid/solution ratios. Also in both cases, the mode of uptake from solution changes as a function of pH and formation of an Fe(III)-O containing solid phase occurs at alkaline pH values if a certain Sb/FeS ratio is exceeded.

In the case of As(III), reduction leads to As(II), present in a realgar-like precipitate, whereas antimony was under all conditions investigated not further reduced than Sb(III) and precipitation of a stibnite-like solid phase (Sb_2S_3) was, even at the highest Sb concentrations, not observed. Greigite was found as a mackinawite oxidation product for reduction of Sb(V) at acidic pH and was derived as the oxidation product of FeS at acidic pH for the reduction of As(III) to AsS by mackinawite.[124]

U(VI) versus Sb(V)

Sorption onto and reduction of U(VI) by mackinawite was investigated by Moyes et al. (2000)[127] and Hua et al. (2008),[141] using XAS and XPS, respectively.

Moyes et al. (2000)[127] investigated the effect of different U/FeS ratios at pH 7 and found complete removal of U from solution at all concentrations tested ($2\cdot10^{-4}$M to $5\cdot10^{-3}$M U(VI), 10 g/L FeS, resulting in loadings of $2\cdot10^{-5}$ up to $5\cdot10^{-4}$ mol U/g FeS). At low U/FeS ratios ($2\cdot10^{-5}$ and $4\cdot10^{-5}$ mol U/g FeS), U(VI) was not reduced and formed surface complexes at locally oxidized regions of the mackinawite surface. At the higher U loadings, the equatorial oxygen shell needed to be split in two during the shell fit. From the fitted U-O distances and from increased DW factors of axial O, it was concluded that U was present in a uranium oxide phase of mixed oxidation state, such as U_3O_8. The authors suppose that reduction of uranium occurs through a mechanism of surface oxidation once that sorption sites for U(VI) are saturated. Oxidation products of mackinawite oxidation were not investigated and the presence of U_3O_8 or U_4O_9 was not confirmed by another technique such XRD.

Hua et al. (2008)[141] investigated the kinetics of pH dependent sorption of U(VI) onto and reduction of U(VI) by mackinawite (pH 6 to 10, 0.18 g/L FeS, $1.68\cdot10^{-4}$ M U(VI), resulting in loadings of $9.3\cdot10^{-4}$ mol U/g FeS). While sorption was fast and complete at all pH values ([U]aq was below the detection limit of 0.4 µM within up to 3 h), the reduction rate (which they claimed to measure through extractability of U(VI) by $NaHCO_3$ from the solid phase, assuming that U(IV) might only be present in a uraninite like UO_2 phase and thus not considering possible occurrence of non-uraninite U(IV)) strongly depended on pH and increased with decreasing pH. Reduction half-times ranged from less than 1 h at pH 6 to over 100 h at pH 10.2. At acidic and neutral pH, U sorption was accompanied by a simultaneous release of Fe(II). The concentration of released [Fe(II)]aq was directly proportional to the amount of U(VI) removed from solution. A sample containing $9.3\cdot10^{-5}$ mol U/g FeS (that is, a U loading 10 times lower than in the pH dependent sorption and reduction samples) was analyzed by XPS. Formation of U_3O_8 or U_4O_9, UO_2, polysulfide, and sulfur and oxygen bound ferric iron was observed. The relative contribution of structural Fe(II) and sulfide to the reduction of U(VI) could not

be differentiated and no Fe(III) containing crystalline phase was identified. As can be seen in Figure 4.5.1, both the XPS and reduction kinetics experiments carried out by Hua et al. (2008)[141] were performed at U/FeS loadings and at a pH at which Moyes et al. (2000)[127] had observed at partial reduction of U(VI). The identifications of a U_3O_8-like phase by EXAFS[127] and of U_3O_8 (or U_4O_9) and UO_2 by XPS[141] under similar conditions are thus in good agreement with each other. Moyes et al. (2000)[127] did not determine U(VI) reduction rates as they investigated sorption/reduction of U(VI) only after 24 h of reaction at pH 7. The reduction rates obtained by Hua et al. (2008)[141] via $NaHCO_3$ extraction thus cannot be verified through in-situ spectroscopic data. Hua et al. (2008)[141] consider that the uptake of U(VI) occurs through a ion exchange mechanism where Fe(II) would be replaced by U(VI). A similar displacement of Fe(II) from mackinawite was observed for retention of lead and cadmium by mackinawite where up to 3 mmol Fe(II)/g FeS were dissolved.[136] In this case the displacement of Fe^{2+} was explained through the compared to FeS lower solubilities of CdS and PbS and formation of (Pb,Fe)S and (Cd,Fe)S on the mackinawite surface.[136] In the case of U(VI) removal from solution, formation of a uranium sulfide phase was not observed by XAS or XPS and the mechanisms both of U(VI) sorption and (partial) reduction to U(IV) remain unresolved.

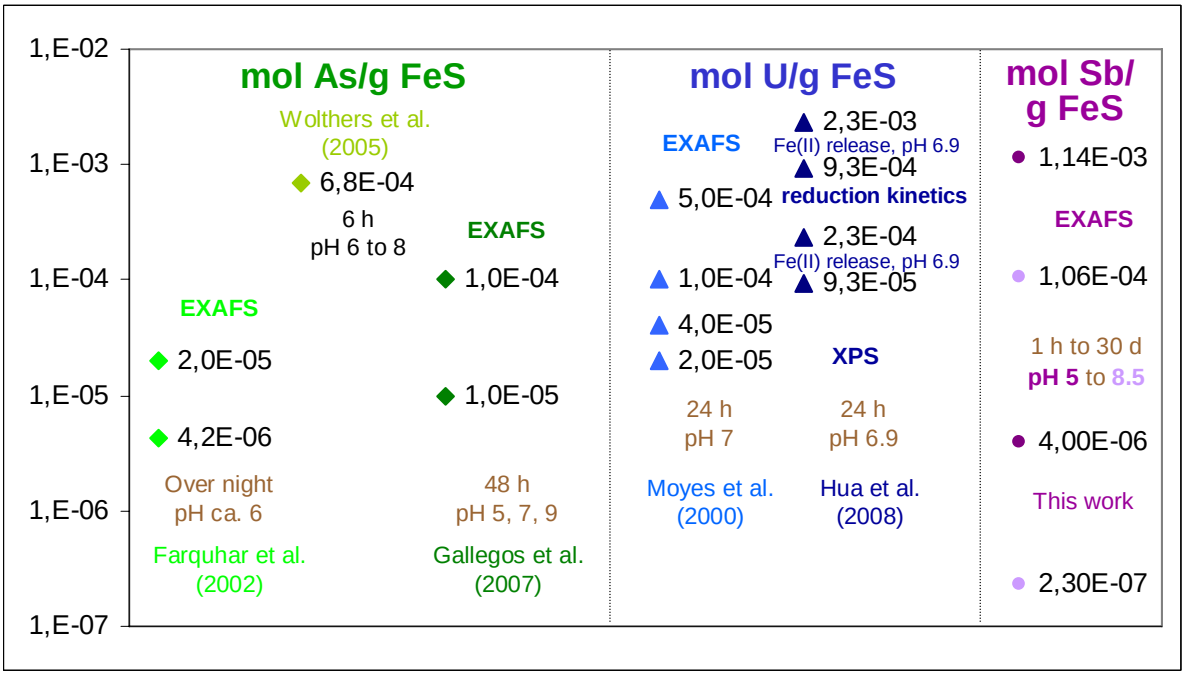

Figure 4.5.1. Reaction conditions in terms of pH, reaction time and loading (mol U, mol As or mol Sb /g FeS) resulting from complete sorption of initial U or As concentrations during the studies on arsenic and uranium sorption and reduction by mackinawite discussed in this chapter.

Interestingly, the reduction of U(VI) by mackinawite at pH 7 resembles that of As(III)[128] in that, at least at certain pH values, a certain U/FeS or As/FeS ratio must be attained for reduction to occur and decreasing pH favors reduction in both cases. Also, adsorption both of As(III) or U(VI) to oxidized surface hydroxyl groups was suggested. However, it is not clear if at low As(III) solution concentrations only partial reduction to AsS occurs or if, as in the case of U(VI), reduction rates at

alkaline pH are much slower than at acidic pH but, at least at pH 8.8, still lead to complete reduction.[141]

While, similarly to the behavior of U(VI) and As(III), both removal from solution and reduction of Sb(V) by mackinawite increase with decreasing pH, a main difference is that no minimum Sb loading or Sb/FeS ratio in suspension is required for reduction to occur. Rather, if, at alkaline pH, a certain Sb/FeS ratio is exceeded, not only sulfur coordinated Sb(III) but also oxygen coordinated Sb(V) is found in the solid phase. Similarly to the U(VI) sorption/reduction process, Fe(II) concentrations increased during Sb(V) sorption/reduction at acidic pH. As HCl was added during the experiment to keep the pH close to its original value, it is not clear what percentage of the added HCl served to neutralize hydroxide ions released during Sb(V) reduction and what percentage of added HCl served to dissolve FeS. It can thus not be differentiated to what extent release of Fe(II) to solution is due to greigite formation during the reduction of Sb(V) by mackinawite and in how far release of Fe(II) results from FeS dissolution due to HCl addition.

As could be expected, redox reactions between Cr, As, U and Sb differ greatly from each other and the main similarity may lie in higher and/or faster removal from solution at lower pH even though for each element a different mechanisms may be responsible for this observation. A main outcome of this literature review and the summary in figure 4.5.1 may then be that observations on occurring or not occuring redox reactions vary as a function of contaminant/FeS loading, pH and reaction time (not considering other factors such as presence of dissolved H_2). To obtain reliable results, different loadings at several pH values and reacted for different times should be investigated with more than one method. Combining XAS, XRD and XPS appears a good approach to characterize oxidation states of substrates and contaminants, local structural environments and formation of new phases. However, also for such spectroscopy based studies, redox potentials should be acquired to facilitate comparison with other studies and possible thermodynamic considerations.

4.6. Conclusions

It was shown that the redox potentials measured in mackinawite suspensions as a function of pH agree well with the equilibrium pe expected from the FeS-Fe_3S_4 redox couple. This would be in agreement with the observed transformation of FeS into Fe_3S_4 upon oxidation of FeS by Sb(V) that was observed by XRD. Transformation of FeS into Fe_3S_4 has also been observed previously under acidic, anoxic conditions[145] and greigite is known to be an intermediate in the transformation of FeS into pyrite following the polysulfide pathway.[146] From exposure of mackinawite (FeS) to Sb(III) and Sb(V) and oxidation state analysis of solid phase associated Sb using XAS, a few insites into the mechanisms of reduction and immobilization of antimony as a function of pH could be gained. It was found that sorption and reduction of Sb(V) on mackinawite were strongly pH dependent. At acidic pH, sorption was fast and resulted in low residual Sb concentrations ($\leq 10^{-7}$ M). In this case, Sb(V) was completely reduced to an Sb(III)-sulfide complex that was associated with the solid phase. Reduction of Sb(V)

was coupled to oxidation of mackinawite and formation of greigite (Fe_3S_4). At alkaline pH, Sb(V) was slowly removed from solution and reduction to Sb(III) was complete only at very small Sb/FeS ratios, probably indicating that specific surface sites must be available for reduction to occur. At lower pH were dissolution of FeS is much higher, more such active sites might be available. At higher Sb/FeS, Sb(V) removal occurred partly through reduction to solid phase associated Sb(III)-S_3 and partly through co-precipitation with Fe(III).

Annex to chapter 4

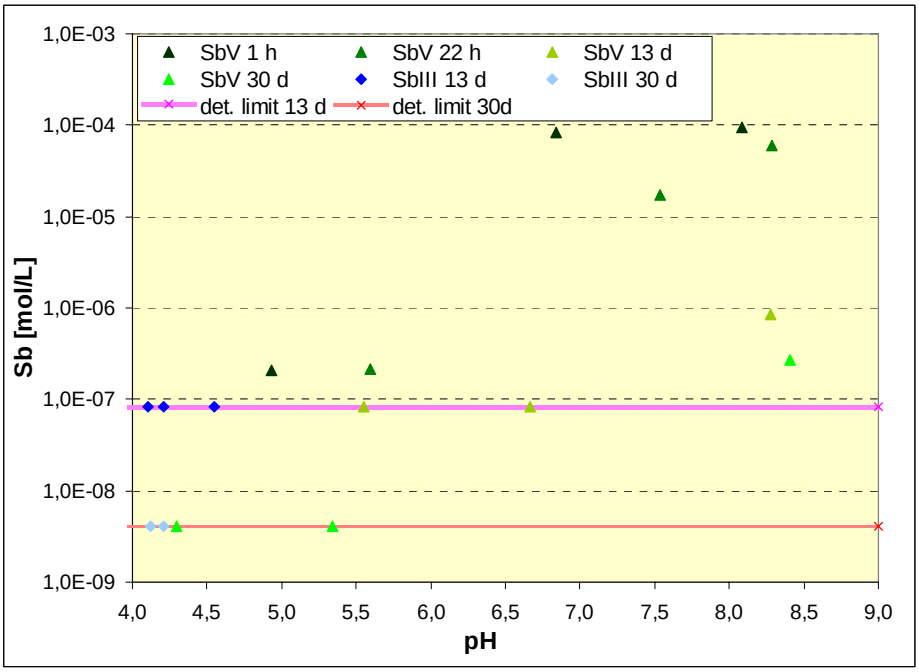

Figure A4.1. Final $[Sb]_{total}$ concentrations as a function of pH for samples of XAS-experiment A (Table 4.2).

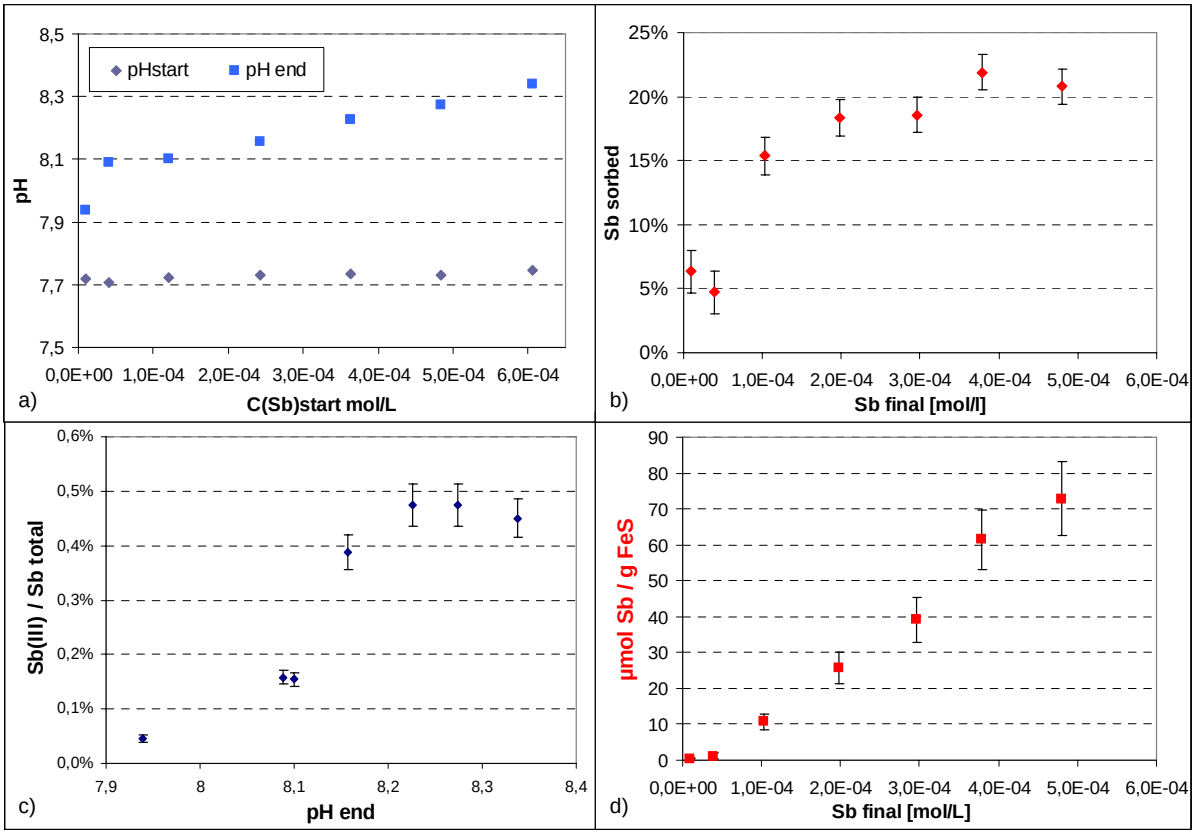

Figure A4.2. Siso_bas experiment: a) pH change as a function of initial Sb concentration, b) % Sb sorbed as a function of final Sb concentration, c) Sb(III) over total dissolved Sb, d) loading of Sb on FeS as a function of final Sb concentration.

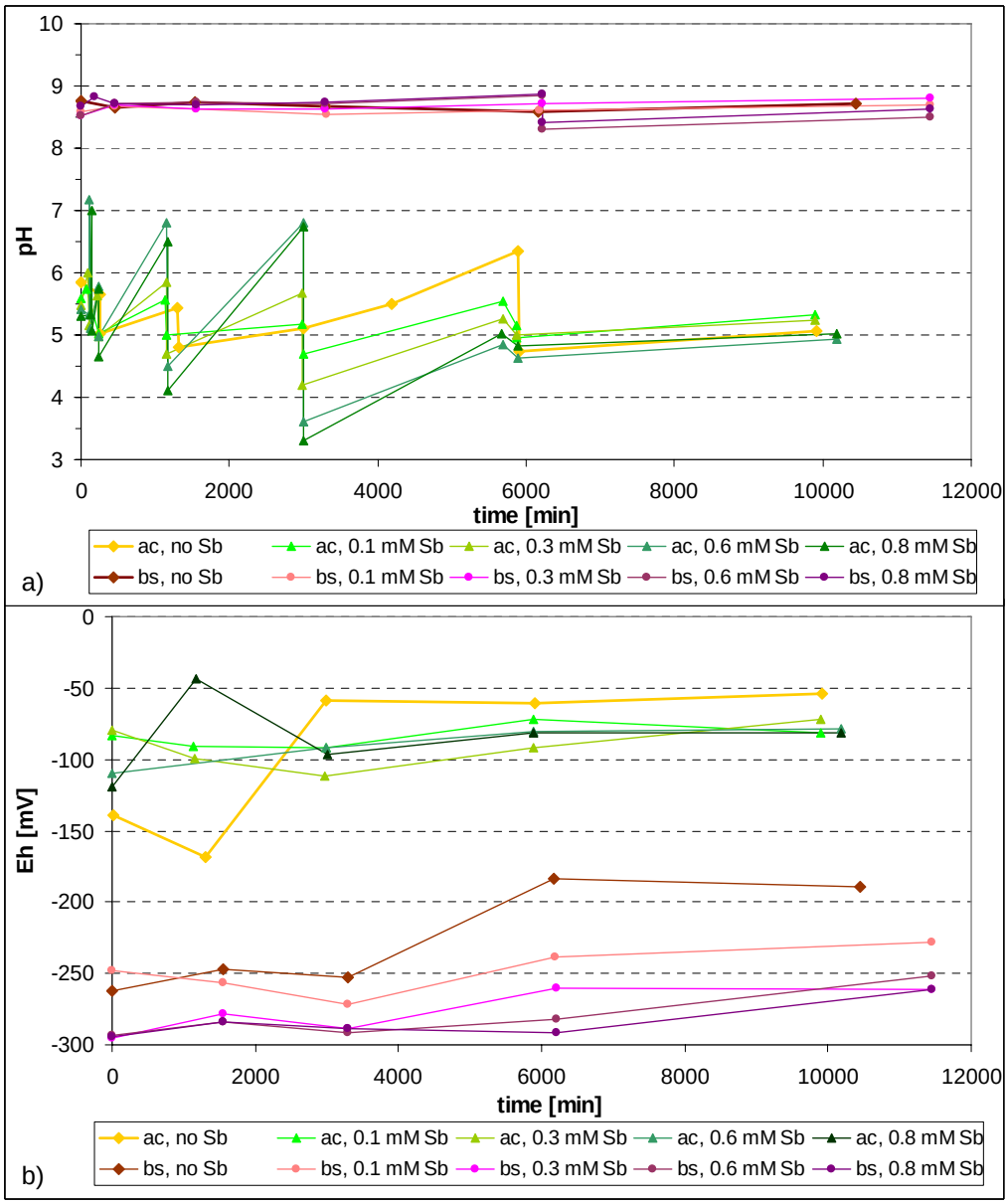

Figure A4.3. Reaction conditions for XAS-experiment B. a) pH over time, b) Redox potential over time for samples to which Sb was added and for reference samples without added Sb at acidic and basic pH.

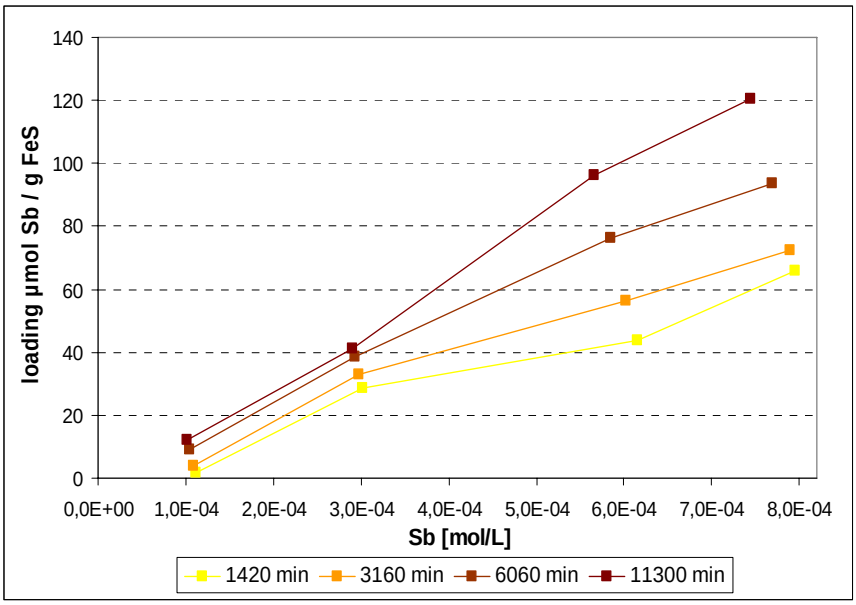

Figure A4.4. Loading of Sb on mackinawite as function of Sb concentration in solution 1 d, 2 d, 4 d, and 8 d after Sb addition. Data from samples Xb_bas_1 to 4.

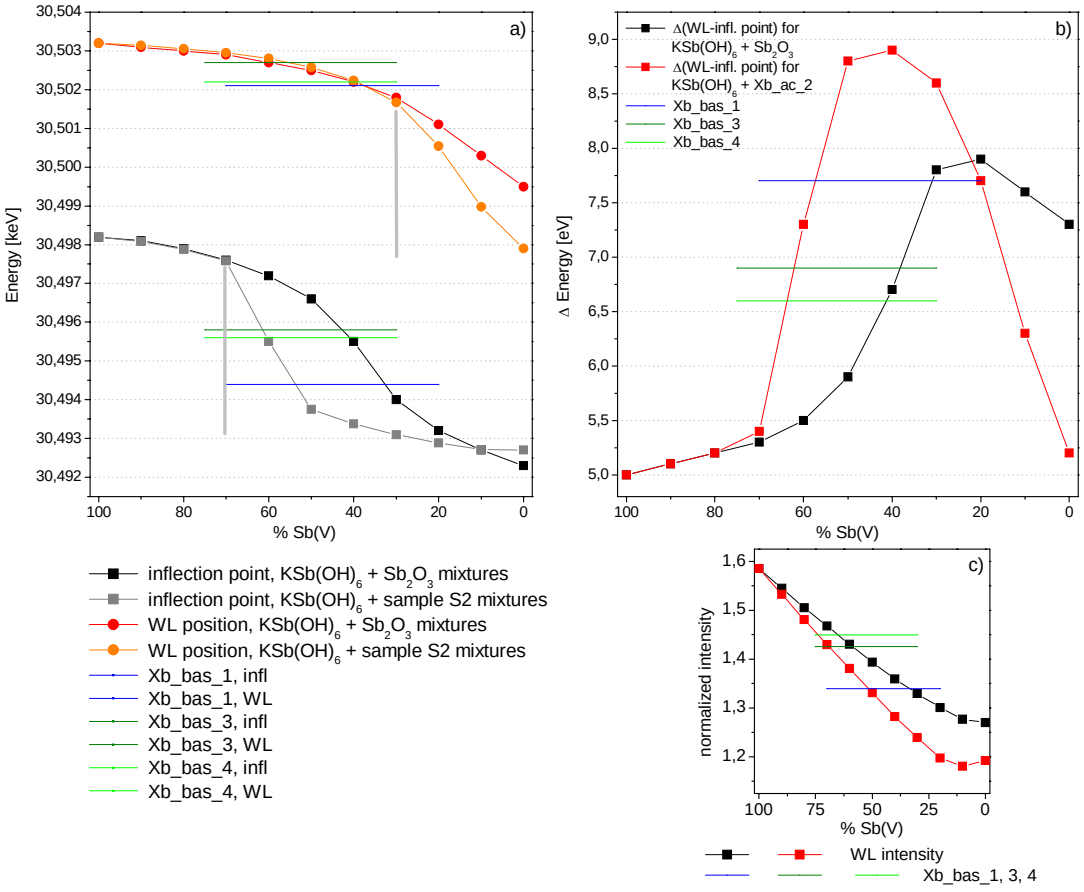

Figure A4.5. Comparison of XANES features of artificial spectra of Sb(V)-Sb(III) mixtures with Xb_bas_1, 3, 4 samples. Normalized spectra of $KSb(OH)_6$ were mixed either with a Sb(III) oxygen or sulfur compound (Sb_2O_3 or sample Xb_ac_2). a) WL position and inflection point as a function of Sb(V) content. b) Distance between WL position and inflection point as a function of Sb(V) content. c) WL intensity as a function of Sb(V) content.

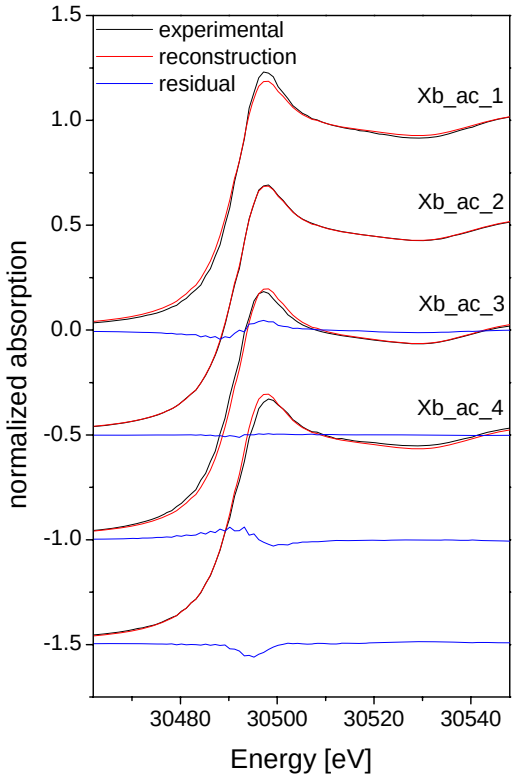

Figure A4.6. Reconstruction of the XANES regions of Xb_ac sample spectra with one EV in the energy range 30460 to 30550 eV.

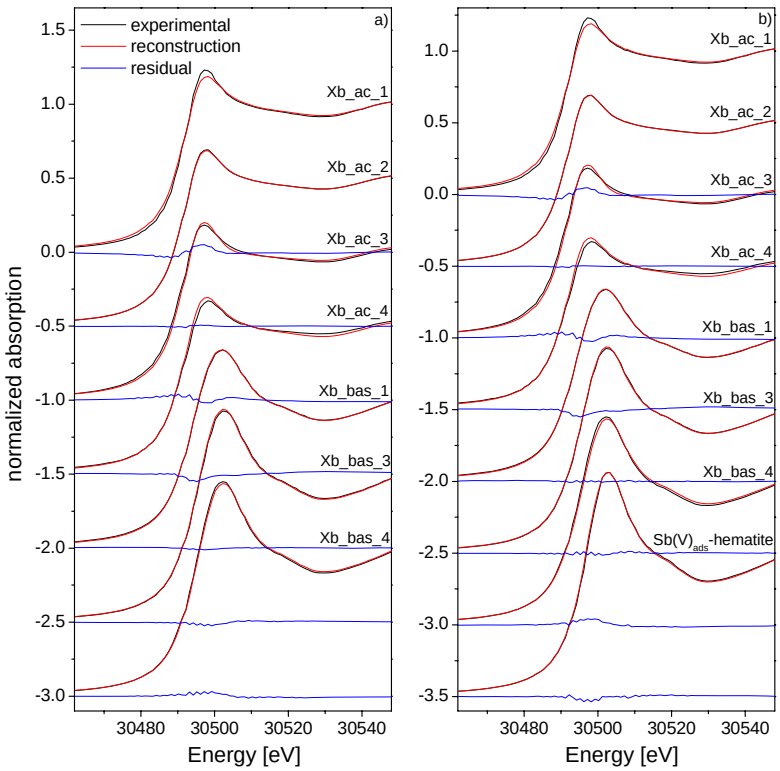

Figure A4.7. Reconstruction of XANES regions of Xb_ac and Xb_bas samples (a) and Xb_ac, Xb_bas samples and Sb(V)$_{ads}$-hematite (b) with two EV in the energy range 30460 to 30550 eV.

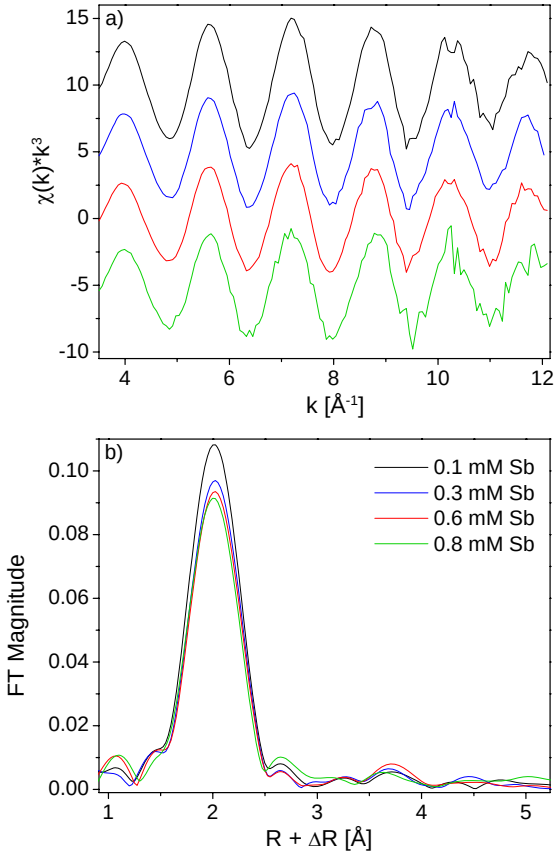

Figure A4.8 k^3-weighted EXAFS spectra (a) and Fourier Transform (FT) (b) of Xb_ac_1 to 4. FT based on $\chi(k)*k^3$ with $3.5 \leq k \leq 12.1$.

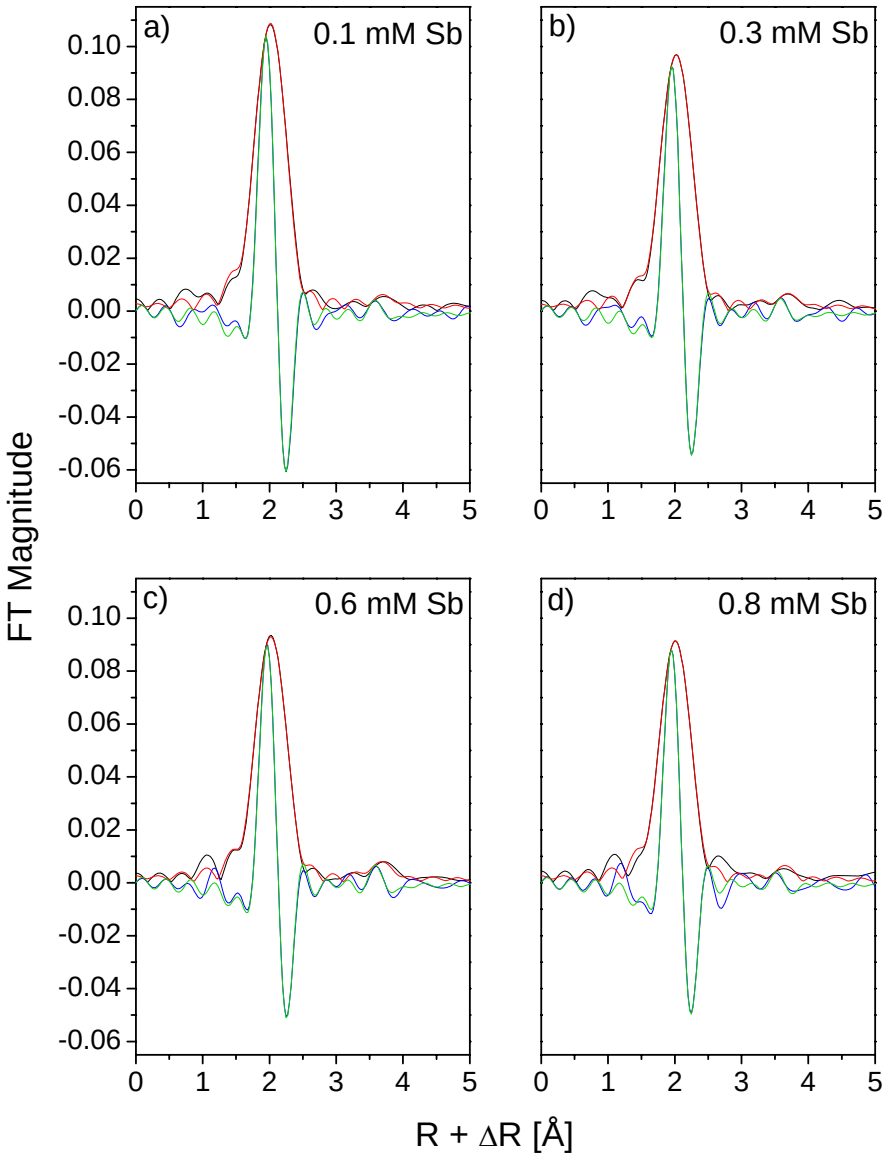

Figure A4.9. a) to d) Fourier Transform (experimental spectrum and two shell fit) of $\chi(k)*k^3$ ($3.5 \leq k \leq 12.1$) for Xb_ac_1 to 4 samples. For fit parameters see Table A4.1. Black – magnitude (experimental), blue – imaginary part (experimental), red – magnitude (fit), green – imaginary part (fit).

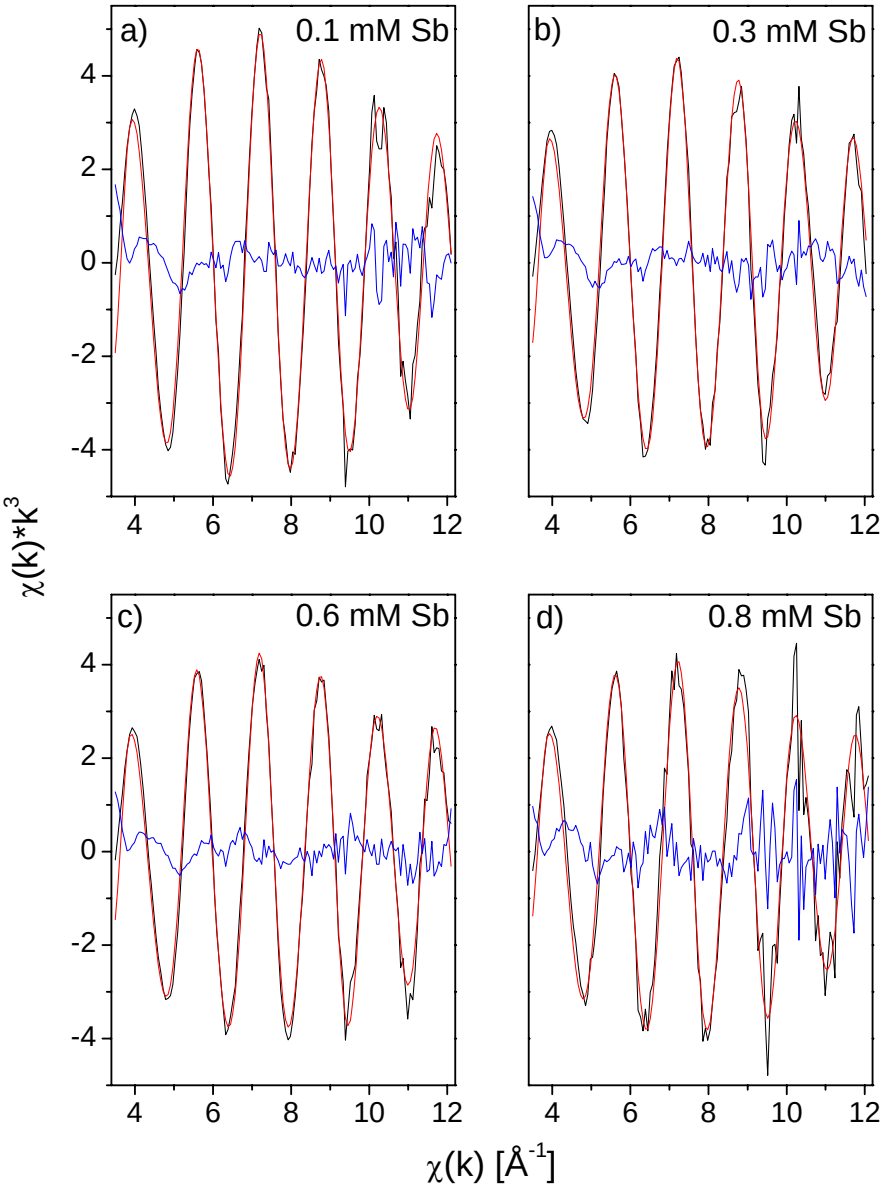

Figure A4.10. a) to d) k^3-weighted EXAFS spectrum (experimental and two shell fit) for Xb_ac_1 to 4 samples. Fit carried out in R-space. For fit parameters see Table A4.1. Black – experimental, red – fit, blue – redisual.

Table A4.1. Shell fit parameters for for Xb_ac_1 to 4 samples For comparison, results for both a one- (Sb-S) (1st line) and a two-shell fit (Sb-S, Sb-Sb) (2nd and 3rd line) are given for each sample. Fit residual [%] as calculated by WinXAS (eq A4.1) and standard deviation (SD) (eq. A4.2).

$[Sb]_{start}$	shell	CN	R(Å)	σ^2(Å^2)	ΔE_0	Res (%)	SD*
0.1 mM Sb	Sb-S	3.83	2.47	0.0043	11.6	5.8	0.43
	Sb-S	3.83	2.47	0.0043	11.6	4.2	0.42
	Sb-Sb	1.17	3.81	0.0132			
0.3 mM Sb	Sb-S	3.29	2.47	0.0039	11.9	5.6	0.38
	Sb-S	3.28	2.47	0.0039	11.9	3.1	0.35
	Sb-Sb	1.00	3.81	0.0112			
0.6 mM Sb	Sb-S	3.12	2.47	0.0038	11.4	7.3	0.35
	Sb-S	3.12	2.47	0.0038	11.3	3.9	0.32
	Sb-Sb	1.41	3.81	0.0117			
0.8 mM Sb	Sb-S	3.16	2.46	0.0041	10.9	7.7	0.57
	Sb-S	3.15	2.46	0.0041	10.9	5.7	0.55
	Sb-Sb	0.56	3.75	0.0081			
	k-range	$3.5 \le k \le 12.1$+/- 0.05 Å^{-1}				*SD for $\chi(k)*k^3$, $3.5 \le k \le 12.0$ Å^{-1}	
	R-range	$1.55 \le R \le 4.11$ Å					

Residual [%] calculated in WinXAS:

$$\text{Residual}[\%] = \frac{\sum_{i=1}^{N} \left| y_{\exp}(i) - y_{theo}(i) \right|}{\sum_{i=1}^{N} \left| y_{\exp}(i) \right|} \cdot 100 \qquad \text{(A4.1)}$$

Standard deviation (SD) calculated as:

$$SD = \sqrt{\frac{\sum_{i=1}^{n} \left(y_{theo}(i) - y_{\exp}(i) \right)^2}{n}} \qquad \text{(A4.2)}$$

with: n – number of data points.

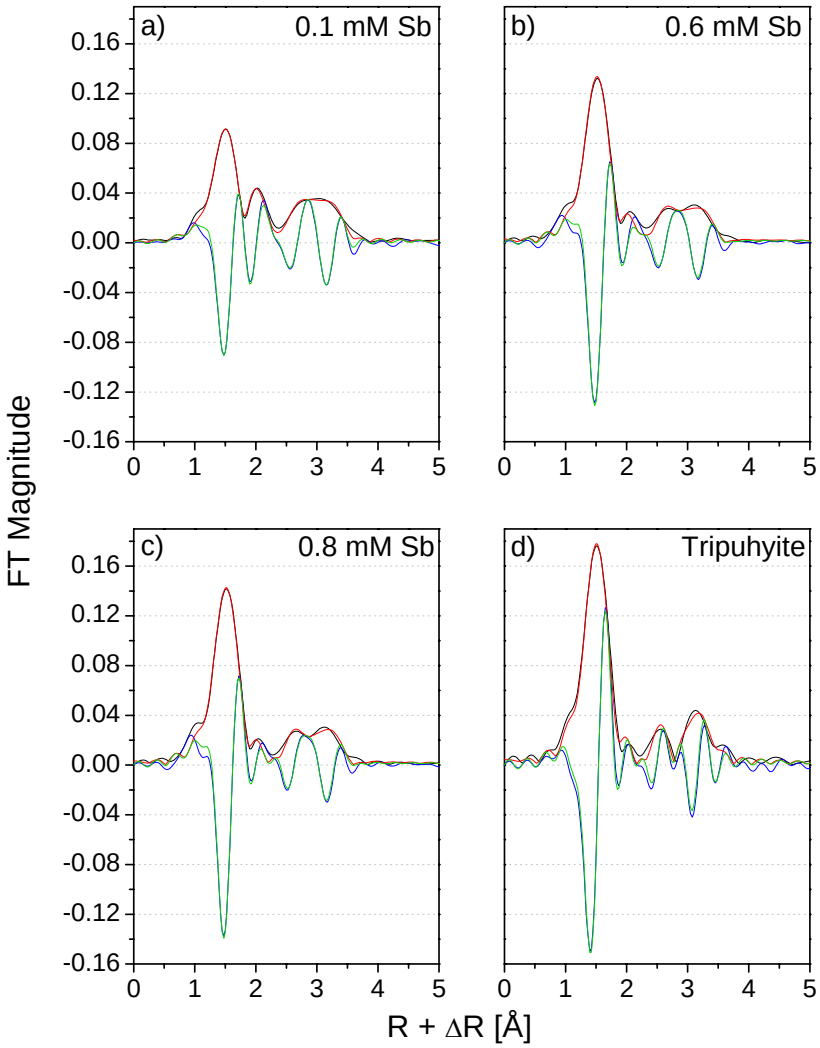

Figure A4.11. a) to c) Fourier Transform (experimental spectrum and fit) of $\chi(k)*k^3$ ($2.6 \leq k \leq 12.6$) for Xb_bas_1 to 4 samples, d) Experimental and fitted spectrum of tripuhyite ($FeSbO_4$) for comparison. For fit parameters see Table A4.2. Black – magnitude (experimental), blue – imaginary part (experimental), red – magnitude (fit), green – imaginary part (fit).

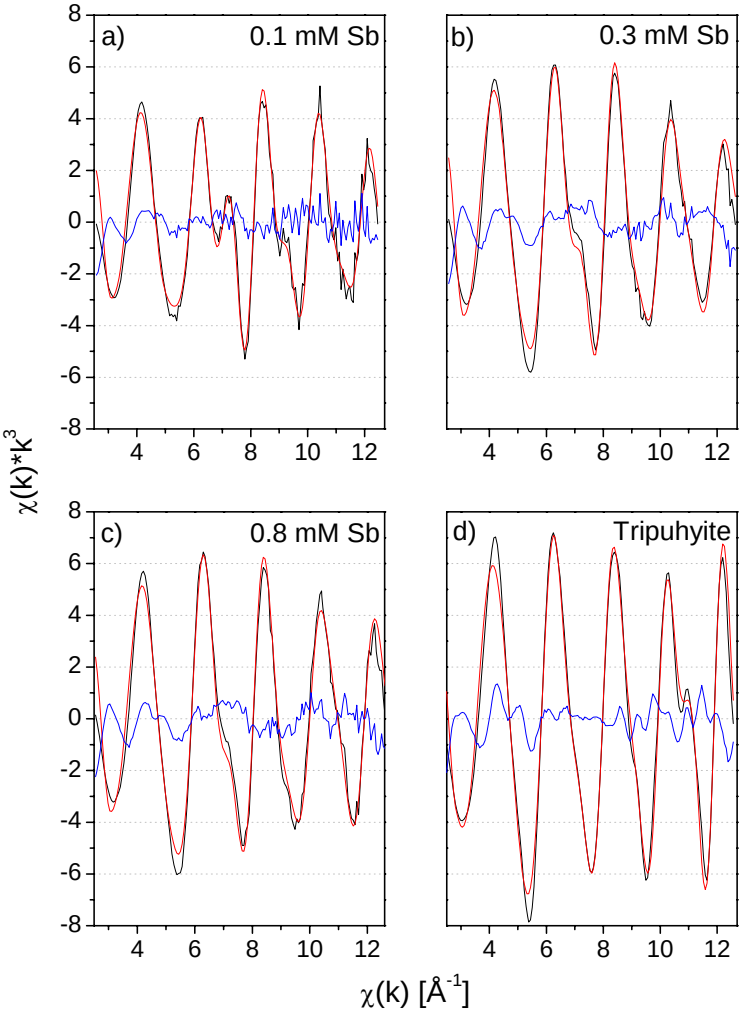

Figure A4.12. k^3-weighted EXAFS spectra (experimental and fit) of Xb_bas_1 to 4 samples (a to c) and of tripuhyite (d). For fit parameters see Table A4.2. Black – experimental, red – fit, blue – redisual.

Table A4.2. Shell fit parameters for spectra from Xb_bas_1 to 4 samples. For comparison, tripuhyite ($FeSbO_4$) fit is given as well.

$[Sb]_{start}$	shell	CN	R(Å)	σ^2(Å^2)	ΔE_0	Res (%)
0.1 mM Sb,	Sb-O	3.22	1.97	0.0029[a]	11.8	5.3
	Sb-S	0.85	2.45	0.0029[a]		
	Sb-Fe	0.91	3.11	0.0028[b]		
	Sb-Fe	1.95	3.54	0.0028[b]		
0.6 mM Sb	Sb-O	4.36	1.97	0.0025[c]	12.0	7.5
	Sb-S	0.22	2.50	0.0025[c]		
	Sb-Fe	1.15	3.10	0.0062[d]		
	Sb-Fe	2.61	3.56	0.0062[d]		
0.8 mM Sb	Sb-O	4.44	1.97	0.0022[e]	11.6	7.1
	Sb-S	0.06	2.50	0.0022[e]		
	Sb-Fe	0.94	3.10	0.0049[f]		
	Sb-Fe	2.18	3.55	0.0049[f]		
Tripuhyite	Sb-O	5.52	1.97	0.0023	10.3	9.3
	Sb-Fe	0.76	3.09[h]	0.0034[g]		
	Sb-Sb	0.51	3.09[h]	0.0034[g]		
	Sb-Fe	2.71	3.59[j]	0.0034[g]		
	Sb-Sb	1.17	3.59[j]	0.0034[g]		

a, b, c, d, e, f, g, h, j - correlated

k range	$2.6 \leq k \leq 12.6$ +/- 0.05 Å^{-1}, apart from tripuhyite, for which $2.25 \leq k \leq 12.6$ Å^{-1}
R-range	$1.14 \leq R \leq 3.88$ Å

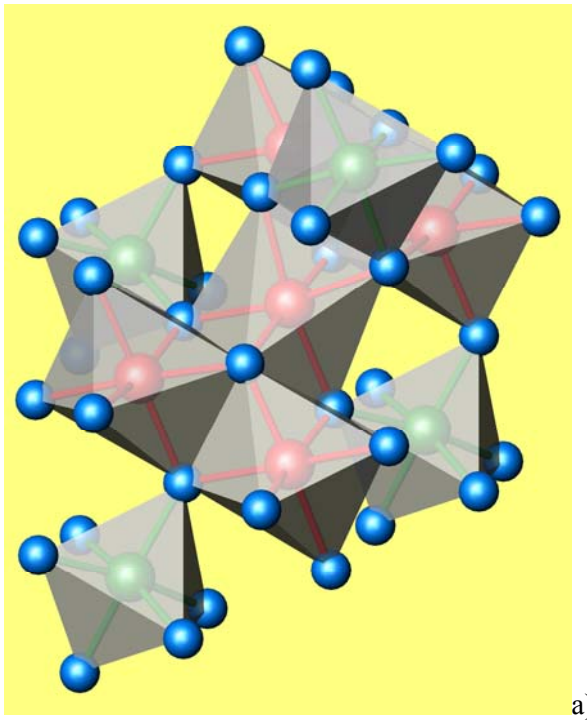

a)

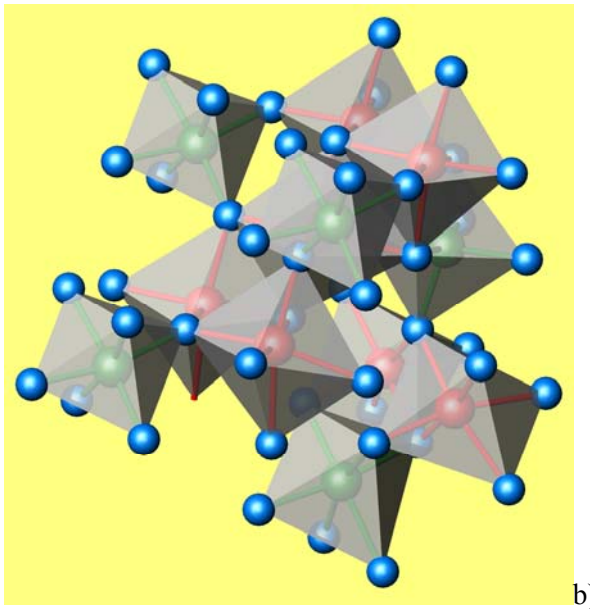

b)

Figure A4.13. Possible structure of Sb(V) – $Fe(OH)_3$ coprecipitated generated by substituting some $Fe(III)O_6$-octahedra against $Sb(V)O_6$-octahedra in the ferrihydrite structure proposed by Michel et al., (2007)[131].

Sorption data

Table A4.3. – Sorption of Sb(V) to mackinawite over time (Stime_ac and Stime_bas).

General conditions:
solid/liquid ratio 1.73 g/L FeS ionic background 25 mM CaCl2 Sb(V) start $1.01 \cdot 10^{-04}$ mol/L
sample conditioning: HCl was added 15 h prior to Sb addition, samples were shaken (Vibramax, 900 rpm) for 13 h prior to Sb addition

Stime_ac

time* [min]	pH (susp)‡	pH (filt)§	Sb_{tot} [mol/L]	± Sb_{tot} [mol/L]	Fe [mol/L]	± Fe [mol/L]	Sb sorbed	+/- Sb sorbed	FeS diss.[a]	+/- FeS diss.	loading [mol Sb /mol FeS]	+/- [mol Sb /mol FeS]	loading [mol Sb /g FeS]	+/- [mol Sb /g FeS]	Sb(III) [mol/L]	+/- Sb(III) [mol/L]	Sb(III) /Sb_{tot}	+/- Sb(III) /Sb_{tot}
33	5.59	5.75	$7.44 \cdot 10^{-5}$	$2.2 \cdot 10^{-6}$	$1.08 \cdot 10^{-3}$	$3.23 \cdot 10^{-5}$	26.0 %	2.2 %	5.5 %	0.16	$1.41 \cdot 10^{-3}$	$1.18 \cdot 10^{-4}$	$1.60 \cdot 10^{-5}$	$1.3 \cdot 10^{-6}$	$2.0 \cdot 10^{-6}$	$9.9 \cdot 10^{-8}$	2.7 %	0.1 %
153	5.88	6.14	$2.91 \cdot 10^{-5}$	$8.7 \cdot 10^{-7}$	$1.06 \cdot 10^{-3}$	$3.18 \cdot 10^{-5}$	71.1 %	0.9 %	5.4 %	0.16	$3.85 \cdot 10^{-3}$	$4.04 \cdot 10^{-5}$	$4.38 \cdot 10^{-5}$	$4.6 \cdot 10^{-7}$	$8.7 \cdot 10^{-7}$	$4.4 \cdot 10^{-8}$	3.0 %	0.2 %
538	6.11	6.35	$6.29 \cdot 10^{-6}$	$1.9 \cdot 10^{-7}$	$1.05 \cdot 10^{-3}$	$3.16 \cdot 10^{-5}$	93.8 %	0.2 %	5.4 %	0.16	$5.07 \cdot 10^{-3}$	$1.52 \cdot 10^{-6}$	$5.77 \cdot 10^{-5}$	$1.7 \cdot 10^{-8}$	$1.1 \cdot 10^{-7}$	$5.6 \cdot 10^{-9}$	1.8 %	0.1 %
1513	6.37	6.70	$6.37 \cdot 10^{-7}$	$3.0 \cdot 10^{-8}$	$1.02 \cdot 10^{-3}$	$5.11 \cdot 10^{-5}$	99.4 %	0.0 %	5.2 %	0.26	$5.37 \cdot 10^{-3}$	$1.31 \cdot 10^{-5}$	$6.10 \cdot 10^{-5}$	$1.5 \cdot 10^{-7}$	$1.6 \cdot 10^{-9}$	$1.6 \cdot 10^{-10}$	0.3 %	0.0 %
4393	6.36	6.72	$4.32 \cdot 10^{-8}$	$2.1 \cdot 10^{-9}$	$1.00 \cdot 10^{-3}$	$5.01 \cdot 10^{-5}$	100.0 %	0.0 %	5.1 %	0.25	$5.39 \cdot 10^{-3}$	$1.44 \cdot 10^{-5}$	$6.13 \cdot 10^{-5}$	$1.6 \cdot 10^{-7}$	$1.3 \cdot 10^{-9}$	$1.3 \cdot 10^{-10}$	3.1 %	0.3 %

Stime_bas

time* [min]	pH (susp)	pH (filt)	Sb_{tot} [mol/L]	± Sb_{tot} [mol/L]	Fe [mol/L]	± Fe [mol/L]	Sb sorbed	+/- Sb sorbed	FeS diss.	+/- FeS diss.	loading [mol Sb /mol FeS]	+/- [mol Sb /mol FeS]	loading [mol Sb /g FeS]	+/- [mol Sb /g FeS]	Sb(III) [mol/L]	+/- Sb(III) [mol/L]	Sb(III) /Sb_{tot}	+/- Sb(III) /Sb_{tot}
45	8.14	8.22	$1.01 \cdot 10^{-4}$	$3.0 \cdot 10^{-6}$	$7.05 \cdot 10^{-5}$	$1.06 \cdot 10^{-5}$	0.0 %	3.0 %	0.4 %	0.05	0.00	$1.55 \cdot 10^{-4}$	0.00	$1.8 \cdot 10^{-6}$	$1.6 \cdot 10^{-8}$	$1.6 \cdot 10^{-9}$	0.02	0.00 %
82	8.08	8.22	$9.90 \cdot 10^{-5}$	$3.0 \cdot 10^{-6}$	$6.04 \cdot 10^{-5}$	$9.05 \cdot 10^{-6}$	2.5 %	2.9 %	0.3 %	0.05	$1.28 \cdot 10^{-4}$	$1.52 \cdot 10^{-4}$	$1.45 \cdot 10^{-6}$	$1.7 \cdot 10^{-6}$	$2.2 \cdot 10^{-8}$	$2.2 \cdot 10^{-9}$	0.02	0.00 %
532	8.06	7.99	$9.88 \cdot 10^{-5}$	$3.0 \cdot 10^{-6}$	$5.87 \cdot 10^{-5}$	$8.81 \cdot 10^{-6}$	2.7 %	2.9 %	0.3 %	0.04	$1.39 \cdot 10^{-4}$	$1.51 \cdot 10^{-4}$	$1.58 \cdot 10^{-6}$	$1.7 \cdot 10^{-6}$	$2.2 \cdot 10^{-8}$	$2.2 \cdot 10^{-9}$	0.02	0.00 %
1502	8.02	8.12	$9.49 \cdot 10^{-5}$	$2.8 \cdot 10^{-6}$	$5.62 \cdot 10^{-5}$	$8.43 \cdot 10^{-6}$	6.5 %	2.8 %	0.3 %	0.04	$3.35 \cdot 10^{-4}$	$1.45 \cdot 10^{-4}$	$3.81 \cdot 10^{-6}$	$1.7 \cdot 10^{-6}$	$4.6 \cdot 10^{-7}$	$4.6 \cdot 10^{-8}$	0.48	0.03 %
4382	8.11	8.16	$8.63 \cdot 10^{-5}$	$2.6 \cdot 10^{-6}$	$5.00 \cdot 10^{-5}$	$7.51 \cdot 10^{-6}$	15.0 %	2.6 %	0.3 %	0.04	$7.74 \cdot 10^{-4}$	$1.32 \cdot 10^{-4}$	$8.81 \cdot 10^{-6}$	$1.5 \cdot 10^{-6}$	$9.6 \cdot 10^{-8}$	$9.6 \cdot 10^{-9}$	0.11	0.01 %

* the time given is with respect to addition of Sb(V) to the mackinawite suspension
‡: susp - pH measured in suspension, §: filt - pH measured after filtration, a: diss. = dissolution

5. Conclusion

A number of iron minerals with varying composition and structure, including an iron(II) sulfide and iron(II)-hydroxycarbonate in addition to iron (oxyhydr)oxides with various iron(II) contents, have been exposed to aqueous Pu(III) and Pu(V) under laboratory anoxic conditions. With X-ray absorption spectroscopy, the *in-situ* oxidation state of Pu associated with the solid phase could be identified and was found to strongly depend on the structure and Fe(II) content of the solid. In particular, the amount of Pu present in the trivalent oxidation state depends on the available mineral surface area, which varied in the experiments with the solid/solution ratio used.

With hematite and goethite, Pu associated with the solid phase is mainly in the tetravalent oxidation state, with some Pu probably present as Pu(V). This result was independent of whether Pu(III) or Pu(V) had been added to hematite. Reduction of Pu(V) is most likely due to trace amounts of Fe(II) contained in hematite due to the synthesis route chosen and despite the fact that α-Fe_2O_3 ideally is a pure Fe(III) oxide. As electrons can move through its structure,[147, 148] hematite can act as a source or sink for electrons and can thus participate in either oxidation of Pu(III) or (partial) reduction of Pu(V). Despite identification of a Pu-Fe scattering path, the EXAFS data do not allow to elucidate in what form Pu is associated with hematite and goethite. No inner-sphere surface complex could be clearly identified but also formation of PuO_2 was not apparent in the EXAFS signal, even though under oxic conditions formation of PuO_2 nanoparticles with hematite has been observed by TEM.[149]

With magnetite (Fe_3O_4 = $Fe^{II}Fe^{III}{}_2O_4$), in which ideally one third of the iron is present as Fe(II), reduction of Pu(V) to Pu(III) and stabilization of Pu(III) in the trivalent oxidation state is observed. From the EXAFS spectra in combination with Feff-Monte Carlo simulation, an inner-sphere surface complex formed by Pu(III) on magnetite (111) faces could be identified. Presence of PuO_2 in addition to the Pu(III) surface complex in the sample with the highest Pu/mineral ratio and highest reaction pH suggest that once the aqueous Pu(III) concentration in equilibrium with the surface complex exceeds that in equilibrium with PuO_2 (PuO_2(am,hyd) or PuO_2(coll,hyd)), formation of a PuO_2 solid phase sets in. In contrast to hematite and goethite and similarly to mackinawite and chukanovite, the PuO_2 phase formed in the presence of magnetite was clearly apparent in the EXAFS signal.

With maghemite (γ-Fe_2O_3) containing residual Fe(II), Pu(IV) and Pu(III)/Pu(IV) were formed. The final oxidation state distribution with this solid phase was independent of whether Pu(III) or Pu(V) had been added and in all cases, strong iron backscattering suggests that Pu is present on maghemite as an inner-sphere surface complex similar to the one observed to form by Pu(III) on magnetite. However, some uncertainties remain with respect to the Pu-Fe coordination number and integration of Pu into the maghemite structure of formation of a co-precipitated mixed Pu-Fe solid cannot be excluded.

With mackinawite (FeS) at the lowest reaction pH ($\approx$ 6), only Pu(III) was found associated to the solid phase, probably in the form of an outer-sphere sorption complex. Pu(III) was thus stabilized and formation of PuO_2 was not observed. At higher pH values (7 - 8.5), PuO_2 formed and in two out of

five samples small amounts of Pu(III) were also present, indicating that above pH 6 sorption of Pu(III) also occurs.

With chukanovite ($Fe_2(CO_3)(OH)_2$), 15 to 40 % of plutonium associated with the solid phase were present as Pu(III), the remaining 60 to 85 % being present as PuO_2. Whether Pu(III) was present in an inner- or outersphere surface complex could not be derived from the EXAFS data.

If thermodynamic equilibrium has been attained, the observation of Pu(III) and PuO_2 occurring simultaneously with magnetite, chukanovite and mackinawite requires $\{Pu^{3+}\}_{eq/PuO2}$, the activity of aqueous Pu(III) at equilibrium with PuO_2 at a given pe and pH (eq. a), to be equal to $\{Pu^{3+}\}_{eq/Pu(III)ads}$, the activity of aqueous Pu(III) at equilibrium with a Pu(III) surface complex (eq. b or c).

$$PuO_2 + e^- + 4\,H^+ \rightleftarrows Pu^{3+} + 2\,H_2O \quad \text{(a-1)}$$

$$\{Pu^{3+}\}_{eq/PuO2} = K_a\ \{H^+\}^4\ \{e^-\} \quad \text{(a-2)}$$

$$Pu^{3+} + \equiv Fe\text{-}OH \rightleftarrows \equiv Fe\text{-}OPu^{2+} + H^+ \quad \text{(b-1)}$$

$$\{Pu^{3+}\}_{eq/Pu(III)ads} = \{\equiv Fe\text{-}OPu^{2+}\}\ \{H^+\}\ K_b^{-1}\ \{\equiv Fe\text{-}OH\}^{-1} \quad \text{(b-2)}$$

$$Pu^{3+} + \equiv Fe\text{-}S^- \rightleftarrows \equiv Fe\text{-}S\text{-}Pu^{2+} \quad \text{(c-1)}$$

$$\{Pu^{3+}\}_{eq/Pu(III)ads} = \{\equiv Fe\text{-}S\text{-}Pu^{2+}\}\ K_c^{-1}\ \{\equiv Fe\text{-}S^-\}^{-1} \quad \text{(c-2)}$$

Generally, $\{Pu^{3+}\}_{eq/Pu(III)ads}$ depends on the stability of the surface complex (inner-sphere or outer-sphere, denticity), on pH, at least in case of outer-sphere complexation, and, following a mineral specific sorption isotherm, on the surface coverage. As long as $\{Pu^{3+}\}_{eq/Pu(III)ads} < \{Pu^{3+}\}_{eq/PuO2}$ precipitation of PuO_2 is not expected.

What percentage of Pu can, in a given system, be expected to be present as surface bound Pu(III) should then be dependent on

1) pe, pH and ionic strength as $[Pu(III)_{eq/PuO2}]$ decreases with increasing pH and pe and increases with increasing ionic strength
2) the crystallinity and particle size of PuO_2, as $\{Pu(III)_{eq/PuO2}\}$ increases with decreasing particle size and increasing disorder in the PuO_2 structure
3) the nature of the mineral and its surface area (and thus its particle size and concentration)
4) the presence of other ions that can compete with Pu(III) for sorption sites.

If Pu(III) is present as an outer-sphere complex, competition with other ions can be expected to have a greater impact than if it is sorbed as inner-sphere complex.

If a sorption site with a specific geometry is needed, another possible factor that influences how much Pu(III) can be stabilized by a mineral is probably the synthesis route as it might influence what percentage of surfaces display a certain face (e.g. biogenic magnetite vs. magnetite formed as a corrosion product of steel).

In a real-world system, microbes and natural organic matter will be present in addition to dissolved inorganic ions and small organic molecules. These can cover mineral surfaces, occluding binding sites, or impeding the establishment of thermodynamic equilibrium between dissolved Pu(III) and possible

mineral surface binding sites. In addition, complexation with NOM and microbial metabolisms can also contribute to the stabilization of Pu(III) in anoxic environments.

From exposure of mackinawite (FeS) to Sb(III) and Sb(V) and oxidation state analysis of solid phase associated Sb using XAS, a few insites into the mechanisms of reduction and immobilization of antimony as a function of pH could be gained. It was found that sorption and reduction of Sb(V) on mackinawite were strongly pH dependent. At acidic pH, sorption was fast and resulted in low residual Sb concentrations ($\leq 10^{-7}$ M). In this case, Sb(V) was completely reduced to an Sb(III)-sulfide complex that was associated with the solid phase. Reduction of Sb(V) was coupled to oxidation of mackinawite and formation of a greigite (Fe_3S_4) could be observed by XRD. At basic pH, Sb(V) was slowly removed from solution and reduction to Sb(III) was complete only at very small Sb/FeS ratios, probably indicating that specific surface sites must be available for reduction to occur . At higher Sb/FeS, Sb(V) removal occurred partly through reduction to solid phase associated Sb(III)-S_3 and partly through co-precipitation with Fe(III).

The experimental results presented in the preceding pages underline the importance of surface complexation with iron(II) containing minerals as mechanisms of plutonium retention and stabilization of Pu(III). For antimony, the link between antimony reduction and oxidation of Fe(II) could be clearly established.
If the role these mechanisms play in controlling the environmental fate of plutonium is to be assessed the following remarks should be considered for the conception of the experimental set-up:
a) In the context of long-term confinement of nuclear waste in deep underground repositories, it will be important to consider the specific host geological material (granite, salt, clay formation) and waste form (spent fuel, vitrified waste) and how different actinides, that might be leached from the waste together, might compete with each other for surface sorption sites under a given set of conditions.
b) Fe-phyllosilicate, that have been identified as major corrosion products in steel corrosion experiments with Callovo-oxfordian (COx) clay,[150, 151] should be included into Pu sorption experiments under conditions where their formation was observed.
c) Generally, it is important to come closer to real world conditions where NOM and microbes are present and where iron(II) containing minerals are present in addition to other solid phases and not as the only ones. As conditions may vary widely, focusing laboratory experiments on conditions of a specific site of contamination, as has been done for oxic conditions, might be the only way to obtain applicable reduction rates and retention coefficients for Pu under anoxic conditions.

References

(1) Rossberg, A.; Reich, T.; Bernhard, G., Complexation of uranium(VI) with protocatechuic acid - application of iterative transformation factor analysis to EXAFS spectroscopy. *Analytical and Bioanalytical Chemistry* **2003,** *376* (5), 631-638.

(2) Greenwood, N. N.; Earnshaw, A., *Chemistry of the Elements*. 2nd ed.; Butterworth-Heinemann: Oxford, UK, 1997.

(3) Choppin, G. R., Actinide speciation in the environment. *Journal of Radioanalytical and Nuclear Chemistry* **2007,** *273* (3), 695–703.

(4) Tananaev, I. G.; Nikonov, M. V.; Myasoedov, B. F.; Clark, D. L., Plutonium in higher oxidation states in alkaline media. *J. Alloys Compd.* **2007,** *444-445*, 668-672.

(5) Fendorf, S. E., Surface reaction of chromium in soils and waters. *Geoderma* **1995,** *67*, 55-71.

(6) Morris, K.; Livens, F. R.; Charnock, J. M.; Burke, I. T.; McBeth, J. M.; Begg, J. D. C.; Boothman, C.; Lloyd, J. R., An X-ray absorption study of the fate of technetium in reduced and reoxidised sediments and mineral phases. *Applied Geochemistry* **2008,** *23* (4), 603-617.

(7) Scheinost, A. C.; Charlet, L., Selenite reduction by mackinawite, magnetite and siderite: XAS characterization of nanosized redox products. *Environ. Sci. Technol.* **2008,** *42* (6), 1984-1989.

(8) Neck, V.; Altmaier, M.; Fanghanel, T., Solubility of plutonium hydroxides/hydrous oxides under reducing conditions and in the presence of oxygen. *Comptes Rendus Chimie* **2007,** *10* (10-11), 959-977.

(9) Lutze, W.; Chen, Z.; Diehl, D.; Gong, W. L.; Nuttall, H. E.; Kieszig, G., Microbially mediated reduction and immobilization of uranium in groundwater at Konigstein. *Bioremediation of Inorganic Compounds* **2001,** *6* (9), 155-163.

(10) Filella, M.; Williams, P. A.; Belzile, N., Antimony in the environment: knowns and unknowns. *Environmental Chemistry* **2009,** *6* (2), 95-105.

(11) Leuz, A. K.; Monch, H.; Johnson, C. A., Sorption of Sb(III) and Sb(V) to goethite: Influence on Sb(III) oxidation and mobilization. *Environ. Sci. Technol.* **2006,** *40* (23), 7277-7282.

(12) Xi, J.; He, M.; Lin, C., Adsorption of antimony(III) and antimony(V) on bentonite: kinetics, thermodynamics and anion competition. *Microchemical Journal* **2011,** *97*, 85-91.

(13) Stumm, W.; Morgan, J. J., *Aquatic chemistry - chemical equilibria and rates in natural waters*. 3rd ed.; John Wiley & Sons, Inc.: New York, 1996.

(14) Choppin, G. R., Actinide speciation in aquatic systems. *Marine Chemistry* **2006,** *99*, 83-92.

(15) Buesseler, K. O.; Kaplan, D. I.; Dai, M.; Pike, S., Source-Dependent and Source-independent Controls on Plutonium Oxidation State and Colloid Associations in Groundwater. *Environ. Sci. Technol.* **2009,** *43* (5), 1322-1328.

(16) Rickard, D.; Morse, J. W., Acid volatile sulfide (AVS). *Marine Chemistry* **2005,** *97* (3-4), 141-197.

(17) Wersin, P.; Johnson, L. H.; Schwyn, B.; Berner, U.; Curti, E. *Redox conditions in the near field of a repository for SF/HLW and ILW in Opalinus clay*; technical report 02-13; nagra: Wettingen, Switzerland, 2003.

(18) Neff, D.; Saheb, M.; Monnier, J.; Perrin, S.; Descostes, M.; L'Hostis, V.; Crusset, D.; Millard, A.; Dillmann, P., A review of the archaeological analogue approaches to predict the long-term corrosion behaviour of carbon steel overpack and reinforced concrete structures in the French disposal systems. *Journal of Nuclear Materials* **2010,** *402* (2-3), 196-205.

(19) Wyllie, S.; Cunningham, M. L.; Fairlamb, A. H., Dual action of antimonial drugs on thiol redox metabolism in the human pathogen Leishmania donovani. *Journal of Biological Chemistry* **2004,** *279* (38), 39925-39932.

(20) Filella, M.; Belzile, N.; Chen, Y. W., Antimony in the environment: a review focused on natural waters I. Occurrence. *Earth-Science Reviews* **2002,** *57* (1-2), 125-176.

(21) Bienert, G. P.; Thorsen, M.; Schussler, M. D.; Nilsson, H. R.; Wagner, A.; Tamas, M. J.; Jahn, T. P., A subgroup of plant aquaporins facilitate the bi-directional diffusion of As(OH)(3) and Sb(OH)(3) across membranes. *Bmc Biology* **2008,** *6*.

(22) Filella, M.; Belzile, N.; Lett, M. C., Antimony in the environment: A review focused on natural waters. III. Microbiota relevant interactions. *Earth-Science Reviews* **2007,** *80* (3-4), 195-217.

(23) Porquet, A.; Filella, M., Structural evidence of the similarity of Sb(OH)3 and As(OH)3 with glycerol: implications for their uptake. *Chem. Res. Toxicol.* **2007,** *20*, 1269-1276.
(24) Krishnakumar, T.; Jayaprakash, R.; Pinna, N.; Phani, A. R.; Passacantando, M.; Santucci, S., Structural,optical and electrical characterization of antimony-substituted tin oxide nanoparticles. *J. Phys. Chem. Solids* **2009,** *70*, 993–999.
(25) Paoletti, F.; Sirini, P.; Seifert, H.; Vehlow, J., Fate of antimony in municipal solid waste incineration. *Chemosphere* **2001,** *42* (5-7), 533-543.
(26) Krachler, M.; Zheng, J.; Koerner, R.; Zdanowicz, C.; Fisher, D.; Shotyk, W., Increasing atmospheric antimony contamination in the northern hemisphere: snow and ice evidence from Devon Island, Arctic Canada. *Journal of Environmental Monitoring* **2005,** *7* (12), 1169-1176.
(27) Qi, C. C.; Liu, G. J.; Chou, C. L.; Zheng, L. Q., Environmental geochemistry of antimony in Chinese coals. *Science of the Total Environment* **2008,** *389* (2-3), 225-234.
(28) Looser, M. O.; Parriaux, A.; Bensimon, M., Landfill underground pollution detection and characterization using inorganic traces. *Water Research* **1999,** *33* (17), 3609-3616.
(29) Douay, F.; Pruvot, C.; Roussel, H.; Ciesielski, H.; Fourrier, H.; Proix, N.; Waterlot, C., Contamination of urban soils in an area of northern France polluted by dust emisions of two smelters. *Water Air and Soil Pollution* **2008,** *188*, 247-260.
(30) Rapant, S.; Dietzova, Z.; Cicmanova, S., Environmental and health risk assessment in abandoned mining area, Zlata Idka, Slovakia. *Environmental Geology* **2006,** *51* (3), 387-397.
(31) Reimann, C.; Matschullat, J.; Birke, M.; Salminen, R., Antimony in the environment: Lessons from geochemical mapping. *Applied Geochemistry* **2010,** *25* (2), 175-198.
(32) Salma, I.; Maenhaut, W., Changes in elemental composition and mass of atmospheric aerosol pollution between 1996 and 2002 in a Cenral European city. *Environmental Pollution* **2006,** *143*, 479-488.
(33) Iijima, A.; Sato, K.; Yano, K.; Kato, M.; Kozawa, K.; Furuta, N., Emission factor for antimony in brake abrasion dusts as one of the major atmospheric antimony sources. *Environ. Sci. Technol.* **2008,** *42* (8), 2937-2942.
(34) Hjortenkrans, D. S. T.; Bergback, B. G.; Haggerud, A. V., Metal Emissions from brake linings and tires: Case studies of Stockholm, Sweden 1995/1998 and 2005. *Environ. Sci. Technol.* **2007,** *41*, 5224-5230.
(35) Takayanagi, K.; Cossa, D., Vertical distributions of Sb(III) and Sb(V) in Pavin Lake, France. *Water Research* **1997,** *31* (3), 671-674.
(36) Frohne, T.; Rinklebe, J.; Diaz-Bone, R. A.; Du Laing, G., Controlled variation of redox conditions in a floodplain soil: Impact on metal mobilization and biomethylation of arsenic and antimony. *Geoderma* **2010,** *doi:10.1016/j.geoderma.2010.10.012*.
(37) Duester, L.; Vink, J. P. M.; Hirner, A. V., Methylantimony and -arsenic species in sediment pore water tested with the sediment or fauna incubation experiment. *Environ. Sci. Technol.* **2008,** *42* (16), 5866-5871.
(38) Mosselmans, J. F. W.; Helz, G. R.; Pattrick, R. A. D.; Charnock, J. M.; Vaughan, D. J., A study of speciation of Sb in bisulfide solutions by X-ray absorption spectroscopy. *Applied Geochemistry* **2000,** *15* (6), 879-889.
(39) Helz, G. R.; Valerio, M. S.; Capps, N. E., Antimony speciation in alkaline sulfide solutions: Role of zerovalent sulfur. *Environ. Sci. Technol.* **2002,** *36* (5), 943-948.
(40) Sherman, D. M.; Ragnarsdottir, K. V.; Oelkers, E. H., Antimony transport in hydrothermal solutions: an EXAFS study of antimony(V) complexation in alkaline sulfide and sulfide-chloride brines at temperatures from 25 degrees C to 300 degrees C at P-sat. *Chemical Geology* **2000,** *167* (1-2), 161-167.
(41) Tossell, J. A., The speciation of antimony in sulfidic solutions - a theoretical study. *Geochimica Et Cosmochimica Acta* **1994,** *58* (23), 5093-5104.
(42) Tossell, J. A., Calculation of the energetics for the oxidation of Sb(III) sulfides by elemental S and polysulfides in aqueous solution. *Geochimica Et Cosmochimica Acta* **2003,** *67* (18), 3347-3354.
(43) Scheinost, A. C.; Rossberg, A.; Vantelon, D.; Xifra, I.; Kretzschmar, R.; Leuz, A. K.; Funke, H.; Johnson, C. A., Quantitative antimony speciation in shooting-range soils by EXAFS spectroscopy. *Geochimica Et Cosmochimica Acta* **2006,** *70* (13), 3299-3312.

(44) Takaoka, M.; Fukutani, S.; Yamamoto, T.; Horiuchi, M.; Satta, N.; Takeda, N.; Oshita, K.; Yoneda, M.; Morisawa, S.; Tanaka, T., Determination of chemical form of antimony in contaminated soil around a smelter using X-ray absorption fine structure. *Analytical Sciences* **2005,** *21* (7), 769-773.

(45) Ceriotti, G.; Amarasiriwardena, D., A study of antimony complexed to soil-derived humic acids and inorganic antimony species along a Massachusetts highway. *Microchemical Journal* **2009,** *91* (1), 85-93.

(46) Steely, S.; Amarasiriwardena, D.; Xing, B. S., An investigation of inorganic antimony species and antimony associated with soil humic acid molar mass fractions in contaminated soils. *Environmental Pollution* **2007,** *148* (2), 590-598.

(47) Majzlan, J.; Bronislava, L.; Chovan, M.; Bläß, U.; Brecht, B.; Göttlicher, J.; Steininger, R.; Hug, K.; Ziegler, S.; Gescher, J., A mineralogical, geochemical, and microbiogical assessment of the antimony- and arsenic-rich neutral mine drainage tailings near Pezinok, Slovakia. *American Mineralogist* **2011,** *96*, 1-13.

(48) Mitsunobu, S.; Harada, T.; Takahashi, Y., Comparison of antimony behavior with that of arsenic under various soil redox conditions. *Environ. Sci. Technol.* **2006,** *40* (23), 7270-7276.

(49) Mitsunobu, S.; Takahashi, Y.; Terada, Y.; Sakata, M., Antimony(V) Incorporation into Synthetic Ferrihydrite, Goethite, and Natural Iron Oxyhydroxides. *Environ. Sci. Technol.* **2010,** *44* (10), 3712-3718.

(50) Belzile, N.; Chen, Y. W.; Wang, Z. J., Oxidation of antimony (III) by amorphous iron and manganese oxyhydroxides. *Chemical Geology* **2001,** *174* (4), 379-387.

(51) Leuz, A. K.; Johnson, C. A. R., Oxidation of Sb(III) to Sb(V) by O-2 and H2O2 in aqueous solutions. *Geochimica Et Cosmochimica Acta* **2005,** *69* (5), 1165-1172.

(52) Buschmann, J.; Canonica, S.; Sigg, L., Photoinduced oxidation of antimony(III) in the presence of humic acid. *Environ. Sci. Technol.* **2005,** *39* (14), 5335-5341.

(53) Mitsunobu, S.; Takahashi, Y.; Sakai, Y.; Inumaru, K., Interaction of Synthetic Sulfate Green Rust with Antimony(V). *Environ. Sci. Technol.* **2009,** *43* (2), 318-323.

(54) Kirsch, R.; Scheinost, A. C.; Rossberg, A.; Banerjee, D.; Charlet, L., Reduction of antimony by nano-particulate magnetite and mackinawite. *Mineralogical Magazine* **2008,** *71* (1), 185-189.

(55) Chen, Y. W.; Deng, T. L.; Filella, M.; Belzile, N., Distribution and early diagenesis of antimony species in sediments and porewaters of freshwater lakes. *Environ. Sci. Technol.* **2003,** *37* (6), 1163-1168.

(56) Akatsu, E.; Tomizawa, T.; Aratono, Y., Separation of antimony-125 in fission products. *Journal of Nuclear Science and Technology* **1974,** *11* (12), 571-574.

(57) Paatero, J.; Kulmala, S.; Jaakkola, T.; Saxen, R.; Buyukay, M., Deposition of Sb-125, Ru-106, Ce-144, Cs-134 and Cs-137 in Finland after the Chernobyl accident. *Boreal Environment Research* **2007,** *12* (1), 43-54.

(58) Jan, F.; Aslam, M.; Orfi, S. D.; Wahid, A., Removal of silver and antimony radionuclides from low-level liquid radioactive waste of a research reactor through different scavenging precipitations. *Radiochimica Acta* **2004,** *92* (7), 433-438.

(59) Kaplan, D. I.; Powell, B. A.; Demirkanli, D. I.; Fjeld, R. A.; Molz, F. J.; Serkiz, S. M.; Coates, J. T., Influence of oxidation states on plutonium mobility during long-term transport through an unsaturated subsurface environment. *Environ. Sci. Technol.* **2004,** *38* (19), 5053-5058.

(60) Kaplan, D. I.; Demirkanli, D. I.; Gumapas, L.; Powell, B. A.; Fjeld, R. A.; Molz, F. J.; Serkiz, S. M., Eleven-year field study of Pu migration from PuIII, IV, and VI sources. *Environ. Sci. Technol.* **2006,** *40* (2), 443-448.

(61) Kaplan, D. I.; Powell, B. A.; Duff, M. C.; Demirkanli, D. I.; Denham, M.; Fjeld, R. A.; Molz, F. J., Influence of sources on plutonium mobility and oxidation state transformations in vadose zone sediments. *Environ. Sci. Technol.* **2007,** *41*, 7417-7423.

(62) Duff, M. C.; Hunter, D. B.; Triay, I. R.; Bertsch, P. M.; Reed, D. T.; Sutton, S. R.; Shea-Mccarthy, G.; Kitten, J.; Eng, P.; Chipera, S. J.; Vaniman, D. T., Mineral associations and average oxidation states of sorbed Pu on tuff. *Environ. Sci. Technol.* **1999,** *33* (13), 2163-2169.

(63) Kersting, A. B.; Efurd, D. W.; Finnegan, D. L.; Rokop, D. J.; Smith, D. K.; Thompson, J. L., Migration of plutonium in ground water at the Nevada Test Site. *Nature* **1999,** *397*, 56-59.

(64) Novikov, A. P.; Kalmykov, S. N.; Utsunomiya, S.; Ewing, R. C.; Horreard, F.; Merkulov, A.; Clark, S. B.; Tkachev, V. V.; Myasoedov, B. F., Colloid Transport of Plutonium in the Far-Field of the Mayak Production Association, Russia. *Science* **2006,** *314*, 638-641.

(65) Jeanson, A.; Ferrand, M.; Funke, H.; Hennig, C.; Moisy, P.; Solari, P. L.; Vidaud, C.; Den Auwer, C., The Role of Transferrin in Actinide(IV) Uptake: Comparison with Iron(III). *Chemistry-a European Journal* **2009,** *16* (4), 1378-1387.

(66) Jeanson, A.; Berthon, C.; Coantic, S.; Den Auwer, C.; Floquet, N.; Funke, H.; Guillaneux, D.; Hennig, C.; Martinez, J.; Moisy, P.; Petit, S.; Proux, O.; Quemeneur, E.; Solari, P. L.; Subra, G., The role of aspartyl-rich pentapeptides in comparative complexation of actinide(IV) and iron(III). Part 1. *New J. Chem.* **2009,** *33* (5), 976-985.

(67) Schmeide, K.; Reich, T.; Sachs, S.; Bernhard, G., Plutonium(III) complexation by humic substances studied by X-ray absorption fine structure spectroscopy. *Inorg. Chim. Acta* **2006,** *359* (1), 237-242.

(68) Marquardt, C. M.; Seibert, A.; Artinger, R.; Denecke, M. A.; Kuczewski, B.; Schild, D.; Fanghanel, T., The redox behaviour of plutonium in humic rich groundwater. *Radiochimica Acta* **2004,** *92* (9-11), 617-623.

(69) Moll, H.; Merroun, M. L.; Hennig, C.; Rossberg, A.; Selenska-Pobell, S.; Bernhard, G., The interaction of Desulfovibrio aspoensis DSM 10631(T) with plutonium. *Radiochimica Acta* **2006,** *94* (12), 815-824.

(70) Neu, M. P.; Icopini, G. A.; Boukhalfa, H., Plutonium speciation affected by environmental bacteria. *Radiochimica Acta* **2005,** *93*, 705-714.

(71) Runde, W., The chemical interactions of actinides in the environment. *Los Alamos Science* **2000,** (26), 392-411.

(72) Powell, B. A.; Fjeld, R. A.; Kaplan, D. I.; Coates, J. T.; Serkiz, S. M., $Pu(V)O_2^+$ adsorption and reduction by synthetic hematite and goethite. *Environ. Sci. Technol.* **2005,** *39* (7), 2107-2114.

(73) Keeney-Kennicutt, W. L.; Morse, J. W., The redox chemistry of $Pu(V)O_2^+$ interaction with common mineral surfaces in dilute solutions and seawater. *Geochimica et Cosmochimica Acta* **1985,** *49*, 2577-2588.

(74) Romanchuk, A. Y.; Kalmykov, S. N.; Aliev, R. A., Plutonium sorption onto hematite colloidds at femto- and nanomolar concentrations. *Radiochim. Acta* **2011,** *99*, 137-144.

(75) Sanchez, A. L.; Murray, J. W.; Sibley, T. H., The adsorption of plutonium IV and V on goethite. *Geochimica et Cosmochimica Acta* **1985,** *49*, 2297-2307.

(76) Rothe, J.; Walther, C.; Denecke, M. A.; Fanghanel, T., XAFS and LIBD investigation of the formation and structure of colloidal Pu(IV) hydrolysis products. *Inorganic Chemistry* **2004,** *43* (15), 4708-4718.

(77) Kalmykov, S. N.; Kriventsov, V. V.; Teterin, Y. A.; Novikov, A. P., Plutonium and neptunium speciation bound to hydrous ferric oxide colloids. *Comptes Rendus Chimie* **2007,** *10* (10-11), 1060-1066.

(78) Sposito, G., *Chemical equilibiria and kinetics in soils*. 1st ed.; Oxford University Press: New York, 1994; p 268.

(79) Langmuir, D., *Aqueous environmental geochemistry*. 1st ed.; Prentice-Hall: Upper Saddle River, 1997; p 600.

(80) Guillaumont, R.; Fanghänel, T.; Fuger, J.; Grenthe, I.; Neck, V.; Palmer, D. A.; Rand, M. H., *Update on the Chemical Thermodynamics of Uranium, Neptunium, Plutonium, Americium and Technetium*. Elsevier: Amsterdam, 2003.

(81) Neck, V.; Kim, J. I., Solubility and hydrolysis of tetravalent actinides. *Radiochimica Acta* **2001,** *89* (1), 1-16.

(82) Sorum, C. H., The preparation of chloride free colloidal ferric oxide from ferric chloride. *Journal of the American Chemical Society* **1928,** *50* (5), 1263-1267.

(83) Varanda, L. C.; Morales, M. P.; Jafelicci, M.; Serna, C. J., Monodispersed spindle-type goethite nanoparticles from Fe^{III} solutions. *Journal of Materials Chemistry* **2002,** *12*, 3649-3653.

(84) Teillet, J.; Varret, F., MOSFIT program. *unpublished*, Université du Maine: Le Mans, France.
(85) Gotic, M.; Music, S., Mössbauer, FT-IR and FE SEM invstigation of iron oxides precipitated from FeSO4 solutions. *J. Mol. Struct.* **2007,** *834-836*, 445-453.
(86) Fysh, S. A.; Clark, P. E., A M:ossbauer Study on the iron mineralogy of acid-leaching bauxite. *Hydrometallurgy* **1983,** *10*, 285-303.
(87) Morin, G.; Ona-Nguema, G.; Wang, Y. H.; Menguy, N.; Juillot, F.; Proux, O.; Guyot, F.; Calas, G.; Brown, G. E., Extended X-ray absorption fine structure analysis of arsenite and arsenate adsorption on maghemite. *Environ. Sci. Technol.* **2008,** *42* (7), 2361-2366.
(88) Gorski, C. A.; Nurmi, J. T.; Tratnyek, P. G.; Hofstetter, T. B.; Scherer, M. M., Redox Behavior of Magnetite: Implications for Contaminant Reduction. *Environ. Sci. Technol.* **2010,** *44* (1), 55-60.
(89) Yamamoto, M.; Urata, K.; Murashige, K.; Yamamoto, Y., Differential determination of arsenic(III) and arsenic(V), and antimony(III) and antimony(V) by hydride generation atomic-absorption spectrophotometry, and its application to the determination of these species in sea-water. *Spectrochimica Acta Part B-Atomic Spectroscopy* **1981,** *36* (7), 671-677.
(90) Miravet, R.; Lopez-Sanchez, J. F.; Rubio, R., Comparison of pre-reducing agents for antimony determination by hydride generation atomic fluorescence spectrometry. *Analytica Chimica Acta* **2004,** *511* (2), 295-302.
(91) Webb, S. M., SIXpack: a graphical user interface for XAS analysis using IFEFFIT. *Phys. Scr.* **2005,** *T115*, 1011-1014.
(92) Ravel, B.; Newville, M., Athena, Artemis, Hephaestus: data analysis for X-ray absorption spectroscopy using IFEFFIT. *Journal of Synchrotron Radiation* **2005,** *12*, 537-541.
(93) Ressler, T., WinXAS: a program for X-ray absorption spectroscopy data analysis under MS-Windows. *Journal of Synchrotron Radiation* **1998,** *5*, 118-122.
(94) Ankudinov, A. L.; Bouldin, C.; Rehr, J. J.; Sims, J.; Hung, H., Parallel calculation of electron multiple scattering using Lanczos algorithms. *Phys. Rev. B* **2002,** *65* (10), 104107.
(95) Bayliss, P.; Nowacki, W., Refinement of the crystal structure of stibnite, Sb_2S_3. *Zeitschrift für Kristallographie* **1972,** *135*, 308-315.
(96) Basso, R.; Cabella, R.; Lucchetti, G.; Marescotti, P.; Martinelli, A., Structural studies on synthetic and natural Fe-Sb-oxides of MO2 type. *Neues Jahrbuch Fur Mineralogie-Monatshefte* **2003,** (9), 407-420.
(97) Oman, S. F.; Camoes, M. F.; Powell, K. J.; Rajagopalan, R.; Spitzer, P., Guidelines for potentiometric measurements in suspensions, part A. The suspension effect. *Pure Appl. Chem.* **2007,** *79* (1), 67-79.
(98) Wolthers, M.; Charlet, L.; Van der Linde, P. R.; Rickard, D.; Van der Weijden, C. H., Surface chemistry of disordered mackinawite (FeS). *Geochimica Et Cosmochimica Acta* **2005,** *69* (14), 3469-3481.
(99) Conradson, S. D.; Abney, K. D.; Begg, B. D.; Brady, E. D.; Clark, D. L.; den Auwer, C.; Ding, M.; Dorhout, P. K.; Espinosa-Faller, F. J.; Gordon, P. L.; Haire, R. G.; Hess, N. J.; Hess, R. F.; Keogh, D. W.; Lander, G. H.; Lupinetti, A. J.; Morales, L. A.; Neu, M. P.; Palmer, P. D.; Paviet-Hartmann, P.; Reilly, S. D.; Runde, W. H.; Tait, C. D.; Veirs, D. K.; Wastin, F., Higher order speciation effects on plutonium L_3 X-ray absorption near edge spectra. *Inorganic Chemistry* **2004,** *43* (1), 116-131.
(100) Denecke, M. A., Actinide speciation using X-ray absorption fine structure spectroscopy. *Coord. Chem. Rev.* **2006,** *250* (7-8), 730-754.
(101) Conradson, S. D.; Begg, B. D.; Clark, D. L.; den Auwer, C.; Ding, M.; Dorhout, P. K.; Espinosa-Faller, F. J.; Gordon, P. L.; Haire, R. G.; Hess, N. J.; Hess, R. F.; Keogh, D. W.; Lander, G. H.; Manara, D.; Morales, L. A.; Neu, M. P.; Paviet-Hartmann, P.; Rebizant, J.; Rondinella, V. V.; Runde, W.; Tait, C. D.; Veirs, D. K.; Villella, P. M.; Wastin, F., Charge distribution and local structure and speciation in the UO2+x and PuO2+x binary oxides for x <= 0.25. *Journal of Solid State Chemistry* **2005,** *178* (2), 521-535.
(102) Neck, V.; Altmaier, M.; Seibert, A.; Yun, J. I.; Marquardt, C. M.; Fanghanel, T., Solubility and redox reactions of Pu(IV) hydrous oxide: Evidence for the formation of PuO2+x(s, hyd). *Radiochimica Acta* **2007,** *95* (4), 193-207.

(103) Committee, I. S. a. C. *Error reporting recommendations: A report of the standards and criteria committee*; 2000.
(104) Rai, D.; Gorby, Y. A.; Fredrickson, J. K.; Moore, D. A.; Yui, M., Reductive dissolution of PuO_2(am): The effect of Fe(II) and hydroquinone. *J. Solution Chem.* **2002,** *31* (6), 433-453.
(105) Felmy, A. R.; Moore, D. A.; Rosso, K. M.; Qafoku, O.; Rai, D.; Buck, E. C.; Ilton, E. S., Heterogeneous reduction of PuO_2 with Fe(II): importance of the Fe(III) reaction product. *Environ. Sci. Technol.* **2011,** *45*, 3952-3958.
(106) Teo, B. K., *EXAFS: Basic principles and data analysis*. Springer-Verlag: Berlin, 1986.
(107) Wechsler, B. A.; Lindsley, D. H.; Prewitt, C. T., Crystal structure and cation distribution in titanomagnetites ($Fe_{3-x}Ti_xO_4$). *American Mineralogist* **1984,** *69*, 754-770.
(108) Shmakov, A. N.; Kryukova, G. N.; Tsybulya, S. V.; Chuvilin, A. L.; Soloveva, L. P., Vacancy ordering in gamma-Fe_2O_3: synchrotron x-ray powder diffraction and high-resolution electron microscopy studies. *J. Appl. Crystallogr.* **1995,** *28*, 141-145.
(109) Brice-Profeta, S.; Arrio, M.-A.; Tronc, E.; Menguy, N.; Letard, I.; Cartier dit Moulin, C.; Nogues, M.; Chaneac, C.; Jolivet, J.-P.; Sainctavit, P., Magnetic order in γ-Fe_2O_3 nanoparticles: a XMCD study. *J. Magn. Magn. Mater.* **2005,** *288*, 354-365.
(110) Grigoriev, M. S.; Fedoseev, A. M.; Gelis, A. V.; Budantseva, N. A.; Shilov, V. P.; Perminov, V. P.; Nikonov, M. V.; Krot, N. N., Study of the interaction of Pu(IV) and Np(IV, V, VI) with Fe hydroxides to predict the behavior of actinides in environmental media. *Radiochim. Acta* **2001,** *89* (2), 95-100.
(111) Jolivet, J. P.; Tronc, E., Interfacial electron transfer in colloidal spinel iron oxide. Conversion of Fe_3O_4-γFe_2O_3 in aqueous medium. *Journal of Colloid and Interface Science* **1988,** *125* (2), 688-701.
(112) White, A. F.; Peterson, M. L.; Hochella, M. F., Electrochemistry and dissolution kinetics of magnetite and ilmenite. *Geochimica Et Cosmochimica Acta* **1994,** *58* (8), 1859-1875.
(113) Zhao, P.; Zavarin, M.; Tumey, S.; Williams, R.; Dai, Z.; Kips, R.; Snow, M.; Kersting, A. B., Sorption isotherms of plutonium and neptunium onto goethite over ten orders of magnitude concentration range and sorption mechanisms investigation using TEM and nanoSIMS. *Abstracts of the 13th International Conference on the Chemistry and Migration Behaiour of Actinides and Fission Products in the Geosphere* **2011**, 370-371.
(114) Lu, N.; Cotter, C. R.; Kitten, H. D.; Bentley, J.; Triay, I. R., Reversibility of Sorption of Plutonium-239 onto Hematite and Goethite Colloids. *Radiochimica Acta* **1998,** *83*, 167-173.
(115) Lu, N.; Reimus, P. W.; Parker, G. R.; Conca, J. L.; Triay, I. R., Sorption kinetics and impact of temperature, ionic strength and colloid concentration on the adsorption of plutonium-239 by inorganic colloids. *Radiochimica Acta* **2003,** *91*, 713-720.
(116) Hu, Y. J.; Schwaiger, L. K.; Booth, C. H.; Kukkadapu, R. K.; Cristiano, E.; Kaplan, D.; Nitsche, H., Molecular interactions of plutonium(VI) with synthetic manganese-substituted goethite. *Radiochimica Acta* **2010,** *98* (9-11), 655-663.
(117) Powell, B. A.; Dai, Z.; Zavarin, M.; Zhao, P.; Kersting, A. B., Stabilization of Plutonium Nano-Colloids by Epitaxial Distortion on Mineral Surfaces. *Environ. Sci. Technol.* **2011,** *45*.
(118) Kersting, A. B.; Zhao, P.; Zavarin, M.; Sylwester, E. R.; Allen, P. G.; Williams, R. W. *Sorption of Pu(V) on Mineral Colloids*; Lawrence Livermore National Laboratory, Livermore, CA: 2003.
(119) Romanchuk, A. Y.; Egorov, A. V.; Zubavichus, Y. V.; Shiryaev, A. A.; Kalmykov, S. N., $PuO_{2+x}\cdot nH_2O$ nanoparticles formation upon Pu(V,VI) sorption onto hematite. *Mineralogical Magazine* **2011,** *Goldschmidt 2011 conference abstract volume*.
(120) Silvester, E.; Charlet, L.; Tournassat, C.; Gehin, a.; Greneche, J.-M.; Liger, E., Redox potential measurements and Mössbauer spectrometry of Fe^{II} adsorbed onto Fe^{III} (oxyhydr)oxides. *Geochimica et Cosmochimica Acta* **2005,** *69* (20), 4801–4815.
(121) Ohfuji, H.; Rickard, D., High resolution transmission electron microscopic study of synthetic nanocrystalline mackinawite. *Earth and Planetary Science Letters* **2006,** *241* (1-2), 227-233.
(122) Michel, F. M.; Antao, S. M.; Chupas, P. J.; Lee, P. L.; Parise, J. B.; Schoonen, M. A. A., Short- to medium-range atomic order and crystallite size of the initial FeS precipitate from pair distribution function analysis. *Chemistry of Materials* **2005,** *17* (25), 6246-6255.

(123) Scheinost, A. C.; Kirsch, R.; Banerjee, D.; Fernandez-Martinez, A.; Zaenker, H.; Funke, H.; Charlet, L., X-ray absorption and photoelectron spectroscopy investigation of selenite reduction by Fe-II-bearing minerals. *Journal of Contaminant Hydrology* **2008,** *102* (3-4), 228-245.

(124) Gallegos, T. J.; Han, Y. S.; Hayes, K. F., Model Predictions of Realgar Precipitation by Reaction of As(III) with Synthetic Mackinawite Under Anoxic Conditions. *Environ. Sci. Technol.* **2008,** *42* (24), 9338-9343.

(125) Stumm, W.; Morgan, J. J., *Aquatic Chemistry: chemical equilibria and rates in natural waters*. 3 rd ed.; John Wiley & Sons, Inc.: New York, 1996.

(126) Wolthers, M.; Charlet, L.; Van der Weijden, C. H.; Van der Linde, P. R.; Rickard, D., Arsenic mobility in the ambient sulfidic environment: Sorption of arsenic(V) and arsenic(III) onto disordered mackinawite. *Geochimica Et Cosmochimica Acta* **2005,** *69* (14), 3483-3492.

(127) Moyes, L. N.; Parkman, R. H.; Charnock, J. M.; Vaughan, D. J.; Livens, F. R.; Hughes, C. R.; Braithwaite, A., Uranium uptake from aqueous solution by interaction with goethite, lepidocrocite, muscovite, and mackinawite: An X-ray absorption spectroscopy study. *Environ. Sci. Technol.* **2000,** *34* (6), 1062-1068.

(128) Gallegos, T. J.; Hyun, S. P.; Hayes, K. F., Spectroscopic investigation of the uptake of arsenite from solution by synthetic mackinawite. *Environ. Sci. Technol.* **2007,** *41*, 7781-7786.

(129) Carmalt, C. J.; Norman, N. C., Arsenic, antimony and bismuth: some general properties and aspects of periodicity. In *Chemistry of arsenic, antimony and bismuth*, 1st ed.; Norman, N. C., Ed. Blackie Academic & Professional: London, 1998.

(130) Tossell, J. A., Calculation of the visible-UV absorption spectra of hydrogen sulfide, bisulfide, polysulfides, and As and Sb sulfides, in aqueous solution. *Geochemical Transactions* **2003,** *4*, 28-33.

(131) Michel, F. M.; Ehm, L.; Antao, S. M.; Lee, P. L.; Chupas, P. J.; Gang, L.; Strongin, D. R.; Schoonen, M. A. A.; Phillips, B. L.; Parise, J. B., The structure of ferrihydrite, a nanocrystalline material. *Science* **2007,** *316* (316), 1726-1729.

(132) Skinner, B. J.; Erd, R. C.; Grimaldi, F. S., Greigite, the thiospinel of iron; a new mineral. *American Mineralogist* **1964,** *49*, 543-555.

(133) Lennie, A. R.; Redfern, S. A. T.; Schofield, P. F.; Vaughan, D. J., Synthesis and Rietveld crystal structure refinement of mackinawite, tetragonal FeS. *Mineralogical Magazine* **1995,** *59* (397), 677-683.

(134) Mullet, M.; Boursiquot, S.; Abdelmoula, M.; Genin, J. M.; Ehrhardt, J. J., Surface chemistry and structural properties of mackinawite prepared by reaction of sulfide ions with metallic iron. *Geochimica Et Cosmochimica Acta* **2002,** *66* (5), 829-836.

(135) Lennie, A. R.; Redfern, S. A. T.; Champness, P. E.; Stoddart, C. P.; Schofield, P. F.; Vaughan, D. J., Transformation of mackinawite to greigite: An in situ X-ray powder diffraction and transmission electron microscope study. *American Mineralogist* **1997,** *82* (3-4), 302-309.

(136) Coles, C. A.; Rao, S. R.; Yong, R. N., Lead and cadmium interactions with mackinawite: Retention mechanisms and the role of pH. *Environ. Sci. Technol.* **2000,** *34* (6), 996-1000.

(137) Mullet, M.; Boursiquot, S.; Ehrhardt, J. J., Removal of hexavalent chromium from solutions by mackinawite, tetragonal FeS. *Colloids and Surfaces A: Physicochemical and Engineering Aspects* **2004,** *244* (1-3), 77-85.

(138) Patterson, R. R.; Fendorf, S.; Fendorf, M., Reduction of hexavalent chromium by amorphous iron sulfide. *Environ. Sci. Technol.* **1997,** *31* (7), 2039-2044.

(139) Farquhar, M. L.; Charnock, J. M.; Livens, F. R.; Vaughan, D. J., Mechanisms of arsenic uptake from aqueous solution by interaction with goethite, lepidocrocite, mackinawite, and pyrite: An X-ray absorption spectroscopy study. *Environ. Sci. Technol.* **2002,** *36* (8), 1757-1762.

(140) Wolthers, M.; Butler, I. B.; Rickard, D., Influence of arsenic on iron sulfide transformations. *Chemical Geology* **2007,** *236* (3-4), 217-227.

(141) Hua, B.; Deng, B., Reductive immobilization of uranium(VI) by amorphous iron sulfide. *Environ. Sci. Technol.* **2008,** *42*, 8703-8708.

(142) Kim, C.; Zhou, Q.; Deng, B.; Thornton, E. C.; Xu, H., Chromium(VI) reduction by hydrogen sulfide in aqueous media: Stoichiometry and kinetics. *Environ. Sci. Technol.* **2001,** *35* (11), 2219-2225.

(143) Polack, R.; Chen, Y. W.; Belzile, N., Behaviour of Sb(V) in the presence of dissolved sulfide under controlled anoxic aqueous conditions. *Chemical Geology* **2009,** *262* (3-4), 179-185.

(144) O'Day, P. A.; Vlassopoulos, D.; Root, R.; Rivera, N., The influence of sulfur and iron on dissolved arsenic concentrations in the shallow subsurface under changing redox conditions. *Proceedings of the National Academy of Sciences of the United States of America* **2004,** *101* (38), 13703-13708.

(145) Bourdoiseau, J. A.; Jeannin, M.; Remazeilles, C.; Sabota, R.; Refait, P., The transformation of mackinawite into greigite studied by Raman spectroscopy. *Journal of Raman Spectroscopy* **2011,** *42* (3), 496-504.

(146) Hunger, S.; Benning, L. G., Greigite: a true intermediate on the polysulfide pathway to pyrite. *Geochemical Transactions* **2007,** *8*.

(147) Yanina, S. V.; Rosso, K. M., Linked reactivity at mineral-water interfaces through bulk crystal conduction. *Science* **2008,** *320*, 218-222.

(148) Rosso, K. M.; Dupuis, M., Electron transfer in environmental systems: a frontier for theoretical chemistry. *Theor. Chem. Acc.* **2006,** *116*, 124-136.

(149) Romanchuk, A. Y.; Egorov, A. V.; Zubavichus, Y. V.; Shiryaev, A. A.; Kalmykov, S. N., $PuO_{2+x}{\cdot}nH_2O$ nanoparticles formation upon Pu(V,VI) sorption onto hematite. *Mineralogical Magazine* **2011**, 1745.

(150) de Combarieu, G.; Barboux, P.; Minet, Y., Iron corrosion in Callovo–Oxfordian argilite: From experiments to thermodynamic/kinetic modelling. *Physics and Chemistry of the Earth* **2007,** *32*, 346-358.

(151) Schlegel, M. L.; Bataillon, C.; Blanc, C.; Pret, D.; Foy, E., Anodic Activation of Iron Corrosion in Clay Media under Water-Saturated Conditions at 90 degrees C: Characterization of the Corrosion Interface. *Environ. Sci. Technol.* **2010,** *44* (4), 1503-1508.

List of Figures

Figures from chapter 3.2 and from the annexes to chapter 3 and 4 do not appear in this list.

Figure 3.3.14. LC fit of sample Mk-8m-III-pH7 in the range 18040 to 18105 eV using Pu(III)aq and sample Mk-8m-III-pH8 (as representative of non-calcinated PuO_2) as references. For fit results see Table 3.3.5.

Figure 3.3.15. LC fit of sample Mk-8m-III-pH7 in the range 18105 to 18330 eV using Pu(III)aq and either Mk-8m-III-pH8 or Mk-8m-V-pH7 (as representatives of non-calcinated PuO_2) as references. For fit results see Table 3.3.6

Figure 3.3.16. XANES spectra of artificially created PuO_2(cr)-Pu(III) (a) and PuO_2(cr)-Pu(V) mixtures.

Figure 3.3.17. k^3-weighted EXAFS spectra of a) PuO_2(cr) + Pu(V)aq and of b) PuO_2(cr) + Pu(III)aq mixtures. Spectral features differently affected by the presence of Pu(III) or Pu(V) are circled in grey.

Figure 3.3.18. Comparison of PuO_2 spectra consisting of 90 % PuO_2(cr) and either 10 % Pu(III) or 10 % Pu(V). a) k^3 – weighted EXAFS spectrum; b) FT (based on $2 \leq k \leq 11.8$ Å^{-1}, hanning window, dk1) with window for BT shown in c) marked in green; c) Back-transform of the first oxygen shell ($1.3 \leq R+\Delta R \leq 2.35$). The split minimum at 6.3 Å^{-1} is circled in grey as it is affected differently by the presence of Pu(III) and Pu(V).

Figure 3.3.19. Comparison of PuO_2 spectra consisting of 80 % PuO_2(cr) and either 20 % Pu(III) or 20 % Pu(V).

a) k^3 – weighted EXAFS spectrum; b) FT (based on $2 \leq k \leq 11.8$Å^{-1}, hanning window, dk1) with window for BT shown in c) marked in green; c) Back-transform of the first oxygen shell ($1.3 \leq R+\Delta R \leq 2.35$). The split minimum at 6.3 Å^{-1} is circled in grey as it is affected differently by the presence of Pu(III) and Pu(V).

Figure 3.3.20. The structural disorder of Pu-O shells as indicated by σ (σ = sqrt(σ^2)) as a function of distance. a) σ as obtained by fitting with adjustable CN; b) σ as obtained by fitting with CN fixed to the crystallographic values of PuO_2. The corresponding σ^2 values are tabulated in Tables 3.3.7, 3.3.8 and 3.3.9 (apart from values for a fit with fixed CN for spectra with 10 % Pu(III) or Pu(V) which are not reported in tabulated form). Lines between data points are drawn only as a guide to the eye and to facilitate pattern recognition.

Figure 3.3.21. k^3-weighted EXAFS spectra of Pu-mackinawite samples and PuO_2(cr) for reference.

Figure 3.3.22. Edge jump of XAS spectra as a function of Pu mass loadings (a) and noise level of the unweighted k-spectra as a function of edge jump (b).

Figure 3.3.23. FT of Pu-mackinawite samples from Fig. 3.3.21. FT parameters: $3 \leq k \leq 12.6$, hannig window, dk1.

Figure 3.3.24. FT of 8 months Pu-mackinawite samples from Fig. 3.3.21. FT parameters: $3 \leq k \leq 15.15$ Å^{-1}, hannig window, dk1. Large graph: overview up to R + ΔR 25 Å. The noise level is indicated by the amplitude of peaks above ca. 12 Å. Inset: zoom of the on the 1.2 to 4.3 Å region.

Figure 3.3.25. Fit residual as a function of the spectral noise level in k-range (same values as tabulated in Table 3.3.10) for fits with fixed and adjustable CN; FT based on $3.0 \leq k \leq 15.2$ Å^{-1}. Fit range in R-space was a) $1.3 \leq R \leq 4.1$ Å, b) $1.3 \leq R \leq 6.7$ Å. Apart from PuO_2(cr) in a) all four 8 months Pu-mackinawite sample appear (data from Tables 3.3.11 – 14). In b) only Mk-8m-V-pH7 and Mk-8m-V-pH7 were included (data from Tables 3.3.15, 16).

Figure 3.3.26. The structural disorder of Pu-O (2.33 and 4.42 Å) and Pu-Pu (3.83 Å) paths as indicated by σ (σ = sqrt(σ^2)) as a function of distance. a) σ as obtained by fitting with adjustable CN; b) σ as obtained by fitting with CN fixed to the crystallographic values of PuO_2. The corresponding σ^2 values are tabulated in Tables A3.23–26. Fits based on $3 \leq k \leq 15.2$ Å^{-1} and $1.3 \leq R \leq 4.1$ Å. Lines between data points are drawn only as a guide to the eye and to facilitate pattern recognition.

Figure 3.4.1. pe_{sus} (a) and pH_{sus} (b) values and total dissolved Pu concentrations (c) over time for Pu-chukanovite samples. Data points corresponding to values at or below the detection limit are marked by red outer line. The samples are designated by the initial Pu oxidation state and reaction time.

Figure 3.4.2. XANES region of Pu-L_{III}-edge X-ray absorption spectra of Pu-chukanovite samples (red, orange and yellow) and PuO_2(cr), Pu(III)aq, Pu(IV)aq and two Pu-mackinawite samples for comparison. a) Overview of the XANES region, b) zoom on the edge region, c) WL-maximum region, d) post-WL minimum region.

Figure 3.4.3. LC fit of sample Chuk-8m-III using Pu(III)aq and Mk-8m-III-pH8 as references. a) XANES (fit range: 18.040 to 18.105 keV), b) early EXAFS region (normalized spectrum) (fit range: 18.105 to 18.33 keV), c) EXAFS (fit range 3.0–12.3 Å^{-1}, E_0 of sample and reference spectra set to 18.060 keV).

Figure 3.4.4. EXAFS spectra acquired at the Pu-L_{III}-edge (large picture) and FT of Pu-chukanovite spectra and PuO_2(cr) for reference. Insets: a) FT of k^3-weighted spectra (k-range of $3 \leq k \leq 15.2$ Å^{-1}) (only 8-months spectra), b) Imaginary part of the FT in a), c) FT over $3 \leq k \leq 12.6$ Å^{-1} (including Chuk-40d-V).

Figure 3.4.5. The structural disorder of Pu-O (2.33 and 4.42 Å) and Pu-Pu (3.83 Å) paths as indicated by σ (σ = sqrt(σ^2)) as a function of distance. a) σ as obtained by fitting with adjustable CN; b) σ as obtained by fitting with CN fixed to the crystallographic values of PuO_2. The corresponding σ^2 values are tabulated in Tables A.3.23–26, 33, 34. Fits based on $3 \leq k \leq 15.2$ Å^{-1} and $1.3 \leq R \leq 4.1$ Å. Lines between data points are drawn only as a guide to the eye.

Figure 3.4.6. The structural disorder of Pu-O shells as indicated by σ (σ = sqrt(σ^2)) as a function of distance. a) σ as obtained by fitting with adjustable CN (open triangle for second Pu-O shell (4.4.3 Å) signify values that had to be correlated to the first Pu-O shell); b) σ as obtained by fitting with CN fixed to the crystallographic values of PuO_2. Lines between data points are drawn only as a guide to the eye.

Figure 3.4.7. a) Relative increase (positive values) or decrease (negative values) of σ(PuO_2+Pu(III)) vs σ(PuO_2(cr)) calculated as: Δσ/σ(PuO_2(cr)) = (σ(PuO_2+Pu(III))-σ(PuO_2(cr)) / σ(PuO_2(cr) for fits with adjustable CN. b) σ(Pu-O) and σ(Pu-Pu) over Pu(III) content for fits with fixed CN calculated from data points in Fig. 3.4.5.

Figure 3.4.8. Sigma as a function of r obtained for the hypothetical PuO_2 component in mixed Pu(III)-PuO_2 Pu-chukanovite samples obtained by applying the equations from Fig. 3.4.7 to data plotted in Fig. 3.4.5 and Fig. A3.1. a) Fits with adjustable CN. Pu-mackinawite samples, Chuk-8m-III, Chuk-8m-V and PuO_2(cr): $3 \leq k \leq 15.2$ Å^{-1}. For Chuk-40d-V and Chuk-8m-V: $3 \leq k \leq 12.1$ Å^{-1}. b) Fits with fixed CN. Pu-mackinawite samples, Chuk-8m-III, Chuk-8m-V and PuO_2(cr): $3 \leq k \leq 15.2$ Å^{-1}. Chuk-40d-V, Chuk-8m-V and Chuk-8m-III: $3 \leq k \leq 12.1$ Å^{-1} For all: fit range in R-space: $1.3 \leq R \leq 4.1$ Å.

Figure 3.5.1. pH_{sus} (a), pe_{sus} (b), zoom on pH_{sus} (left ordinate) and pe_{sus} (right ordinate) for 8m samples (c), and total dissolved Pu concentrations (d) over time for Pu-magnetite samples. Legend for a, b and d given in d. In d) data points corresponding to values at or below the detection limit are marked by red outer line. The samples are designated by the initial Pu oxidation state and reaction time. Lines between data points are plotted as guide to the eye.

Figure 3.5.2. pe_{sus} (a), pH_{sus} (b) and total dissolved Pu concentrations (c) over time for Pu-maghemite samples. Legend for a, b and d given in c. In c) data points corresponding to values at or below the detection limit are marked by red outer line. The samples are designated by the initial Pu oxidation state and reaction time. Lines between data points are plotted as guide to the eye.

Figure 3.5.3. XANES region of Pu-L_{III}-edge X-ray absorption spectra of Pu-magnetite samples and Pu(III)aq and Pu(IV)aq references for comparison. a) Spectra shifted in height for clarity, dotted lines marking positions of Pu(III) WL maximum and first post-WL maximum, b) Overlay of five Pu-magnetite spectra and Mk-8m-V-pH7 as representative of non-calcinated PuO_2.

Figure 3.5.4. EXAFS region (a) and FT (b) of Pu-L_{III}-edge X-ray absorption spectra of two Pu-magnetite samples (Mg-40d-V-pH8 and Mg-8m-V-pH8) and PuO_2 (sample Mk-8m-V-pH7). FT based on $3 \leq k \leq 12.6$ Å^{-1}, hannig window, dk1.

Figure 3.5.5. LC fit of Pu-L_{III}-edge XAS spectrum of sample Mg-8m-V-pH7 using $Pu(III)_{ads\text{-}Mg}$ (sample Mg-40d-V-pH8) and PuO_2 (Mk-8m-III-pH8) as references. a) XANES (fit range: 18040 to 18100 eV), b) EXAFS (fit range 2.8–9.7 Å^{-1}, E_0 of sample and reference spectra set to 18060 eV).

Figure 3.5.6. XANES region of Pu-L_{III}-edge X-ray absorption spectra of Pu-maghemite samples, of Pu(III) adsorbed to magnetite and of Pu(III)aq, Pu(IV)aq, Pu(V)aq references for comparison.

Figure 3.5.7. Comparison of Pu-magnetite (green) and Pu-maghemite (blue) EXAFS spectra.

Figure 3.5.8. a) EXAFS and b) Fourier Transform of Pu(III) on magnetite (green) and of Pu(III) reacted with maghemite (40 d light blue vs 8 m, blue) (FT based on $3 \leq k \leq 10$ Å^{-1}, Kaiser-Bessel window, dk1).

Figure 3.5.9. Shell fits of Pu-magnetite and Pu-maghemite samples from Table 3.5.5. a), b) Mg-40d-V-pH8, c), d) Mg-40d-III-pH6, e), f) Mh-40d-III. a, c, e EXAFS, b, d, f Fourier Transform.

Figure 3.5.10. Shell fits of Pu-magnetite and Pu-maghemite samples from Table 3.5.5. a),b) Mh-40d-V, c), d) Mh-8,-III e), f) Mh-8m-V. a, c, e EXAFS, b, d, f Fourier Transform.

Figure 3.5.11. a) Magnetite (111) face vs b) maghemite (111) face. (magnetite based on icsd 30860[107], maghemite based on icsd 79196[108]).

Figure 3.6.1.. . pH_{sus} (a), pe_{sus} (b), total dissolved Pu concentrations over time for Pu-hematite and Pu-goethite samples (c) and comparison with Pu-sorption as a function of time using the formula published by Powell et al. (2005)[72]. Key to samples for b, c, d given in a. In c) and d) data points corresponding to values at or below the

detection limit are marked by red outer line. Samples are designated by the initial Pu oxidation state and reaction time. Lines between data points are plotted as guide to the eye.

Figure 3.6.2. Plot of $-\ln([Pu]_t/[Pu]_0)$ over time and resulting apparent rate constants according to (pseudo)-first order kinetics.

Figure 3.6.3. XANES region of Pu-L_{III}-edge X-ray absorption spectra of Pu-hematite and Pu-goethite samples, of Pu(IV)aq and Pu(V)aq for reference and of one Pu-maghemite sample and two Pu-mackinawite samples for comparison.

Figure 3.6.4. XANES region linear combination fit of sample He-8m-III using aqueous Pu references.

Figure 3.6.5. Pu(IV)aq and Pu(V)aq references, Pu-hematite and Pu-goethite spectra (blue), reconstruction of samples spectra (red) and Pu(IV) and Pu(V) factors (green) found by ITT analysis of the XANES region (18040 – 18100 eV) (plot corresponds to data in Table 3.6.3 b).

Figure 3.6.6. EXAFS spectra (left), FT Magnitude (right) and imaginary part of the FT (right, inset) of Pu-hematite and goethite spectra, of Mh-8m-III for comparison and of Pu(IV)aq and Pu(V)aq for reference. FT based on $2.9 \leq k \leq 10.7$ Å^{-1}, hannig window, dk1.

Figure 4.2.1. pe-pH predominance diagram for the Fe – S – H_2O system, considering equilibria between mackinawite (FeS(am)), greigite (Fe_3S_4), ferri-hydroxide ($Fe(OH)_3$(am)), and dissolved ferrous iron. Sulfide oxidation is neglected. Concentrations of dissolved iron and sulfide are fixed to 10^{-3} M (blue) or 10^{-6} M (violet). Data points from FeS dissolution (1,7 g/L) in 1.9 or 25 mM $CaCl_2$.

Figure 4.2.2. pe-pH predominance diagram for the Fe – S – H_2O system, considering equilibria between mackinawite (FeS(am)), greigite (Fe_3S_4), ferrihydroxide ($Fe(OH)_3$(am)), and dissolved ferrous iron. Sulfide oxidation and precipitation of $Fe(OH)_2$(s) is neglected. Concentrations of dissolved iron and sulfide result from dissolution of FeS as a function of pH. Solid phase names are printed in bold, solution species in italics. Dotted lines in the centre of the greigite field represent equilibria between FeS(am) and $Fe(OH)_3$(am) in the absence of greigite formation. Rose line in the greigite field results when a lower $\{H_2S\}$aq activity is assumed, e.g. through loss of H_2S(g); in this case, a decrease by 97 % of $\{H_2S\}$aq is assumed. Data points from FeS dissolution (green), from FeS + Sb(V) redox (light violet), and from FeS + Pu redox experiments from chapter 3.3 (purple). Triangles represent data are from the supporting information of Gallegos et al. (2008).[118]

Figure 4.2.3. Same as Fig. 4.2, but using a $\Delta_f G$ value of -692 kJ/mol for $Fe(OH)_3$(am) instead of -688.35 kJ/mol.

Figure 4.3.1. pH suspension, $[Sb]_{total}$, and [Sb(III)] plotted over time for sample Stime_ac.

Figure 4.3.2. a) Stime_bas experiment: pH, $[Sb]_{total}$ and Sb(III) over time, b) Sb sorption [%] over time for pH 5.6 to 6.4 (Stime_ac) and at pH 8.1 (Stime_bas).

Figure 4.3.3. Plot of $-\ln([Sb]_t/[Sb]_0)$ over time for samples Stime_ac (a) and Stime_bas (b) and pseudo-first order rate constant as a function of proton activity (c).

Figure 4.3.1. pH suspension, $[Sb]_{total}$, and [Sb(III)] plotted over time for sample Stime_ac.

Figure 4.3.2. a) Stime_bas experiment: pH, $[Sb]_{total}$ and Sb(III) over time, b) Sb sorption [%] over time for pH 5.6 to 6.4 (Stime_ac) and at pH 8.1 (Stime_bas).

Figure 4.3.3. Plot of $-\ln([Sb]_t/[Sb]_0)$ over time for samples Stime_ac (a) and Stime_bas (b) and pseudo-first order rate constant as a function of proton activity (c).

Figure 4.3.4. Sorption of Sb(V) to mackinawite as a function of pH (experiments SpH_a and b). a) % Sb sorption and % FeS dissolution, b) final $[Sb]_{total}$ and [Sb(III)] concentrations as a function of pH and Sb(III) content in percent (in 25 mM $CaCl_2$).

Figure 4.3.5. a) pH increase as a funtion of initial Sb(V) concentration in Siso_ac experiment. b) Comparison of Sb sorption as a function of the final pH in Siso_ac with pH dependent sorption from experiments SpH_a and SpH_b. c) Final total dissolved Sb, Sb(III) and Sb(III) over Sb_{total}.

Figure 4.3.1. pH suspension, $[Sb]_{total}$, and [Sb(III)] plotted over time for sample Stime_ac.

Figure 4.3.2. a) Stime_bas experiment: pH, $[Sb]_{total}$ and Sb(III) over time, b) Sb sorption [%] over time for

pH 5.6 to 6.4 (Stime_ac) and at pH 8.1 (Stime_bas).

Figure 4.3.3. Plot of $-\ln([Sb]_t/[Sb]_0)$ over time for samples Stime_ac (a) and Stime_bas (b) and pseudo-first order rate constant as a function of proton activity (c).

Figure 4.3.4. Sorption of Sb(V) to mackinawite as a function of pH (experiments SpH_a and b). a) % Sb sorption and % FeS dissolution, b) final $[Sb]_{total}$ and [Sb(III)] concentrations as a function of pH and Sb(III) content in percent (in 25 mM $CaCl_2$).

Figure 4.3.5. a) pH increase as a funtion of initial Sb(V) concentration in Siso_ac experiment. b) Comparison of Sb sorption as a function of the final pH in Siso_ac with pH dependent sorption from experiments SpH_a and SpH_b. c) Final total dissolved Sb, Sb(III) and Sb(III) over Sb_{total}.

Figure 4.4.1. Dissolved Sb over time (a) and Sb sorption over time (b) for XAS experiment B. Xb_ac_1 to 4 samples are shown in green, Xb_bas_1 to 4 samples in pink-violet. Lines between data points are guide to the eye. In b) Xb_bas samples refer to the right side ordinate.

Figure 4.4.2. Sb-K-edge XANES spectra of XAS experiment B, Sb(V) adsorbed to hematite is shown for reference.

Figure 4.4.3. Experimental spectra and reconstruction of the 8 XANES spectra (Xb_ac, Xb_bas, Sb(V) on hematite) on which composition analysis by ITT with two factors (see text) was performed.

Figure 4.4.4. EXAFS (a) and FT (b) of samples Xb_ac_2 (black), Xb_bas_1 (green) and Xb_bas_4 (red).

Figure 4.4.5. Diffraction patterns for Xb_ac (red-violet) and Xb_bas (green or blue) samples acquired by synchrotron diffraction at a wavelength of 0.3738 Å compared to greigite (ICSD 42535)[126] (grey) and mackinawite (ICSD 81087)[127] (black) patterns.

Figure 4.5.1. Reaction conditions in terms of pH, reaction time and loading (mol U, mol As or mol Sb /g FeS) resulting from complete sorption of initial U or As concentrations during the studies on arsenic and uranium sorption and reduction by mackinawite discussed in this chapter.

List of Tables

Table 3.4.4. LC fit of samples Chuk-8m-III with Pu(III)aq and non-calcinated PuO_2 (Mk-8m-III-pH8) in k-space in the range 3.0–8.85 and 3.0–12.3 $Å^{-1}$. For exemplary plot see Fig. 3.4.3.

Table 3.5.1. List of Pu-magnetite and Pu-maghemite samples to be discussed in this chapter.

Table 3.5.2. LC fit of sample Mg-8m-V-pH8 with $Pu(III)_{ads\text{-}Mg}$ (= Mg-40d-V-pH8) and non-calcinated PuO_2 (either sample Mk-8m-V-pH7 or Mk-8m-III-pH8) as references in the energy range 18040 to 18100 eV and in k-range 2.8–6.8 and 2.8–9.7 $Å^{-1}$. For fit in k-space E_0 was set to 18060 eV for all spectra. For plot see Fig. 3.5.5.

Table 3.5.3. LC fit of samples Mg-8m-V-pH8 with $Pu(III)_{ads\text{-}Mg}$ (= Mg-40d-V-pH8) and non-calcinated PuO_2 (Mk-8m-III-pH8) in k-space in the range 2.8–6.8 and 2.8–9.7 $Å^{-1}$. E0 was chosen as the inflection point of each spectrum or was for all three spectra set to the value of one of the reference spectra.

Table 3.5.4. LC fitting of XANES region of Pu-maghemite spectra using Pu(III)aq, Pu(IV)aq and Pu(V)aq as references.

Table 3.5.5. Shell fitting results of Pu-maghemite samples, 2 Pu-magnetite samples and 2 artificial oxidation state mixture spectra. Also given is the correlation factor between CN and DW for Pu-O and Pu-Fe paths.*

Table 3.5.6. Shell fitting results after back transforms of the Pu-Fe peak for Pu-maghemite and 2 Pu-magnetite samples.*

Table 3.6.1. List of Pu-hematite and Pu-goethite samples to be discussed in this chapter.

Table 3.6.2. Oxidation state analysis of the XANES region of Pu-hematite and Pu-goethite spectra using linear combination (LC) fitting in the range 18040 – 18100 eV. Aqueous Pu(III), Pu(IV) and Pu(V) species are used as references.

Table 3.6.3. Oxidation state distribution in Pu-hematite and Pu-goethite samples according to analysis of the XANES region (18040 – 18100 eV) by Iterative Target Testing (ITT) using a) Pu(III)aq, Pu(IV)aq and Pu(V)aq or b) Pu(IV)aq and Pu(V)aq as references.

Table 3.6.4. Standard deviation (SD) of Pu-hematite and goethite spectra fits (LC) and reproductions (ITT) and of reference spectra reproductions (ITT).

Table 3.6.5. Shell fitting results of Pu-hematite and Pu-goethite and of 2 artificial oxidation state mixture spectra. Also given is the correlation factor between CN and DW for Pu-O and/or Pu-Fe paths.*

Table 4.1.1. Overview of experiments undertaken to investigate the sorption of Sb(V) to mackinawite as a function of time, pH and initial Sb concentration.

Table 4.1.2. Experimental conditions for XAS-experiment A

Table 4.1.3. Experimental conditions for XAS-experiment B.

Table 4.2.1. Gibbs free energies of formation for species used to calculate the diagrams in figures 4.1 to 4.3.

Table 4.2.2. Equations and logK values used to compute diagrams in Fig. 4.1 to 4.3. logK values are based on $\Delta_f G$ values from Table 4.4; for equilibria containing FeS(am) and $Fe(OH)_3$am logK are based on $\Delta_f G$ = -81.5 kJ/mol and -692 kJ/mol, respectively. The equations in the bottom row indicates how, for each pH value, a H_2S(aq) concentration was computed. Based on this concentration, concentrations for HS^- and S^{2-} and Fe^{2+} were computed. Based on Fe^{2+} obtained as a function of H_2S(aq), concentrations for all other Fe(II) species were calculated. pH steps of 0.1 unit were used. No ionic strength correction was carried out for the calculation of the diagrams in Fig. 4.1 to 4.3. As for each pH, all sulfide species have a specific value corresponding to the H_2S - HS^- - S^{2-} equilibria, equations based on either of them yield the same pe for a given pH. Thus only equilibria including HS^- are given.

Table 4.4.1. Composition analysis by ITT of the Xb_ac and Xb_bas samples using Xb_ac_2 and Sb(V) adsorbed on hematite as references, containing 100 % of factor 1 and factor 2, respectively. Energy range: 30460 eV to 30555 eV.

Table 4.4.2. Shell fitting results for samples Xb_ac_2, Xb_bas1 and Xb_bas_4.